CHEMICAL REACTIONS AT AQUEOUS INTERFACES

Thesis by

Chad David Vecitis

In Partial Fulfillment of the Requirements

for the Degree of

Doctor of Philosophy

California Institute of Technology

Pasadena, California

2009

(Defended March 13th, 2009)

..:: dedicated to my family ::..
ccclskk

ACKNOWLEDGEMENTS

Over the last six years as a graduate student at Caltech I have learned a great deal not only about science and academics, but also about myself, and for this I give thanks. First and foremost, I must thank Professor Michael Hoffmann, a model advisor and a great friend. Professor Hoffmann allowed me the freedom to research a variety of topics in environmental chemistry and discover my path. This freedom led to a broad knowledge of the global environment, a variety of roles in collaborative projects, and an extensive publication list. Professor Hoffmann gave me opportunities such as scientifically leading a research project, teaching a graduate-level class, and giving presentations at conferences and renowned institutions. All of these experiences, which were very nerve-wracking at the time, have made me prepared and confident to take on a scientific career. I have learned a great deal from Professor Hoffmann directly and by subtle or not-so-subtle example. Professor Hoffmann has also been a great friend and was always ready to listen and advise on personal issues. We bonded over many things such as our grand ol' birthplace (Wisconsin) and shared many good times, such as side adventures on conference trips (Kegel's Inn). It has been a great experience as well as an honor and privilege to work in the Hoffmann Lab at Caltech.

During my time at Caltech, I have also had the honor to work with a number of mentors. Dr. Brian Mader of 3M Company Environmental Laboratory taught me a great deal about industrial-environmental and industrial-academic relations, the importance of being well prepared well ahead of time, and the value of simplicity and cost efficacy in engineering solutions. The collaboration with 3M allowed me the opportunity to lead a scientific project, and Dr. Mader always gave me the respect and support needed to

succeed. We also have shared a number of good times outside the workplace, such as Death Cab in Minneapolis and the Hookah Café in New Orleans. Dr. Agustín Colussi, a Senior Research Associate at Caltech, has a great passion for science and taught me the value of pre-experiment research, that even the simplest experiments can yield valuable results, and helped me develop the poise to defend myself academically. Dr. Nathan Dalleska of the Environmental Analytical Center at Caltech taught me about analytical chemistry, and in particular the joys of mass spectrometry, by answering all of my continual questions and allowing me to take apart, reconfigure and attempt to put back together the instruments under his watch. As Dr. Dalleska's Environmental Organic Chemistry TA, I learned a great deal on class instruction and the difficulties of maintaining student interest. And how could I forget the fun of hitting balls on the tennis court and the short, but sweet, sailing career. I would also like to thank my thesis committee of Professor Vincent McKoy, Professor Nathan Lewis, and Professor Jack Beauchamp for taking the time to read my work, give helpful comments and suggestions and listen to my arguments.

I owe many thanks to Jie Cheng and Professor Hyunwoong Park, with whom I have collaborated on a number of projects. We made a great team on the fluorochemical remediation project! And I think I still owe them a dinner. Jie and I initially worked together on the ozone-electrospray project, which resulted in my first co-authored papers at Caltech. I enjoyed the Chinese dinners with Jie and Li, even if my brother was scared, and the Wii was always a fun time. Professor HP and I also collaborated on the electrochemistry project and he showed by example the value of hard work. We had many great discussions about science and life over morning coffee and I appreciated his sound advice. Dr. Shinichi Enami and I collaborated on the ozone-electrospray project and he was always ready for a beer or two. I would like to thank Tammy Campbell for allowing me to mentor her on the fluorochemical project. Tammy's success has given me confidence for my future academic endeavors. I worked with Fabien Paulot on flow tube construction and he was always up for a good chemistry discussion. Dr. Yajuan Wang collaborated on AFFF sonolysis and assembled a great dim sum. It was a pleasure to work with Professor Eileen Spain and Keegan Nelson of Occidental College. I would also like to thank collaborators Professor Wonyong Choi, golf enthusiast, and Dr. Oleh Weres.

My graduate experience at Caltech was enjoyable due to all the friendly and helpful members of the Hoffmann and Keck labs. We spent many group meetings, celebrations at the Hoffmann house, and Friday nights at the Ath together. Dr. Timothy Lesko enthusiastically introduced me to the labs and everyone involved. Dr. Christopher Boxe has shared many insightful post-Caltech experiences. Dr. Marcelo Guzman had a good attitude on life and new perspective on any situation. Dr. Su Young Ryu always had something interesting to say and could put together an excellent Korean meal. Dr. William Balcerski was a good conversation, if available. Jina Choi always brought a smile to the lab. Will Ford was a dutiful GSC chair and added a dash of spice to Keck 4. Professor Janet Hering and her lab group gave helpful comments and suggestions during group meetings. Rich Wildman's organization of EHS and Swiss hospitality were both great experiences. I thank Fran Matzen, Cecilia Gamboa, Linda Scott, and Mike Vondrus for keeping the lab and department running smoothly. And I'd like to thank those who inspired me to undertake a scientific career, my undergraduate research advisor, Professor Howard Fairbrother, and my Science Olympiad coach, Al Stawicki, a.k.a. The Great Pheoc.

I would also like to thank my running crew for making sure I had some fun and kept my sanity over the years. This goes out to Dr. David Ebner, Dr. Erik Rodriguez, Dr. Gavin Murphy, Dr. Cristal Gama, Dr. Heather Murrey, Adam Dennis, and Tammy Campbell. We had many exciting times together and I'm sure the memories will make great stories one day. And Erik has the pictures to make sure we remember them all! I also had many good times with Philippe Martiny, Ryan Songco, Sky Rashby, and Will Ford. Special thanks go out to the lovely Katherine Sirles for her persistence and dedication, which brought us together and for going through the tail end of the journey with me, which has been a bit more difficult than expected.

Finally, I would like to thank my family for their constant support of my academic ventures from the beginning to the present. None of this would have been possible without them. We have had many good times including but not limited to Caribbean cruises, birthdays in Vegas, adventures in Mexico, and Wisconsin fun. I especially thank my parents for all of their hard work over the years. Thank you!

ABSTRACT

Interfaces or phase boundaries are a unique chemical environment relative to individual gas, liquid, or solid phases. Interfacial reaction mechanisms and kinetics are often at variance with homogeneous chemistry due to mass transfer, molecular orientation, and catalytic effects. Aqueous interfaces are a common subject of environmental science and engineering research, and three environmentally relevant aqueous interfaces are investigated in this thesis: 1) fluorochemical sonochemistry (bubble-water), 2) aqueous aerosol ozonation (gas-water droplet), and 3) electrolytic hydrogen production and simultaneous organic oxidation (water-metal/semiconductor). Direct interfacial analysis under environmentally relevant conditions is difficult, since most surface-specific techniques require relatively 'extreme' conditions. Thus, the experimental investigations here focus on the development of chemical reactors and analytical techniques for the completion of time/concentration-dependent measurements of reactants and their products. Kinetic modeling, estimations, and/or correlations were used to extract information on interfacially relevant processes.

We found that interfacial chemistry was determined to be the rate-limiting step to a subsequent series of relatively fast homogeneous reactions, for example: 1) Pyrolytic cleavage of the ionic headgroup of perfluorooctanesulfonate (PFOS) and perfluorooctanoate (PFOA) adsorbed to cavitating bubble-water interfaces during sonolysis was the rate-determining step in transformation to their inorganic constituents CO, CO_2, and F^-; 2) $O_{3(g)}$ oxidation of $I^-_{(aq)}$ to $HOI_{(aq)}$ at the aerosol-gas interface is the rate-determining step in the oxidation of $Br^-_{(aq)}$ and $Cl^-_{(aq)}$ to dihalogens; 3) Electrolytic formation of $>TiOH^\bullet$ groups at the BiO_x-TiO_2/Ti anode is rate-limiting for the overall

oxidation of organics by the dichloride radical, $Cl_2^{\bullet -}$. We also found chemistry unique to the interface, for example: 1) Adsorption of dilute $PFOS_{(aq)}$ and $PFOA_{(aq)}$ to acoustically cavitating bubble interfaces was greater than equilibrium expectations due to high-velocity bubble radial oscillations; 2) Relative $O_{3(g)}$ oxidation kinetics of $I^-_{(aq)}$ and SO_3^{2-} /$S_2O_3^{2-}$ were at variance with previously reported bulk aqueous kinetics; 3) Organics that directly chelated with the BiO_x-TiO_2/Ti anode were oxidized by direct electron transfer, resulting in immediate CO_2 production but slower overall oxidation kinetics. Chemical reactions at aqueous interfaces can be the rate-limiting step of a reaction network and often display novel mechanisms and kinetics as compared to homogeneous chemistry.

TABLE OF CONTENTS

LIST OF FIGURES

LIST OF TABLES

LIST OF SCHEMES

SCHEME PAGE

Chapter 1

Introduction and Summary

Introduction to Interfacial Chemistry

The general subject of this thesis is to investigate environmentally relevant reaction mechanisms and kinetics at aqueous interfaces and to demonstrate that in many cases heterogeneous chemistry may be just as, or more, important than homogeneous chemistry. Chemical reaction models tend to focus on homogeneous chemistry, as the fraction of total molecules associated with an interface is generally very small. However, there are cases when interfacial processes should be taken into consideration, such as when mass transfer between phases is rate-limiting and/or when reactions undergo surface catalysis. Recent observations have shown that interfacial chemical reaction mechanisms and kinetics are at variance with results from homogeneous systems.

Mass-transfer limitations can lead to interfacially dominated processes. The most obvious case is that of reactions at gas-solid and liquid-solid interfaces, since diffusion into amorphous and crystalline solids is negligible at standard temperatures and pressures. Biphasic reactions are therefore limited to the interface between the gas or liquid and solid. Similar mass-transfer limitations are active for gas-liquid interfaces. In particular, the air-water interface has been the focus of many recent experimental and computational studies. The distinct differences between gas-phase and aqueous-phase bulk properties lead to strong chemical partitioning between phases. Thus, most chemical species will be found predominantly either in the gas phase, such as nonpolar and large molecules, or in the aqueous phase, such as ions and hydrogen-bond donors and/or acceptors. Thermodynamically, the partitioning is mediated by a balance between the hydrogen bonds lost when forming a water cavity for the solute and the added intermolecular interactions between water and the solute. Some specific examples, with a focus on aqueous aerosols, of gas-interface-water partitioning and their implications for interfacial chemistry are given below.

Scheme 1.1. Representation of a collision of an ozone molecule with an air-water interface

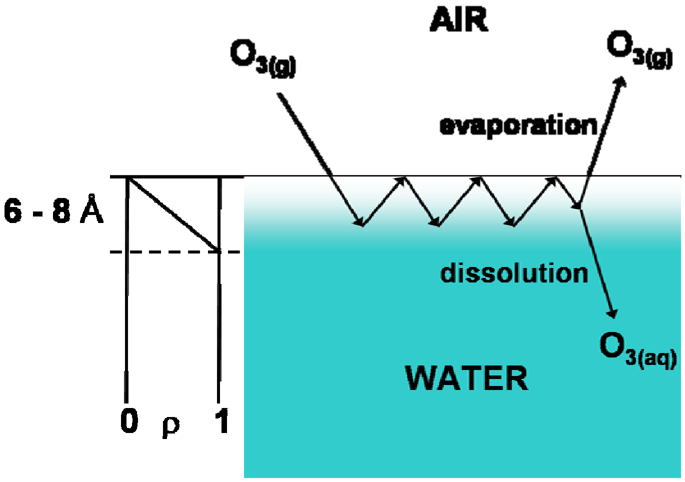

Low molecular weight, nonpolar molecules will preferentially partition into the gaseous phase. For example, the atmospherically relevant gaseous oxidant ozone is found at surface concentrations in the range of 10 to 100 ppt and has an air-water partitioning or Henry's constant, $K_{\text{a-w/H}}^{\text{Ozone}} = 0.0094\,\text{mol/kg/bar}$, yielding $O_{3(g)}/O_{3(aq)}$ = 5 for equal volumes of air and water. The maximal sea spray aerosol-volume-to-air volume ratio in the marine boundary layer is in the range of 100 μL/m^3 or 10^{-7} v/v, which is similar to maximal aerosol-to-gas volume ratios in clouds. Although the majority of the ozone molecules will be in the gas phase, it does not preclude heterogeneous reactions. Gaseous ozone molecules will frequently collide with aerosol interfaces, at 10^{-7} v/v : aerosol/water once per second, with an aerosol surface, and spend a short amount of time at the air-water interface before preferentially diffusing back into the gas phase. (See Scheme 1.1.) Gaseous ozone will undergo 100 to 1000 collisions with 'pure' water droplets before dissolution, thus there are many opportunities for the gaseous ozone molecule to react at the air-water interface.

Mass-transfer effects are not only observed in transferring from air to water, but also in transferring from water to air. Non-polar molecules that are either very high in molecular weight or that also contain an ionic functional group will preferentially accumulate at the air-water interface as the evaporation rate is limited by mass or hydration energy, respectively. Assuming the interfacial layers are limited to monolayers, the surface partitioning can be modeled with a Langmuir isotherm, eq. 1.1.

$$\Gamma^{X}(\mathrm{mol/m^2}) = \Gamma^{X}_{\mathrm{MAX}} \frac{K^{X}_{\mathrm{eq}}[X]}{1 + K^{X}_{\mathrm{eq}}[X]} \qquad (1.1)$$

Γ^{X} is the surface concentration of x in moles/m^2, $\Gamma^{X}_{\mathrm{MAX}}$ is the maximum possible surface concentration of x in moles/m^2, [X] is the bulk concentration of x, and K^{X}_{eq} is the bulk-water to air-water interfacial partitioning coefficient in M^{-1}. The air-water interface partitioning effects will be relevant for bubbles and aerosols, both of which have been examined in this thesis, where the surface-area-to-volume ratio is relatively large. Using the aerosol example again, in Table 1.1, the aqueous aerosol radius required for more

Table 1.1. Langmuir isotherm parameters for a number of hydrocarbons and fluorocarbons

	Γ_{max} (mol/m^2)	**K (M^{-1})**	**r (μm)**
Acetate	8.5×10^{-6}	0.17	0.004
Hexanoate	6.3×10^{-6}	67	1.2
Decanoate	8.5×10^{-6}	2,000	43
Fulvic Acids	3.2×10^{-6}	1,200	11
Na-SDS	10×10^{-6}	110	3.3
Na-SDS (0.5 M NaCl)	3.7×10^{-6}	180,000	710
PFOS	5.0×10^{-6}	1870	28
PFHS	5.7×10^{-6}	160	2.7
PFBS	4.4×10^{-6}	40	0.53
PFOA	4.4×10^{-6}	360	4.7
PFHA	4.8×10^{-6}	76	1.0
PFBA	2.9×10^{-6}	32	0.42

than 99% of various organics at under surface saturation concentrations can be found at the air-water interface vs. bulk water.

In the first half of Table 1.1, the droplet radius values for number of hydrocarbons are listed. In all cases except acetate, at an aqueous droplet radius greater than 1 micron, the organic will be predominantly found at the interface. As the average radius of marine boundary layer droplets is 2 micron, most environmentally relevant marine organics (see fulvics) will be associated with droplet interfaces. The results for sodium dodecyl sulfate (SDS) are shown for both 'pure' water and typical marine ionic strengths (0.5 M). It is of note that in the high ionic strength system, the 'salting out' effect increases the SDS air-water interfacial partitioning coefficient by over three orders of magnitude. In the second half of Table 1.1 is listed the Langmuir isotherm parameters for a series of perfluorinated surfactants, which are the subject of a number of chapters of this thesis. It is of note that perfluoroctanesulfonate (PFOS$^-$, $CF_3(CF_2)_7SO_3^-$) and perfluorooctanoate (PFOA, $CF_3(CF_2)_6CO_2^-$) have 8 and 7 hydrophobic tail carbons, respectively, yet both have greater air-water-interface partition coefficients as compared to the hydrocarbon SDS, which has 12 tail carbons. PFOS has a similar partitioning coefficient to decanoate, which has 9 tail carbons.

Scheme 1.2. Representation of perpendicular and parallel orientations of naphthalene at the air-water interface

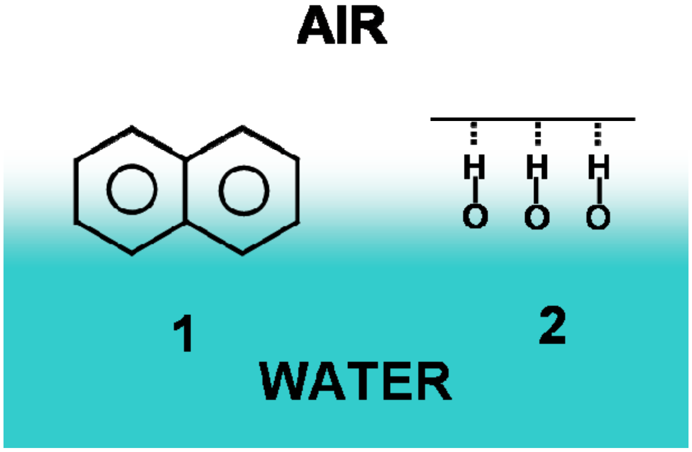

Organics adsorbed at an air-water interface will have a specific molecular orientation. For example, in Scheme 1.2 the perpendicular (1) and parallel planar (2) orientations of naphthalene at the air-water interface are depicted. Due to hydrogen bonding with the conjugated p-orbitals and lower energy of bulk water cavity formation, the parallel planar configuration is preferred. Another example of molecular orientation of chemicals at the air-water interface is that of surfactants such as sodium dodecyl sulfate ($CH_3(CH_2)_{11}OSO_3^-Na^+$, SDS), which are composed of a hydrophobic alkyl tail and a hydrophilic anionic headgroup. SDS preferentially partitions to the air-water interface since the hydrophobic tail is pushed out of the bulk aqueous phase, yet the hydrophilic sulfate group is anchored to the bulk aqueous phase. At low surface concentrations, the hydrophobic tail lays down flat against the air-water interface to maximize its intermolecular interactions through van-der-waals-dipole forces with the interfacial water molecules. At high surface concentrations, the hydrophobic tails pack closely and align themselves nearly perpendicular to the air-water interface (Scheme 1.3). The alkyl tail hydrophobicity and tail-tail interactions are great enough such that the tails act like ‘buoys’ that pull the hydrophilic headgroups closer to the air-water interface and each other than would be predicted by only Coulombic repulsion. It is expected that both

Scheme 1.3. Representation of SDS molecular orientation at low and high air-water interface concentrations.

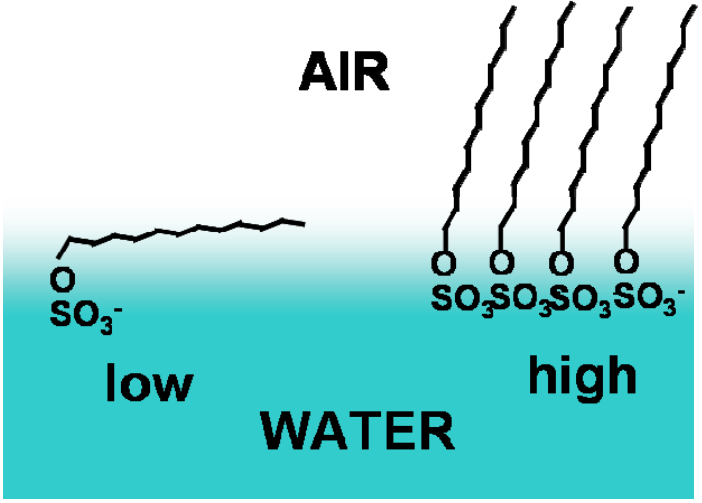

interfacial partitioning (mass transfer) and molecular orientation at the interface will to some extent affect chemical mechanisms and kinetics, as compared to previously determined bulk chemistry.

Mass transfer limitations act to limit homogeneous chemical kinetics, necessitating chemistry at the interface between two phases. The partitioning of a particular chemical is usually easy to experimentally measure or even calculate through simple thermodynamic estimations. Thus, it is easy to answer the question of ‘where’ a reaction is most likely to occur in terms of homogenously or heterogeneously. If the answer to this question is an interface between two distinct phases, then questions follow, such as; How do we predict the chemical mechanism and kinetics? How do we experimentally investigate the interface of low site density as compared to the bulk phases? And so on. Many of these questions have been answered for solid interfaces, where low instrumental penetration depths can allow for surface specific analyses and diffusion in the bulk is negligible. However, when dealing with the more fluid air-water interface, surface-specific analyses become more difficult.

In this thesis, the kinetic and mechanistic relevance of interfacial aqueous chemistry to the overall observed chemistry is evaluated for a number of environmentally relevant systems. Reaction mechanisms and kinetics are investigated using time-dependent reactant and product analyses of batch chemical reactions. The chemical reaction time-dependencies are fit to kinetic models, which give insight into the plausible chemical mechanisms. This procedure is applied to various initial reactor conditions such as applied power, reactant speciation, reactant concentrations, etc., to make more in-depth conclusions about the observed chemistry. In most cases, it is determined that the aqueous interface chemistry dominates the overall reaction chemistry, primarily due to mass transfer effects. In some cases, the interfacial mechanisms and kinetics are determined to be unique as compared to previously determined homogeneous chemistry. The detailed results of the thesis are briefly overviewed in the following section.

Thesis Overview

Chemical reactions at air-water and at water-solid interfaces were examined for three environmentally relevant systems and are presented in the chapters in this order: 1) sonochemical remediation of aqueous fluorochemicals, 2) gaseous ozone oxidation of marine aerosol anions, and 3) electrochemical water-splitting for simultaneous hydrogen production and organic oxidation. Sonochemical remediation of fluorochemicals (1) involves the partitioning of fluorochemicals to the air-water interface of acoustically cavitating bubbles where they are pyrolytically destroyed. The thesis examines how this air-water interface partitioning mediates sonochemical transformation kinetics and how the adsorption kinetics is affected by high-velocity bubble oscillations. Gaseous ozone oxidation of marine aerosol species (2) is observed to primarily occur at the air-water interface. The short-lived products and intermediates suggest that interfacial ozone oxidation kinetics and mechanisms may be at variance with bulk aqueous chemistry. Electrochemical water splitting for hydrogen production using organic waste as a sacrificial electron donor (3) involves reactions at water-metal and water-semiconductor interfaces. Sections of most of the subsequent chapters have been published as scientific papers in journals such as the *Journal of Physical Chemistry* and *Chemical Physics Letters*.

Remediation of aqueous fluorochemicals and in particular PFOS and PFOA is the subject of Chapters 2 to 5. The chapters are results from a project that was funded by 3M, who used fluorochemicals in their formulations of stain-resistant coatings. My role in this project, was as scientific lead in determining the direction and objectives of the project and primary contact with 3M. I was the editor of all scientific papers (Chapter 2 will be submitted to ES&T, Chapters 3 to 5 are in press, a paper first-authored by graduate student Jie Cheng is in press, and at least eight more papers will be submitted for peer review in the near future). I also developed and maintained the primary analytical technique, HPLC-MS, used to analyze all fluorochemicals in question. Iwill now briefly review the subject of each chapter.

Chapter 2 is a review of the methods reported for the remediation of aqueous PFOS and PFOA. It is divided into removal, reductive, oxidative, and thermal methods, with the most promising degradation methods evaluated in terms of products, reaction kinetics, competition effects, and energy consumption. The most efficient destruction methods (persulfate photolysis, iodide photolysis, direct photolysis, sonolysis) still require at least 10,000,000 kJ/mol to transform PFOS and PFOA into their inorganic constituents, which is 3 to 4 orders of magnitude greater than the energy required to synthesize PFOS and PFOA electrochemically.

Chapter 3 investigates the sonochemical transformation of PFOS and PFOA into their mineralization products or inorganic constituents through time-dependent product analyses and kinetic estimations. The initial rate-determining step is determined to involve pyrolytic cleavage of the ionic headgroup at the acoustically cavitating bubble-water interface. The neutral, fluorochemical product partitions to the transiently cavitating bubble vapor where temperatures can near 4000 K. The neutral, fluorochemical intermediate is quickly transformed into CO, CO_2, and HF through a series of pyrolytic, oxidative, and reductive pathways. HF will hydrolyze to a proton and fluoride. PFOS and PFOA mineralization kinetics were determined to be similar to initial PFOS and PFOA sonochemical decomposition kinetics, thus precluding the formation of any toxic intermediates.

Chapter 4 examines the adsorption of PFOS and PFOA to acoustically cavitating bubbles. The absolute sonochemical rate dependence on the initial PFOS/PFOA concentration was fit to the Langmuir-Hinshelwood model using empirically determined rate maximums. The air-water interfacial partitioning coefficient determined from the observed sonochemical kinetics was at variance with the equilibrium partitioning coefficient determined from surface tension measurements. This lead to the conclusion that when the bubble interface is lightly populated with PFOS and PFOA, the adsorption is sonochemically mediated due to high velocity radial bubble oscillations being much faster than bulk diffusion.

Chapter 5 investigates the decomposition kinetics and products of PFOS, PFOA, and shorter-chain fluorochemicals (C_6 and C_4) by aqueous electrons. Aqueous electrons are generated by UV photolysis of iodide and are observed to react with PFOS faster than PFOA in batch reactions. The perfluoroalkylsulfonates (PFAS) are observed to have prominent chain-length effects, whereas the perfluoroalkylcarboxylates (PFAC) had no such effects. The PFAS chain length affected the extent of defluorination (e.g., the number of fluorides produced was approximately the number of tail carbons), in contrast, all of the PFACs proceeded through 1 to 2 defluorinations. As PFAS chain-length decreased, so did the initial PFAS reduction kinetics. In contrast, PFAC chain length had no effect on reduction kinetics. Gaseous PFAS and PFAC reduction products were consistent with extent of defluorination.

The chemistry of aqueous, aerosol anions is the subject of Chapters 6 to 9. This was the first project I worked on in the Hoffmann Lab and the initial objective was quite different than the now published scientific papers. Experimental kinetic isotope effects and kinetic simulations of peroxone (ozone + hydrogen peroxide) chemistry suggested that the primary branching pathway of O_3-H_2O_2 reaction yielded H_2O_3. I developed an electrospray-mass-spectrometry-based (ES-MS) technique to monitor the products of this reaction on relatively short timescales, 1 to 10 ms. The ozone-ES-MS reactor can be thought of as a gas-aerosol stopped-flow reactor. The electrospray chamber was modified such that a Teflon ozone tube was brought into the chamber and held in place by a Teflon piece attached to the nebulizer needle, which only minimally affected the MS sensitivity. Although I have stated this work in a single sentence, the modification and optimization of the ozone-ES-MS system took nearly a year and a half. At $[H_2O_2] > 100$ mM, H_2O_2 could be detected mass spectrometrically as a positive cluster on the form $(H_2O)_m(H_2O_2)_nNa^+$. Initially, we believed we had detected H_2O_3 as a reaction product; however, it was an artifact of the ozone generator. Although the initial project did not come to fruition, the developed ozone-ES-MS system has now been utilized for examination of a number of gaseous oxidant-aqueous aerosol reactions.

After a seminar in Atmospheric Chemistry II where I suggested the developed system could be utilized for research into reactions specific to the air-water interface, graduate student Jie Cheng and I completed the initial ozone-ES-MS experiments on the gaseous ozone oxidation of aqueous iodide, which yielded some very interesting results. Since then the ozone-ES-MS system has been used to study reactions of gaseous ozone with sulfite, thiosulfate, iodide, ascorbic acid, tocopherol, and various combinations of these aqueous species, as well as to study reactions of gaseous NO_2 with various anions. Results have given insight into the importance of the air-water interface to aerosol reactions with low solubility gaseous oxidants and how the air-water interface affects chemical mechanisms and kinetics as compared to bulk aqueous or gaseous chemistry. There are some questions about the applicability of the results to real situations, as the reactions take place under a large electric field (> kV/cm).

As a result of developing the ozone-ES-MS system, researching the pertinent experiments (particularly those involving ozone and iodide), and teaching others how to operate and maintain the system, I was co-author on four scientific papers, three of which are included in this thesis. The first examined anion fractionation during the electrospray of aqueous anions (Cheng J.; Vecitis, C. D.; Colussi, A. J.; Hoffmann, M. R. *J. Phys. Chem. B,* **2006**, *110,* 25598.) and is not included in this thesis. It was observed that when equimolar anions were electrosprayed, the relative fractionation, as determined by relative mass spectrometric signal intensity, was correlated to anion radius or hydration energy and followed the Hofmeister series.

The second published scientific paper, Chapter 9, investigated the iodide-mediated gaseous ozone oxidation of bromide and chloride in aqueous aerosols. Aerosolic iodide reacts at diffusion-controlled rates with gaseous ozone to yield triiodide, I_3^-, and iodate, IO_3^-. Bromide and chloride are kinetically unreactive towards ozone alone; however, in the presence of iodide, dibromoiodide (IBr_2^-), and dichloroiodide, (ICl_2^-), are detected as reaction products, respectively. This suggests that iodide can mediate the gaseous ozone oxidation of aerosolic bromide and chloride, likely through the production of the promiscuous hypoiodous acid, HOI, which oxidizes most species at diffusion-controlled rates. These reactions could possibly yield gaseous species such as ICl, IBr, Br_2, and Cl_2. These species would be quickly photolyzed ($\tau_{1/2} \sim 1$ to 2 min) in the atmosphere, yielding halogen radicals that could contribute to catalytic ozone destruction cycles, which are of importance to arctic ozone depletion events during polar sunrise, and general tropospheric ozone levels.

Chapters 7 and 8 encompass reactions of aqueous aerosolic thiosulfate ($S_2O_3^{2-}$) and sulfite (SO_3^{2-}) with gaseous ozone with and without iodide. The results of both are similar in many respects. Kinetic modeling of gaseous ozone oxidation of both $S_2O_3^{2-}$ and SO_3^{2-} suggests that the reaction predominantly (> 90%) occurs at the air-water interface. In both cases, intermediates containing I-S bonds are directly detected for the first time, indicating that an iodine-containing intermediate, likely HOI, can quickly oxidize both $S_2O_3^{2-}$ and SO_3^{2-}. This result is similar to that of Br^- and Cl^-, suggesting a 'universal' iodide-mediated oxidation pathway via the hypoiodous acid (HOI) intermediate. In both cases, results from competition experiments suggest that either the interfacial ozone reaction with $S_2O_3^{2-}$ and SO_3^{2-} is enhanced vs. the bulk reaction or that interfacial ozone reaction with I^- is reduced, with the former being more likely than the latter since the bulk aqueous kinetics underestimate the measured product intensity from $O_{3(g)} + I^-_{(aer)}$ experiments. Overall these experiments display the importance of the air-water interface as a reaction 'zone' for chemistry between marine aerosols and gaseous oxidants such as ozone.

The final three chapters, 9 to 11, of this thesis focus on the hybridized electrochemical system for the production of hydrogen (H_2) and simultaneous degradation of organic pollutants. I worked on this project during my last few years at Caltech in collaboration with Dr. Hyunwoong Park. My role in the project was to develop analytical techniques and procedures (realtime EI-MS for monitoring gas products and HPLC-UV for analysis of phenol and phenol derivatives), manuscript editing, and discussion of results. The water-solid (metal-cathode, metal-oxide-anode) interface is vital, since all of the observed electrochemistry will initiate at these interfaces. Electron transfer activation barriers across the water-solid interface will mediate the energy required to drive observed chemistry. Energetic losses will occur if the oxidants produced at the metal oxide surface subsequently yield lower potential homogeneous oxidants (e.g., $\equiv$Ti-OH· ($E^0 = 2.7$ V) → $Cl_2\cdot^-$ ($E^0 = 2.0$ V)) or homogenous oxidants are quenched at the cathodic surface (e.g., $Cl_2\cdot^- + e^- \rightarrow 2\ Cl^-$).

Chapter 9 serves as a brief introduction to the idea of hybridizing alternative energy production with wastewater treatment. Electrolytic hydrogen (H_2) production is less economically viable than battery storage due to energetic losses during electrolytic H_2 production and its transformation back to electrical energy. By hybridizing electrolytic H_2 production with wastewater treatment, some of these losses will be negated by cleansing the water. An electrochemical system composed of a stainless steel cathode for H_2 production and a Bi-doped TiO_2 anode for oxidant production is presented. Results show that the hybrid system has H_2 production energy efficiencies (30% to 70%) that compete with commercial electrolyzers (50% to 75%), which operate under more extreme conditions (50 mM NaCl, $6 < pH < 11$, 1 atm vs. 1 M NaOH, $pH > 13$, 20 atm).

It is shown that the system can degrade a number of common organic pollutants such as phenols and small acids. The electrochemical system can also be driven by a photovoltaic cell. Chapter 10 elaborates on the results of Chapter 9. The effects of variations in electrochemical cell current, voltage, and power, and initial phenol concentration on the H_2 and O_2 production rates, and current and energy efficiencies was investigated. Time-dependent electrolysis measurements of phenol, phenol oxidation intermediates, pH, total organic carbon (TOC), and mineralization products (CO_2) were also made. Maximum cathodic H_2 production current efficiencies were near 60% without phenol, near 70% with phenol with NaCl as background electrolyte, and reached 95% using Na_2SO_4 as background electrolyte. Anodic current efficiencies ranged from 3% to 17% depending on specific conditions. The hybrid system was shown to be applicable for the degradation of a range of organics, and it was also observed that upon addition of organic with NaCl as an electrolyte, the cathodic current efficiency increased.

Chapter 11 further investigates the primary oxidant in the electrochemical system and how this oxidant is involved in the observed enhancement in cathodic (H_2) current efficiencies upon addition of organics. The phenol electrolytic oxidation intermediates all contain chlorine, with the extent of chlorine increasing with time, indicating a chlorine-based oxidant. The degradation kinetics of a number of phenol derivatives was determined through time-dependent measurements and were plotted against known rate constants for a number of possible oxidants, such as $\cdot OH$, $Cl_2\cdot^-$, $Cl\cdot$, and HOCl. Only known $Cl_2\cdot^-$ second-order rate constants correlated with the observed rate constants, indicating it was the primary oxidant. When no organics are present, it is postulated that $Cl_2\cdot^-$ can act as an electron shuttle and accept electrons at the cathode, thus reducing the

H_2 production current efficiency. Thus, when organics are present and consume $Cl_2{\cdot}^-$, its effect as an electron shuttle is reduced and the H_2 current efficiency subsequently increases.

Through the various areas of study in this thesis, aqueous interfaces are shown to be highly relevant to the chemistry observed. In many cases, the overall rate-limiting step of a chemical reaction series involves an interfacial chemical transformation, which subsequently leads to relatively fast homogeneous chemical kinetics in the liquid or gas phase. Phase transfer limitations of reactive species or mass transfer of species to the most reactive phase is the simplest explanation for interfacial rate determining steps. However, the more difficult question to answer is how these interfacial processes differ mechanistically and kinetically from their homogeneous analogs. Therefore, the cumulative research compiled in this thesis indicates that chemical reactions at aqueous interfaces are an important aspect of many environmentally relevant processes and that much more research is required to fully understand chemical processes occurring at aqueous interfaces.

Chapter 2

Treatment Technologies for Aqueous Perfluorooctanesulfonate (PFOS) and Perfluorooctanoate (PFOA)

Abstract

Fluorochemicals (FCs) are oxidatively recalcitrant and thus environmentally persistent and resistant to most conventional treatment technologies. FCs have unique physiochemical properties derived from fluorine being the most electronegative of elements. Recent concern has grown over the FCs perfluorooctanesulfonate (PFOS) and perfluorooctanoate (PFOA), as they have been detected globally in the hydrosphere, atmosphere, and biosphere. Halting further fluorochemical release into the environment will require improved containment during application and manufacturing processes and remediation of the primary sources such as manufacturing waste. Removal technologies such as reverse osmosis, nanofiltration, and activated carbon can remove FCs from water. Incineration of the concentrated waste is required for complete fluorochemical destruction. Recently, a number of alternative technologies for on-site FC decomposition have been reported. The fluorochemical degradation technologies span a range of chemical processes including direct photolysis, photocatalytic oxidation, photochemical oxidation, photochemical reduction, thermally induced reduction, and sonochemical pyrolysis. We review these FC degradation technologies in terms of kinetics, mechanism, energetic cost, and applicability. The optimal PFOS/PFOA remediation method is strongly dependent upon the initial FC concentration, background organic and metal concentration, and available degradation time.

Introduction

Fluorochemicals (FCs) have a wide variety of applications such as inert, nonstick polymers (e.g., telfon), water- and stain- proof coatings for paper and textiles (e.g., Scotchguard), oxidative protective coatings on metals, inert surfactants for semi-conductor etching, aqueous film forming foams (AFFFs), and thermally stable lubricants. The diverse FC applications are due to the unique physiochemical properties[1-3] gained upon replacing the majority of the hydrogens in an organic with fluorines. Organic poly-, and moreso, per-, fluorination yields a more thermally stable (i.e., C_2H_5-H 101 kcal/mol vs. C_2F_5-F 127 kcal/mol, and CF_3-CF_3 99 kcal/mol vs. CH_3-CH_3 89 kcal/mol), a more oxidatively resistant (i.e., $F + e \rightarrow F^-$, $E_0 = 3.6$ V)[4], and a weakly polarizable (i.e., $\alpha_{PFOS} = 3.2$ Å^3 vs. $\alpha_{SDS} = 12.4$ Å^3)[5] organic. The thermal and oxidative resistance from fluorination makes fluorochemicals useful for extreme applications such as high-temperature lubricants and AFFFs. The relatively low perfluorochemical polarizability makes fluorochemicals useful for non-stick, protective coatings.

The physiochemical properties of fluorochemicals make them difficult to treat using most conventional remediation strategies[6-8]. Perfluorochemicals (PFCs), organics with all of their hydrogens replaced by fluorines, are particularily recalcitrant and environmentally persistent. For example, atmospheric lifetimes of perfluorinated gases have been estimated to be > 1000 years.[9] Recently, concern has increased over the environmental impact of perfluorinated surfactants such as perfluorooctanoate (PFOA) and perfluorooctanesulfonate (PFOS), or PFOX where (X = S or A). Perfluorinated surfactants have a perfluorinated carbon tail, which preferentially partitions out of the aqueous phase, and an ionic headgroup, which preferentially partitions in to the aqueous phase. Due to their biphasic or surfactant nature, they tend to accumulate at the air-water interface[10-13]. PFOX has been observed to primarily accumulate in the hydrosphere[14-34] and the biosphere[22,24,35-59]. PFOX is released to the environment primarily during manufacturing and coating processes[60], as well as from use of FC-based products[61-65]. PFOX can be indirectly created via atmospheric[66-68], aquatic[69], or biologic transformation[70-74] of fluorotelomer alcohols[75] and fluoroalkylsulfonamides[76,77]. Recent data suggests the phasing-out of the production of PFOS and PFOA in 2000 by 3M[78] and later by DuPont has reduced their proliferation in the environment[53,66,77,79]. It has been recently shown that landfill leachate from primary fluorochemical disposal sites may also be a source of PFCs tin the environment[80], which is currently treated with granular activated carbon post-WWTP.

The very dilute (i.e., ppt or pM) hydrosphere concentrations of PFOS and PFOA make remediation of the perfluorinated surfactants previously released to and distributed in the environment difficult using most conventional technologies[81]. The onsite control of the primary FC discharges from their primary source (i.e., concentrated manufacturing effluents) is a more viable approach. A number of fluorochemical, specifically PFOS and PFOA, treatment technologies have been evaluated in the literature. Granular activated carbon has been shown to be effective at removing PFOA and PFOS at ppb levels from relatively clean water (i.e., post-WWTP)[6,82] and is utilized today. The activated carbon must then be incinerated[83] to destroy the adsorbed fluorosurfactants. A fraction of the fluorochemicals entering the WWTP will adsorb to the sludge[7,84,85] where anaerobic digestion has a minimal effect on their concentration[86]. The digested sludge may subsequently be disposed of in a landfill, allowing the adsorbed fluorochemicals to be re-released into the environment.

Most conventional degradation technologies are ineffective for the *in situ* degradation of aqueous PFOS and PFOA, since they are inherently recalcitrant to chemical and microbiological treatment[7,8,86–89]. Advanced oxidation processes (AOPs)[90], which utilize the hydroxyl radical,—such as alkaline ozonation, peroxone (i.e., a mixture of O_3 and H_2O_2), or Fenton's reagent (i.e., H_2O_2 and Fe^{2+} salts)—have been shown to be relatively ineffective for PFOA and PFOS destruction[91–93]. A number of photolytic methods, such as direct photolysis[93–99], persulfate photolysis[94,100–102], alkaline isopropanol photolysis[99] ,and photocatalysis[93,103–107] have shown varying degrees of efficacy on higher concentrations of perfluorocarboxylates. Reduction by elemental iron under near super-critical water conditions has been shown to be possible for PFOS degradation. Ultrasonic irradiation of aqueous solutions of PFOS and PFOA[92] has been observed to degrade these compounds. Recently it has been reported that PFOS and PFOA are completely mineralized during this process[108] and that sonolysis can be used effectively for environmentally relevant concentrations and matrices.

We will now overview these techniques in more detail in terms of their viability to remediate and degrade aqueous PFOS and PFOA. These techniques will be reviewed in terms of their reaction conditions, degradation kinetics, degradation products and energy requirements. The techniques will be initially divided into four treatment groups: conventional, oxidative, reductive, and thermal. It is likely that the optimal treatment technology will be highly dependent on initial PFOX concentration (i.e., high for manufacturing waste or low for environmental distribution) and the matrix in question.

Tertiary Water Treatment

Conventional wastewater treatment techniques[109], such as trickling filtration, activated sludge, anaerobic digestion, and chlorination have been reported to have little effect on

PFOA and PFOS mass flows (i.e, $[\mathrm{PFOX}]_{\mathrm{WWTP,influent}} \approx [\mathrm{PFOX}]_{\mathrm{WWTP,effluent}}$[7,8,80,110,111]). Microbial communities can not metabolize PFOS and PFOA[86–89]. In some cases, PFOS and PFOA concentrations were greater in the WWTP effluent as compared to the influent[7,8] which suggest microbial transformation[7,8,111] of fluorosulfonamides such as FOSE and FOSA to PFOS[70–73,110]and fluorotelomer alcohols to PFOA[112], or the release of residual PFOX from disposed products[110]. Incineration[113] of sludge containing PFCs[84,111] is effective for the complete destruction of fluorochemicals and fluoropolymers. Tertiary water treatment technologies such as granular activated carbon (GAC)[6], ion-exchange[82], and reverse osmosis[114,115] have been shown to be effective in removing PFOS from water. GAC[6,80] is currently utilized to remove PFCs from WWTP effluent and effectively removes > 90% of PFOS and PFOA. PFOX equilibrium adsorption to various surfaces is lower than observed for organics of similar molecular weight[116,117]. The adsorption process is observed to be kinetically slow[116]. Isopropanol as a co-solvent was shown to have a deleterious effect on reverse osmosis for the removal of PFOS[114]. In all tertiary treatment cases, a subsequent destruction step such as incineration is required for complete perfluorochemical remediation.

PFOX Oxidation

Perfluorinated chemicals such as PFOS and PFOA are recalcitrant towards oxidation due to the complete substitution of fluorine (C-F bond) for hydrogen (C-H bond). Fluorine is the most electronegative of elements and will retain its electrons (i.e., will resist oxidation) at all cost. Fluorine is nearly always found in the (-1) oxidation state with the only exception being F_2 where its oxidation state is (0). The fluorine atom is the most powerful inorganic oxidant known, with a reduction potential of 3.6 V (eq. 2.1)[4] and thus it is thermodynamically unfavorable to create the fluorine atom with any other one-electron oxidant.

$$F\cdot + e^- \rightarrow F^- \ (E^0 = 3.6 \text{ V}) \quad (2.1)$$

Perfluorination will also reduce the oxidizability of the ionic headgroup ($-SO_3^-$ for PFOS and $-CO_2^-$ for PFOA) since it inductively reduces headgroup electron density. Thus PFOX are quite resistant to oxidation as compared with their alkyl analogs.

Advanced Oxidation Processes—Oxygen-Containing Radicals

For particularily recalcitrant organics, advanced oxidation processes which utilize the hydroxyl radical, ozone, or O-atom are a viable solution[90,118–120]. Hydroxyl radical can be generated through hydrogen peroxide photolysis[121], ozonation[122,123], photo-Fenton's[124], sonolysis[125], and peroxone chemistry[126]. A hydroxyl radical normally reacts with saturated organics through an H-atom abstraction to form water (eq. 2.2) and will react with unsaturated organics primarily via an addition reaction. The hydroxyl radical reacts with most aliphatic and aromatic organics at near diffusion-controlled rates[127]. At environmentally relevant pHs, PFOS and PFOA contain no hydrogens to abstract, thus the hydroxyl radical must act through a direct electron transfer to form the less thermodynamically favored hydroxyl ion (eq. 2.3).

$$HO\cdot + e^- \rightarrow H_2O \ (E^0 = 2.7 \text{ V}) \quad (2.2)$$

$$HO\cdot + e^- \rightarrow HO^- \ (E^0 = 1.9 \text{ V}) \quad (2.3)$$

Thus the perfluorination or substitution of all of the organic hydrogens for fluorines in PFOS and PFOA renders these compounds inert to advanced oxidation techniques[91]. The addition of H_2O_2 is detrimental to the photolytic degradation of PFOA by competitively adsorbing photons[93]. An upper limit for the second-order rate of HO· + PFOA has been estimated to be $k_{HO\cdot + PFOA} \leq 10^5 \text{ M}^{-1} \text{ s}^{-1}$; multiple orders of magnitude slower than the reaction of hydroxyl radical with most hydrocarbons[127]. The futility of conventional advanced oxidation for the degradation of PFOS and PFOA is noted in the use of perfluorinated compounds to enhance advanced oxidation of other organics. PFOS is used as an additive to increase aqueous solubility of PAHs[128,129], enhancing their degradation by UV-H_2O_2. PFOS has also been utilized as a TiO_2 surface coating to increase adsorption of PCBs[130] and chlorinated aromatics[106], leading to enhanced oxidation rates. Biphasic water-perfluorocarbon systems have been utilized to increase organic ozonation rates[131] by increasing dissolved ozone concentrations. Convential advanced oxidation methods utilizing oxygen-based radicals are not practical methods for the decomposition of perfluorochemicals.

Persulfate Photolysis—Sulfate Radical Oxidation

Persulfate photolysis has been utilized for the oxidative degradation of a number of organics[132–136]. Persulfate photolysis[137] or thermolysis[138] generates two sulfate radicals, $SO_4\cdot^-$, (eq. 2.4). The sulfate radical is an oxidizing radical that reacts by a direct one-electron transfer to form sulfate (eq. 2.5). The sulfate radical has a one-electron reduction potential of 2.3 V[4], making it a stronger direct electron transfer oxidant than the hydroxyl radical.

$$S_2O_8^{2-} + h\nu\ (< 270\ \text{nm}) / \Delta \rightarrow 2\ SO_4\cdot^- \qquad (2.4)$$

$$SO_4\cdot^- + e^- \rightarrow SO_4^{2-}\ \ (E^0 = 2.3\ \text{V}) \qquad (2.5)$$

Persulfate photolysis has been utilized to degrade a number of perfluoroalkylcarboxylates of various chain length[94,100–102]. PFOA degradation by sulfate radical oxidation has achieved minimum half-lives on the order of 1 hour, with fluoride accounting for 15% of the total fluorine over the same period of time ($[\text{PFOA}]_i$ = 1.35 mM, $[S_2O_8^{2-}]$ = 50 mM, 9000 W L^{-1}, Xe-Hg lamp, 4.7 atm O_2)[94,100]. The percent of total fluorine as fluoride can be used as a measure of PFOA mineralization.

A reaction mechanism for the sulfate radical mediated degradation of perfluoroalkylcarboxylates was proposed by Kutsuna and Hori[102]. The initial degradation is postulated to occur through an electron transfer from the carboxylate terminal group to the sulfate radical (eq. 2.6). The oxidized PFOA subsequently decarboxylates to form a perfluoroheptyl radical (eq. 2.7), which reacts quantitatively with molecular oxygen to form a perfluoroheptylperoxy radical (eq. 2.8). The perfluoroheptylperoxy radical will react with another perfluoroheptylperoxy radical in solution, since there are no reductants present to yield two perfluoroalkoxy radicals and molecular oxygen (eq. 2.9). The perfluoroheptyloxy has two branching pathways: unimolecular decomposition to yield the perfluorohexyl radical and carbonyl fluoride (eq. 2.10), or an H-atom abstraction from an acid such as HSO_4^- to yield perfluoroheptanol (eq. 2.12). The perfluorohexyl radical formed in eq. 10 will react with O_2 (eq. 2.9) and resume the radical ‘unzipping’ cycle. The COF_2 will hydrolyze to yield CO_2 and two HF (eq. 2.11). The perfluoroheptanol from eq. 2.12 will unimolecularly decompose to give the perfluoroheptylacyl fluoride and HF (eq. 2.13). Perfluoroheptyl acyl fluoride will hydrolyze to yield perfluoroheptanoate (eq. 2.14).

$$CF_3(CF_2)_6COO^- + SO_4\cdot^- \rightarrow CF_3(CF_2)_6COO\cdot + SO_4^{2-} \tag{2.6}$$

$$CF_3(CF_2)_6COO\cdot \rightarrow CF_3(CF_2)_5CF_2\cdot + CO_2 \tag{2.7}$$

$$CF_3(CF_2)_5CF_2\cdot + O_2 \rightarrow CF_3(CF_2)_5CF_2OO\cdot \tag{2.8}$$

$$CF_3(CF_2)_5CF_2OO\cdot + R_FOO\cdot \rightarrow CF_3(CF_2)_5CF_2O\cdot + R_FO\cdot + O_2 \tag{2.9}$$

$$CF_3(CF_2)_5CF_2O\cdot \rightarrow CF_3(CF_2)_4CF_2\cdot + COF_2 \tag{2.10}$$

$$COF_2 + H_2O \rightarrow CO_2 + 2\ HF \tag{2.11}$$

$$CF_3(CF_2)_5CF_2O\cdot + HSO_4^- \rightarrow CF_3(CF_2)_5CF_2OH + SO_4^{\cdot -} \qquad (2.12)$$

$$CF_3(CF_2)_5CF_2OH \rightarrow CF_3(CF_2)_5COF + HF \qquad (2.13)$$

$$CF_3(CF_2)_5COF + H_2O \rightarrow CF_3(CF_2)_5COO^- + HF + H^+ \qquad (2.14)$$

During photolysis, Kutsuna and Hori observed the pH decrease to < 3, due to HF production making eq. 2.12 the major branching pathway (75%). The shorter chain carboxylates produced will be just as recalcitrant as PFOA.

Persulfate photolysis in liquid carbon dioxide/water mixtures[101] has been reported to be a good medium for the degradation of longer chain carboxylic acids normally insoluble in water. Through kinetic modeling of batch reactions, the second-order rate constants of the sulfate radical with various chain-length perfluorocarboxylates have been determined to be on the order of 10^4 M^{-1} s^{-1} [102], consistent with a flash photolysis study[139] which measured sulfate radical reaction with trifluoroacetate to be 1.6 x 10^4 M^{-1} s^{-1}. A relatively slow rate when compared to second-order rates of the sulfate radical with hydrocarbons; short-chain alcohols and carboxylic acids are at the lower end with reaction rates on the order of 10^6 M^{-1} s^{-1} and aromatic organics are at the upper end with reaction rates being diffusion controlled, 10^9-10^{10} M^{-1} s^{-1} [140]. The presence of any other dissolved organic species with aqueous PFOA will competitively inhibit degradation. Persulfate photolysis would be a practical technique for the degradation of 'pure' aqueous PFOA. When other organics are present, significant PFOA degradation will only occur when the PFOA concentration greatly exceeds the total organic concentration ($[PFOA]/[Org]_{total} > 100$). Persulfate photolysis under the previously stated conditions would be a viable decomposition method for perfluoroalkylcarboxylates of all chain lengths, since they have similar second-order kinetics with the sulfate radical[102].

Direct UV Photolysis

Photolysis is chemical bond-breaking driven by light. UV-Vis light adsorption yields an electronically excited molecule. An electronically excited molecule has a bonding (molecular) or non-bonding (atomic) electron promoted to an anti-bonding orbital. An electronically excited molecule is more susceptible to chemical reaction and may open new chemical reaction pathways unavailable to the ground state species. Terrestrial solar-driven photolytic processes require utilization of 290–600 nm photons, due to atmospheric absorption of higher energy light. Organics with large chromophores can be directly photolyzed by solar irradiation[141,142]. Simulated sunlight applied to aqueous solutions of PFOS[97], PFOA[98], and N-EtFOSE[143] for 30 days had no effect on their concentration ($[FC]_i = 100\ \mu M$, $\lambda = 290\text{-}600$ nm, 10 W, 5 W/L). The 8:2 fluorotelomer alcohol did not significantly degrade under direct photolysis[144].

Ultraviolet-C (UV-C, $\lambda < 300$ nm) and vacuum ultraviolet (VUV, $\lambda < 200$ nm) have been utilized for a number of disinfection and advanced oxidation processes[90]. UV-C, generated by a black or germicidal lamp ($\lambda = 250 \pm 10$ nm), is primarily used for indirect photolyses (e.g., persulfate photolysis), disinfection, and in some cases direct photolysis[145]. VUV irradiation is of high enough energy to photodissociate water into an H-atom and HO· (eq. 2.15) with a quantum yield of 0.3 at 185 nm[146,147].

$$H_2O + h\nu\ (\lambda < 200\ \text{nm}) \rightarrow H\cdot + HO\cdot \qquad (2.15)$$

VUV has a very short liquid penetration depth (< 100 μm) due to the strong adsorption by water yielding a strongly oxidizing region near the lamp surface. Organic degradation during VUV photolysis is primarily via HO oxidation[148–150]. Hori et al.[93] reported on the photolytic degradation of PFOA which occurred with a half-life of 24 hrs ($[PFOA]_i$ =

1.35 mM, 200 W Xe-Hg lamp, 22 mL, 4.8 atm O_2). The primary photoproducts were shorter chain carboxylic acids with fluoride accounting for 15% of the decomposed PFOA fluorine after 24 hours. Aqueous PFOA VUV photolysis[94,151] proceeds at a faster rate, having a photolysis half-life of 90 minutes ($[\mathrm{PFOA}]_i = 100$ μM, $\lambda = 254$ nm w/ minor 185 nm, 15 W, 800 mL, pH 3.7, 40 °C, N_2) with fluoride accounting for 12% of the degraded PFOA fluorine. The gas-phase VUV photolysis of trifluoroacetic acid yields CO_2, CF_3, and H-atom as predominant photoproducts (eq. 2.16)[152]. Aqueous PFOA will be dissociated into its ion products at pH 3.7, and direct photolysis will be of the PFOA anion (eq. 2.17), which may unimolecularily decompose to a perfluoro alkyl anion, CO_2 and an aqueous electron which will protonate under the experimental conditions (eq. 2.18).

$$CF_3COOH + h\nu\ (\lambda = 172\ \mathrm{nm}) \rightarrow CF_3COOH^* \rightarrow CF_3\cdot + CO_2 + H\cdot \qquad (2.16)$$

$$CF_3(CF_2)_6COO^- + h\nu\ (\lambda < 220\ \mathrm{nm}) \rightarrow CF_3(CF_2)_6COO^{-*} \qquad (2.17)$$

$$CF_3(CF_2)_6COO^{-*} + H^+ \rightarrow CF_3(CF_2)_6\cdot + CO_2 + H\cdot \qquad (2.18)$$

The hydroxyl radical concentration in the region near the VUV lamp surface may be great enough to also lead to PFOA oxidation and perfluoroalkyl radical formation. Since the photolysis conditions are anoxic (i.e., N_2 atmosphere) the perfluoroalkylradical will react at diffusion-controlled rates with HO produced via water photolysis to form the perfluoroalkyl alcohol (eq. 2.19).

$$CF_3(CF_2)_6\cdot + HO\cdot \rightarrow CF_3(CF_2)_6OH \qquad (2.19)$$

The overall degradation mechanism will occur through similar reactions, as seen in persulfate photolysis (eqs. 2.7–2.14), to yield a perfluoroalkyl carboxylate (PFAC) one -CF_2- unit shorter than the initial species. The produced PFAC will undergo photolysis until the perfluorinated tail is completely unzipped. PFOS photolytic degradation has also been reported[99] and has a slower photolysis rate, half-life of 5.3 days, than PFOA under similar conditions ($[PFOS]_i = 40$ μM, $\lambda = 254$ nm, 32 W, 750 mL, 36–that 40 ^oC, N_2). Shorter chain perfluorocarboxylates and perfluoroalkyl alcohols were detected as reaction intermediates. After 50% of the PFOS is decomposed, fluoride accounts for 59% of the decomposed PFOS fluorine. The greater fluoride mass balance than observed with PFOA is likely due to faster photolysis rates of the PFAC intermediates than of the initial PFOS. Direct photolysis of PFOS and PFOA will be negligible under environmental conditions. Higher energy UV and VUV photolysis can degrade PFOX. Competitive UV light absorption by solvent and other matrix components will limit photolysis rates.

Phosphotungstic Acid Photocatalysis

Phosphotungstic acid, $H_3PW_{12}O_{40}$, is a heteropolyacid or polyoxometalate that has been utilized for photocatalytic degradation of contaminants[153,154] and as an electron shuttle[155–157]. $PW_{12}O_{40}^{3-}$ is the predominant form when pH < 2 and absorbs light with $\lambda < 390$ nm. Upon light adsorption, $PW_{12}O_{40}^{3-}$ enters a photo-excited state enhancing its oxidation strength (eq. 2.20).

$$PW_{12}O_{40}^{3-} + h\nu\ (< 390\ \text{nm}) \rightarrow PW_{12}O_{40}^{3-*} \tag{2.20}$$

PFOA[93], PFPA[104], and TFA[158] have been reported to be decomposed by $H_3PW_{12}O_{40}$ photocatalysis. PFOA has half-life of 24 hours during phosphotungstic acid photolysis ($[PFOA]_i = 1.35$ mM, $[H_3PW_{12}O_{40}] = 6.7$ mM, pH < 2, 9000 W L^{-1}, Xe-Hg lamp, 4.8 atm O_2). After 24 hours of photolysis when 50% of the PFOA is degraded, fluoride accounts for 20% of the total fluorine. The extent of fluoride production is similar to that observed during persulfate photolysis, suggesting a similar degradation mechanism where the carboxylate headgroup is oxidatively removed and a shorter-chain perfluoroalkylcarboxylate is formed.

Hori et al.[104] proposed that $PW_{12}O_{40}^{3-}$ photocatalytic PFOA decomposition involves a photo-Kolbe type mechanism where PFOA first complexes with $PW_{12}O_{40}^{3-}$ (eq. 2.21) and upon photon adsorption an electron is directly transferred from PFOA to $PW_{12}O_{40}^{3-}$ (eq. 2.22)[104]. Similar to the sulfate radical mechnism, PFOA will decarboxylate to form the perfluoroheptyl radical. Oxygen is essential to the photocatalytic cycle in that it accepts an electron from the reduced phosphotungstic acid, $PW_{12}O_{40}^{4-}$, (eq. 2.23) returning it to its photoactive state.

$$CF_3(CF_2)_6COO^- + PW_{12}O_{40}^{3-} \rightarrow CF_3(CF_2)_6COO^- \cdots PW_{12}O_{40}^{3-} \qquad (2.21)$$

$$CF_3(CF_2)_6COO^- \cdots PW_{12}O_{40}^{3-} + h\nu\ (< 390\text{ nm}) \rightarrow CF_3(CF_2)_5CF_2\cdot + CO_2 + PW_{12}O_{40}^{4-} \qquad (2.22)$$

$$PW_{12}O_{40}^{4-} + O_2 \rightarrow PW_{12}O_{40}^{3-} + O_2\cdot^- \qquad (2.23)$$

The superoxide produced in eq. 20.13 will protonate when pH < 2 to the hydroperoxy radical (eq. 2.24) which can act as a reductant for pefluoroalkylperoxy (eq. 2.25) and perfluoroalkoxy radicals (eq. 2.26). The perfluoroalkylhydroperoxide produced in eq. 25 will likely photolyze to a perfluoroalkoxy radical and a hydroxyl radical (eq. 2.27).

$$H^+ + O_2\cdot^- \leftrightarrow HO_2\cdot \qquad (2.24)$$

$$CF_3(CF_2)_5CF_2OO\cdot + HO_2\cdot \rightarrow CF_3(CF_2)_5CF_2OOH + O_2 \qquad (2.25)$$

$$CF_3(CF_2)_5CF_2O\cdot + HO_2\cdot \rightarrow CF_3(CF_2)_5CF_2OH + O_2 \qquad (2.26)$$

$$CF_3(CF_2)_5CF_2OOH + h\nu \rightarrow CF_3(CF_2)_5CF_2O\cdot + HO\cdot \qquad (2.27)$$

The subsequent reactions of the various perfluoroalkyl radicals are analogous to those found in the sulfate radical PFOA decomposition mechanism, eq. 2.7–2.14. Due to the slow phosphotungstic-acid-mediated PFOA decomposition kinetics, perfsulfate photolysis would be a preferred perfluoroalkylcarboxylate oxidation technique since it operates by a similar mechanism and its degradation rate is at least an order of magnitude faster. Phosphotungstic acid has also been shown to enhance the TiO_2 photocatalytic degradation rates of PFOA[105] by acting as both an electron shuttle from TiO_2 to O_2 and as a photocatalyst.

TiO_2 Photocatalysis

TiO_2 photocatalysis has been shown to degrade a large number of pollutants through oxidative and reductive pathways[159]. The TiO_2 photocatalytic degradation of a number of perfluoroalkyl carboxylates and perfluoroalkylsulfonates was investigated[105] and was observed to be effective for the degradation of the carboxylates but not the sulfonates. The observation is consistent with investigations of PFOS as an inert, reusable TiO_2 surface coating[106,107,130] to enhance adsorption of hydrophobic contaminants onto TiO_2 ,where PFOS was stable to photolysis periods of up to 30 hours. The TiO_2 photocatalytic degradation of PFOA was reported to be quite slow, requiring 60 hours of UV photolysis to achieve 50% mineralization ($[PFOA]_i = 4.4$ mM, $[TiO_2]_i = 2.0$ g L^{-1}, pH = 1, O_2, $\lambda =$ 310–400 nm, 1500 W L^{-1}). Photonic efficiencies were determined to be less than 1.0×10^{-5}. The degradation mechanism is postulated to occur via a photo-Kolbe mechanism, similar to phosphotungstic acid[104], since rates increase with decreasing pH from 2.4 to 1.0[160]. The pKa of PFOA is estimated to be -0.5[1]. The degradation mechanism involves adsorption of PFOA onto the TiO_2 and direct oxidation by a TiO_2 valence band hole (eq. 2.28).

$$>TiOH\cdot^{+}\ (h_{vb}^{+}) + > CF_3(CF_2)_6COO^{-} \rightarrow >TiOH + CF_3(CF_2)_5CF_2\cdot + CO_2 \qquad (2.28)$$

The subsequent perfluoroalkyl radical reactions will be analogous to those observed during phosphotungstic acid photocatalysis due to the presence of oxygen. Thus, due to kinetic considerations, persulfate photolysis is a more viable perfluoroalkylcarboxylate oxidation technique.

The TiO_2 photocatalytic degradation of PFOA is slightly enhanced by the addition of phosphotungstic acid[161] or by electrophotocatalysis utilizing TiO_2 with a sub-monolayer Ni-Cu coating[103]. The phosphotungstic acid addition was completed under the same conditions as listed above TiO_2 photocatalysis. The optimal phosphotungstic acid concentration was 0.5 mM, yielding a degradation rate twice as fast as TiO_2 alone; at higher concentrations the degradation rate began to decrease. The PFOA half-life during TiO_2/Ni-Cu photocatalysis was 90 min with fluoride accounting for 5% of the total fluorine ($[PFOA]_i = 50\ \mu M$, $\lambda = 254$ nm, 90 W L^{-1}, air). A direct comparison between the TiO_2 and TiO_2/Ni-Cu systems is not easy due to the variations between $[PFOA]_i$, power density and wavelength used. A rough analysis yields a power density normalized absolute rate of TiO_2/Ni-Cu to be 7.4 times faster than TiO_2 alone. Applying a potential of -0.1 V to the TiO_2/Ni-Cu system decreases the half-life by a factor of two, 45 minutes, and increases the fluoride yield at the half-life to 20% of the total fluorine. The authors state that PFOA is photoreductively degraded, yet the majority of the fluorine is accounted for by shorter chain perfluoroalkylcarboxylates, which would suggest an oxidative mechanism. A reductive mechanism would be expected to defluorinate rather than decarboxylate. Electrochemistry using a boron-doped diamond electrode has also been shown to degrade PFOA[162].

Fe(II)/Fe(III) Photocatalysis

Photolysis of Fe(III)-carboxylate complexes involves charge transfer from the carboxylate functional group to the Fe(III). For example, ferrioxalate photolysis[163–166] will yield two CO_2 molecules under oxic conditions and is commonly used as a chemical actinometer. Perfluoroalkylcarboxylates (C_2-C_5) have been observed to decompose during UV photolysis in the presence of Fe(III)[167] ($[PFC]_i = 67.3$ mM, $[Fe^{3+}]_i = 5.0$ mM, pH = 1.5, 4.9 atm O_2, Xe-Hg Lamp, 9000 W L^{-1}). The Fe(III) photolysis PFC degradation half-life is approximately 20 hours with fluoride accounting for 45% of the total fluorine after 50% of the PFC is degraded. The fluoride yield is nearly double that of other PFC direct electron transfer oxidations. Low pH aqueous iron photolysis can also initiate indirect oxidations through photo-Fenton chemistry[124]. Fe(III)-perfluorocarboxylate photochemistry is postulated to react by chemistry similar to the analogous hydrocarbons. Initially, aqueous Fe(III) will complex with the PFAC (eq. 2.29). Fe(III)-PFAC UV photon adsorption results in a charge transfer from the PFAC to the Fe(III) yielding Fe(II), CO_2 and a perfluoroalkylradical (eq. 2.30). The perfluoroalkyl radical will follow the chemistry observed in other oxic systems as well as additional oxidative chemistry due to Fenton chemistry. The O_2 reduction by Fe(II) will regenerate Fe(III) (eq. 2.31).

$$CF_3(CF_2)_3COO^- + Fe^{3+} \rightarrow [CF_3(CF_2)_3COO^-Fe^{3+}]^{2+} \tag{2.29}$$

$$[CF_3(CF_2)_3COO^-Fe^{3+}]^{2+} + h\nu\ (\lambda < 300\text{ nm}) \rightarrow CF_3(CF_2)_2CF_2\cdot + CO_2 + Fe^{2+} \tag{2.30}$$

$$Fe^{2+} + O_2 \rightarrow Fe^{3+} + O_2\cdot^- \tag{2.31}$$

The photolytic Fe(III) degradation of PFCs follows a similar mechanism as the other oxidative degradations, in that an electron is removed directly from the carboxylate group leading to decarboxylation and formation of a shorter chain PFAC through a series of subsequent reactions.

PFOX Reduction

PFOS and PFOA oxidation is slow due to the high electronegativity of the fluorine atoms coating the carbon chain. Per- and poly-halogenation is a common chemical attribute found in environmentally persistent pollutants as they are oxidatively protected. For example, the Stockholm Convention greatly restricted the use of the most persistent organic pollutants (POPs) such as chlordane, DDT, hexachlorobenzene, polychlorinated biphenyls, and polychlorinated dioxins. All of these organics were partially chlorinated with $0.3 < Cl/C < 1.2$ and $\langle Cl/C \rangle = 0.63$. For comparison, PFOS and PFOA have a F/C ~ 2 and fluorine is more electronegative than chlorine. PFOS is being reviewed for addition to the Stockholm Convention POP list along with organics such as polybrominated diphenyl ethers, hexachlorocyclohexane, and endosulfan[168]. Reductive dehalogenation[169–174] has been utilized to remediate persistent halogenated organic contamination, leading to an increased susceptibility to oxidation and thus reduction of their environmental persistence. Once dehalogenation is complete, the organic ceases to be further reduced. A subsequent oxidative, microbial, or pyrolytic/combustion step is required to completely mineralize the reduced halo-organic.

Reductive remediation of perfluorocarboxylates and perfluorosulfonates is feasible[99,175,176]. For example, PFOS can be reduced by elemental iron, Fe(0), in water under high-temperature, high-pressure conditions (e.g., 350 ^{o}C, 20 MPa)[176]. Unsaturated per- and poly-fluoroorganics (i.e., those containing aromatic, benzylic, olefinic, and tertiary functional groups) will readily reductively defluorinate[177–182]. Fluoroorganics containing only secondary and primary C-F bonds are difficult to defluorinate due to low reduction potentials ($E < -2.7$ V)[183,184]. Only the aqueous electron and elemental alkali and alkaline metals have lower standard reduction potentials. Reductive defluorination kinetics are influenced by a number of FC chemical properties[178,179,183,185–187] and electron-donating strength of the reductant[188]. For example, branched PFOX is observed to have faster reduction kinetics than linear PFOX[99,189].

Sub-Critical Elemental Iron Reduction

Elemental iron, Fe(0), is a reductant and has been utilized for remediation of natural water halocarbon contamination due to iron's natural abundance and nontoxicity. Fe(0) has a reduction potential of - 0.447 V (eq. 2.32) and has been shown to reduce a large number of halocarbons[169,190,191].

$$Fe^0 \rightarrow Fe^{2+} + 2\ e^-,\ E_0 = 0.447 \qquad (2.32)$$

Fe(0) reactive barriers have been applied in the field to degrade chlorinated solvents and other chemicals in groundwater[192–194]. Recently, nano-Fe(0) has become popular due to the increased reactive surface area and thus reduction kinetics[173,174,195]. Alternatively, bimetallic systems using metals such as Pt(0), Ni(0), or Pd(0) at percent levels with Fe(0) have also shown faster reduction kinetics[196–198] and are postulated to be H-atom production catalysts[199,200]. The application of sub-critical water with the Fe(0) has been used to enhance reaction rates and mass transfer for remediation of soils and sediments[170,172,201]. Sub-critical Fe(0) has been shown to degrade PFOS[176], PFHS[175], and shorter-chain perfluoroalkylsulfonate components of an anti-reflective coating ($[PFOS]_i$ = 370 μM, [Fe(0)] = 50 g L^{-1}, 350 °C, 200 atm, Ar). The sub-critical Fe(0) PFOS degradation half-life is 45 minutes, with fluoride accounting for 55% of the total fluorine after 6 hours. No shorter-chain carboxylic acids were observed suggesting that reductive defluorination is the primary degradation mechanism. Application of a subsequent oxidation step could completely mineralize PFOX.

UV-KI Photolysis—Aqueous Electron Reduction

The aqueous electron is a powerful one-electron reductant, E = -2.87 V[4]. The aqueous electron is characterized by an electron surrounded by a shell of 5 water molecules, and is also known as the hydrated or aquated electron[202]. The aqueous electron can reduce most halogenated contaminants at near diffusion-controlled rates[127,171,203–206]. Electron tunneling leads to activation energies for reaction with halogenated organics that are invariable and small (6 to 30 kJ/mol)[207]. Reaction rates of the aqueous electron with fluorinated compounds have been reported[178,179,186,187,208]. Organic fluoro-saturation decreases aqueous electron reduction kinetics, since fluorine doesn't have any low-lying vacant d-orbital to accept an electron. As fluoro-saturation increases the rates tend to decrease (i.e., rates are fastest for tertiary fluorocarbons, then secondary, then primary).

Aqueous electrons can be produced by radiolytic[209], photolytic[210], chemical[127], and direct injection[211] methods. In surface waters, the photolysis of humic materials[212–214] and hard-UV photolysis of water[202] are the most common sources of natural aqueous electrons which have a steady-state concentration of 10^{-15} M. Second-order reaction rates of aqueous electrons with perfluorocarboxylates have been determined to be on the order of $10^{7}\ M^{-1}s^{-1}$ using pulse radiolysis and flash photolysis methods[186,187]. This is the fastest reported second-order rate constant of these perfluorocarboxylates with any chemical species (e.g., $k_{PFOS+HO\cdot} \sim k_{PFOS+SO4\cdot-} \sim 10^{4}\ M^{-1}\ s^{-1}$). Pulse radiolysis experiments[186] reported $k_{PFOS+e}(M^{-1}\ s^{-1}) > k_{PFOA+e}(M^{-1}\ s^{-1})$, suggesting sulfur-containing PFOS is easier to reduce. Batch reactions utilizing the aquated electron (e_{aq}^{-}, $E°_{aq/e} = -2.9$ V), produced by iodide photolysis, are observed to decompose both PFOS and PFOA ($[PFOS]_i = [PFOA]_i = 200$ nM, $[I^-] = 10$ mM, $\lambda = 254$ nm, 40 W L^{-1}, Ar). Aquated electrons are generated from UV-photolysis of aqueous iodide solutions via charge-transfer-to-solvent (CTTS) states (eq. 2.33).

$$I^- + h\nu \rightarrow I^{-*}_{CTTS} \rightarrow I\cdot + e^-_{aq}\ (QY_{\lambda=248\ nm} = 0.286)^{215} \qquad (2.33)$$

Fluoride is produced as a nonstoichiometric product, 10% for PFOA and 50% for PFOS, and thus the initial PFOX molecule is degraded but not completely destroyed by aqueous-electron-based reductive methods. Prior to complete defluorination, the ionic headgroup is reductively cleaved to yield an unsaturated, gaseous fluorochemical. The process is photocatalytic, as I-atom carriers (i.e., $I^{\bullet}$, $I_2^{\bullet-}$, $I_3^{\bullet-}$) and aqueous iodofluorocarbons will readily react with reducing species such as e_{aq}^-, $H^{\bullet}$ to regenerate I^-, the photo-active species.

Perfluoroalkyl carboxylate or sulfonate ($C_nF_{2n+1}X^-$; n = 8, X = SO_3 for PFOS; n = 7, X = CO_2 for PFOA) reaction with the aquated electron, e_{aq}^-, yields the corresponding radical anion ($C_nF_{2n+1}X^{\bullet 2-}$, eq. 2.34). The radical anion will quickly decompose via fluoride elimination in an aqueous environment to yield a perfluoroalkyl radical ($C_nF_{2n}X^{\bullet-}$, eq. 2.35). The electrophilic perfluoroalkyl radicals will oxidize iodide to yield the perfluoroalkyl carbanion ($C_nF_{2n}X^{2-}$, eq. 2.36). Perfluoroalkyl radicals may also react with e_{aq}^- to also yield an aqueous perfluoroalkyl carbanion which will protonate (eq. 2.37), or with $I^{\bullet}$ carriers (i.e., $I^{\bullet}$, $I_2^{\bullet-}$, $I_3^{\bullet-}$) to yield a perfluoroalkyl iodide ($C_nF_{2n}IX^-$, eq. 2.38). The perfluoroalkyl iodide may be converted back to a perfluoroalkyl radical via photolytic homolysis of the C-I bond (eq. 2.39), or by reaction with e^-_{aq} to yield the radical and I^- (eq. 2.40). An overall H/F exchange may also occur via reaction of a fluoroalkyl radical anion ($C_nF_{2n}X^{\bullet-}$) with an $H^{\bullet}$ (eq. 2.41).

$$C_nF_{2n+1}X^- + e_{aq}^- \rightarrow C_nF_{2n+1}X^{\bullet 2-} \tag{2.34}$$

$$C_nF_{2n+1}X^{\bullet 2-} \rightarrow C_nF_{2n}X^{\bullet -} + F^- \tag{2.35}$$

$$C_nF_{2n}X^{\bullet -} + I^- \rightarrow C_nF_{2n}X^{2-} + I^{\bullet} \tag{2.36}$$

$$C_nF_{2n}X^{\bullet -} + e_{aq}^- \rightarrow C_nF_{2n}X^{2-} \tag{2.37}$$

$$C_nF_{2n}X^{\bullet -} + I^{\bullet} \leftrightarrow C_nF_{2n}IX^- \tag{2.38}$$

$$C_nF_{2n}IX^- + e_{aq}^- \rightarrow C_nF_{2n}X^{\bullet -} + I^- \tag{2.39}$$

$$C_nF_{2n}X^{2-} + H^+/H_2O \rightarrow C_nF_{2n}HX^- \quad (2.40)$$

$$C_nF_{2n}X^{\bullet -} + H^\bullet \rightarrow C_nF_{2n}HX^- \quad (2.41)$$

If an H/F exchange product retains the anionic carboxylate or sulfonate terminal group, it will remain in the aqueous phase and proceed through sequential H/F exchanges. Subsequent e_{aq}^- reductions with partially defluorinated intermediates ($C_nF_{2n}IX^-$, $C_nF_{2n-1}X^-$, or $C_nF_{2n}HX^-$) should be faster than the initial defluorination step[181]. After partial reductive defluorination of PFOX, the ionic headgroup is cleaved. Ionic headgroup cleavage yields a neutral, polyfluorinated organic, which preferentially partitions to the gas-phase. The gaseous fluoroorganic could be completely destroyed using thermal or plasma techniques.

Alkaline 2-Propanol Photolytic Reduction

Photolysis of alkaline 2-propanol will catalytically yield the isopropyl radical through various radical chain initiation and propagation steps. The isopropyl radical has been reported to dechlorinate PCBs and pesticides[216–218]. Photolytic production of a strong one-electron oxidation, $Ox^\bullet$, will abstract an H-atom from 2-propanol to yield the isopropyl radical (eq. 2.38)[4], $(CH_3)_2COH$, which under alkaline conditions will deprotonate to yield (eq. 2.39)[219], $(CH_3)_2CO^{\bullet -}$, a stronger reductant (eqs. 2.40–2.41).

$$(CH_3)_2CHOH + Ox^\bullet \rightarrow (CH_3)_2COH + Ox^- \quad (2.38)$$

$$(CH_3)_2COH \leftrightarrow (CH_3)_2CO^{\bullet -} + H^+ \ (pKa = 12.03) \quad (2.39)$$

$$(CH_3)_2CO + e_{aq}^- + H^+ \rightarrow (CH_3)_2COH \ (E = -1.4\ V) \quad (2.40)$$

$$(CH_3)_2CO + e_{aq}^- \rightarrow (CH_3)_2CO^{\bullet -} \ (E = -2.1\ V) \quad (2.41)$$

UV photolysis of alkaline 2-propanol[99] has been observed to decompose PFOS with a pseudo-first-order half-life of 17.8 hours ($[PFOS]_i = 40\ \mu M$, $[NaOH]_i = 90\ mM$, $\lambda = 254$

nm, 43 W L^{-1}, T = 38-50 °C, N_2). The branched PFOS isomers degraded faster than the linear isomers consistent with electrochemical perfluoroorganic reduction where increased PF branching yielded easier reductions[183,184]. The primary product observed during the reduction is $NaF_{(s)}$. Similar to aqueous electron reduction, perfluoroalkyl carboxylate or sulfonate ($C_nF_{2n+1}X^-$; n = 8, X = SO_3 for PFOS; n = 7, X = CO_2 for PFOA) reaction with $(CH_3)_2CO^{\bullet-}$ yields the perfluoroalkyl radical and fluoride (eq 2.42). The produced perfluoroalkyl radical will then abstract an H-atom from 2-propanol to propagate the radical chain (eq. 2.43). Radical chain termination would occur via reaction of two radicals (eq. 2.44).

$$(CH_3)_2CO^{\bullet-} + C_nF_{2n+1}X^- \rightarrow (CH_3)_2CO + C_nF_{2n}X^{\bullet-} + F^- \tag{2.42}$$

$$C_nF_{2n}X^{\bullet-} + (CH_3)_2CHOH \rightarrow C_nF_{2n}HX^- + (CH_3)_2COH \tag{2.43}$$

$$C_nF_{2n}X^{\bullet-}/(CH_3)_2CO^{\bullet-} + C_nF_{2n}X^{\bullet-} \rightarrow \tag{2.44}$$

The radical chain mechanism makes alkaline 2-propanol an efficient PFOS degradation technology. A degradation mass balance has yet to be completed.

B_{12} Mediated Reduction

Vitamin B_{12} is a class of cobalamins, a cobalt ion complexed tetrapyrrole or corrin ring, which in certain forms are metabolically active coenzymes that catalyze rearrangement and methylation reactions[220]. Various B_{12} cofactors have been shown effective for the dechlorination of a number of organics such as PCE, TCE, CCl_4, and HCB[221–224]. The complexed cobalt ion is reduced to active Co(I) through two one-electron transfers (eqs. 2.45–2.46)[225,226] which can be completed in aqueous solution using Ti(III)-citrate as a bulk reductant (eq. 2.47)[227].

$$B_{12a}[Co(III)] + e^- \rightarrow B_{12r}[Co(II)] \quad (E^0 = -0.11\ V,\ pH = 9) \tag{2.45}$$

$$B_{12r}[Co(II)] + e^- \rightarrow B_{12s}[Co(I)] \quad (E^0 = -0.85,\ pH = 9) \tag{2.46}$$

$$\text{Ti(III)-cit} \rightarrow \text{Ti(IV)-cit} + e^- \quad (E^0 = -0.7, \text{pH} = 9) \tag{2.47}$$

The B_{12}-Co(I) has been postulated to reduce TCE by two mechanisms: an outer-sphere one-electron transfer[223,228] yielding chloride and a radical (eq. 2.48), followed by decay of the radical (eq. 2.49)

$$B_{12}\text{-Co(I)} + Cl_2C{=}CHCl \rightarrow B_{12}\text{-Co(II)} + ClC{=}CHCl + Cl^- \tag{2.48}$$

$$ClC{=}CHCl \rightarrow ClC{\equiv}CH + Cl\cdot \tag{2.49}$$

or a nucleophilic attack by B_{12}-Co(I), one of the strongest known nucleophiles[229], yielding a carbanion[222,224] (eq. 2.50) which is transformed to the reduced form (eq. 2.51).

$$B_{12}\text{-Co(I)} + Cl_2C{=}CHCl \rightarrow B_{12}\text{-Co(III)}Cl_2CCHCl^- \tag{2.50}$$

$$B_{12}\text{-Co(III)}Cl_2CCHCl^- + e^- + H^+ \rightarrow B_{12}\text{-Co(II)} + ClHC{=}CHCl + Cl^- \tag{2.51}$$

The overall TCE B_{12} reduction mechanism eventually yields acetylene as a final product.

Vitamin B_{12} has recently been shown to be an effective electron transfer mediator for the reduction of PFOS[189], with Ti(III)-citrate used as the bulk electron source ($[\text{PFOS}]_i$ = 332 μM, [Ti(III)-cit] = 36 mM, 70 °C, pH = 9.0). Reduction kinetics were determined to be 12.3 times faster for branched PFOS ($\tau_{1/2}$ = 33 hrs) then linear PFOS ($\tau_{1/2}$ = 410 hrs). The faster kinetics for the branched form are consistent with reduction potentials increasing as branching increases[183,184]. The branched form of PFOS gave a greater F^- yield per PFOS degraded, $[F^-]/[\text{PFOS}]_{br,deg} = 12$ vs. $[F^-]/[\text{PFOS}]_{lin,deg} = 3$, implying a change in the overall reduction mechanism. Ti(III)-citrate was also observed to reduce PFOS, but at a significantly lower rate than when using B_{12} as a electron transfer mediator. As with the Fe(0) reduction of PFOS and PFHS, a greater-than-standard temperature is required to drive the reaction on a reasonable time scale. The ability of

B_{12} to reduce PFOS, suggests that it may be possible for anaerobic bacteria to decompose perfluorochemicals and that it is more likely for them to degrade nonlinear PFCs.

PFOX Thermolysis

The high-temperature processing of organic materials will lead to pyrolytic reactions in the absence of oxygen and combustion reactions in the presence of oxygen. The thermolysis of fluorochemicals has been documented experimentally under more controlled conditions to determine individual reaction kinetics and mechanisms[230–241] and under more industrial conditions to test incinerability[83,111,113] or other thermal degradation processes[242]. A comprehensive experimental and theoretical database of C_1 and C_2 fluorochemical pyrolytic and combustion mechanisms, thermochemistry, and kinetics has been reported[243]. Fluorochemical C-C bonds (100 kcal/mol) in a fluorochemical will break prior to C-F bonds (120 kcal/mol) to yield fluoroalkyl radicals. The fluoroalkyl radical produced will be electrophilic and less stable towards thermal decomposition than the parent compound. Pyrolysis of longer perfluorochemical chains will tend to yield tetrafluoroethene, C_2F_4, difluorocarbene, CF_2, and the trifluoromethyl radical, CF_3 as the primary C_1 and C_2 products. Under combustion conditions, these radicals are readily transformed into CO, CO_2, and HF [243]

Thermal degradation of solid PFOA and PFOS salts[244–246] and gaseous PFOA (acid and ammonium salts)[230,247] has been reported. The primary products during the thermolysis of perfluoroalkylcarboxylates are the analogous 1H-perfluoroalkane for the salts (NH_4^+, H^+, eq. 2.52)[230,245,247], and the perfluoroolefin as well as the acyl fluoride and the anhydride for metal salts (Na^+, K^+, Ca^{2+}, etc.)[245]. A similar mechanism may be expected for perfluoroalkylsulfonates (eq. 2.53), as the C-S bond has been observed to be mostly broken during PFOS pyrolysis[248].

$$CF_3(CF_2)_6COO^-NH_4^+{}_{(s\ or\ g)} + \Delta \rightarrow CF_3(CF_2)_5CF_2H_{(g)} + CO_{2(g)} + NH_{3(g)} \qquad (2.52)$$

$$CF_3(CF_2)_7SO_3^-K^+{}_{(s\ or\ g)} + \Delta \rightarrow CF_3(CF_2)_5CF{=}CF_{2(g)} + SO_{3(g)} + K^+F^-{}_{(s)} \qquad (2.53)$$

A C-C bond breaking mechanism may also be the initial unimolecular decomposition step as observed in perfluorohexane pyrolysis[231]. A comparison of the extent of pyrolysis of similar carboxylate and sulfonate salts[246] reveals temperatures required for equivalent sulfonate salt decomposition to be 100 to 200 K greater than the corresponding carboxylate salt. The acid and ammonium salts are thermally converted to 1H-perfluoroalkane[245–247] and have a significantly lower decomposition temperature since no C-F bonds are broken. Thermolysis in the presence of ethylene glycol also primarily produces the1H-perfluoroalkane[245] suggesting that the perfluoroalkylanion is a weaker acid ($pKa_{HOCH2CH2OH} = 14.2$).The produced perfluoroolefin or 1H-perfluoroalkane will undergo further pyrolytic reactions to eventually yield C_2F_6 and C_2F_4[231,243]. If water and/or oxygen are present, the primary end-products will be CO, CO_2, and HF.

Incineration

Combustion is the most common thermal treatment of waste. Incineration, a combustion-based process, is one of the oldest chemical destruction techniques and today the waste heat from incineration can be converted usable energy. Incineration involves heating a substance to >1000 °C for at least 2 s. Incineration is commonly used in countries where land is scarce and solid waste must be thermally processed, > 95%, prior to landfill disposal. The test for determining the applicability of incineration for a chemical is to detemine the temperature at which > 99% of a chemical is destroyed after 2 s of applied heat. A number of fluorochemicals have been tested for incinerability. A fluorotelomer based acrylic polymer was found to be > 99% destroyed at 950 °C as a free polymer and at 700 °C when coated on a fabric[113]. Carbon tetrafluoride, CF_4, one of the most recalcitrant fluorochemicals, will be > 99% destroyed under incinerator conditions[83]. CF_4 has an estimated atmospheric lifetime of > 50,000 years with the dominant degradation pathway being diffusion into high-temperature incinerators and power plants[249]. Laboratory scale studies have shown PFOS and perfluorosulfonamides to be > 99% destroyed at 600 ^{o}C[248,250]. Gas-phase NMR studies have determined the > 99% destruction temperature for various PFOA salts to be in the range of 300–350 ^{o}C[230,247]. Therefore, incinerator conditions will be sufficient to completely destroy fluorochemicals in polymer, coating, and monomer forms. Incineration is most energy efficient for solid wastes, since all the heat will go into destroying the contaminant in question. Highly concentrated aqueous fluorochemical solutions and fluorochemicals adsorbed to a solid matrix could also be incinerated, but energy will be wasted on destroying the matrix.

Sonochemistry

Sonochemistry is the driving of chemical reactions by application of an acoustic field to a solution[251–253]. The chemistry is generated by acoustic cavitation of microscopic bubbles and has been utilized for the decomposition of a number of aqueous chemical contaminants[254–258] including chlorocarbons[259–261] and perfluorocarbons[92,262]. Application of ultrasonic field to an aqueous solution initially nucleates cavitation bubbles which will undergo stable and transient bubble collapse events[251,263–266]. Transiently collapsing bubbles generate the observed chemistry. After expanding to a radial maximum, transient bubbles undergo a quasi-adiabatic compression and the PdV energy is converted into kinetic energy of the trapped gas molecules. Transient bubble collapses generate average vapor temperatures near 5,000 K[267,268] and much higher bubble vapor core temperatures (> 10,000 K), which generate sonoluminescence[269,270]. Hot vapor will collide with the collapsing bubble wall; transfer of heat from the vapor to the bubble wall will generate interfacial temperatures measured to be at least 800 K[251,255]. Water vapor within the collapsing bubble will pyrolyze to yield an H-atom and a hydroxyl radical (eq. 2.54), the hydroxyl eventually pyrolyzes as well to yield an O-atom and an H-atom (eq. 2.55)[251].

$$H_2O + \Delta \rightarrow HO\cdot + H\cdot \qquad (2.54)$$

$$HO\cdot + \Delta \rightarrow O + H\cdot \qquad (2.55)$$

The radicals produced will react preferentially with chemicals partitioning to the bubble gas-phase. A fraction of the radicals will be transported to the bubble interface and a smaller fraction to the bulk aqueous phase where they can react with aqueous contaminants. Chemicals preferentially partitioning to the bubble vapor will decompose via pyrolytic and combustion reactions[259]. Hydrocarbon surfactants will degrade via hydroxyl radical oxidation at the interface[271]. Surfactants that are difficult to oxidize, such as PFOS and PFOA, will pyrolytically decompose at the bubble-water interface[92].

Sonochemistry has been observed to degrade PFOS and PFOA[92] with the primary ionic products being fluoride and sulfate ($[PFOS]_i = 20\ \mu M$, f = 200 kHz, 200 W, 3 W/cm^2, 20 ^oC, argon). Under these conditions the sonochemical half-life of PFOA was 22 minutes and of PFOS was 43 minutes. The initial decomposition step was determined to occur at the bubble-water interface. Time-dependent product analyses during PFOS and PFOA sonolysis was used to investigate the mechanism and kinetics of the overall degradation process ($[PFOS]_i = 10\ \mu M$, f = 358/618 kHz, 250 WL, 6.4 W/cm^2, 10 ^oC, argon)[262]. Under these conditions, the decomposition half-life was reduced to 17 and 26 minutes for PFOA and PFOS, respectively. The nearly immediate production of mineralized fluorine (fluoride), sulfur (sulfate), and carbon (CO and CO_2) products after decomposition of the initial perfluorinated surfactant implies that sonochemical PFOS/PFOA mineralization (i.e., conversion to inorganic products) has overall kinetics similar to the decomposition of the perfluorinated surfactant (eq. 2.56),

$$\frac{-d[PFOX]}{dt} = \frac{d\{Mineralization\}}{dt} \tag{2.56}$$

or that the primary intermediates produced from PFOS and PFOA sonolysis have much shorter half-lives than their parent surfactants. Assuming that the initial decomposition step is pyrolytic, the primary fluorochemical intermediates are expected to be perfluoroolefins and 1H-perfluoroalkanes, eqs. 2.52–2.53. The high Henry's constants[3] of the primary fluorochemical intermediates favor partitioning into the bubble vapor ,where they will be pyrolyzed into their C_1 fluororadical constituents (eq. 2.57)[231,272].

$$CF_3(CF_2)_5CF_2H_{(g)} + \Delta \rightarrow CF_3 + 5\ {:}CF_2 + CF_2H \tag{2.57}$$

The C_1 fluororadicals will subsequently react with H_2O, HO·, H·, and O-atom in the bubble vapor to yield CO, CO_2, and HF[243]. More recent studies have shown that perfluorochemical adsorption to acoustically cavitating bubble interfaces is enhanced when the bubble interfaces are lightly populated. The adsorption enhancements increase the effective concentration of dilute perfluorochemical solutions by 1–2 orders of magnitude. Sonochemical degradation studies on groundwater containing perfluorochemicals have shown that organic content has only minimal effects on decomposition rates, even when organic concentrations are many orders of magnitude greater than fluorochemical concentrations, due to preferential adsorption of PFCs to the bubble-water interface.

PFOX Degradation Technology Summary

In Tables 2.1 & 2.2 we have compiled the aqueous PFOX degradation parameters for the most viable techniques: reactions conditions, initial concentrations, degradation kinetics, degradation products, and energy required to reduce the initial PFOX concentration by 50% and the energy required per μmole. However, neither the absolute or normalized energy is optimal for comparison of the reviewed techniques. As $[PFOX]_i$ increases, the inherent efficiency of any chemical process will also increase if the concentration is below kinetic saturation. For example, see the data on UV-KI or sonolytic degradation of PFOX at $[PFOX]_i$ = 200 nM vs. 20 μM. In both cases for PFOS and PFOA the absolute amount of energy required for 50% degradation decreases by 45–75% upon decreasing $[PFOX]_i$. However, since the concentration decreases by 2 orders of magnitude, the energy required to degrade a μmole of PFOX will increase by at least an order of magnitude.

In terms of reaction conditions, the techniques with no chemical additives such as photoelectrocatalysis, sonolysis, and direct photolysis are advantageous. Although, the sulfate (persulfate), $TiO_{2(s)}$, iron (Fe(0), Fe^{2+}/Fe^{3+}), and iodide (UV-KI) are relatively innocuous and shouldn't be an environmental issue. Sub-critical Fe(0) has safety implications of operating under high-pressure, high-temperature conditions.[273] Acoustic and UV-based systems will require reactor cooling.

A comparison of degradation kinetics will be headgroup dependent (i.e, PFOS and PFOA have dissimilar degradation rates). PFOA is more kinetically susceptible to oxidative, and photolytic processes, whereas PFOS is more susceptible to reductive processes. Both PFOS and PFOA are susceptible to sonolysis, a thermal-based process. For example, PFOA has a degradation half-life less than 60 minutes by direct photolysis (λ = 195 nm), persulfate photolysis (λ = 254 nm), photoelectrocatalysis, and sonolysis, and PFOS has a degradation half-life under 60 min for sub-critical Fe(0) and sonolysis. Sonolysis is the only technique that has been shown to quickly degrade both as it can create incinerator level temperatures, if only for a short (ns) period of time. Kinetics will be of importance in flowing systems where the aqueous PFOX will only be in the reactor for a finite period. Whereas there are batch reactor cases (e.g., manufacturing waste) where treatment time is not a factor and the kinetics will be relatively unimportant.

PFOX degradation products are dependent upon whether the technique used is oxidative, reductive or thermal. Thermal methods, such as sonolysis and incineration, have a distinct advantage. PFOX is sonolytically mineralized to F^-, SO_4^{2-}, CO, and CO_2 nearly immediately after the initial degradation step. Thus PFOX sonolytic mineralization efficacy is equivalent to its degradation efficacy. Reductive methods, such as sub-critical Fe(0), UV-KI, and UV-NaOH-IPA, will to some extent defluorinate PFOS and PFOA. Defluorination will yield either an olefin or a hydride which will be easier to oxidize than PFOX. However, even partially fluorinated species have long environmental lifetimes. For example, fluoroform, CF3H, has an atmospheric lifetime of 250–390 years.[274] Direct photolytic and oxidative processes are weakest in terms of degradation products. Oxidation of PFOX cleaves the headgroup and after a series of subsequent reactions the highest yield product is a perfluorocarboxylate with one less -CF_2- group, which is just as recalcitrant as the initial compound. For example, persulfate photolysis is one of the most energy-efficient processes for PFOA degradation, but would require approximately 50x more energy to completely mineralize PFOA, which is similar to the energy requirement for sonolytic mineralization.

As discussed earlier, it is difficult to directly compare energetic efficiencies due to factors such as initial concentration used and whether interest is in initial PFOX degradation or complete mineralization. Tables 2.1 & 2.2 can be used for a rough measure of which treatment technology is energetically viable. The PFOX treatment technology utilized will strongly depend on the situation in question and the desired results. For example, our group has shown that sonolysis is a viable method for the degradation of PFOX in groundwater, even though they were at relatively low concentrations, 100 ppb, as compared to other matrix components. This is a result of PFOX being strong surfactants and thus will preferentially adsorb to the bubble-water interface, the active site in sonolysis, over other chemical species. Redox and photolytic methods would have a much greater loss of efficacy when utilized to degrade PFOX in groundwater due to reactive radical scavenging by NOM, dissolved and solid metals, and co-contaminants.

It is of note that none of the reviewed methods approaches the normalized energy for production of PFOX. The concentration effect (i.e., production concentrations are much greater than waste/water concentrations) is a major factor in this deficiency. Assuming C-F bond formation is the most energetically consuming step in producing PFOS, we will make a rough estimate of energy per μmole to produce PFOS. Electrochemical conversion of octanesulfonyl fluoride to perfluorooctane sulfonyl fluoride is completed in concentrated HF with an applied voltage of 4-7 V, 2 electrons are required to convert C(-I)-H to C(+I)-F, and there are 17 C-F bonds in PFOS. Thus approximately 1.31–2.28 x 10^4 kJ mol^{-1} or 1.31–2.28 x 10^{-2} kJ μmol^{-1} is necessary to create PFOS—a value orders of magnitude greater than the energy required for sonolytic mineralization of 10 μM PFOS: 95 kJ μmol^{-1}. Therefore, investigations into the energy usage optimization of the currently reviewed methods, as well as research into new techniques for aqueous PFOX removal or degradation, would be fruitful in reducing the overall environmental impact of this class of chemicals. Hybrid methods containing two or more of the previously stated techniques are likely to be viable solutions. For example, we have found that the iron and DOC levels in leachate reduce the PFOS and PFOA sonolytic degradation rates by factors of four and three, respectively. However, the sonozone process[275–278], the simultaneous application of ozone and ultrasound, nearly rectifies the rates to those observed under pristine conditions. Further investigations are needed into novel oxidative and reductive techniques as well as hybrid (synergistic) remediation techniques to degrade particularly recalcitrant pollutants such as aqueous PFOS and PFOA.

.

Tables

Table 2.1. Summary of technologies for aqueous PFOA degradation

Technique	Conditions	Power/Vol.	k(lab)[a]	Product[b]	Energy[c]	Ref.
UV Direct Photolysis	1.35 mM PFOA λ = 220–460 nm	22 mL 200 W	0.69 d^{-1} $\tau_{1/2}$ = 1440 min	33% F$^-$ 38% CO$_2$ 65% PFacids	792,000 kJ (1,170 kJ/μmol)	93
UV Phosphotungstic Photocatalysis	1.35 mM PFOA λ = 220–460 nm 0.48 MPa O$_2$ 6.6 mM PTA	22 mL 200 W	2.0 d^{-1} $\tau_{1/2}$ = 500 min	30% F$^-$ 25% CO$_2$ 70% PF acids	276,000 kJ (410 kJ/μmol)	93
TiO$_2$ Photocatalysis	1.0 mM PFOA λ = 310–400 nm pH 2–3 0.1 g TiO$_2$	50 mL 75 W	0.69 d^{-1} $\tau_{1/2}$ = 1440 min	50% F$^-$ 50% CO$_2$	132,000 kJ (265 kJ/μmol)	161
UV Direct Photolysis	50 μM PFOA λ = 185 nm	1000 mL 23 W	0.017 min^{-1} $\tau_{1/2}$ = 41 min	10% F$^-$ 90% PFacids	49 kJ (1 kJ/μmol)	94
UV Persulfate Photolysis	50 μM PFOA λ = 254 nm 1.5 mM S$_2$O$_8^{2-}$	1000 mL 23 W	0.012 min^{-1} $\tau_{1/2}$ = 58 min	5% F$^-$ 95% PFacids	69 kJ (1.2 kJ/μmol)	94
UV Persulfate Photolysis	1.35 mM PFOA λ = 220–460 nm 0.48 MPa O$_2$ pH 2–3 10 mM S$_2$O$_8^{2-}$	22 mL 200 W	0.69 h^{-1} $\tau_{1/2}$ = 58 min	12% F$^-$ 85% PFacids	33,600 kJ (50 kJ/μmol)	100
Photocatalysis TiO$_2$/Ni-Cu	50 μM PFOA λ = 254 nm	250 mL 23 W	0.0077 min^{-1} $\tau_{1/2}$ = 90 min	10 % F$^-$ 90% PFacids	500 kJ (20 kJ/μmol)	103
Photoelectro-catalysis TiO$_2$/Ni-Cu	50 μM PFOA λ = 254 nm -0.1 V	250 mL 23 W	0.015 min^{-1} $\tau_{1/2}$ = 45 min	20% F$^-$ 80% PFacids	250 kJ (10 kJ/μmol)	103
Persulfate Photolysis	2.5 mM PFBA λ = 254 nm 50 mM S$_2$O$_8^{2-}$	200 mL 60 W	0.0096 min^{-1} $\tau_{1/2}$ = 72 min	~ 10^4 M^{-1}s^{-1}[d] SO$_4^{\cdot -}$ + PFBA$^-$	1300 kJ (1.0 kJ/μmol)	102
Hydrogen Peroxide	2.5 mM PFBA λ = 254 nm	200 mL 60 W	3.0e-5 min^{-1} $\tau_{1/2}$ = 23100 min	n/a	420000 kJ (320 kJ/μmol)	102

Photolysis	250 mM H_2O_2					
Flash Photolysis	5e-5 M $Fe(CN)_6$ 0.02–0.1 M PFOA	266 nm 10 ns 3 mJ/pulse	$\sim 10^7$ $M^{-1}s^{1d}$	n/a	n/a	187
Sonolysis	20 µM PFOA f = 354 kHz	150 W 600 mL	0.018 min^{-1} $\tau_{1/2}$ = 39 min	95% F^-	670 kJ (67 kJ/µmol)	279
Sonolysis	200 nM PFOA f = 354 kHz	150 W 600 mL	0.047 min^{-1} $\tau_{1/2}$ = 15 min	95% F^-	260 kJ (1300 kJ/µmol)	279
UV-KI Photolysis	20 µM PFOA λ = 254 nm	1.5 W 30 mL	0.0014 min^{-1} $\tau_{1/2}$ = 500 min	10% F^- gaseous fluoroalkanes	1500 kJ (150 kJ/µmol)	
UV-KI Photolysis	200 nM PFOA λ = 254 nm	1.5 W 30 mL	0.0025 min^{-1} $\tau_{1/2}$ = 280 min	10% F^- gaseous fluoroalkanes	820 kJ (8200 kJ/µmol)	
Ferro-photolysis	2.5 mM $Fe_2(SO_4)_3$ 67 mM PFBA λ = 220–460 nm	200 W 105 mL	0.028 h^{-1} $\tau_{1/2}$ = 1490 min	45% F^- 55% short chains	89400 kJ (2.7 kJ/ µmol)	167

Table 2.2. Summary of technologies for aqueous PFOS degradation

Technique	Conditions	Power/Vol.	k(lab)[a]	Products[b]	Energy[c]	Ref.
Sub-Critical Fe(0)	370 μM PFOS 0.5 g Fe(0) 350 °C, 20 MPa	10 mL	0.013 min^{-1} $\tau_{1/2}$ = 53 min	50% F^-	2,000 kJ (11 kJ / μmol)	176
UV Direct Photolysis	40 μM PFOS λ = 254 nm	32 W 750 mL	0.13 day^{-1} $\tau_{1/2}$ = 7700 min	71% F^- 90% SO_4^{2-}	17,000 kJ (850 kJ / μmol)	99
UV Alkaline IPA Photolysis	40 μM PFOS λ = 254 nm	32 W 750 mL	0.93 day^{-1} $\tau_{1/2}$ = 1070 min	$NaF_{(s)}$	2,500 kJ (125 kJ / μmol)	99
Sonolysis	20 μM PFOS f = 354 kHz	150 W 600 mL	0.011 min^{-1} $\tau_{1/2}$ = 63 min	95% F^- 100% SO_4^{2-}	945 kJ (95 kJ / μmol)	279
Sonolysis	200 nM PFOS f = 354 kHz	150 W 600 mL	0.023 min^{-1} $\tau_{1/2}$ = 30 min	95% F^- 100% SO_4^{2-}	450 kJ (4500 kJ/μmol)	279
UV-KI Photolysis	20 μM PFOS λ = 254 nm [KI] = 10 mM	1.5 W 30 mL	0.002 min^{-1} $\tau_{1/2}$ = 350 min	50% F^- 50% fluoroalkanes	960 kJ (96 kJ / μmol)	
UV-KI Photolysis	200 nM PFOS λ = 254 nm [KI] = 10 mM	1.5 W 30 mL	0.008 min^{-1} $\tau_{1/2}$ = 87 min	50% F^- 50% fluoroalkanes	260 kJ (1250 kJ/μmol)	

References

(1) Goss, K. U. *Environ. Sci. Technol.* **2008**, *42*, 456.

(2) Goss, K. U.; Bronner, G. *J. Phys. Chem. A* **2006**, *110*, 9518.

(3) Goss, K. U.; Bronner, G.; Harner, T.; Monika, H.; Schmidt, T. C. *Environ. Sci. Technol.* **2006**, *40*, 3572.

(4) Wardman, P. *J. Phys. Chem. Ref. Data* **1989**, *18*, 1637.

(5) 3M Company. *The Science of Organic Fluorochemistry*; Docket AR226-0547; Office of Pollution Prevention and Toxics, U.S. Environmental Protection Agency: Washington, D.C., 1999; p. 12.

(6) 3M Company. *Removal of PFOA with Granular Activated Carbon: 3M Wastewater Treatment System Monitoring*; Docket AR226-1699; Office of Pollution Prevention & Toxics, U.S. Environmental Protection Agency: Washington, D.C., 2004; p 5.

(7) Sinclair, E.; Kannan, K. *Environ. Sci. Technol.* **2006**, *40*, 1408.

(8) Schultz, M. M.; Higgins, C. P.; Huset, C. A.; Luthy, R. G.; Barofsky, D. F.; Field, J. A. *Environ. Sci. Technol.* **2006**, *40*, 7350.

(9) Morris, R. A.; Miller, T. M.; Viggiano, A. A.; Paulson, J. F.; Solomon, S.; Reid, G. *J. Geophys. Res.—Atmos.* **1995**, *100*, 1287.

(10) Shinoda, K.; Hato, M.; Hayashi, T. *J. Phys. Chem.* **1972**, *76*, 909.

(11) Lopez-Fontan, J. L.; Sarmiento, F.; Schulz, P. C. *Colloid Polym. Sci.* **2005**, *283*, 862.

(12) Lu, J. R.; Ottewill, R. H.; Rennie, A. R. *Colloid Surf. A—Physicochem. Eng. Asp.* **2001**, *183*, 15.

(13) Simister, E. A.; Lee, E. M.; Lu, J. R.; Thomas, R. K.; Ottewill, R. H.; Rennie, A. R.; Penfold, J. *J. Chem. Soc.—Faraday Trans.* **1992**, *88*, 3033.

(14) Boulanger, B.; Peck, A. M.; Schnoor, J. L.; Hornbuckle, K. C. *Environ. Sci. Technol.* **2005**, *39*, 74.

(15) Boulanger, B.; Vargo, J.; Schnoor, J. L.; Hornbuckle, K. C. *Environ. Sci. Technol.* **2004**, *38*, 4064.

(16) Hansen, K. J.; Johnson, H. O.; Eldridge, J. S.; Butenhoff, J. L.; Dick, L. A. *Environ. Sci. Technol.* **2002**, *36*, 1681.

(17) Harada, K.; Saito, N.; Sasaki, K.; Inoue, K.; Koizumi, A. *Bull. Environ. Contam. Toxicol.* **2003**, *71*, 31.

(18) Kim, S. K.; Kannan, K. *Environ. Sci. Technol.* **2007**, *41*, 8328.

(19) McLachlan, M. S.; Holmstrom, K. E.; Reth, M.; Berger, U. *Environ. Sci. Technol.* **2007**, *41*, 7260.

(20) Moody, C. A.; Hebert, G. N.; Strauss, S. H.; Field, J. A. *J. Environ. Monit.* **2003**, *5*, 341.

(21) Moody, C. A.; Martin, J. W.; Kwan, W. C.; Muir, D. C. G.; Mabury, S. C. *Environ. Sci. Technol.* **2002**, *36*, 545.

(22) Schultz, M. M.; Barofsky, D. F.; Field, J. A. *Environ. Eng. Sci.* **2003**, *20*, 487.

(23) Yamashita, N.; Kannan, K.; Taniyasu, S.; Horii, Y.; Petrick, G.; Gamo, T. *Mar. Pollut. Bull.* **2005**, *51*, 658.

(24) 3M Company. *Sulfonated perfluorochemicals in the environment: Sources, dispersion, fate and effects*; Docket AR226-0620; Office of Pollution Prevention & Toxics, U.S. Environmental Protection Agency: Washington, D.C., 2000; p 51.

(25) Armitage, J.; Cousins, I. T.; Buck, R. C.; Prevedouros, K.; Russell, M. H.; MacLeod, M.; Korzeniowski, S. H. *Environ. Sci. Technol.* **2006**, *40*, 6969.

(26) Saito, N.; Harada, K.; Inoue, K.; Sasaki, K.; Yoshinaga, T.; Koizumi, A. *J. Occup. Health* **2004**, *46*, 49.

(27) Schultz, M. M.; Barofsky, D. F.; Field, J. A. *Environ. Sci. Technol.* **2004**, *38*, 1828.

(28) Scott, B. F.; Moody, C. A.; Spencer, C.; Small, J. M.; Muir, D. C. G.; Mabury, S. A. *Environ. Sci. Technol.* **2006**, *40*, 6405.

(29) Scott, B. F.; Spencer, C.; Mabury, S. A.; Muir, D. C. G. *Environ. Sci. Technol.* **2006**, *40*, 7167.

(30) Senthilkumar, K.; Ohi, E.; Sajwan, K.; Takasuga, T.; Kannan, K. *Bull. Environ. Contam. Toxicol.* **2007**, *79*, 427.

(31) So, M. K.; Miyake, Y.; Yeung, W. Y.; Ho, Y. M.; Taniyasu, S.; Rostkowski, P.; Yamashita, N.; Zhou, B. S.; Shi, X. J.; Wang, J. X.; Giesy, J. P.; Yu, H.; Lam, P. K. S. *Chemosphere* **2007**, *68*, 2085.

(32) So, M. K.; Taniyasu, S.; Yamashita, N.; Giesy, J. P.; Zheng, J.; Fang, Z.; Im, S. H.; Lam, P. K. S. *Environ. Sci. Technol.* **2004**, *38*, 4056.

(33) Yamashita, N.; Kannan, K.; Taniyasu, S.; Horii, Y.; Okazawa, T.; Petrick, G.; Gamo, T. *Environ. Sci. Technol.* **2004**, *38*, 5522.

(34) Yamashita, N.; Taniyasu, S.; Petrick, G.; Wei, S.; Gamo, T.; Lam, P. K. S.; Kannan, K. *Chemosphere* **2008**, *70*, 1247.

(35) Calafat, A. M.; Kuklenyik, Z.; Caudill, S. P.; Reidy, J. A.; Needham, L. L. *Environ. Sci. Technol.* **2006**, *40*, 2128.

(36) Calafat, A. M.; Needham, L. L.; Kuklenyik, Z.; Reidy, J. A.; Tully, J. S.; Aguilar-Villalobos, M.; Naeher, L. P. *Chemosphere* **2006**, *63*, 490.

(37) Martin, J. W.; Whittle, D. M.; Muir, D. C. G.; Mabury, S. A. *Environ. Sci. Technol.* **2004**, *38*, 5379.

(38) Martin, J. W.; Smithwick, M. M.; Braune, B. M.; Hoekstra, P. F.; Muir, D. C. G.; Mabury, S. A. *Environ. Sci. Technol.* **2004**, *38*, 373.

(39) Giesy, J. P.; Kannan, K. *Environ. Sci. Technol.* **2001**, *35*, 1339.

(40) Holmstrom, K. E.; Jarnberg, U.; Bignert, A. *Environ. Sci. Technol.* **2005**, *39*, 80.

(41) Houde, M.; Balmer, B. C.; Brandsma, S.; Wells, R. S.; Rowles, T. K.; Solomon, K. R.; Muir, D. C. G. *Environ. Toxicol. Chem.* **2006**, *25*, 2405.

(42) Houde, M.; Martin, J. W.; Letcher, R. J.; Solomon, K. R.; Muir, D. C. G. *Environ. Sci. Technol.* **2006**, *40*, 3463.

(43) Kannan, K.; Choi, J. W.; Iseki, N.; Senthilkumar, K.; Kim, D. H.; Masunaga, S.; Giesy, J. P. *Chemosphere* **2002**, *49*, 225.

(44) Kannan, K.; Corsolini, S.; Falandysz, J.; Fillmann, G.; Kumar, K. S.; Loganathan, B. G.; Mohd, M. A.; Olivero, J.; Van Wouwe, N.; Yang, J. H.; Aldous, K. M. *Environ. Sci. Technol.* **2004**, *38*, 4489.

(45) Kannan, K.; Corsolini, S.; Falandysz, J.; Oehme, G.; Focardi, S.; Giesy, J. P. *Environ. Sci. Technol.* **2002**, *36*, 3210.

(46) Kannan, K.; Koistinen, J.; Beckmen, K.; Evans, T.; Gorzelany, J. F.; Hansen, K. J.; Jones, P. D.; Helle, E.; Nyman, M.; Giesy, J. P. *Environ. Sci. Technol.* **2001**, *35*, 1593.

(47) Kannan, K.; Newsted, J.; Halbrook, R. S.; Giesy, J. P. *Environ. Sci. Technol.* **2002**, *36*, 2566.

(48) Kannan, K.; Tao, L.; Sinclair, E.; Pastva, S. D.; Jude, D. J.; Giesy, J. P. *Arch. Environ. Contam. Toxicol.* **2005**, *48*, 559.

(49) Nakata, H.; Kannan, K.; Nasu, T.; Cho, H. S.; Sinclair, E.; Takemura, A. *Environ. Sci. Technol.* **2006**, *40*, 4916.

(50) Olsen, G. W.; Church, T. R.; Larson, E. B.; van Belle, G.; Lundberg, J. K.; Hansen, K. J.; Burris, J. M.; Mandel, J. H.; Zobel, L. R. *Chemosphere* **2004**, *54*, 1599.

(51) Olsen, G. W.; Church, T. R.; Miller, J. P.; Burris, J. M.; Hansen, K. J.; Lundberg, J. K.; Armitage, J. B.; Herron, R. M.; Medhdizadehkashi, Z.; Nobiletti, J. B.; O'Neill, E. M.; Mandel, J. H.; Zobel, L. R. *Environ. Health Perspect.* **2003**, *111*, 1892.

(52) Olsen, G. W.; Huang, H. Y.; Helzlsouer, K. J.; Hansen, K. J.; Butenhoff, J. L.; Mandel, J. H. *Environ. Health Perspect.* **2005**, *113*, 539.

(53) Olsen, G. W.; Mair, D. C.; Reagen, W. K.; Ellefson, M. E.; Ehresman, D. J.; Butenhoff, J. L.; Zobel, L. R. *Chemosphere* **2007**, *68*, 105.

(54) Sinclair, E.; Mayack, D. T.; Roblee, K.; Yamashita, N.; Kannan, K. *Arch. Environ. Contam. Toxicol.* **2006**, *50*, 398.

(55) Smithwick, M.; Mabury, S. A.; Solomon, K. R.; Sonne, C.; Martin, J. W.; Born, E. W.; Dietz, R.; Derocher, A. E.; Letcher, R. J.; Evans, T. J.; Gabrielsen, G. W.; Nagy, J.; Stirling, I.; Taylor, M. K.; Muir, D. C. G. *Environ. Sci. Technol.* **2005**, *39*, 5517.

(56) Taniyasu, S.; Kannan, K.; Horii, Y.; Hanari, N.; Yamashita, N. *Environ. Sci. Technol.* **2003**, *37*, 2634.

(57) Tomy, G. T.; Budakowski, W.; Halldorson, T.; Helm, P. A.; Stern, G. A.; Friesen, K.; Pepper, K.; Tittlemier, S. A.; Fisk, A. T. *Environ. Sci. Technol.* **2004**, *38*, 6475.

(58) Van de Vijver, K. I.; Hoff, P. T.; Das, K.; Van Dongen, W.; Esmans, E. L.; Siebert, U.; Bouquegneau, J. M.; Blust, R.; De Coen, W. M. *Mar. Pollut. Bull.* **2004**, *48*, 992.

(59) Verreault, J.; Berger, U.; Gabrielsen, G. W. *Environ. Sci. Technol.* **2007**, *41*, 6671.

(60) Prevedouros, K.; Cousins, I. T.; Buck, R. C.; Korzeniowski, S. H. *Environ. Sci. Technol.* **2006**, *40*, 32.

(61) Kubwabo, C.; Stewart, B.; Zhu, J. P.; Marro, L. *J. Environ. Monit.* **2005**, *7*, 1074.

(62) Moriwaki, H.; Takata, Y.; Arakawa, R. *J. Environ. Monit.* **2003**, *5*, 753.

(63) Ellis, D. A.; Mabury, S. A.; Martin, J. W.; Muir, D. C. G. *Nature* **2001**, *412*, 321.

(64) Tittlemier, S. A.; Pepper, K.; Seymour, C.; Moisey, J.; Bronson, R.; Cao, X. L.; Dabeka, R. W. *J. Agric. Food Chem.* **2007**, *55*, 3203.

(65) Begley, T. H.; White, K.; Honigfort, P.; Twaroski, M. L.; Neches, R.; Walker, R. A. *Food Addit. Contam.* **2005**, *22*, 1023.

(66) Young, C. J.; Furdui, V. I.; Franklin, J.; Koerner, R. M.; Muir, D. C. G.; Mabury, S. A. *Environ. Sci. Technol.* **2007**, *41*, 3455.

(67) D'Eon, J. C.; Hurley, M. D.; Wallington, T. J.; Mabury, S. A. *Environ. Sci. Technol.* **2006**, *40*, 1862.

(68) Martin, J. W.; Ellis, D. A.; Mabury, S. A.; Hurley, M. D.; Wallington, T. J. *Environ. Sci. Technol.* **2006**, *40*, 864.

(69) 3M Company. *Study of the Stability of MeFOSEA in Aqueous Buffers*; Docket AR226-0380; Office of Pollution Prevention and Toxics, U.S. Environmental Protection Agency: Washington, D.C., 1999; p. 69.

(70) Tomy, G. T.; Tittlemier, S. A.; Palace, V. P.; Budakowski, W. R.; Braekevelt, E.; Brinkworth, L.; Friesen, K. *Environ. Sci. Technol.* **2004**, *38*, 758.

(71) Xu, L.; Krenitsky, D. M.; Seacat, A. M.; Butenhoff, J. L.; Anders, M. W. *Chem. Res. Toxicol.* **2004**, *17*, 767.

(72) *Additional Characterization of Metabolites of T-6292, T-6293 and T-6294 from Rat and Human Hepatocytes*; Docket AR226-0163; Office of Pollution Prevention and Toxics, U.S. Environmental Protection Agency: Washington, D.C., 1998; p. 69.

(73) *Effect of N-Alkyl Perfluorooctylsulfonamides on Mitochondrial Bioenergetics In Vitro*; Docket AR226-0166; Office of Pollution Prevention and Toxics, U.S. Environmental Protection Agency: Washington, D.C., 1998; p. 10.

(74) Hagen, D. F.; Belisle, J.; Johnson, J. D.; Venkateswarlu, P. *Anal. Biochem.* **1981**, *118*, 336.

(75) Ellis, D. A.; Martin, J. W.; De Silva, A. O.; Mabury, S. A.; Hurley, M. D.; Andersen, M. P. S.; Wallington, T. J. *Environ. Sci. Technol.* **2004**, *38*, 3316.

(76) Stock, N. L.; Lau, F. K.; Ellis, D. A.; Martin, J. W.; Muir, D. C. G.; Mabury, S. A. *Environ. Sci. Technol.* **2004**, *38*, 991.

(77) Shoeib, M.; Harner, T.; Vlahos, P. *Environ. Sci. Technol.* **2006**, *40*, 7577.

(78) 3M Company. *Phase-out Plan for POSF-Based Products* Docket AR226-0588; Office of Pollution Prevention & Toxics, U.S. Environmental Protection Agency: Washington, D.C., 2000; p. 11.

(79) Yarwood, G.; Kemball-Cook, S.; Keinath, M.; Waterland, R. L.; Korzeniowski, S. H.; Buck, R. C.; Russell, M. H.; Washburn, S. T. *Environ. Sci. Technol.* **2007**.

(80) *Investigation of Perfluorochemical (PFC) Contamination in Minnesota Phase 1*; Senate Environment Committee: Minnesota, 2006; p. 79.

(81) Schwarzenbach, R. P.; Escher, B. I.; Fenner, K.; Hofstetter, T. B.; Johnson, C. A.; von Gunten, U.; Wehrli, B. *Science* **2006**, *313*, 1072.

(82) Lampert, D. J.; Frisch, M. A.; Speitel, G. E. *Practice Periodical of Hazardous, Toxic and Radioactive Waste Management* **2007**, *11*.

(83) Tsang, W.; Burgess, D. R.; Babushok, V. *Combustion Science and Technology* **1998**, *139*, 385.

(84) Higgins, C. P.; Field, J. A.; Criddle, C. S.; Luthy, R. G. *Environ. Sci. Technol.* **2005**, *39*, 3946.

(85) Schroder, H. F. *J. Chromatogr. A* **2003**, *1020*, 131.

(86) Hollingsworth, J.; Sierra-Alvarez, R.; Zhou, M.; Ogden, K. L.; Field, J. A. *Chemosphere* **2005**, *59*, 1219.

(87) Key, B. D.; Howell, R. D.; Criddle, C. S. *Environ. Sci. Technol.* **1998**, *32*, 2283.

(88) 3M Company. *Biodegradation studies of fluorocarbons—III*; Docket AR226-0489; Office of Pollution Prevention & Toxics, U.S. Environmental Protection Agency: Washington, D.C., 1978; p. 19.

(89) 3M Company. *Biodegradation studies of Fluorocarbons*; Docket AR226-0058; Office of Pollution Prevention & Toxics, U.S. Environmental Protection Agency: Washington, D.C., 1994; p. 4.

(90) Oppenlander, T. *Photochemical Purification of Water and Air*; Wiley-VCH: Weinheim, 2003.

(91) Schroder, H. F.; Meesters, R. J. W. *J. Chromatogr. A* **2005**, *1082*, 110.

(92) Moriwaki, H.; Takagi, Y.; Tanaka, M.; Tsuruho, K.; Okitsu, K.; Maeda, Y. *Environ. Sci. Technol.* **2005**, *39*, 3388.

(93) Hori, H.; Hayakawa, E.; Einaga, H.; Kutsuna, S.; Koike, K.; Ibusuki, T.; Kiatagawa, H.; Arakawa, R. *Environ. Sci. Technol.* **2004**, *38*, 6118.

(94) Chen, J.; Zhang, P. *Water Sci. Technol.* **2006**, *54*.

(95) Chen, J.; Zhang, P.; Liu, J. *Journal of Environmental Sciences—China* **2007**, *19*.

(96) Yamamoto, T.; Noma, Y.; Sakai, S.; Shibata, Y. *Environ. Sci. Technol.* **2007**.

(97) 3M Company. *Summary of Photolysis Studies using Simulated Sunlight on the Potassium Salt of Perfluorooctanesulfonic Acid*; Docket AR226-0056; Office of Pollution Prevention & Toxics, U.S. Environmental Protection Agency: Washington, D.C., 1978; p. 17.

(98) 3M Company. *FC-143 Photolysis Study using Simulated Sunlight*; Docket AR226-0490; Office of Pollution Prevention & Toxics, U.S. Environmental Protection Agency: Washington, D.C., 1979; p. 15.

(99) Yamamoto, T.; Noma, Y.; Sakai, S. I.; Shibata, Y. *Environ. Sci. Technol.* **2007**, *41*, 5660.

(100) Hori, H.; Yamamoto, A.; Hayakawa, E.; Taniyasu, S.; Yamashita, N.; Kutsuna, S.; Kiatagawa, H.; Arakawa, R. *Environ. Sci. Technol.* **2005**, *39*, 2383.

(101) Hori, H.; Yamamoto, A.; Kutsuna, S. *Environ. Sci. Technol.* **2005**, *39*, 7692.

(102) Kutsuna, S.; Hori, H. *Int. J. Chem. Kin.* **2007**, 276.

(103) Chen, J.; Zhang, P. Y.; Zhang, L. *Chem. Lett.* **2006**, *35*, 230.

(104) Hori, H.; Hayakawa, E.; Koike, K.; Einaga, H.; Ibusuki, T. *J. Mol. Catal. A—Chem.* **2004**, *211*, 35.

(105) Dillert, R.; Bahnemann, D.; Hidaka, H. *Chemosphere* **2007**, *67.*

(106) Yuan, Q.; Ravikrishna, R.; Valsaraj, K. T. *Sep. Purif. Technol.* **2001**, *24.*

(107) Hidaka, H.; Jou, H.; Nohara, K.; Zhao, J. *Chemosphere* **1992**, *25*, 1589.

(108) Vecitis, C. D.; Park, H.; Cheng, J.; Mader, B. M.; Hoffmann, M. R. *J. Phys. Chem. C* **2008**, *112*, 43, 16850.

(109) Sundstrom, D. W.; Klei, H. E. *Wastewater Treatment*; Prentice-Hall: Englewood Cliffs, 1979.

(110) Boulanger, B.; Vargo, J. D.; Schnoor, J. L.; Hornbuckle, K. C. *Environ. Sci. Technol.* **2005**, *39*, 5524.

(111) Loganathan, B. G.; Sajwan, K. S.; Sinclair, E.; Kumar, K. S.; Kannan, K. *Water Research* **2007**, *41*, 4611.

(112) DuPont. *Accelerated Biodegradation of 8-2 Telomer B Alcohol*; Docket AR226-1264; Office of Pollution Prevention and Toxics, U.S. Environmental Protection Agency: Washington, D.C., 2003; p. 45.

(113) Yamada, T.; Taylor, P. H.; Buck, R. C.; Kaiser, M. A.; Giraud, R. J. *Chemosphere* **2005**, *61*, 974.

(114) Tang, C. Y. Y.; Fu, Q. S.; Robertson, A. P.; Criddle, C. S.; Leckie, J. O. *Environ. Sci. Technol.* **2006**, *40*, 7343.

(115) Tang, C. Y.; Fu, Q. S.; Criddle, C. S.; Leckie, J. O. *Environ. Sci. Technol.* **2007**, *41*, 2008.

(116) Higgins, C. P.; Luthy, R. G. *Environ. Sci. Technol.* **2006**, *40*, 7251.

(117) Johnson, R. L.; Anschutz, A. J.; Smolen, J. M.; Simcik, M. F.; Penn, R. L. *J. Chem. Eng. Data* **2007**, *52*, 1165.

(118) Pera-Titus, M.; Garcia-Molina, V.; Banos, M. A.; Gimenez, J.; Esplugas, S. *Appl. Catal. B—Environ.* **2004**, *47*, 219.

(119) Andreozzi, R.; Caprio, V.; Insola, A.; Marotta, R. *Catal. Today* **1999**, *53*, 51.

(120) Legrini, O.; Oliveros, E.; Braun, A. M. *Chem. Rev.* **1993**, *93*, 671.

(121) Kochany, J.; Bolton, J. R. *Environ. Sci. Technol.* **1992**, *26*, 262.

(122) Hoigne, J.; Bader, H. *Water Research* **1983**, *17*, 173.

(123) Hoigne, J.; Bader, H. *Water Research* **1983**, *17*, 185.

(124) Zepp, R. G.; Faust, B. C.; Hoigne, J. *Environ. Sci. Technol.* **1992**, *26*, 313.

(125) Hua, I.; Hoffmann, M. R. *Environ. Sci. Technol.* **1997**, *31*, 2237.

(126) Acero, J. L.; Haderlein, S. B.; Schmidt, T. C.; Suter, M. J. F.; Von Gunten, U. *Environ. Sci. Technol.* **2001**, *35*, 4252.

(127) Buxton, G. V.; Greenstock, C. L.; Helman, W. P.; Ross, A. B. *J. Phys. Chem. Ref. Data* **1988**, *17*, 513.

(128) An, Y. J.; Jeong, S. W. *Journal of Colloid and Interface Science* **2001**, *242*, 419.

(129) An, Y. J.; Carraway, E. R.; Schlautman, M. A. *Water Research* **2002**, *36*, 300.

(130) Huang, Q.; Hong, C. S. *Chemosphere* **2000**, *41*.

(131) Gromadzka, K.; Swietlik, J. *Water Research* **2007**, *41*, 2572.

(132) Waldemer, R. H.; Tratnyek, P. G.; Johnson, R. L.; Nurmi, J. T. *Environ. Sci. Technol.* **2007**, *41*, 1010.

(133) Lau, T. K.; Chu, W.; Graham, N. J. D. *Environ. Sci. Technol.* **2007**, *41*, 613.

(134) Anipsitakis, G. P.; Dionysiou, D. D. *Environ. Sci. Technol.* **2004**, *38*, 3705.

(135) Anipsitakis, G. P.; Dionysiou, D. D. *Environ. Sci. Technol.* **2003**, *37*, 4790.

(136) Ball, D. L.; Edwards, J. O. *J. Am. Chem. Soc.* **1956**, *78*, 1125.

(137) Dogliott, L.; Hayon, E. *J. Phys. Chem.* **1967**, *71*, 2511.

(138) Kolthoff, I. M.; Miller, I. K. *J. Am. Chem. Soc.* **1951**, *73*, 3055.

(139) Maruthamuthu, P.; Padmaja, S.; Huie, R. E. *Int. J. Chem. Kin.* **1995**, *27*.

(140) Neta, P.; Huie, R. E.; Ross, A. B. *J. Phys. Chem. Ref. Data* **1988**, *17*, 1027.

(141) Schwarzenbach, R. P.; Gschwend, P. M.; Imboden, D. M. *Environmental Organic Chemistry, Second ed.*; Wiley: New York, 2003.

(142) Zepp, R. G.; Cline, D. M. *Environ. Sci. Technol.* **1977**, *11*, 359.

(143) 3M Company. *FM-3422: Photolysis Study using Simulated Sunlight*; Docket AR226-0363; Office of Pollution Prevention & Toxics, U.S. Environmental Protection Agency: Washington, D.C., 1981; p. 20.

(144) Gauthier, S. A.; Mabury, S. A. *Environ. Toxicol. Chem.* **2005**, *24*, 1837.

(145) Lee, C.; Choi, W.; Kim, Y. G.; Yoon, J. *Environ. Sci. Technol.* **2005**, *39*, 2101.

(146) Getoff, N.; Schenck, G. O. *Photochemistry and Photobiology* **1968**, *8*, 167.

(147) Fricke, H.; Hart, E. J. *J. Chem. Phys.* **1936**, *4*, 418.

(148) Oppenlander, T.; Gliese, S. *Chemosphere* **2000**, *40*, 15.

(149) Jakob, L.; Hashem, T. M.; Burki, S.; Guindy, N. M.; Braun, A. M. *Journal of Photochemistry and Photobiology A—Chemistry* **1993**, *75*, 97.

(150) Quici, N.; Litter, M. I.; Braun, A. A.; Oliveros, E. *Journal of Photochemistry and Photobiology A—Chemistry* **2008**, *197*, 306.

(151) Chen, J.; Zhang, P. Y.; Liu, J. *J. Environ. Sci* **2007**, *19*, 387.

(152) Osborne, M. C.; Li, Q.; Smith, I. W. M. *Physical Chemistry Chemical Physics* **1999**, *1*, 1447.

(153) Ozer, R. R.; Ferry, J. L. *Environ. Sci. Technol.* **2001**, *35*, 3242.

(154) Fox, M. A.; Cardona, R.; Gaillard, E. *J. Am. Chem. Soc.* **1987**, *109*, 6347.

(155) Lee, J.; Kim, J.; Choi, W. *Environ. Sci. Technol.* **2007**, *41*, 3335.

(156) Weinstock, I. A. *Chem. Rev.* **1998**, *98*, 113.

(157) Akid, R.; Darwent, J. R. *J. Chem. Soc.—Dalton Trans.* **1985**, 395.

(158) Hori, H.; Takano, Y.; Koike, K.; Takeuchi, K.; Einaga, H. *Environ. Sci. Technol.* **2003**, *37*, 418.

(159) Hoffmann, M. R.; Martin, S. T.; Choi, W. Y.; Bahnemann, D. W. *Chem. Rev.* **1995**, *95*, 69.

(160) Kormann, C.; Bahnemann, D. W.; Hoffmann, M. R. *Environ. Sci. Technol.* **1991**, *25*, 494.

(161) Dillert, R.; Bahnemann, D.; Hidaka, H. *Chemosphere* **2007**, *67*, 785.

(162) Guan, B.; Zhi, J.; Zhang, X.; Murakami, T.; Fujishima, A. *Electrochem. Commun.* **2007**, *9*, 2817.

(163) Lee, J.; Seliger, H. H. *J. Chem. Phys.* **1964**, *40*, 519.

(164) Hatchard, C. G.; Parker, C. A. *Proceedings of the Royal Society of London Series A—Mathematical and Physical Sciences* **1956**, *235*, 518.

(165) Parker, C. A. *Proceedings of the Royal Society of London Series A—Mathematical and Physical Sciences* **1953**, *220*, 104.

(166) Allmand, A. J.; Webb, W. W. *Journal of the Chemical Society* **1929**, 1518.

(167) Hori, H.; Yamamoto, A.; Koike, K.; Kutsuna, S.; Osaka, I.; Arakawa, R. *Chemosphere* **2007**, *68*, 572.

(168)*http://chm.pops.int/Convention/POPsReviewCommittee/Chemicalsunderreview/tabid/242/language/en-US/Default.aspx*.

(169) Sayles, G. D.; You, G. R.; Wang, M. X.; Kupferle, M. J. *Environ. Sci. Technol.* **1997**, *31*, 3448.

(170) Yak, H. K.; Wenclawiak, B. W.; Cheng, I. F.; Doyle, J. G.; Wai, C. M. *Environ. Sci. Technol.* **1999**, *33*, 1307.

(171) Jones, C. G.; Silverman, J.; Al-Sheikhly, M.; Neta, P.; Poster, D. L. *Environ. Sci. Technol.* **2003**, *37*, 5773.

(172) Hinz, D. C.; Wai, C. M.; Wenclawiak, B. W. *J. Environ. Monit.* **2000**, *2*, 45.

(173) Zhang, W. X. *J. Nanopart. Res.* **2003**, *5*, 323.

(174) Wang, C. B.; Zhang, W. X. *Environ. Sci. Technol.* **1997**, *31*, 2154.

(175) Hori, H.; Nagaoka, Y.; Sano, T.; Kutsuna, S. *Chemosphere* **2008**, *70*, 800.

(176) Hori, H.; Nagaoka, Y.; Yamamoto, A.; Sano, T.; Yamashita, N.; Taniyasu, S.; Kutsuna, S.; Osaka, I.; Arakawa, R. *Environ. Sci. Technol.* **2006**, *40*, 1049.

(177) Macnicol, D. D.; Robertson, C. D. *Nature* **1988**, *332*, 59.

(178) Shoute, L. C. T.; Mittal, J. P.; Neta, P. *J. Phys. Chem.* **1996**, *100*, 11355.

(179) Shoute, L. C. T.; Mittal, J. P.; Neta, P. *J. Phys. Chem.* **1996**, *100*, 3016.

(180) Watson, P. L.; Tulip, T. H.; Williams, I. *Organometallics* **1990**, *9*, 1999.

(181) Combellas, C.; Kanoufi, F.; Thiebault, A. *Journal of Physical Chemistry B* **2003**, *107*, 10894.

(182) Corvaja, C.; Farnia, G.; Formenton, G.; Navarrini, W.; Sandona, G.; Tortelli, V. *J. Phys. Chem.* **1994**, *98*, 2307.

(183) Marsella, J. A.; Gilicinski, A. G.; Coughlin, A. M.; Pez, G. P. *J. Org. Chem.* **1992**, *57*, 2856.

(184) Pud, A. A.; Shapoval, G. S.; Kukhar, V. P.; Mikulina, O. E.; Gervits, L. L. *Electrochim. Acta* **1995**, *40*, 1157.

(185) Chen, X. D.; Lemal, D. M. *J. Fluor. Chem.* **2006**, *127*, 1158.

(186) Szajdzinska-Pietek, E.; Gebicki, J. L. *Res. Chem. Intermed.* **2000**, *26*, 897.

(187) Huang, L.; Dong, W. B.; Hou, H. Q. *Chem. Phys. Lett.* **2007**, *436*, 124.

(188) Ono, T.; Fukaya, H.; Hayashi, E.; Saida, H.; Abe, T.; Henderson, P. B.; Fernandez, R. E.; Scherer, K. V. *J. Fluor. Chem.* **1999**, *97*, 173.

(189) Ochoa-Herrera, V.; Sierra-Alvarez, R.; Somogyi, A.; Jacobsen, N. E.; Wysocki, V. H.; Field, J. A. *Environ. Sci. Technol.* **2008**, *42*, 3260.

(190) Johnson, T. L.; Scherer, M. M.; Tratnyek, P. G. *Environ. Sci. Technol.* **1996**, *30*, 2634.

(191) Roberts, A. L.; Totten, L. A.; Arnold, W. A.; Burris, D. R.; Campbell, T. J. *Environ. Sci. Technol.* **1996**, *30*, 2654.

(192) Puls, R. W.; Paul, C. J.; Powell, R. M. *Appl. Geochem.* **1999**, *14*, 989.

(193) Tratnyek, P. G.; Johnson, T. L.; Scherer, M. M.; Eykholt, G. R. *Ground Water Monit. Remediat.* **1997**, *17*, 108.

(194) Cantrell, K. J.; Kaplan, D. I.; Wietsma, T. W. *J. Hazard. Mater.* **1995**, *42*, 201.

(195) Liu, Y. Q.; Majetich, S. A.; Tilton, R. D.; Sholl, D. S.; Lowry, G. V. *Environ. Sci. Technol.* **2005**, *39*, 1338.

(196) Elliott, D. W.; Zhang, W. X. *Environ. Sci. Technol.* **2001**, *35*, 4922.

(197) Kim, Y. H.; Carraway, E. R. *Environ. Sci. Technol.* **2000**, *34*, 2014.

(198) Zhang, W. X.; Wang, C. B.; Lien, H. L. *Catal. Today* **1998**, *40*, 387.

(199) Bransfield, S. J.; Cwiertny, D. M.; Livi, K.; Fairbrother, D. H. *Appl. Catal. B—Environ.* **2007**, *76*, 348.

(200) Cwiertny, D. M.; Bransfield, S. J.; Livi, K. J. T.; Fairbrother, D. H.; Roberts, A. L. *Environ. Sci. Technol.* **2006**, *40*, 6837.

(201) Marshall, W. D.; Kubatova, A.; Lagadec, A. J. M.; Miller, D. J.; Hawthorne, S. B. *Green Chem.* **2002**, *4*, 17.

(202) Hart, E. J.; Anbar, M. *The Hydrated Electron*; John Wiley & Sons, Inc.: New York, 1970.

(203) Mezyk, S. P.; Helgeson, T.; Cole, S. K.; Cooper, W. J.; Fox, R. V.; Gardinali, P. R.; Mincher, B. J. *J. Phys. Chem. A* **2006**, *110*, 2176.

(204) Milosavljevic, B. H.; LaVerne, J. A.; Pimblott, S. M. *J. Phys. Chem. A* **2005**, *109*, 7751.

(205) Johnson, H. D.; Cooper, W. J.; Mezyk, S. P.; Bartels, D. M. *Radiat. Phys. Chem.* **2002**, *65*, 317.

(206) Nickelsen, M. G.; Cooper, W. J.; Secker, D. A.; Rosocha, L. A.; Kurucz, C. N.; Waite, T. D. *Radiat. Phys. Chem.* **2002**, *65*, 579.

(207) Rahn, R. O.; Stephan, M. I.; Bolton, J. R.; Goren, E.; Shaw, P.-S.; Lykke, K. R. *Photochem. Photobiol.* **2003**, *78*, 146.

(208) Anbar, M.; Hart, E. J. *J. Phys. Chem.* **1965**, *69*, 271.

(209) Czapski, G.; Schwarz, H. A. *J. Phys. Chem.* **1962**, *66*, 471.

(210) Matheson, M. S.; Mulac, W. A.; Rabani, J. *J. Phys. Chem.* **1963**, *67*, 2613.

(211) Hart, E. J.; Boag, J. W. *J. Am. Chem. Soc.* **1962**, *84*, 4090.

(212) Thomas-Smith, T. E.; Blough, N. V. *Environ. Sci. Technol.* **2001**, *35*, 2721.

(213) Hoigne, J.; Faust, B. C.; Haag, W. R.; Scully, F. E.; Zepp, R. G. *Acs Symposium Series* **1989**, *219*, 363.

(214) Zepp, R. G.; Braun, A. M.; Hoigne, J.; Leenheer, J. A. *Environ. Sci. Technol.* **1987**, *21*, 485.

(215) Lian, R.; Oulianov, D. A.; Crowell, R. A.; Shkrob, I. A.; Chen, X. Y.; Bradforth, S. E. *J. Phys. Chem. A* **2006**, *110*, 9071.

(216) Nishiwaki, T.; Usui, M.; Anda, K.; Hida, M. *Bull. Chem. Soc. Jpn.* **1979**, *52*, 821.

(217) Yao, Y.; Kakimoto, K.; Ogawa, H. I.; Kato, Y.; Hanada, Y.; Shinohara, R.; Yoshino, E. *Chemosphere* **1997**, *35*, 2891.

(218) Hawari, J.; Demeter, A.; Samson, R. *Environ. Sci. Technol.* **1992**, *26*, 2022.

(219) Schwarz, H. A.; Dodson, R. W. *J. Phys. Chem.* **1989**, *93*, 409.

(220) Murakami, Y.; Kikuchi, J.; Hisaeda, Y.; Hayashida, O. *Chem. Rev.* **1996**, *96*, 721.

(221) Gantzer, C. J.; Wackett, L. P. *Environ. Sci. Technol.* **1991**, *25*, 715.

(222) Costentin, C.; Robert, M.; Saveant, J. M. *J. Am. Chem. Soc.* **2005**, *127*, 12154.

(223) Glod, G.; Angst, W.; Holliger, C.; Schwarzenbach, R. P. *Environ. Sci. Technol.* **1997**, *31*, 253.

(224) Wood, J. M.; Kennedy, F. S.; Wolfe, R. S. *Biochemistry* **1968**, *7*, 1707.

(225) Lexa, D.; Saveant, J. M. *J. Am. Chem. Soc.* **1978**, *100*, 3220.

(226) Lexa, D.; Saveant, J. M.; Zickler, J. *J. Am. Chem. Soc.* **1977**, *99*, 2786.

(227) Zehnder, A. J. B.; Wuhrmann, K. *Science* **1976**, *194*, 1165.

(228) Shey, J.; van der Donk, W. A. *J. Am. Chem. Soc.* **2000**, *122*, 12403.

(229) Schrauze, G.N.; Deutsch, E.; Windgass, R.J.. *J. Am. Chem. Soc.* **1968**, *90*, 2441.

(230) Krusic, P. J.; Marchione, A. A.; Roe, D. C. *J. Fluor. Chem.* **2005**, *126*, 1510.

(231) Ainagos, A. F. *Kinet. Catal.* **1991**, *32*, 720.

(232) Hynes, R. G.; Mackie, J. C.; Masri, A. R. *J. Phys. Chem. A* **1999**, *103*, 54.

(233) Atkinson, B.; McKeagan, D. *Chem. Commun.* **1966**, 189.

(234) Bauer, S. H.; Hou, K. C.; Resler, E. L. *Phys. Fluids* **1969**, *12*, I125.

(235) Blake, P. G.; Tomlinso.A. D. *Journal of the Chemical Society B—Physical Organic* **1971**, 1596.

(236) Brown, C. E.; Smith, D. R. *Can. J. Chem.—Rev. Can. Chim.* **1988**, *66*, 609.

(237) Chowdhury, P. K. *J. Phys. Chem.* **1995**, *99*, 12084.

(238) Longfellow, C. A.; Smoliar, L. A.; Lee, Y. T.; Lee, Y. R.; Yeh, C. Y.; Lin, S. M. *J. Phys. Chem. A* **1997**, *101*, 338.

(239) Matula, R. A. *J. Phys. Chem.* **1968**, *72*, 3054.

(240) Millward, G. E.; Tschuiko.E. *J. Phys. Chem.* **1972**, *76*, 292.

(241) Tschuiko, E. *J. Chem. Phys.* **1968**, *49*, 3115.

(242) Lee, M. C.; Choi, W. *J. Ind. Eng. Chem.* **2004**, *10*, 107.

(243) Burgess, D. R.; Zachariah, M. R.; Tsang, W.; Westmoreland, P. R. *Prog. Energy Combust. Sci.* **1995**, *21*, 453.

(244) Lines, D.; Sutcliffe, H. *J. Fluor. Chem.* **1984**, *25*, 505.

(245) Lazerte, J. D.; Hals, L. J.; Reid, T. S.; Smith, G. H. *J. Am. Chem. Soc.* **1953**, *75*, 4525.

(246) Glockner, V.; Lunkwitz, K.; Prescher, D. *Tenside Surf. Det.* **1989**, *26*.

(247) Krusic, P. J.; Roe, D. C. *Anal. Chem.* **2004**, *76*, 3800.

(248) 3M Company. *Laboratory-Scale Thermal Degradation of Perfluorooctanyl Sulfonate and Related Substances*; Docket AR226-1366; Office of Pollution Prevention & Toxics, U.S. Environmental Protection Agency: Washington, D.C., 2003; p. 13.

(249) Ravishankara, A. R.; Solomon, S.; Turnipseed, A. A.; Warren, R. F. *Science* **1993**, *259*, 194.

(250) 3M Company. *Final Report—Laboratory-Scale Thermal Degradation of Perfluoro-Octanyl Sulfonate and Related Substances*; Docket AR226-1367; Office of Pollution Prevention & Toxics, U.S. Environmental Protection Agency: Washington, D.C., 2003; p. 142.

(251) Leighton, T. G. *The Acoustic Bubble*; Academic Press: London, 1994.

(252) Mason, T. J.; Lorimer, J. P. *Sonochemistry: theory, applications and uses of ultrasound in chemistry*; Halsted Press: New York, 1988.

(253) Suslick, K. S. *Ultrasound: Its Chemical, Physical, and Biological Effects;* VCH, New York, 1988.

(254) Destaillats, H.; Hung, H. M.; Hoffmann, M. R. *Environ. Sci. Technol.* **2000**, *34*, 311.

(255) Kotronarou, A.; Mills, G.; Hoffmann, M. R. *J. Phys. Chem.* **1991**, *95*, 3630.

(256) Vinodgopal, K.; Ashokkumar, M.; Grieser, F. *J. Phys. Chem. B* **2001**, *105*, 3338.

(257) Manousaki, E.; Psillakis, E.; Kalogerakis, N.; Mantzavinos, D. *Water Res.* **2004**, *38*, 3751.

(258) Petrier, C.; Lamy, M. F.; Francony, A.; Benahcene, A.; David, B.; Renaudin, V.; Gondrexon, N. *J. Phys. Chem.* **1994**, *98*, 10514.

(259) Hung, H. M.; Hoffmann, M. R. *J. Phys. Chem. A* **1999**, *103*, 2734.

(260) Jennings, B. H.; Townsend, S. N. *J. Phys. Chem.* **1961**, *65*, 1574.

(261) Petrier, C.; David, B.; Laguian, S. *Chemosphere* **1996**, *32*, 1709.

(262) Vecitis, C. D.; Park, H.; Cheng, J.; Mader, B. T.; Hoffmann, M. R. *J. Phys. Chem. A* **2008**, *112*, 4261.

(263) Suslick, K. S.; Hammerton, D. A.; Cline, R. E. *J. Am. Chem. Soc.* **1986**, *108*, 5641.

(264) Price, G. J.; Ashokkumar, M.; Hodnett, M.; Zequiri, B.; Grieser, F. *J. Phys. Chem. B* **2005**, *109*, 17799.

(265) Sunartio, D.; Ashokkumar, M.; Grieser, F. *J. Am. Chem. Soc.* **2007**, *129*, 6031.

(266) Brennen, C. E. *Cavitation and Bubble Dynamics*; Oxford University Press: New York, 1995.

(267) Didenko, Y. T.; McNamara, W. B.; Suslick, K. S. *J. Am. Chem. Soc.* **1999**, *121*, 5817.

(268) Ciawi, E.; Rae, J.; Ashokkumar, M.; Grieser, F. *J. Phys. Chem. B* **2006**, *110*, 13656.

(269) Ashokkumar, M.; Grieser, F. *J. Am. Chem. Soc.* **2005**, *127*, 5326.

(270) Eddingsaas, N. C.; Suslick, K. S. *J. Am. Chem. Soc.* **2007**, *129*, 3838.

(271) Sostaric, J. Z.; Riesz, P. *J. Am. Chem. Soc.* **2001**, *123*, 11010.

(272) Kato, S.; Makide, Y.; Tominaga, T.; Takeuchi, K. *J. Phys. Chem.* **1987**, *91*, 4278.

(273) Kolaczkowski, S. T.; Plucinski, P.; Beltran, F. J.; Rivas, F. J.; McLurgh, D. B. *Chem. Eng. J.* **1999**, *73*, 143.

(274) Chang, M. B.; Chang, J. S. *Industrial & Engineering Chemistry Research* **2006**, *45*, 4101.

(275) Destaillats, H.; Colussi, A. J.; Joseph, J. M.; Hoffmann, M. R. *J. Phys. Chem. A* **2000**, *104*, 8930.

(276) Weavers, L. K.; Malmstadt, N.; Hoffmann, M. R. *Environ. Sci. Technol.* **2000**, *34*, 1280.

(277) Lesko, T.; Colussi, A. J.; Hoffmann, M. R. *Environ. Sci. Technol.* **2006**, *40*, 6818.

(278) Weavers, L. K.; Ling, F. H.; Hoffmann, M. R. *Environ. Sci. Technol.* **1998**, *32*, 2727.

(279) Vecitis, C. D.; Park, H.; Cheng, J.; Mader, B. T.; Hoffmann, M. R. *J. Phys. Chem. C* **2008**, *112*, 16850.

Chapter 3

Sonolytic Conversion of the Aqueous Perfluorinated Surfactants, Perfluorooctanoate (PFOA) and Perfluorooctanesulfonate (PFOS) into Inorganic Constituents

Sections reprinted with permission from Vecitis, C. D.; Park H.; Cheng J.; Mader, B. T.; Hoffmann, M. R. *Journal of Physical Chemistry A* **2008**, *112*, 4261–4270.

Abstract

The perfluorinated surfactants perfluorooctane sulfonate (PFOS) and perfluorooctanoate (PFOA) are recognized as widespread in the environment as well as recalcitrant towards most conventional water treatment technologies. In this study acoustic cavitation as driven by high-frequency ultrasound is shown to be effective in the degradation of aqueous solutions of PFOS and PFOA, and effective over a wide range of concentrations from 10 nM to 10 μM for a given compound. Sulfur, fluorine, and carbon mass balances indicate that mineralization occurs immediately following the degradation of the initial perfluorinated surfactant. Near-complete conversion of PFOS and PFOA to CO, CO_2, F^-, and SO_4^{2-} occurs due to pyrolytic reactions at the surface and vapor phase of transiently collapsing cavitation bubbles. The initial PFOS or PFOA pyrolytic degradation occurs at the bubble-water interface and involves the loss of the ionic functional group leading to the formation of the corresponding 1H-fluoroalkane or perfluoroolefin. The fluorochemical intermediates undergo a series of pyrolytic reactions in the bubble vapor leading to C_1 fluoro-radicals. Secondary vapor-phase bimolecular reactions coupled with concomitant hydrolysis converts the C_1 fluoro-radicals to carbon monoxide, carbon dioxide and HF, forming a proton and fluoride upon dissolution. Sonochemical half-lives, which are calculated from high-temperature gas-phase kinetics, are consistent with kinetic observations and suggest that mineralization occurs shortly after an initial perfluorinated surfactant interfacial pyrolysis.

Introduction

Over the last 60 years, fluorochemicals (FCs) have been used for a wide variety of applications such as water-proofing of materials, protective coating of metals, fire-fighting foams for electrical and grease fires, semi-conductor etching, and lubrication. The widespread use of these compounds is due to their favorable physical properties, which include chemical stability, low coefficients of friction, and low polarizabilities (i.e., fluorophilicity)[1]. The same properties that make FCs valuable as commercial products make them difficult to treat using most conventional environmental remediation strategies or waste treatment technologies[2–4]. For example, Schultz et al.[3] reported that the total mass of PFOA and PFOS is not reduced (i.e., is resistant to physical and biological treatments) during conventional wastewater treatment processes. Consequently, fluorochemicals have become widespread in the environment[5–7].

Most conventional degradation technologies are ineffective for the *in situ* degradation of aqueous PFOS and PFOA, present in the aqueous phase, since they are inherently recalcitrant to chemical and microbiological treatment[2,3,8–11]. Advanced oxidation processes (AOPs)[12], which utilize the hydroxyl radical, such as UV-ozonation[13], peroxone (i.e., a mixture of O_3 and H_2O_2)[13], or Fenton's reagent (i.e., H_2O_2 and Fe^{2+} salts)[13–15] have been shown to be ineffective for PFOA and PFOS destruction. A number of photolytic methods such as direct photolysis[15–20], persulfate photolysis[16,21–23], alkaline isopropanol photolysis[19] and photocatalysis[15,24–28] have shown varying degrees of efficacy on higher concentrations of perfluorocarboxylates. However, none of these methods lead to the mineralization of PFOS and PFOA. Reduction by elemental iron under near-super-critical water conditions has been shown to be possible for PFOS degradation[29]. However, scale-up of high-pressure, high-temperature treatment systems is difficult[30]. Moriwaki et al.[14] have shown that ultrasonic irradiation of aqueous solutions can degrade these compounds with fluoride and sulfate as the primary degradation products.

Sonochemistry, as induced by ultrasonic irradiation of aqueous solutions at near-ambient temperatures and pressures, has been shown to be effective for the treatment of a wide variety of chemical contaminants[31–35]. Ultrasonic pressure waves force the formation and quasi-adiabatic collapse of vapor bubbles formed from pre-existing gas nuclei[36]. The transient collapse of aqueous cavitation bubbles has been shown through chemical methods to raise average internal vapor temperatures near 4000 K[37–39] and are supported by single-bubble collapse models[40–42], while bubble-water interface temperatures have been calculated to be in the range of 600 to 1000 K[34]. These transient high temperatures lead to *in situ* pyrolytic reactions in the vapor and interfacial regions of each collapsing bubble, resulting in the breakdown of water-producing hydroxyl radicals ($^{\cdot}$OH), oxygen atoms (O), and hydrogen atoms (H$^{\cdot}$). These transient radicals react readily with compounds in the bubble gas-phase or at the bubble interface. Some of the radical species are dispersed into the bulk solution by nonspherical bubble collapse. Ultrasonic degradation is effective for the removal of contaminants with high Henry's Law constants[43–45] that partition into the vapor phase of the bubble, or for chemical contaminants which partition to the air-water interface[46–48] such as PFOS and PFOA[14].

We hereby report a detailed investigation into the kinetics and mechanism of the sonochemical conversion of aqueous PFOS and PFOA to inorganic constituents.

Experimental Methods

Ammonium perfluorooctanoate (APFO) and potassium perfluorooctanesulfonate (PFOS) standards, consisting of a mixture of branched and linear isomers, were provided by 3M Company. Ammonium acetate (> 99 %) and methanol (HR-GC > 99.99 %) were obtained from EMD Chemicals, Inc. Aqueous solutions were prepared with purified water using a Milli-Q system (18.2 MΩ cm^{-1} resistivity).

Sonications at frequencies of 354 and 618 kHz were performed using an Allied Signal Elac Nautik ultrasonic transducer (23.6 cm^2) at an applied power of 150 W with the solution contained in a 600 mL jacketed glass reactor. The temperature was controlled with a Neslab RTE-111 refrigerated bath maintained at 10 ºC. Sonications performed at 500 kHz were completed with an Undatim ultrasonic transducer (25.5 cm^2) at an applied power of 75 W with the solution contained in a 400 mL jacketed glass reactor. The temperature was controlled with a Haake A80 refrigerated bath set to 10 ^oC. All reactions were sparged with argon for at least 30 minutes prior to reaction. Initial solution pH was between 7 and 8 for all reactions. Calorimetry was done to determine the acoustic power transferred to solution. At 354, 500, and 618 kHz the applied (calorimetric) power densities in W L^{-1} were 250 (200), 150 (128), and 250 (208), respectively. The applied acoustic power densities will be referred to in the text.

A number of reactor configurations, initial concentrations, and mixtures were used for the various experiments. PFOS and PFOA were analyzed for in all experiments by an HPLC-MSD-Ion Trap (Agilent). Fluoride and sulfate were analyzed by ion chromatography (Dionex) and completed using 618 kHz, 250 W L^{-1}, and 6.4 W cm^{-2} on a closed system where the produced gas was resparged into solution to retain all products: PFOS and PFOA were sonicated separately at initial concentrations of approximately 10 μM. Trace gas analyses by GC-MS (Agilent) and FT-IR (Midac) were sonicated at 500 kHz, 150 W L^{-1}, and 2.9 W cm^2 on a closed system where the headspace was recirculated but not resparged through a 300 mL multiple reflection FT-IR cell with an in-line valved port for GC-MS sampling: PFOS and PFOA were sonicated simultaneously at a total initial concentration of 20 μM (10 μM each). The experiments where CO and CO_2 were measured during sonication were completed using 354 kHz, 250 W L^{-1} and 6.4 W cm^{-2} using a continuously sparged (100 to 125 mL min^{-1}) open system where the product gas was evacuated (≈ 100 mL min^{-1}) into a high-vacuum chamber through a stainless-steel membrane inlet to be analyzed by EI-MS (Balzers): PFOS and PFOA were sonicated separately at initial concentrations of 100 μM. Reactor configurations and analytical procedures are detailed in the supporting information.

Results

Ultrasonic irradiation degradation kinetics of aqueous PFOS, $[PFOS]_i$ = 200 nM , and PFOA, $[PFOA]_i$ = 240 nM are plotted in Figure 3.1 (υ = 358 kHz, ρ_{PD} = 250 W L^{-1}, I_P = 6.4 W cm^{-2}). The observed kinetics are quasi-exponential (i.e., the ln $([PFOX]_t/[PFOX]_i)$ vs. time plot is linear) and is typical of what would be expected for PFOS and PFOA co-contamination in an environmental system where concentrations are in the picomolar to micromolar range[7]. Apparent pseudo-first-order kinetics are given in eq. 3.1

$$\frac{d[PFOX]}{dt} = -k_{app}^{-PFOX}[PFOX] \tag{3.1}$$

where X = A or S and [PFOX] are the representative carboxylate or sulfonate concentrations and k_{app}^{-PFOX} are the apparent first-order rate constants for each species. A linear fit of the kinetic plots gives k_{app}^{-PFOA} = 0.041 min^{-1} ($\tau_{1/2}$ = 16.9 minutes) and k_{app}^{-PFOS} = 0.027 min^{-1} ($\tau_{1/2}$ = 25.7 minutes). The PFOA degradation rate constant is 1.5 times that of PFOS. The observed pseudo-first-order kinetics are in agreement with results previously reported by Moriwaki et al.[14] for the sonolytic degradation (200 kHz and 3 W cm^{-2}) of aqueous PFOS and PFOA at 20 and 24 μM, respectively. Similar sonochemical kinetics were also observed for hydrocarbon surfactants such as Triton X-100[32] and linear alkyl benzyl sulfonates[49].

A time-dependent sulfur mass balance for an aqueous PFOS solution where $[\mathrm{PFOS}]_i = 10\ \mu\mathrm{M}$ was obtained at ultrasonic conditions of 618 kHz, 250 W L^{-1}, and 6.4 W cm^{-2}. The PFOS sulfur mass balance is shown in Figure 3.2 in units of moles sulfur per each species over total initial moles of PFOS sulfur. Aqueous sulfate ion, as detected by ion chromatography, was the only observed sulfur-containing product and has a formation half-life equivalent to the PFOS degradation half-life and thus is formed as PFOS is initially destroyed. At each point in time, the total sulfur balance, given by the sum of sulfate and PFOS sulfur, is equal to or greater than one.

The corresponding mass balance for fluorine of aqueous PFOS, $[\mathrm{PFOS}]_i = 10\ \mu\mathrm{M}$, and PFOA, $[\mathrm{PFOA}]_i = 12\ \mu\mathrm{M}$, during sonication for the same conditions is shown in Figure 3.3 in terms of moles fluorine per species over total initial moles PFOX fluorine. In earlier work, Moriwaki et al. detected low-levels of shorter-chain perfluoro-acids as reaction intermediates during the sonolytic degradation of PFOS and PFOA[14]; however, we did not detect any of these intermediates during our experiments. Aqueous fluoride accounted for greater than 90% of the fluorine from the degraded PFOS and PFOA at any point in time during the reaction, as shown in Figures 3.3a and b, respectively.

The solid line through the PFOS, PFOA, sulfate, and fluoride data points shown in Figures 3.2 and 3.3 are obtained from kinetic analyses. For example, the PFOA fluorine mass balance data is fit using eq. 3.2

$$\frac{\{moles\ \ F\}_{PFOA,t}}{\{moles\ \ F\}_{PFOA,i}} = \exp(-k_1^{-PFOA}t) \tag{3.2}$$

while the fluoride and sulfate mass balance data are fit to a double exponential involving a single intermediate decay, (e.g., PFOS → I → F^- or SO_4^{2-}). k_1^{-PFOX} , as determined from eq. 3.2, is the rate constant for the initial decay, PFOS → I, and $k_2^{X^-}$ is the rate constant for the second decay, I → F^- or SO_4^{2-}. For example, $k_2^{SO_4^{2-}}$ is determined through fitting the sulfate-normalized mass balance data to eq. 3.3.

$$\frac{\{moles\ S\}_{SO_4^{2-},t}}{\{moles\ S\}_{PFOS,i}} = \frac{1}{k_1^{-PFOS} + k_2^{SO_4^{2-}}}(k_2^{SO_4^{2-}}(1-\exp(-k_1^{-PFOS}t)) - k_1^{-PFOS}(1-\exp(-k_2^{SO_4^{2-}}t))) \quad (3)$$

The rate constants determined from the kinetic fits are given in Table 3.1. The PFOS and PFOA sonochemical decomposition rate constants decrease slightly at the somewhat higher initial concentrations used in the mass balance experiments as compared to those shown in Figure 3.1. The intermediate, I, conversion rate constant to sulfate, $k_2^{SO_4^{2-}}$, is > 1 min^{-1}, thus the sulfonate moiety ($-CF_2-SO_3^-$) is converted quantitatively to sulfate (SO_4^{2-}) shortly after the PFOS decomposition, $-d[PFOS]/dt \approx d[SO_4^{2-}]/dt$. This suggests that the sonolytic decomposition of PFOS proceeds via pyrolytic C-S bond cleavage[50] to yield an oxysulfur intermediate such as SO_3 or SO_3F^- which is readily hydrolyzed or oxidized to SO_4^{2-}. A similar mechanism is expected for PFOA sonolysis where the initial bond cleavage occurs at the carbon-carbon bond between the carboxylate group and the fluorinated tail, $R_FCF_2-CO_2^-$, releasing CO_2[51,52]. Initial ionic headgroup cleavage mechanism should produce a fluorinated alkane or alkene as the other primary sonolysis intermediate. These are transformed to F^- at a rate constant of 0.3 min^{-1} for both PFOS and PFOA, suggesting a similar fluoride production pathway for both species. The slower rate of fluoride production as compared to sulfate production during PFOS sonolysis is consistent with an initial C-S bond cleavage mechanism producing a fluorinated alkane intermediate that requires multiple, sequential pyrolytic steps prior to fluoride production[53].

The time-dependent sulfur and fluorine measurements are also consistent with the analysis of headspace gases by multiple reflection FT-IR and GC-MS during simultaneous sonication of PFOS and PFOA, $[\text{PFOS}]_i = 10\ \mu\text{M}$ and $[\text{PFOA}]_i = 10\ \mu\text{M}$ (500 kHz, 188 W L^{-1} and 2.9 W cm^{-2}). A large number of fluorinated gases were detected by GC-MS of the reactor headspace which was captured in an evacuated cannister. The gases that were detected include 1) polyfluorinated alkanes, CHF_3, CH_2F_2, CH_3F, C_2F_5H, C_3F_7H, 2) polyfluorinated alkenes, $C_2F_2H_2$, C_2F_4, C_3F_6, C_4F_8, and 3) C_4-C_8 polyfluorinated alkenes. No sulfur-containing gases were detected. The most abundant of the fluorinated gas species were fluoroform and difluoromethane, whose gas concentrations were monitored by online multiple reflection FT-IR (Figure 3.4: note the scale of the y-axis is a factor of 10^4 lower than that of Figure 3.3 at all points in time). The maximum concentration of these two species amounted to < 0.1% of the total fluorine during the simultaneous sonolysis of PFOS and PFOA. After these gas-phase products were formed, they were reentrained into the aqueous phase destroyed by continued sonolysis. However, these species were not completely eliminated since the headspace was not resparged back into the reactor, as the experiment was designed to accumulate any intermediate fluorochemicals for detection. Thus, passive gas transfer back into the sonicated solution was the limiting kinetic step of fluoroform and difluoromethane degradation. A table of all of the trace species detected by GC-MS after 120 minutes of sonolysis is listed in the supporting information: the total fluorine mole fraction of these species is 0.005 or less than 1%.

A carbon mass balance for the sonolytic degradation of PFOA and PFOS is plotted in Figures 3.5a and b as moles of carbon per species over the total initial moles of carbon vs. time, $[PFOS]_i$ = 100 μM and $[PFOA]_i$ = 100 μM (354 kHz, 250 W L^{-1}, and 6.4 W cm^{-2}). The primary carbon-containing species were the initial surfactant as detected by HPLC-MS and CO and CO_2, which were detected using real-time EI-MS. Other possible gaseous intermediates including formaldehyde, carbonyl fluoride, HF did not exceed the limit of detection. Real-time mass spectrometry was used to reduce the effect of any secondary gas product oxidation, $CO_{(g)} \rightarrow CO_{2(g)}$, or reduction/thermolysis, $CO_{2(g)} \rightarrow CO_{(g)}$[54,55], that may occur in subsequent bubble collapse events. After 120 minutes of sonolysis, 64.6 ± 9.2% of the carbon from decomposed PFOA was converted to CO and 32.1 ± 7.0% was converted to CO_2, while, in the case of PFOS sonolysis, the conversions to CO and CO_2 are 74.0 ± 5.3 % and 14.6 ± 5.0%, respectively, yielding observed product ratios of $[CO]/[CO_2]_{PFOA} = 2.0$ and $[CO]/[CO_2]_{PFOS} = 5.1$.

Discussion

Interfacial Pyrolysis of the Initial Perfluorinated Surfactant

PFOS and PFOA are surfactants[56–59]. PFOS is considered to be a more effective surfactant since it has one more carbon than PFOA in its perfluorinated tail. Their surfactant properties coupled with their small Henry's constants (Table 3.2) precludes their diffusive transfer to the bubble vapor phase. These properties are consistent with sonochemical degradation at the bubble-water interface[14] Oxidation by hydroxyl radicals[32,47] at collapsing bubble-water interfaces is a possible mechanism. An upper limit for the second-order rate constant for the reaction of hydroxyl radical, $< 10^6$ $M^{-1}s^{-1}$, with both PFOA and PFOS has been estimated by analogy to the measured rate constant of hydroxyl radical reacting with trifluoroacetate. For comparison, oxalate ($C_2O_4^{2-}$), which is thought to be responsible for the slow TOC elimination during sonication[60], has a second-order rate constant with hydroxyl radical of 4.7 x 10^{7} $M^{-1}s^{-1}$; which is at least an order of magnitude greater than that of PFOS and PFOA. TOC elimination, and thus oxalate oxidation, has a sonolytic half-life under similar conditions of ten hours[60]. Given these arguments, hydroxyl radical oxidation appears to play a minor role in PFOS and PFOA degradation[14]. Thus, interfacial pyrolytic decomposition appears to be the primary pathway for the sonochemical degradation of the perfluorinated surfactants.

Interfacial pyrolysis can be broken down conceptually into two fundamental steps. The first step involves the diffusion and adsorption of PFOS or PFOA to a transiently cavitating bubble interface (Step 1, Scheme 3.1) followed by a second step involving pyrolytic degradation at the cavitating-bubble interface (Step 2, Scheme 3.1).

The time-dependent mass balances shown in Figures 3.2–3.5 provide some insight into the sonolytic degradation mechanism of PFOS and PFOA. Of particular interest is the almost immediate production of inorganic sulfur (sulfate) and fluorine (fluoride) contrasted with a slightly delayed production of CO and CO_2. This suggests that

$$\frac{-d[PFOX]}{dt} = \frac{d(Mineralization)}{dt} \tag{3.4}$$

and that the primary intermediates produced during PFOS and PFOA decomposition appear to have much shorter half-lives than precursors. Given these observations, it is clear that

$$\frac{d[PF - Intermediate]}{dt} >> \frac{d[PFOX]}{dt} \tag{3.5}$$

and that the decomposition of the perfluoro-intermediates occurs in the vapor phase. Sonochemical reactions involving species that can partition to the vapor phase of a collapsing bubble (i.e., those having high Henry’s constants) generally have the fastest degradation rates. The similarity between the fluorochemical surfactant degradation rates and the rates of mineralization suggests that the fluorointermediates formed from the initial pyrolytic reactions have high Henry's constants.

Pyrolysis of perfluorinated surfactants has been reported for several perfluoroalkanecarboxylates and perfluoroalkanesulfonates in the solid phase[50,52,61] and perfluoroalkanecarboxylates in the vapor phase[51,62]. The primary products of perfluoroalkanecarboxylate pyrolysis product are reported to be the analogous 1H-perfluoroalkanes (eq. 3.6) for NH_4^+ salts[52,62], and perfluoroolefins (eq. 3.7) with lesser amounts of perfluoroanhydrides and perfluoroacyl fluorides for alkaline and alkali salts[52].

$$CF_3(CF_2)_6COO^-NH^+_{4(s)} \xrightarrow{\Delta} CF_3(CF_2)_5CF_2H_{(g)} + CO_{2(g)} + NH_{3(g)} \tag{3.6}$$

$$CF_3(CF_2)_6COO^-K^+_{(s)} \xrightarrow{\Delta} CF_3(CF_2)_4CF = CF_{2(g)} + CO_{2(g)} + K^+F^-{}_{(s)} \tag{3.7}$$

Products generated during the thermal degradation of perfluorosulfonates have not been identified[50]. Ammonium perfluorooctanoate, which is thermally converted to the 1H-perfluoroalkane[52,62], decomposes at a temperature 50 to 100 K lower than that of the alkali and alkaline salts[50,52,61]. Excess water has been observed to have an effect on the Arrhenius parameters of PFOA-NH_4^+ thermolysis[62] by increasing log A values from 13.6 s^{-1} to 15.4 s^{-1} and activation energy from 150 kJ mol^{-1} to 172 kJ mol^{-1}. These activation energies are much lower than expected for the $–CF_2$-CF_2- bond breaking which are typically > 300 kJ mol^{-1} (Table 3.3). Initial cleavage of the C-C bond between the perfluorinated tail and the carboxylate group yields gaseous carbon dioxide and a perfluoroalkyl anion (eq. 3.8). The perfluoroanion can form a 1H-perfluoroalkane by proton transfer (eq. 3.9), which eliminates a C-F bond-breaking step (450 kJ mol^{-1}) and circumvents the perfluoroolefin formation pathway (eq. 3.10).

$$CF_3(CF_2)_6COO^- \xrightarrow{\Delta} CF_3(CF_2)_5CF_2^- + CO_{2(g)} \tag{3.8}$$

$$CF_3(CF_2)_5CF_2^- \xrightarrow{+H_2O} CF_3(CF_2)_5CF_2H + HO^- \tag{3.9}$$

$$CF_3(CF_2)_5CF_2^- \xrightarrow{\Delta} CF_3(CF_2)_4CF = CF_2 \tag{3.10}$$

A proton transfer mechanism can explain the lower decomposition temperatures of the ammonium salts (eq. 3.6) as compared to the alkali and alkaline salts (eq. 3.7). Typical thermal decomposition of similar perfluoroalkane-carboxylate and -sulfonate salts[50] indicates that sulfonate salts decompose at higher temperatures (e.g., 100 to 200 K higher) than corresponding carboxylate salts. These observations are consistent with the relative sonolytic degradation rates of PFOA (k_{app}^{-PFOA} = 0.041 min^{-1}) and PFOS (k_{app}^{-PFOS} = 0.027 min^{-1}), in spite of the greater interfacial activity and tendencies of PFOS.

In summary, initial PFOX decomposition involves the loss of the ionic headgroup: CO_2 in the case of PFOA, and SO_3 in the case of PFOS. The pyrolytic cleavage of the ionic headgroups of both molecules leads to the formation of C_7 and C_8 perfluorocarbanion intermediates for PFOA and PFOS, respectively. The perfluorocarbanion is protonated to form a 1H-perfluoroalkane (eq. 3.9) or undergoes fluoride elimination to form a perfluoroolefin (eq. 3.10), (Step 2, Scheme 3.1). SO_3 produced during PFOS decomposition hydrolyzes rapidly (Step 3, Scheme 3.1) to form sulfate with the release of two protons.

Unimolecular Decomposition of the Fluorocarbon Tail

The organo-fluorines in the C_7 and C_8 fluorochemical intermediates are sonochemically converted into F^- with a pseudo-first-order rate constant of 0.3 min^{-1} ($\tau_{1/2}$

= 2.3 min). The fluorochemical intermediate degradation rates are greater than the sonochemical degradation rates reported for chlorinated hydrocarbons[63,64]. The Henry's constants for the likely 1H-perfluoroalkane (eq. 3.9) and perfluoroolefin (eq. 3.10) intermediates have been estimated by two different methods and determined to be on the order of 10^5 to 10^6 atm L mol^{-1} (Table 3.1). Colussi et al.[45] established a correlation between the Henry's constant, K_{A-W}^{x}, for chlorinated hydrocarbons, x, and their apparent sonolytic degradation rate constants where: $k_{sono,app}^{-x} = 4.5 \times 10^{-3}\ {K_{A-W}^{x}}^{0.3}$ (s^{-1}). Given the range of Henry's constants for the perfluorointermediates, we estimate sonolytic half-lives from 1 to 3 s; these times are shorter but consistent with the observed fluoride production kinetics ($\tau_{1/2}$ = 140 s). Partitioning of fluororocarbons between phases can not be estimated accurately using parameters determined for hydrocarbons[65–67]. For example, measurement[66] of Henry's constants for perfluoroolefins is difficult. The perfluoro-intermediates may not immediately partition into the vapor phase rapidly, but dwell for a period of time at the bubble-water interface before pyrolytic vapor-phase decomposition.

The apparent discrepancy between the observed F^- production rates and estimated degradation rates of these fluoro-intermediates may be due to a greater number of acoustic cycles to produce F^-, CO, and CO_2. The unimolecular decomposition kinetics for C_7 and C_8 fluorocarbon-intermediates in question have not been determined experimentally or computationally. Instead, we will use kinetic parameters for shorter-chain fluorochemicals in order to estimate decomposition rates.

Pyrolytic kinetics of (experimental technique listed in parentheses) 1H-perfluoropropane (IRMPD)[68], 1-perfluorobutene (IRMPD)[69], perfluorohexane (VLPP)[53], and their decomposition intermediates are listed in Table 3.3. First-order rate constants and half-lives are estimated using a temperature of 2500 K, which is less than the average vapor temperature achieved during a single transient cavitation event[37,39,70,71] in water. At 2500 K, experimentally determined Arrhenius parameters should be valid. It is noted that all of the possible fluorocarbon-intermediates have at least one estimated C-C bond-breaking decomposition pathway with a half-life under 100 ps, and the subsequent fluoroalkyl radical intermediates all have faster C-C bond-breaking kinetics. The unimolecular decomposition kinetics will dominate the bimolecular reaction kinetics and we can assume that the initial fluoro-intermediate will dissociate into C_1 fluoro-radical constituents prior to any intervening bimolecular reactions.

In Scheme 3.2, we propose a degradation mechanism for perfluorooctene in a cavitating bubble. The values above the reaction arrows are the estimated times for greater than 99% of the reaction. The stoichiometries for 1H-perfluoroheptane and perfluorooctene decompositions are given in eqs. 3.11 and 3.12, respectively.

$$CF_3(CF_2)_5CF_2H \xrightarrow{\Delta} CF_3 + 5\ CF_2 + CF_2H \tag{3.11}$$

$$CF_3(CF_2)_5CF = CF_2 \xrightarrow{\Delta} CF_3 + 6\ CF_2 + CF \tag{3.12}$$

The C_1 fluoro-radical products retain their original C-F bond intact since the average –C-C- bond strength (410 kJ mol^{-1}) is substantially less than the average C-F bond strength (530 kJ mol^{-1}). For comparison, the O-H bond strength of water is 498 kJ mol^{-1}.

Numerical simulations by Yasui et al.[42] and Colussi et al.[40] have modeled the time-dependent temperature evolution and the subsequent chemical reactions taking place during a transiently cavitation event at 300 kHz. In both cases, the maximum bubble-vapor temperatures were above 2500 K. Under these conditions, the characteristic time for the reactions portrayed in Scheme 3.2 to take place is 1 ns. Therefore, the C_7 or C_8

fluoro-intermediates should be completely dissociated into C_1 fluoro-radical constituents in a single acoustic cycle.

Transformation of C_1 Fluoro-radical Intermediates into CO and CO_2

The initial sonochemical decomposition steps of PFOS and PFOA produce either C_7 or C_8 1H-perfluoroalkanes (eq. 3.9) or perfluoroolefins (eq. 3.10), (Step 2, Scheme 3.1). These intermediates are then pyrolytically decomposed into C_1 fluoro-radicals (eqs. 3.11, 3.12): trifluoromethyl radical ($\cdot CF_3$), difluoromethyl radical ($\cdot CHF_2$), fluoromethylidyne (CF), and difluorocarbene ($:CF_2$), (Step 4, Scheme 3.1). The C_1 fluoro-radicals are subsequently transformed into carbon monoxide and carbon dioxide. A series of bimolecular reactions with H_2O, H·, HO·, and O-atom are proposed in Table 3.4 for the conversion of the C_1 fluoro-radicals into CO, CO_2, and HF[72]. The second-order reaction rate constants are estimated at 4000 K, where H_2O thermolysis is significant. Several assumptions are made when estimating the high-temperature kinetics. First, it is assumed that the radical intermediates constitute a neglible fraction of the total bubble vapor content; as a consequence fluoro-radical/fluoro-radical reactions can be neglected. Second, the C_1 fluoro-radical unimolecular decomposition is assumed to be of minor importance, since at aqueous cavitation temperatures[39,70], the thermolytic splitting of water, which has a lesser bond strength than fluoro-radical C-F bonds, is dominant. Finally, the sonolytic interconversion of CO and CO_2[48,54] is assumed to be insignificant since $CO_2 \xrightarrow{)))} CO$ has a half-life on the order of one hour under similar conditions[54]. Furthermore, if interconversion of CO and CO_2 were significant during sonolysis, then the CO/CO_2 product ratios for PFOS and PFOA would be similar; however, we observe $[CO]/[CO_2]_{PFOA} = 2.0$ and $[CO]/[CO_2]_{PFOS} = 5.1$.

The branching ratios for the pyrolytic transformations of the C_1 fluoro-radicals can be calculated using relative H_2O, H·, HO·, and O-atom vapor concentrations estimated from numerical simulations of single bubble cavitation events[40–42]. Storey and Szeri[41] (26.5 kHz, 1.2 bar, Ar) calculate that the bubble will be 14 % water vapor upon reaching its minimum radius and they predict that H_2O, H·, HO·, and O-atom are the dominate chemical species. Yasui et al.[42] (300 kHz, 3.0 bar, air) calculate that the bubble will have 10 to 20% water vapor before and after the bubble reaches a minimum size, while H·, HO·, and O-atom concentrations range from 0.1 to 1.0 % of the bubble contents during temperature maximums. Colussi et al.[40] (300 kHz, 1.8 atm, Ar) have calculated that HO·, H·, and O-atom concentrations are dissimilar during bubble radius minima at 1.0, 0.1, and 0.01 % of the total bubble gas content, respectively.

The $[CO]/[CO_2]$ product ratios for PFOS and PFOA sonolysis are estimated in three cases using relative C_1 fluoro-radical and their secondary C_1 intermediate branching ratios at various concentrations of H_2O, H·, HO·, and O-atom, as shown in Table 3.5. In the first case, H·, HO·, and O-atom concentrations are all set to 1%, in the second case H·, HO·, and O-atom are set to 0.1% and in the final case HO·, H·, and O-atom are set to 1.0%, 0.1%, and 0.01%, respectively. For all three cases, vapor concentrations were set at 10%, 1.0%, or 0.1%. The primary transformation pathways (i.e., those with branching ratios > 0.01) are shown in Scheme 3.3 with the primary reactant listed above the reaction arrow.

In Table 3.5 are the bubble vapor conditions used for the estimations, the CO/CO_2 branching ratios, for the secondary C_1 intermediates, the PFOS and PFOA estimated CO/CO_2 branching ratios and the estimated branching ratio over the experimentally determined branching ratio. The bubble vapor conditions that result in a best fit to the experimental data were 10% water vapor and 1% or 0.1% H·, HO·, and O-atom. When a range of radical concentrations were varied, the CO/CO_2 branching ratios were underestimated by 55 to 80%. This underestimation was primarily due to the reduced H· vapor concentration, H·/HO· = 0.1, yielding a more oxidizing bubble vapor and thus the more oxidized carbon product, CO_2. The CO/CO_2 branching ratios for CFO and CF_2O are observed to favor CO_2 over CO upon decreasing H· concentration. Reducing the relative water vapor concentration increases the CO branching ratio of CF_2O.

An analagous calculation as presented above for the unimolecular decomposition of the initial fluorochemical intermediate can be used to estimate the number of acoustic cycles, or sonication time, for the C_1 fluoroadicals in Scheme 3.3 to completely pyrolyze into CO and CO_2. If we considered the reaction with the longest half-life, $COF_2 + H_2O \rightarrow CO_2 + 2\ HF$, at 8.15 μs (4000 K, 10% H_2O), and that eight half-lives are needed to destroy > 99% of the initial compound, the time for complete transformation would be 65 μs. Using a conservative 0.50 ns high temperature period per cycle, it will take 1.3×10^5 acoustic cycles to completely eliminate COF_2. Likewise, the total time for the sonolytic transformation of the C_1-fluororadical is estimated to be 0.36 s (2.8 μs per cycle at 354 kHz). The calculated time is inline with the characteristic degradation time (e.g., 1 to 3 s) using the empirical Henry's constant estimation[45]. And once again this calculation is in general agreement, but much shorter, than the experimentally observed fluoride production half-life of 2 minutes. The discrepancy between calculation and experiment suggests that fluorochemical intermediates partitioning to the bubble vapor phase and not pyrolytic degradation may be the rate-limiting step in fluoride production. More importantly, both experimental results and kinetic estimations agree with the conclusion that shortly after the sonochemical decomposition of a perfluorinated surfactant, PFOS or

PFOA, their fluoro-intermediates are transformed relatively quickly into inorganic constituents of PFOX: F^-, SO_4^{2-}, CO, and CO_2.

Conclusions

Perfluorinated surfactants are widespread in the environment and recalcitrant towards most conventional water-treatment technologies. Incineration is a viable method for degradation of concentrated manufacturing wastes, yet not efficient for more dilute aqueous solutions. Acoustic cavitation as driven by ultrasonic cavitation has been shown to be both an effective and a relatively fast method for the complete destruction and mineralization of PFOS and PFOA over a wide range of initial concentrations. Conventional methods such as hydroxyl radical oxidation[13] and bio-degradation[8] have been shown to have minimal effect on the elimination on these compounds from water. Photodegradation techniques[15,16,21,22,24,26] as well as elemental iron reduction in sub-critical water[29] have been shown to degrade these species. However, minimum degradation half-lives are in the range of 45 to 120 minutes and achieve a maximum of 50% mineralization. Shorter perfluorinated acids are produced as by-products; these latter products are just as recalcitrant as the initial perfluorinated compounds. The PFOS and PFOA degradation rates presented here both have a degradation half-life of 30 minutes or less and achieve complete mineralization immediately after the decomposition of the initial product, as shown by time-dependent product analysis and kinetic estimations. Previous studies[73] have shown that sonolytic rates can be scaled linearly by increasing acoustic power density and that scaling-up the reactor size has minimal effect on the observed reaction rates. Therefore, ultrasonically driven acoustic cavitation provides a technically viable method for the treatment of aqueous perfluorinated surfactant waste waters over a rather wide range of concentrations (i.e., 10 nM (5 ppb) to 10 mM (5 ppm) in this study).

Figures

Figure 3.1. Pseudo-first-order plots of PFOX sonolysis (354 kHz, 250 W L^{-1}, Ar, 10 °C, $[PFOS]_i$ = 200 nM, $[PFOA]_i$ = 240 nM). PFOS (○) and PFOA (∇)

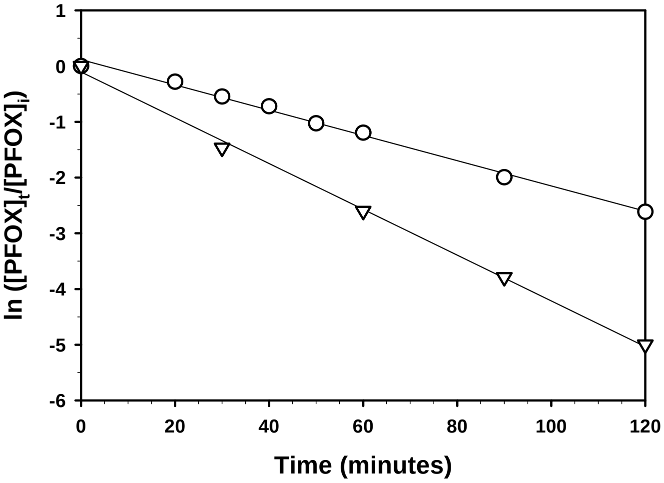

Figure 3.2. Normalized sulfur mass balance during PFOS sonolysis. (618 kHz, 250 W L^{-1},Ar,10 °C, $[PFOS]_i$ = 10 μM). PFOS (●), sulfate (○) and sulfate + PFOS (▼)

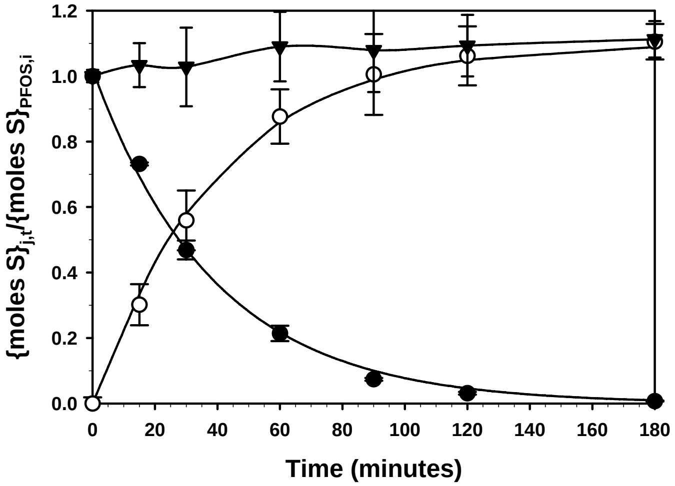

Figure 3.3. Normalized fluorine mass balance during PFOX sonolysis (618 kHz, 250 W L^{-1}, Ar, 10 ^{o}C). **A)** $[PFOS]_i$ = 10 μM; PFOS (●), fluoride (○), and PFOS + fluoride (▼). **B)** $[PFOA]_i$ = 12 μM; PFOA (●), fluoride (○) and PFOA + fluoride (▼).

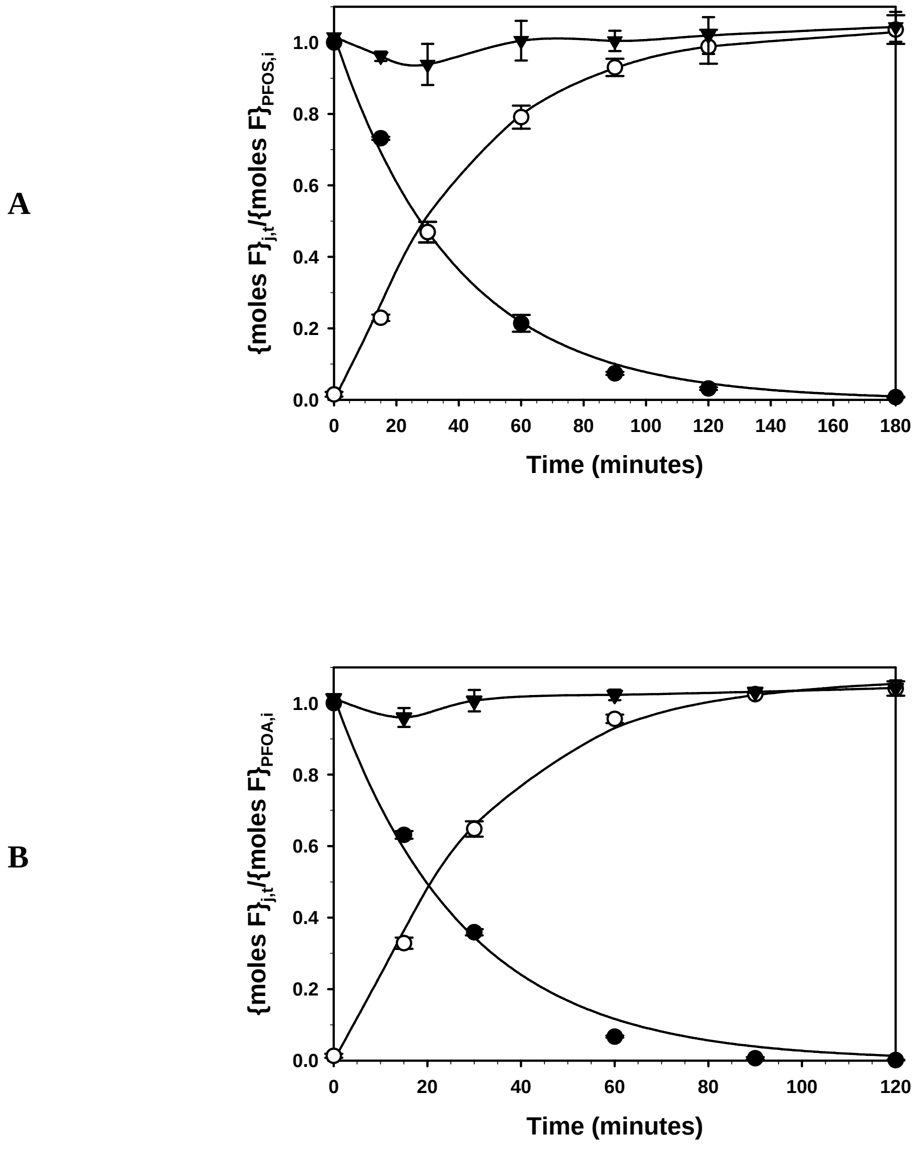

Figure 3.4. Trace gases, CH_2F_2 and CHF_3, detected during PFOX sonolysis (500 kHz, 188 W L^{-1}, Ar, 10 °C, $[PFOS]_i = 10$ μM and $[PFOA]_i = 12$ μM). CH_2F_2 (○) and CHF_3 (●)

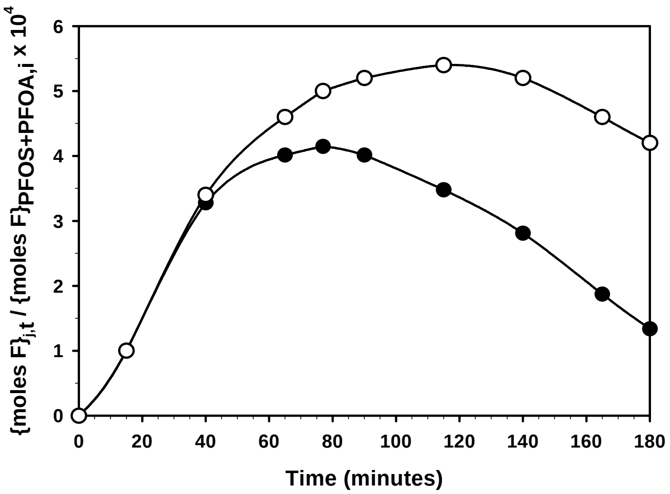

Figure 3.5. Normalized carbon mass balance plots during PFOX sonolysis (354 kHz, 250 W L^{-1}, Ar, 10 ^{o}C). A) $[PFOS]_i$ = 100 μM; PFOS (◊), CO (○), CO_2 (∇), CO + CO_2 (□), and PFOS + CO + CO_2 (♦). B) $[PFOA]_i$ = 100 μM; PFOA (◊), CO (○), CO_2 (∇), CO + CO_2 (□), and PFOA + CO + CO_2 (♦)

A

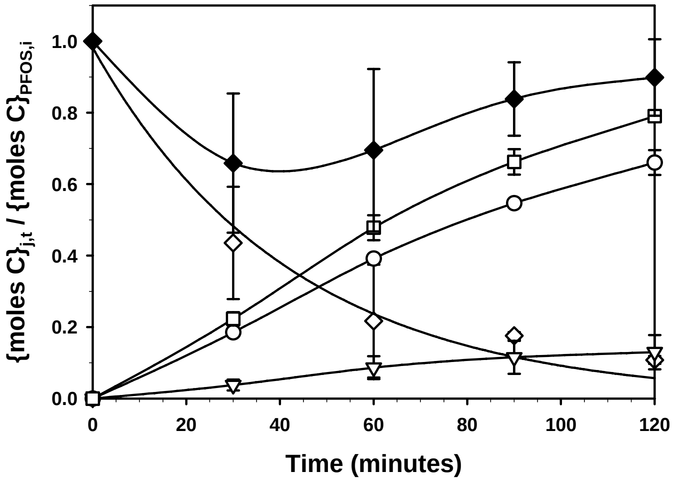

B

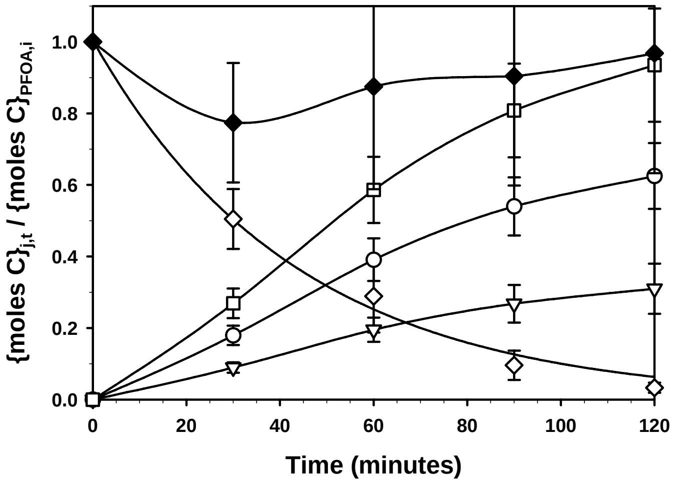

Schemes

Scheme 3.1. A representative scheme of the sonochemical PFOS transformation into its inorganic constituents. Step 1) PFOS adsorption to the bubble-water interface; Step 2) Bubble-water interfacial pyrolytic decomposition of PFOS via cleavage of the C-S bond; Step 3) Hydrolysis of sulfur trioxide to sulfate; Step 4) Bubble vapor pyrolysis of the primary fluoro-intermediate into C_1 fluoro-radicals; and Step 5) Transformation of C_1 fluoro-radicals within the bubble vapor to CO, CO_2, and HF, which is converted to a proton and a fluoride upon hydration. The inorganic products are highlighted in purple boxes.

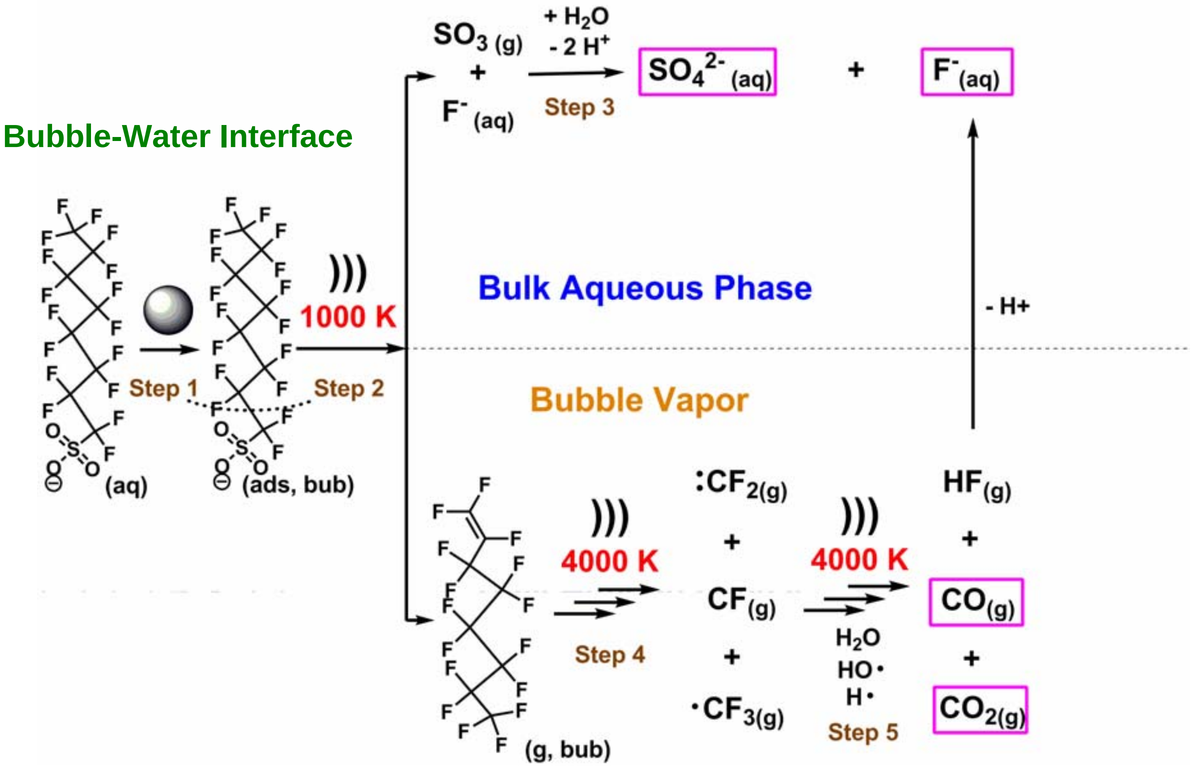

Scheme 3.2. A representative scheme of sonolytic fluorointermediate unimolecular decomposition yielding C_1 fluoro-radicals (Step 4, Scheme 3.1). The time for > 99 % reaction progress at 2500 K is reported above the reaction arrow. The C_1 fluoro-radicals are shown in boxes.

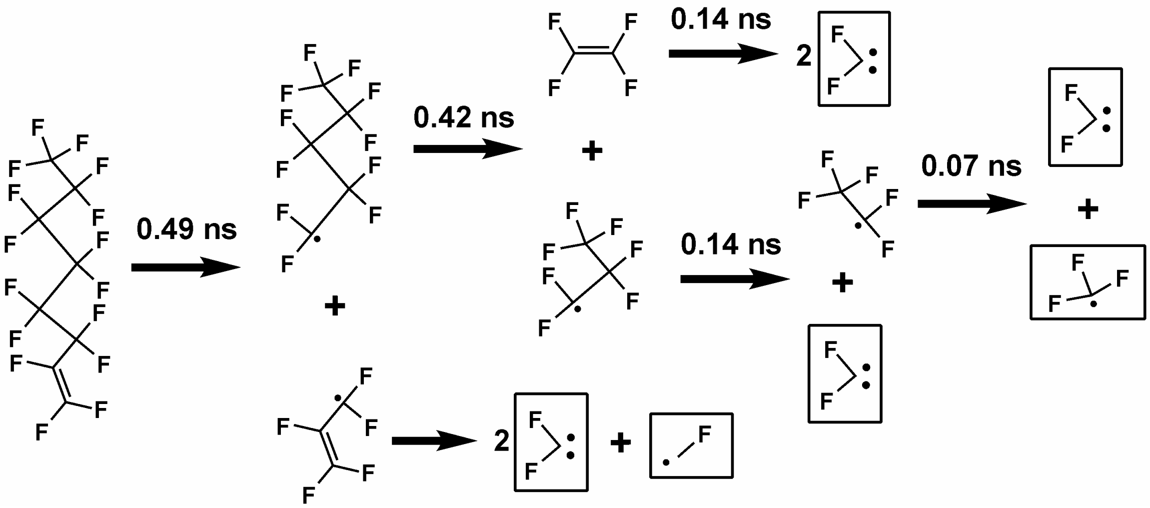

Scheme 3.3. Representation of sonochemical C_1-fluorointermediate reaction pathways (Step 5, Scheme 3.1). The initial C_1 fluoro-radicals are in boxes and the final products are in ovals. The bimolecular reactant is listed either above the reaction arrow or to the right of vertical reaction arrows. If multiple reactants are listed they signify multiple individual pathways and not sequential reactions.

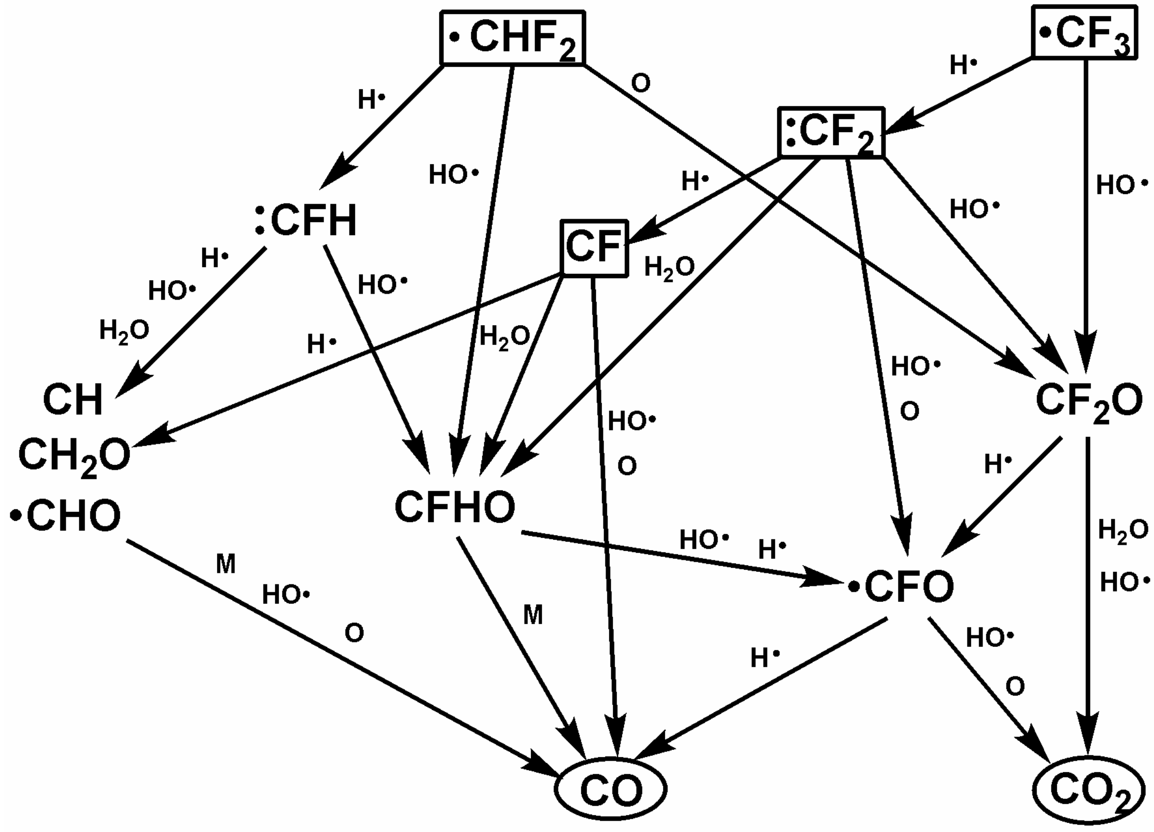

Tables

Table 3.1. Rate constants for PFOX sonochemical transformations

	k_1^{-PFOX} (min^{-1})^a	$k_2^{F^-}$ (min^{-1})^b	$k_2^{SO_4^{2-}}$ (min^{-1})^b
PFOS	0.026	0.3	> 1.0
PFOA	0.036	0.3	

a) PFOX fluorine and sulfur sonochemical time dependence was fit to an exponential decay: exp(-k_1^{-PFOX} t).

b) Inorganic fluorine, fluoride, and sulfur, sulfate, sonochemical time-dependent growth was fit to exponential growth through a single decomposition intermediate: (1/($k_1^{-PFOX} + k_2^{X^-}$))($k_2^{X^-}$ (1-exp(-k_1^{-PFOX} t))- k_1^{-PFOX} (1-exp(-$k_2^{X^-}$ t))).

Table 3.2. Physiochemical properties of PFOX sonochemical intermediates

	$C_{w,sat}$ (M) 20 ^{o}C	p* (atm) 20 ^{o}C	K_H (atm M^{-1})	pKa	$k_{\cdot OH}$
PFOS-K^{+1}	0.002	3.3 x 10^{-9}	N/A	-3.5	< 10^{6} [a]
PFOA-NH_4^+	0.05 (gels)	9.2 x 10^{-8}	N/A	-0.5[67]	< 10^{6} [a]
PF-Octene	1.4 x 10^{-8} [74]	0.03	2.1 x 10^{6}	n/a	2.4 x 10^{-12} [b]
1H-PF-Octane	n/a	n/a	6.2 x 10^{6} [d]	n/a	$10^{-9.2}e^{-63/RT}$ [c]
PF-Heptene	1.4 x 10^{-7}	0.075	5.3 x 10^{5}	n/a	2.4 x 10^{-12} [b]
1H-PF-Heptane	3.5 x 10^{-8} [75]	0.04	3.3 x 10^{5}	n/a	$10^{-9.2}e^{-63/RT}$ [c]

*Vapor pressures for the fluorochemical intermediates are estimated according to Mackay et al.[76]

*$C_{w,sat}$ estimation uses $N_d = 1.28$, $\pi = 0.08$[77]; inserted refs are for experimental BPs.

[a] Aqueous rates measured for hydroxyl plus TFA (M^{-1} s^{-1})[78]

[b] Gas-phase reaction of excess ·OH + perfluoropropene at 295 K[79]

[c] Gas-phase reaction of H· + CF_3CHFCF_3 – H· abstraction (cm^3 molecule^{-1}s^{-1})[80]

[d] Calculated by bond-contribution method[81]

Table 3.3. Kinetic parameters for the unimolecular decomposition of fluorochemicals

Reaction	log A s^{-1}	E_A kJ mol^{-1}	k (T = 2500 K) s^{-1}	$\tau_{1/2}$ (ns)	ref.
$C_3F_7H \rightarrow CF_3\cdot + CF_2HCF_2\cdot$	16.9	372.6	1.29E+09	0.5	68
$C_3F_7H \rightarrow CHF_2\cdot + CF_3CF_2\cdot$	16.6	372.6	6.47E+08	1.1	68
$C_3F_7H \rightarrow HF + C_3F_6$	13.9	280.5	1.29E+06	540	68
$C_4F_8 \rightarrow CF_3\cdot + C_3F_5$	16.1	292.9	9.48E+09	0.07	69
$C_4F_8 \rightarrow C_3F_6 + CF_2$	13.0	380.7	1.10E+05	6,300	69
$C_4F_8 \rightarrow C_2F_4 + C_2F_4$	13.0	418.4	1.79E+04	39,000	69
$C_6F_{14} \rightarrow C_2F_5\cdot + C_4F_9$	17.2	330	2.00E+10	0.03	53
$C_6F_{14} \rightarrow 2\ C_3F_7\cdot$	16.9	330	1.00E+10	0.07	53
$C_6F_{14} \rightarrow CF_3\cdot + C_5F_{11}\cdot$	17.2	364	3.90E+09	0.18	53
$C_5F_{11}\cdot \rightarrow C_3F_7\cdot + C_2F_4$	13.6	168	1.22E+10	0.06	53
$C_4F_9\cdot \rightarrow C_2F_5\cdot + C_2F_4$	13.4	168	7.73E+09	0.09	53
$C_3F_7\cdot \rightarrow CF_3\cdot + C_2F_4$	13.3	186.4	2.53E+09	0.27	53
$C_3F_7\cdot \rightarrow C_2F_5\cdot + CF_2:$	15.5	238.4	3.28E+10	0.02	53
$C_2F_5\cdot \rightarrow CF_3\cdot + CF_2:$	15.6	235.4	4.78E+10	0.01	53
$C_2F_4 \rightarrow 2\ CF_2:$	16.7	294	3.58E+10	0.02	53

* $k = A\ T^b \exp(-E_A / RT)$ where E_A is in kJ mol^{-1}, R = 0.00831 kJ K^{-1} mol^{-1}, and A and thus k is in s^{-1}; in all cases b = 0.

Table 3.4. Kinetic parameters for bimolecular reactions of C_1-fluororadicals

Reaction	A molecule cm^{-3} s^{-1}	b	E_A kJ mol^{-1}	k (T = 4000 K) molecule cm^{-3} s^{-1}
$CHF_2\cdot + H \rightarrow CH_2F_2$	2.75E+06	-0.32	32.2	1.22E-19
$CHF_2\cdot + H \rightarrow CHF: + HF$	1.50E+14	-0.11	0.5	9.85E-11
$CHF_2\cdot + H \rightarrow CF_2: + H_2$	5.50E+03	2.41	0	4.38E-12
$CHF_2\cdot + OH \rightarrow CHF:O + HF$	2.40E+13	0	0	3.99E-11
$CHF_2\cdot + O \rightarrow CF_2:O + H$	3.70E+13	0	0	6.14E-11
$CF_3\cdot + H \rightarrow CF_2: + HF$	5.50E+13	0	0	9.13E-11
$CF_3\cdot + OH \rightarrow CF_2:O$	2.00E+13	0	0	3.32E-11
$CF_3\cdot + O \rightarrow CF_2:O + F$	1.90E+13	0	0	3.16E-11
$CF_2: + H_2O \rightarrow CHF:O + HF$	5.00E+12	0	104.6	3.57E-13
$CF_2: + OH \rightarrow CF:O + HF$	4.00E+12	0	14.6	4.28E-12
$CF_2: + OH \rightarrow CF_2:O + H$	2.00E+13	0	14.6	2.14E-11
$CF_2: + H \rightarrow CF + HF$	2.00E+14	0	14.6	2.14E-10
$CF_2: + O \rightarrow CF:O + F$	7.00E+13	0	4.2	1.02E-10
$CF + H_2O \rightarrow CHF:O + H$	2.00E+13	0	71.1	3.91E-12
$CF + OH \rightarrow CO + HF$	4.00E+13	0	4.2	5.85E-11
$CF + H \rightarrow CH + F$	4.00E+13	0	2.8	6.11E-11
$CF + O \rightarrow CO + F$	4.00E+13	0	4.2	5.85E-11
$CHF: + H_2O \rightarrow CH_2O + HF$	5.00E+12	0	27.2	3.66E-12
$CHF: + OH \rightarrow CHO + HF$	4.00E+12	0	0	6.64E-12

CHF: + OH → CFH:O + H	2.00E+13	0	0	3.32E-11
CHF: + H → CH + HF	3.00E+14	0	0	4.98E-10
CHF: + O → CO + HF	9.00E+12	0	12.9	1.01E-11
CHF:O + M → CO + HF	2.50E+25	-3	179.8	2.90E-12
CHF:O + H → CF:O + H_2	1.10E+08	1.77	12.5	2.98E-10
CHF:O + OH → CF:O + H_2O	1.70E+09	1.18	0	5.03E-11
CHF:O + O → CF:O + OH	9.00E+12	0	12.9	1.01E-11
CF_2:O + H_2O → CO_2 + 2 HF	7.40E-03	3.84	105	3.54E-14
CF_2:O + H → CF:O + HF	1.20E+10	0.83	93.3	1.18E-12
CF_2:O + OH → CO_2 + HF + F	2.70E+03	2.38	87.8	1.20E-13
CF:O + H → CO + HF	1.20E+14	0	0	1.99E-10
CF:O + OH → CO_2 + HF	3.00E+13	0	0	4.98E-11
CF:O + O → CO_2 + F	3.00E+13	0	0	4.98E-11
F + H_2O → HF + OH	1.30E+09	1.5	0	5.46E-10
F + H_2 → HF + H	2.60E+12	0.5	0	2.73E-10
F + OH → HF + O	2.00E+13	0	0	3.32E-11

Table 3.5. Estimated CO/CO_2 product ratios for PFOX sonolysis

	Case I			Case II			Case III		
Water Vapor %	10.0	1.0	0.1	10.0	1.0	0.1	10.0	1.0	0.1
Radical %	1.0	1.0	1.0	0.1	0.1	0.1	Range	Range	Range
CFO									
CO/CO_2	2.00	2.00	2.00	2.00	2.00	2.00	0.40	0.40	0.40
CF_2O									
CO/CO_2	0.90	1.43	1.52	0.19	0.90	1.43	0.06	0.14	0.16
CHF									
CO/CO_2	94.73	89.33	88.79	750.99	479.89	452.78	23.53	17.13	16.49
CHFO									
CO/CO_2	4.43	4.43	4.43	26.32	26.32	26.32	5.45	5.45	5.45
$PFOS^-$ CO/CO_2	5.21	6.66	6.87	4.63	5.99	6.79	1.05	1.21	1.25
Calc/Expt	1.02	1.31	1.35	0.91	1.17	1.33	0.21	0.24	0.25
$PFOA^-$ CO/CO_2	2.48	2.85	2.90	2.20	2.69	2.94	0.78	0.86	0.89
Calc/Expt	1.24	1.43	1.45	1.10	1.35	1.47	0.39	0.43	0.44

References

(1) 3M Company. Docket AR226-0547; Office of Pollution Prevention and Toxics; U.S. Environmental Protection Agency: Washington, D.C., 1999; p. 12.

(2) Sinclair, E.; Kannan, K. *Environ. Sci. Technol.* **2006**, *40*, 1408.

(3) Schultz, M. M.; Higgins, C. P.; Huset, C. A.; Luthy, R. G.; Barofsky, D. F.; Field, J. A. *Environ. Sci. Technol.* **2006**, *40*, 7350.

(4) Boulanger, B.; Vargo, J. D.; Schnoor, J. L.; Hornbuckle, K. C. *Environ. Sci. Technol.* **2005**, *39*, 5524.

(5) Martin, J. W.; Whittle, D. M.; Muir, D. C. G.; Mabury, S. A. *Environ. Sci. Technol.* **2004**, *38*, 5379.

(6) Martin, J. W.; Smithwick, M. M.; Braune, B. M.; Hoekstra, P. F.; Muir, D. C. G.; Mabury, S. A. *Environ. Sci. Technol.* **2004**, *38*, 373.

(7) Schultz, M. M.; Barofsky, D. F.; Field, J. A. *Environ. Eng. Sci.* **2003**, *20*, 487.

(8) Key, B. D.; Howell, R. D.; Criddle, C. S. *Environ. Sci. Technol.* **1998**, *32*, 2283.

(9) Hollingsworth, J.; Sierra-Alvarez, R.; Zhou, M.; Ogden, K. L.; Field, J. A. *Chemosphere* **2005**, *59*, 1219.

(10) 3M Company; Docket AR226-0489; Office of Pollution Prevention & Toxics; U.S. Environmental Protection Agency: Washington, D.C., 1978; p. 19.

(11) 3M Company; Docket AR226-0058; Office of Pollution Prevention & Toxics; U.S. Environmental Protection Agency: Washington, D.C., 1994; p. 4.

(12) Oppenlander, T. *Photochemical Purification of Water and Air*; Wiley-VCH: Weinheim, 2003.

(13) Schroder, H. F.; Meesters, R. J. W. *J. Chromatogr. A* **2005**, *1082*, 110.

(14) Moriwaki, H.; Takagi, Y.; Tanaka, M.; Tsuruho, K.; Okitsu, K.; Maeda, Y. *Environ. Sci. Technol.* **2005**, *39*, 3388.

(15) Hori, H.; Hayakawa, E.; Einaga, H.; Kutsuna, S.; Koike, K.; Ibusuki, T.; Kiatagawa, H.; Arakawa, R. *Environ. Sci. Technol.* **2004**, *38*, 6118.

(16) Chen, J.; Zhang, P. *Water Sci. Technol.* **2006**, *54*.

(17) 3M Company; Docket AR226-0056; Office of Pollution Prevention & Toxics; U.S. Environmental Protection Agency: Washington, D.C., 1978; p. 17.

(18) 3M Company; Docket AR226-0490; Office of Pollution Prevention & Toxics; U.S. Environmental Protection Agency: Washington, D.C., 1979; p. 15.

(19) Yamamoto, T.; Noma, Y.; Sakai, S. I.; Shibata, Y. *Environ. Sci. Technol.* **2007**, *41*, 5660.

(20) Chen, J.; Zhang, P. Y.; Liu, J. *J. Environ. Sci* **2007**, *19*, 387.

(21) Hori, H.; Yamamoto, A.; Hayakawa, E.; Taniyasu, S.; Yamashita, N.; Kutsuna, S.; Kiatagawa, H.; Arakawa, R. *Environ. Sci. Technol.* **2005**, *39*, 2383.

(22) Hori, H.; Yamamoto, A.; Kutsuna, S. *Environ. Sci. Technol.* **2005**, *39*, 7692.

(23) Kutsuna, S.; Hori, H. *Int. J. Chem. Kin.* **2007**, 276.

(24) Chen, J.; Zhang, P. Y.; Zhang, L. *Chem. Lett.* **2006**, *35*, 230.

(25) Hori, H.; Hayakawa, E.; Koike, K.; Einaga, H.; Ibusuki, T. *J. Mol. Catal. A–Chem.* **2004**, *211*, 35.

(26) Dillert, R.; Bahnemann, D.; Hidaka, H. *Chemosphere* **2007**, *67*.

(27) Yuan, Q.; Ravikrishna, R.; Valsaraj, K. T. *Sep. Purif. Technol.* **2001**, *24*.

(28) Hidaka, H.; Jou, H.; Nohara, K.; Zhao, J. *Chemosphere* **1992**, *25*, 1589.

(29) Hori, H.; Nagaoka, Y.; Yamamoto, A.; Sano, T.; Yamashita, N.; Taniyasu, S.; Kutsuna, S.; Osaka, I.; Arakawa, R. *Environ. Sci. Technol.* **2006**, *40*, 1049.

(30) Kolaczkowski, S. T.; Plucinski, P.; Beltran, F. J.; Rivas, F. J.; McLurgh, D. B. *Chem. Eng. J.* **1999**, *73*, 143.

(31) Vinodgopal, K.; Ashokkumar, M.; Grieser, F. *J. Phys. Chem. B* **2001**, *105*, 3338.

(32) Destaillats, H.; Hung, H. M.; Hoffmann, M. R. *Environ. Sci. Technol.* **2000**, *34*, 311.

(33) Hua, I.; Hoffmann, M. R. *Environ. Sci. Technol.* **1996**, *30*, 864.

(34) Kotronarou, A.; Mills, G.; Hoffmann, M. R. *J. Phys. Chem.* **1991**, *95*, 3630.

(35) Petrier, C.; David, B.; Laguian, S. *Chemosphere* **1996**, *32*, 1709.

(36) Brennen, C. E. *Cavitation and Bubble Dynamics*; Oxford University Press: New York, 1995.

(37) Misik, V.; Miyoshi, N.; Riesz, P. *J. Phys. Chem.* **1995**, *99*, 3605.

(38) Leighton, T. G. *The Acoustic Bubble*; Academic Press: London, 1994.

(39) Didenko, Y. T.; McNamara, W. B.; Suslick, K. S. *J. Phys. Chem. A* **1999**, *103*, 10783.

(40) Colussi, A. J.; Weavers, L. K.; Hoffmann, M. R. *J. Phys. Chem. A* **1998**, *102*, 6927.

(41) Storey, B. D.; Szeri, A. J. *Proc. R. Soc. London Ser. A–Math. Phys. Eng. Sci.* **2000**, *456*, 1685.

(42) Yasui, K.; Tuziuti, T.; Kozuka, T.; Towata, A.; Iida, Y. *J. Chem. Phys.* **2007**, *127.*

(43) Krishna, C. M.; Lion, Y.; Kondo, T.; Riesz, P. *J. Phys. Chem.* **1987**, *91*, 5847.

(44) Jennings, B. H.; Townsend, S. N. *J. Phys. Chem.* **1961**, *65*, 1574.

(45) Colussi, A. J.; Hung, H. M.; Hoffmann, M. R. *J. Phys. Chem. A* **1999**, *103*, 2696.

(46) Yang, L. M.; Rathman, J. F.; Weavers, L. K. *J. Phys. Chem. B* **2005**, *109*, 16203.

(47) Sostaric, J. Z.; Riesz, P. *J. Am. Chem. Soc.* **2001**, *123*, 11010.

(48) Henglein, A.; Kormann, C. *Int. J. Radiat. Biol.* **1985**, *48*, 251.

(49) Manousaki, E.; Psillakis, E.; Kalogerakis, N.; Mantzavinos, D. *Water Res.* **2004**, *38*, 3751.

(50) Glockner, V.; Lunkwitz, K.; Prescher, D. *Tenside Surf. Det.* **1989**, *26*.

(51) Krusic, P. J.; Marchione, A. A.; Roe, D. C. *J. Fluor. Chem.* **2005**, *126*, 1510.

(52) Lazerte, J. D.; Hals, L. J.; Reid, T. S.; Smith, G. H. *J. Am. Chem. Soc.* **1953**, *75*, 4525.

(53) Ainagos, A. F. *Kinet. Catal.* **1991**, *32*, 720.

(54) Harada, H. *Ultrason. Sonochem.* **1998**, *5*, 73.

(55) Henglein, A. *Z. Naturforsch. (B)* **1985**, *40*, 100.

(56) Lopez-Fontan, J. L.; Gonzalez-Perez, A.; Costa, J.; Ruso, J. M.; Prieto, G.; Schulz, P. C.; Sarmiento, M. *J. Colloid Interface Sci.* **2006**, *294*, 458.

(57) Lopez-Fontan, J. L.; Sarmiento, F.; Schulz, P. C. *Colloid Polym. Sci.* **2005**, *283*, 862.

(58) Simister, E. A.; Lee, E. M.; Lu, J. R.; Thomas, R. K.; Ottewill, R. H.; Rennie, A. R.; Penfold, J. *J. Chem. Soc.–Faraday Trans.* **1992**, *88*, 3033.

(59) Shinoda, K.; Hato, M.; Hayashi, T. *J. Phys. Chem.* **1972**, *76*, 909.

(60) Lesko, T.; Colussi, A. J.; Hoffmann, M. R. *Environ. Sci. Technol.* **2006**, *40*, 6818.

(61) Lines, D.; Sutcliffe, H. *J. Fluor. Chem.* **1984**, *25*, 505.

(62) Krusic, P. J.; Roe, D. C. *Anal. Chem.* **2004**, *76*, 3800.

(63) Hung, H. M.; Hoffmann, M. R. *Environ. Sci. Technol.* **1998**, *32*, 3011.

(64) Hung, H. M.; Hoffmann, M. R. *J. Phys. Chem. A* **1999**, *103*, 2734.

(65) Goss, K. U.; Bronner, G. *J. Phys. Chem. A* **2006**, *110*, 9518.

(66) Goss, K. U.; Bronner, G.; Harner, T.; Monika, H.; Schmidt, T. C. *Environ. Sci. Technol.* **2006**, *40*, 3572.

(67) Goss, K.-U. *Environ. Sci. Technol.* **2008**, *42*, 456.

(68) Kato, S.; Makide, Y.; Tominaga, T.; Takeuchi, K. *J. Phys. Chem.* **1987**, *91*, 4278.

(69) Longfellow, C. A.; Berrie, C. L.; Suits, A. G.; Lee, Y. T. *J. Chem. Phys.* **1997**, *107*, 7202.

(70) Ciawi, E.; Rae, J.; Ashokkumar, M.; Grieser, F. *J. Phys. Chem. B* **2006**, *110*, 13656.

(71) Didenko, Y. T.; McNamara, W. B.; Suslick, K. S. *J. Am. Chem. Soc.* **1999**, *121*, 5817.

(72) Burgess, D. R.; Zachariah, M. R.; Tsang, W.; Westmoreland, P. R. *Prog. Energy Combust. Sci.* **1995**, *21*, 453.

(73) Destaillats, H.; Lesko, T. M.; Knowlton, M.; Wallace, H.; Hoffmann, M. R. *Ind. Eng. Chem. Res.* **2001**, *40*, 3855.

(74) Galyautdinov, I. V.; Nazmeeva, S. R.; Savchenko, R. G.; Ves'kina, N. A.; Nedopekin, D. V.; Fatykhov, A. A.; Khalilov, L. M.; Odinokov, V. N. *Russ. J. Organ. Chem.* **2004**, *40*, 675.

(75) Huang, B. N.; Haas, A.; Lieb, M. *J. Fluor. Chem.* **1987**, *36*, 49.

(76) Mackay, D.; Bobra, A.; Chan, D. W.; Shiu, W. Y. *Environ. Sci. Technol.* **1982**, *16*, 645.

(77) Schwarzenbach, R. P.; Gschwend, P. M.; Imboden, D. M. *Environmental Organic Chemistry*, *Second ed.*; Wiley: New York, 2003.

(78) Maruthamuthu, P.; Padmaja, S.; Huie, R. E. *Int. J. Chem. Kin.* **1995**, *27*.

(79) Mashino, M.; Ninomiya, Y.; Kawasaki, M.; Wallington, T. J.; Hurley, M. D. *J. Phys. Chem. A* **2000**, *104*, 7255.

(80) Yamamoto, O.; Takahashi, K.; Inomata, T. *J. Phys. Chem. A* **2004**, *108*, 1417.

(81) Hine, J.; Mookerjee, P. K. *J. Org. Chem.* **1975**, *40*, 292.

Chapter 4

Enhancement of Perfluorooctanoate (PFOA) and Perfluorooctanesulfonate (PFOS) Activity at Acoustic Cavitation Bubble Interfaces

Sections reprinted with permission from Vecitis C. D.; Park H.; Cheng J.; Mader, B. T.; Hoffmann, M. R.; J*ournal of Physical Chemistry C* **2008**, *112*, 16850–16857.

Abstract

Acoustic cavitation driven by ultrasonic irradiation decomposes and mineralizes the recalcitrant perfluorinated surfactants, perfluorooctanesulfonate (PFOS) and perfluorooctanoate (PFOA). Pyrolytic cleavage of the ionic headgroup is the rate-determining step. In this study, we examine the sonochemical adsorption of PFOX, where X = S for PFOS and A for PFOA, by determining kinetic order and absolute rates over an initial PFOX concentration range of 20 nM to 200 μM. Sonochemical PFOX kinetics transition from pseudo-first-order at low initial concentrations, $[\mathrm{PFOX}]_i < 20$ μM, to zero-order kinetics at high initial concentrations, $[\mathrm{PFOX}]_i > 40$ μM, as the bubble interface sites are saturated. At PFOX concentrations below 100 μM, concentration-dependent rates were modeled with Langmuir-Hinshelwood kinetics. Empirically determined rate maximums, $V_{Max}^{-PFOA} = 2230 \pm 560$ nM min^{-1} and $V_{Max}^{-PFOS} = 230 \pm 60$ nM min^{-1}, were used in the LH model, and sonochemical surface activities were estimated to be, $K_{Sono}^{PFOS} = 120{,}000$ M^{-1} and $K_{Sono}^{PFOA} = 28{,}500$ M^{-1}—60 and 80 times greater than equilibrium surface activities, K_{Eq}^{PFOS} and K_{Eq}^{PFOA}. These results suggest enhanced sonochemical degradation rates for PFOX when the bubble interface is under-saturated populated. The present results are compared to previously reported sonochemical kinetics of nonvolatile surfactants.

Introduction

Fluorine is the most electronegative of elements. Fluorochemicals (FCs), organics with the majority of their hydrogens replaced by fluorines, display unique properties as compared to their hydrocarbon analogs[1]. The C-F bond is the strongest among organics (> 110 kcal/mol), and low C-F bond polarizabilites gives them both hydrophobic and oleophobic character. Fluorination protects against oxidation and FC coatings provide water and oil resistance. However, these same fluorochemical properties make them environmentally persistent and recalcitrant towards most conventional water-treatment technologies[2,3], since they are inert towards common chemical and microbial treatment[4–6]. Sulfate radical[7–9], advanced reduction[10,11], and photolytic techniques[8,12,13] can degrade perfluorinated surfactants, most yielding shorter-chain FCs as products. Moriwaki et al.[4] reported that ultrasonic irradiation of aqueous perfluorochemical solutions may provide a practical alternative.

Acoustic cavitation, as driven by ultrasonic irradiation, can be utilized for the decomposition of aqueous chemical contaminants[15–18]. Application of ultrasound to aqueous solutions forms cavitation bubbles, which will undergo transient collapse events[5]. Quasi-adiabatic compression of transient bubbles generates average vapor temperatures near 5000 K[20,21] and much higher bubble vapor core temperatures that lead to sonoluminescence[6,7]. Water vapor readily pyrolyzes under the transient high temperatures producing O-atoms, hydroxyl radicals, and H-atoms[8]. Hot vapor colliding with the collapsing bubble wall generates interfacial temperatures of at least 800 K[8,9]. Chemicals preferentially partitioning to the bubble vapor will decompose via pyrolytic and combustion reactions[10]. Involatile surfactants that are difficult to oxidize, such as PFOS and PFOA, will pyrolytically decompose at the bubble-water interface[4].

Understanding the physical processes that control PFOX (X = S or A) degradation rates is key to optimization of their sonochemical kinetics. PFOX sonochemical degradation involves an initial, rate-determining ionic headgroup cleavage at the bubble-water interface followed by relatively quick mineralization of the fluorocarbon tail[11]. However, adsorption of PFOS and PFOA to the bubble-water interface, a physical process required before interfacial sonochemistry can occur, has yet to be investigated.

Henglein and Kormann[12] noted that hydroxyl radical scavenging activity increased with increasing organic chain length at cavitation bubble interfaces, while Fyrillas and Szeri made numerical calculations[13] of nonvolatile surfactant adsorption to an oscillating bubble interface. Their model calculations predicted a decrease in the maximum Gibbs surface excess, $\Gamma_{Max,Sono}$, as compared to the equilibrium max surface excess, $\Gamma_{Max,Eq}$, due to surface site limitations at bubble radial minimums and an increase in sonochemical surface activity, K_{Sono}, relative to equilibrium surface activity, K_{Eq}, due to high-velocity radial oscillations. Concentration-dependent sonochemical degradation kinetics of humic materials[14] and pesticides[15] have been empirically modeled by Langmuir-Hinshelwood kinetics, suggesting adsorption to the bubble-water interface is the initial step in their primary sonochemical decomposition mechanism and is limiting at high concentrations. Sostaric and Reisz[31,32] observed saturation of alkyl radical production during concentration-dependent sonolysis of alkyl sulfates and sulfonates. However, radical production from nonvolatile surfactants of various chain lengths did not correlate well with equilibrium Gibb's surface excess values, Γ_{Eq}. The lack of correlation was concluded to arise from relatively short acoustic bubble lifetimes (100s of μs) as compared to ionic surfactant equilibration times (> 1 ms). Tronson et. al.[16] observed that

Langmuir competitive adsorption modeling using equilibrium SDS surface excess values, Γ_{Eq}^{SDS}, did not fit trends expected from sonoluminescence data. Total acoustic bubble volume measurements as a function of alcohol conentration correlated well with Γ_{Eq}, however, Γ_{Eq} overestimated sonochemical ionic surfactant adsorption[17]. Sonochemical adsorption of nonvolatile (i.e., ionic) surfactants is not well described by equilibrium partitioning.

Here, we investigate sonochemical PFOS and PFOA adsorption to the bubble-water interface by determining absolute rates over 4 orders of magnitude of initial PFOX concentrations. Sonochemical effects on surface activity, K_{Sono}^{PFOX} vs. K_{Eq}^{PFOX}, are evaluated by modeling the concentration-dependent kinetics with the Langmuir-Hinshelwood formalism using an empirically determined V_{Max}^{-PFOX}, and comparing the results to equilibrium surface partitioning determined by surface tension measurements. Sonochemical PFOX surface activity determined here is compared to previously observed results.

Experimental Methods

Ammonium perfluorooctanoate (APFO) and sodium perfluorosulfonate (PFOS) were provided by the 3M Corporation. Ammonium acetate (> 99%) and methanol (HR-GC > 99.99%) were obtained from EMD Chemicals, Inc. Aqueous solutions were prepared with distilled and deionized water that was further purified using a MilliPore system (18.2 MΩ-cm resistivity).

Ultrasonic irradiation was performed at a frequency of 354 kHz and an applied power density of 250 W L^{-1} with an Allied Signal ELAC Nautik ultrasonic transducer. The average energy transferred to solution was 75%, as determined by calorimetry. The reaction solution was contained in a 600 mL water-jacketed, glass reactor. The temperature was controlled with a Haake A80 refrigerated bath maintained at 10 ºC. All reactions were continuously sparged with argon for 30 minutes prior to and for the duration of the reaction. PFOS and PFOA were sonicated simultaneously over an initial concentration range of 20 nM to 200 μM. Higher concentrations were not tested as sonication caused the compounds to precipitate. Concentration vs. time profiles were fitted either to a single exponential decay for first-order kinetics, or linearly for zero-order kinetics.

Analysis of PFOA and PFOS was completed by HPLC-MS. The samples were placed into 750 μL polypropylene autosampler vials and sealed with a PTFE septum crimp cap. For reactions with intial concentrations greater than 250 ppb, serial dilutions to achieve a concentration ~ 50 ppb were completed prior to analysis. Aliquots (20 μL) were injected into an Agilent 1100 LC for separation on a Betasil C18 column (Thermo-Electron) of dimensions 2.1 mm ID, 100 mm length, and 5 μm particle size. A 2 mM aqueous ammonium acetate / methanol mobile phase at a flow rate of 0.75 mL min^{-1} was used with an initial composition of 70:30 water / methanol. Analytical procedures are detailed in previous reports[11]. The HPLC effluents were analyzed with an Agilent Ion Trap MS in the negative ion mode for the perfluorooctanesulfonate molecular ion (m/z = 499) and the decarboxylated perfluoroctanoate (m/z = 369). The nebulizer gas pressure was 40 PSI, while the drying gas flow rate and temperature were 9 L min^{-1} and 325 ºC, respectively. The capillary voltage was set at + 3500 V and the skimmer voltage was – 15 V. Quantification was completed by first producing a calibration curve using 8 concentrations between 1 ppb and 200 ppb fitted to a quadratic with X^{-1} weighting.

Surface tension measurements were made with a De Nouy tensiometer utilizing the standard ring method (ASTM D1331-89). The tensiometer was calibrated with a weight of known mass. Each sample was measured three times with the deviation between measurements less than 1%. The PFOS measurements were completed up to ~ 1 mM where the compound became insoluble. The curve was fitted to the surface pressure equation of state using Matlab to determine the partitioning coefficient and the maximum surface concentration.

Results

PFOX Concentration-Dependent Sonochemical Kinetics

Sonolysis of aqueous solutions containing both PFOS and PFOA were carried out over a range of initial concentrations from 20 nM to 200 μM (ν = 354 kHz, ρ_{PD} = 250 W L^{-1}, I = 6.4 W cm^{-2}). A plot of $[PFOS]_t/[PFOS]_i$ vs. time for a representative set of PFOS concentrations is shown in Figure 4.1a. At PFOS concentrations over the range of 20 nM to 14 μM, the observed kinetics are pseudo-first-order over four half-lives and are fitted to a single exponential decay. Previously reported results on PFOS and PFOA sonochemical decomposition completed at $[PFOS]_i \leq 20$ μM displayed a similar kinetic order[4,11]. At PFOS concentrations of 39 μM to 202 μM, the reaction kinetics are zero-order over the entire time-course. At an intermediate PFOS concentration of 30 μM, the data is fit to a quasi-exponential decay after the concentration dropped below 25 μM after 30 minutes of sonication. The transition from pseudo-first-order kinetics at low concentrations to zero-order kinetics at high concentrations is consistent with saturation kinetics. Initial PFOS sonochemical decomposition occurs pyrolytically at the bubble-water interface, therefore at high $[PFOS]_i$ the number of transiently cavitating bubble-water interfacial adsorption sites becomes saturated.

A qualitatively similar transition was observed for the sonolytic degradation of PFOA upon increasing the initial PFOA concentration. A plot of $[PFOA]_t/[PFOA]_i$ vs. time for a representative set of concentrations is shown in Figure 4.1b. At initial PFOA concentrations over the range of 24 nM to 6.5 μM, the reaction kinetics are pseudo first-order over at least four half-lives and are fitted to an exponential decay. At higher initial concentrations where $[PFOA]_i \geq 35$ μM, the reaction kinetics are zero-order over the entire time-course. At intermediate concentrations of 13.2, 16.6, and 30.5 μM, the reaction kinetics appear to be exponential after the first 30 minutes of reaction. The kinetic transition from pseudo-first-order to zero-order decay is similar to that observed for PFOS, and consistent with saturation kinetics

The observed kinetic parameters are given in Table 4.1. For low initial concentrations, $[PFOS]_i < 25$ μM and $[PFOS]_i < 13$ μM, the time-dependent plot was fitted to an exponential curve to determine the first-order rate constant, k_{app}^{-PFOX} (min^{-1}), and eq. 4.1 was used to determine the absolute rate.

$$\frac{d[PFOX]}{dt} = -k_{app}^{-PFOX}[PFOX] \tag{4.1}$$

For high initial concentrations, $[PFOX]_i > 40$ μM, the time-dependent plot was fitted to a linear curve with the slope, $k_{app}^{-PFOX'}$, taken to be the absolute degradation rate, eq. 4.2.

$$\frac{d[PFOX]}{dt} = -k_{app}^{-PFOX'} \tag{4.2}$$

For intermediate concentrations, the decay for the first 30 minutes was assumed to be linear and fit to eq. 4.2 and the decay after 30 minutes was fit to eq. 4.1. The overall degradation rate in Table 4.1 was taken as the temporal average of these two rates.

Equilibrium Partitioning to the Air-Water Interface

The Langmuir model describes adsorption to an interface. In the Langmuir model, the surface excess, Γ_{ex} , is a function of the equilibrium interface partitioning constant or surface activity, K_{eq} in L mol^{-1}, and the maximum surface concentration, $\Gamma_{\max}$ in mol m^{-2}. For example, equilibrium adsorption of PFOX to the air-water interface is modeled as shown in eq. 4.3.

$$\Gamma_{ex,eq}^{PFOX} = \Gamma_{Max,eq}^{PFOX} \frac{K_{eq}^{PFOX}[PFOX]}{1 + K_{eq}^{PFOX}[PFOX]} \tag{4.3}$$

The corresponding $\Gamma_{eq,ex}^{PFOX}$ and K_{eq}^{PFOX} values are determined from the dependence of surface tension on [PFOX], Figure 4.2, by least-squares fitting of the surface pressure to the Szyszkowski equation, eq. 4.4

$$\Pi = \gamma_0 - \gamma_{[PFOX]} = nRT\ \Gamma_{Max,eq}^{PFOX} \ln(1 + K_{eq}^{PFOX}[PFOX]) \tag{4.4}$$

where Π is the surface pressure in N m^{-1}, γ_0 = 0.072 N m^{-1} is the surface tension of pure water, and $\gamma_{[PFOX]}$ is the surface tension at [PFOX]. Maximum air-water interface concentrations of $\Gamma_{Max,eq}^{PFOA}$ = 4.5 x 10^{-6} mol m^{-2} and $\Gamma_{Max,eq}^{PFOS}$ = 5.1 x 10^{-6} mol m^{-2}, and equilibrium partitioning coefficients of K_{eq}^{PFOA} = 360 L mol^{-1} and K_{eq}^{PFOS} = 1970 L mol^{-1} are determined. The surface tension of solutions containing both PFOS and PFOA at equal concentrations was also measured and is plotted in Figure 4.2a. The stronger surfactant, PFOS, controls the surface tension as observed by the near overlap of the $\gamma_{[PFOS]}$ vs. [PFOS] curve and the $\gamma_{[PFOS]+[PFOA]}$ vs. [PFOS] + [PFOA] curve. Both the PFOS alone and [PFOS] + [PFOA] curves truncate between 1 to 2 mM, as the sodium salt of PFOS becomes insoluble in water. However, the agreement $\Gamma_{Max,eq}^{PFOX}$ and K_{eq}^{PFOX} values calculated here with previously determined values[35–38] shows that solubility limits have minimal effect on the surface pressure fitting. Surface excess values vs. [PFOX] are plotted in Figure 4.2b; solid lines for individual PFOX curves and dashed lines for individual components of [PFOS] + [PFOA] curve. A competitive adsorption isotherm was used to plot the [PFOS] + [PFOA] surface excess values for each component. For example, eq. 4.5 was used for PFOA.

$$\Gamma_{ex,eq}^{PFOA} = \Gamma_{Max,eq}^{PFOA} \frac{K_{eq}^{PFOA}[PFOA]}{1 + K_{eq}^{PFOA}[PFOA] + K_{eq}^{PFOS}[PFOS]} \tag{4.5}$$

PFOS is observed to be the dominant surfactant in Figure 4.2b, as PFOA competition has little effect on the surface excess curve. In contrast, PFOA's surface excess curve under saturation conditions is shifted downward as PFOS outcompetes PFOA for air-water interface sites. The surface excess of PFOA under saturation conditions is decreased 7.2 times in the competition curve (dashed) as compared to the PFOA curve (solid).

Discussion

d[PFOX]/dt vs. [PFOX]$_i$ Sonochemical Kinetic Modeling

The transition from first-order to zero-order kinetics upon increasing the initial concentrations is consistent with saturation kinetics. Using the Langmuir-Hinshelwood approach[18] to model [PFOX]$_i$ sonochemical kinetics, the absolute rate is proportional to θ_{Sono}^{PFOX}, the fraction of total molecules adsorbed to the transiently cavitating bubble-water interface, eqs. 4.6 and 4.7

$$\theta_{Sono}^{PFOX} = \frac{K_{Sono}^{PFOX}[PFOX]}{1 + K_{Sono}^{PFOX}[PFOX]} \tag{4.6}$$

$$\frac{d[PFOX]}{dt} = -V_{Max}^{-PFOX} \theta_{Sono}^{PFOX} \tag{4.7}$$

where V_{Max}^{-PFOX} (M s^{-1}) is the maximum reaction rate when all the available bubble surface sorption sites are occupied.

The transition in kinetic regimes is consistent with Langmuir-Hinshelwood kinetic limits. At low PFOX concentration, when the surface is undersaturated and the observed kinetics are pseudo-first-order:

$$K_{Sono}^{PFOX}[PFOX] << 1 \tag{4.8}$$

$$\theta_{Sono}^{PFOX} = K_{Sono}^{PFOX}[PFOX] \tag{4.9}$$

$$\frac{d[PFOX]}{dt} = k_{app}^{-PFOX}[PFOX] = -V_{Max}^{-PFOX}K_{Sono}^{PFOX}[PFOX] \tag{4.10}$$

$$k_{app}^{-PFOX} = -V_{Max}^{-PFOX}K_{Sono}^{PFOX} \tag{4.11}$$

At intermediate concentration, there is a barrier to continued adsorption as the interfacial sites become increasingly populated, % levels:

$$\frac{d[PFOX]}{dt} = -V_{Max}^{-PFOX}\frac{K_{Sono}^{PFOX}[PFOX]}{1+K_{Sono}^{PFOX}[PFOX]} \tag{4.12}$$

At high concentration, all of the surface sites are occupied and the maximum absolute rate is achieved:

$$K_{Sono}^{PFOX}[PFOX] >> 1 \tag{4.13}$$

$$\frac{d[PFOX]}{dt} = -V_{Max}^{-PFOX} \tag{4.14}$$

Thus, at low and intermediate concentration the kinetics are controlled by the fraction of the total PFOX molecules, which are absorbed to the bubble-water interface, as given by the Langmuir isotherm (eq. 4.6). At high concentration, the bubble-water interface is saturated with PFOX molecules and the rate is limited by the intrinsic chemical reaction rate (e.g., PFOX pyrolysis)[40–45].

Figures 4.3a and b plot the PFOX absolute degradation rate vs. [PFOX]$_i$ in linear-linear and log-log format, respectively; values from Table 4.1. Over the initial concentration range, 20 nM < [PFOX]$_i$ < 2000 nM, k_{app}^{-PFOX} (eq. 1) are constant; k_{app}^{-PFOA} = 0.047 min^{-1}, k_{app}^{-PFOS} = 0.028 min^{-1}, and k_{app}^{-PFOA} = 1.68 k_{app}^{-PFOS}. This indicates that the surface is undersaturated and the observed increase in absolute rate is due to the increasing θ_{Sono}^{PFOX}. However, at similar bulk concentrations, PFOS is expected to have the greater equilibrium activity at the bubble-water interface even though the maximum interfacial concentrations are similar, $\Gamma_{\max}^{PFOA}$ = 1.1 $\Gamma_{\max}^{PFOS}$ because PFOS has a larger partitioning coefficient, K_{eq}^{PFOS} = 5.5 K_{eq}^{PFOA}. Thus the theoretical sonochemical degradation rate for PFOA is greater than that for PFOS or $V_{Max,Theo}^{-PFOA} > V_{Max,Theo}^{-PFOS}$, and if $\theta_{Sono}^{PFOS} > \theta_{Sono}^{PFOA}$ then $V_{Max,Theo}^{-PFOA} / V_{Max,Theo}^{-PFOS} > \theta_{Sono}^{PFOS} / \theta_{Sono}^{PFOA}$. Given that k_{app}^{-PFOA} = 1.68 k_{app}^{-PFOS} (eq. 11) and $K_{eq}^{PFOS} / K_{eq}^{PFOA}$ = 5.5, the theoretical ratio $V_{Max,Theo}^{-PFOA} / V_{Max,Theo}^{-PFOS}$ is determined to be 9.3 under current ultrasonic conditions.

At initial concentrations over the range of 13 μM < [PFOX]$_i$ < 150 μM, PFOS and PFOA absolute rates are observed to saturate at $V_{Max,App}^{-PFOA}$ = 240 ± 60 nM min^{-1} and $V_{Max,App}^{-PFOS}$ = 230 ± 60 nM min^{-1}, confirming that the bubble-water interface is saturated. Convergence of $V_{Max,App}^{-PFOA}$ and $V_{Max,App}^{-PFOS}$ is at variance with relative kinetics at low concentrations. Under saturation conditions, PFOS as the stronger surfactant should out-compete PFOA for bubble surface sites and thus is able to compensate for the difference in the theoretical maximum pyrolytic rate constants causing the apparent rates to converge. This is consistent with equilibrium partitioning where PFOS competition decreased the PFOA surface excess by a factor of 7.2, Fig. 4.2b. If PFOA were to be sonolytically degraded in the absence of PFOS, it would be expected to have a maximum degradation rate approximately 9.3 times greater than the experimentally observed rate or V_{Max}^{-PFOA} = 2230 ± 560 nM. The determined V_{Max}^{-PFOX} values, low concentration k_{app}^{-PFOX}, and eq. 11 are used to calculate K_{Sono}^{PFOX} values of K_{Sono}^{PFOS} = 121,000 M^{-1} and K_{Sono}^{PFOA} = 28,500 M^{-1}. Both values are greater than equilibrium air-water interface partitioning values, yielding relative sonochemical to equilibrium surface activities of $K_{Sono}^{PFOS} / K_{Eq}^{PFOS}$ = 60 and $K_{Sono}^{PFOA} / K_{Eq}^{PFOA}$ = 80, Table 4.2.

The absolute PFOS degradation rates are modeled using the competitive Langmuir-Hinshelwood model, eq. 4.15, as shown in Figure 4.4, where V_{Max}^{-PFOS} is set to the empirically determined value $V_{Max,app}^{-PFOS}$ = 230 nM min^{-1} and K_{Sono}^{PFOS} is set equal to K_{Eq}^{PFOS} (black line), 10 × K_{Eq}^{PFOS} (blue line), and 100 × K_{Eq}^{PFOS} (red line); K_{Eq}^{PFOA} was adjusted accordingly.

$$\frac{d[PFOS]}{dt} = -V_{Max}^{-PFOS} \frac{K_{Sono}^{PFOS}[PFOS]}{1 + K_{Sono}^{PFOS}[PFOS] + K_{Sono}^{PFOA}[PFOA]} \tag{4.15}$$

The primary plots of Figure 4.4 are in log-log format while the inset is in linear-linear format. The best fit to the experimental data (black dots) is obtained when $K_{Sono}^{PFOS} = 100 \times K_{Eq}^{PFOS}$. PFOA surface competition had little effect on the fit as the non-competitive LH model yields a similar result. Altering V_{Max}^{-PFOS} rather than K_{Sono}^{PFOS} does not improve the fitting of the LH model to the experimental data.

Applying the Langmuir-Hinshelwood formalism to PFOA sonochemical kinetics is slightly more difficult since it is the weaker surfactant and competitive adsorption will have a more prominent effect, Figure 4.2. In Figure 4.5a, the absolute PFOA degradation rate vs. initial PFOA concentration is modeled using the competitive LH formalism, eq. 16, with V_{Max}^{-PFOA} set to the empirically determined 240 nM min^{-1} and K_{Sono}^{PFOA} set equal to K_{Eq}^{PFOA} (black line), 10 × K_{Eq}^{PFOA} (blue line), and 100 × K_{Eq}^{PFOA} (red line); K_{Eq}^{PFOS} was adjusted accordingly.

$$\frac{d[PFOA]}{dt} = -V_{Max}^{-PFOA} \frac{K_{Sono}^{PFOA}[PFOA]}{1 + K_{Sono}^{PFOA}[PFOA] + K_{Sono}^{PFOS}[PFOS]} \tag{4.16}$$

The model calculations underestimate the experimental data by at least an order of magnitude in both the surface-saturated and undersaturated regimes. In Fig. 4.5b, V_{Max}^{-PFOA} is set to 2230 nM min^{-1}, as calculated using the relationship $V_{Max,Theo}^{-PFOA}$ / $V_{Max,Theo}^{-PFOA}$ = 9.3 to account for PFOS outcompeting PFOA for bubble interface adsorption sites. When $K_{Sono}^{PFOA} = 100 \times K_{Eq}^{PFOA}$, the best qualitative fit to the experimental data is obtained. d[PFOA]/dt vs. $[PFOA]_i$ fits for noncompetitive LH models are provided in the supporting information document. With V_{Max}^{-PFOA} = 240 nM min^{-1}, $K_{Sono}^{PFOA} = 1000 \times K_{Eq}^{PFOA}$, a good data fit is obtained while at V_{Max}^{-PFOA} = 2230 nM min^{-1}; none of the models result in a good fit to the data.

As $[PFOX]_i$ increases to greater than 200 μM, d[PFOX]/dt increases substantially to > 1000 nM min^{-1}, at variance with the LH kinetic model. Previous reports on ionic surfactant sonochemistry provide insight into this phenomenon. Ashokkumar et al.[19] observed that upon increasing aqueous sodium dodecyl sulfate (SDS) concentration, sonoluminescence (SL) increased, reaching a maximum at [SDS] = 1 mM. The increase in SL was attributed to SDS accumulation and thus build-up of charge on the bubble surface. Electrostatic repulsion between charged bubbles reduced bubble clustering, leading to a greater number of more intense SL active bubble events. Total bubble volume was reported to decrease as bulk [SDS] was increased, with a 50% reduction in total bubble volume at [SDS] = 100 μM[20] suggesting a reduction in bubble coalescence. Increasing [SDS] led to a decrease in broadband acoustic emission, even though total acoustic emission increased[21], suggesting a transition to a greater number of more intense bubble collapse events[22] due to reduction in bubble-bubble clustering and coalescence. As anionic surfactants, PFOS and PFOA would be expected to have a similar effect on bubble-bubble interactions as SDS. The increase in PFOX absolute degradation rate occurs at $[PFOX]_i > 100$ μM , consistent with SDS concentrations where SL, total bubble volume, and acoustic emission effects are observed to take affect. Reduction in bubble-bubble coalescence and clustering leading to a greater number of more intense bubble collapse events would result in a greater number of bubble interface face adsorption sites and consequently an increase in PFOX sonochemical degradation kinetics.

Non-Equilibrium Bubble Surface Activity

Optimized fitting of the experimental kinetic data as a function of [PFOX] to the LH model gives $K_{Sono}^{PFOS} = 60\ K_{Eq}^{PFOS}$ and $K_{Sono}^{PFOA} = 80\ K_{Eq}^{PFOA}$. Data from two previous reports, which are fit to LH kinetics, is presented in Table 4.2. Concentration-dependent alkyl radical production for sodium dodecyl sulfate (SDS) and sodium octyl sulfate (SOS) from the work of Sostaric and Reisz[31] was fit to the LH model using an empirically determined maximum rate of alkyl radical production. For both compounds, K_{Sono} appears to be greater than K_{Eq}. The relative difference between K_{Sono} and K_{Eq} was greater for the weaker surfactant: $K_{Sono}^{SDS} = 12.5\ K_{Eq}^{SDS}$ vs. $K_{Sono}^{SOS} = 410\, K_{Eq}^{SOS}$. This trend is expected to hold for sodium pentyl sulfonate (SPSo), a weaker surfactant than SOS, which had a similar sonochemical surface activity to SOS and SDS. Kim and Jung[29] modeled sonochemical degradation of humic acids (anionic, surface-active, natural organic matter) with LH kinetics and their results give values of $K_{Sono} > K_{Eq}$ as well. The humic acid degradation kinetics gave the greatest relative surface activity difference, $K_{Sono}^{Humic} = 3400\,K_{Eq}^{Humic}$; most likely due to the very high applied acoustic power density, 14,000 W L^{-1}.

Greater sonochemical surface activity over that of the predicted equilibrium surface activity was predicted by the calcuations of Fryllis and Szeri[13]. Their work argues that high-velocity bubble oscillations should increase the transport of surfactants to a lightly populated surface. Their conclusions are in qualitative agreement with the work of Eller and Flynn[23] on rectified diffusion. Under their 'high frequency approximation', which is valid for f > 20 kHz, diffusion can be assumed to be a slow process as compared to the radial motion of acoustic bubbles. For example, the sonochemical surface activity can be broken in the ratio of the rates of adsorption to and desorption from the interface: $K_{Sono} = \frac{k_{ads}}{k_{des}}$. Thus an increase in k_{ads} or a decrease in k_{des} will result in an increase in K_{Sono}. It is much easier to rationalize an increase in k_{ads}. For a lightly populated surface $k_{ads} = k_{dif}$ and processes such as high-velocity bubble oscillations or acoustic microstreaming may enhance diffusion to the bubble interface. A rough, yet insightful example will be presented to further this point.

A transiently cavitating bubble will expand from its average initial radius, R_0, to its max radius, R_{max}, over a period of 0.5f, where f is the ultrasonic frequency[5]. R_{max} (μm) can be calculated using the equation:

$$R_{\max}(\mu m) = (3\ x\ 10^6 / f)(P_a - 1)(P_a)^{-1/2}[1 + 2(P_a - 1)/3]^{1/3} \qquad (4.17)$$

where P_a is the acoustic pressure ($P_a = (2\ \rho\ C_L I_A)^{1/2} / 101325$ bar), ρ is the density of water (1000 kg m^{-3}), C_L is the speed of sound in water (1500 m s^{-1}), and I_A is the acoustic intensity (51000 W m^{-2} at a calorimetric power of 120 watts over a transducer area of 23.5 cm^2). Assuming a monotonic distribution of bubbles[24], R_0 can be estimated as the average of $R_{max}/2.5$, which is the dynamic limit for transient cavitation, and R_B, which is Blake's radius of bubble dissolution[5]. Since $R_B << R_{max}/2.5$ the value of R_0 is roughly $R_{max}/5$. Sonochemical parameters of 354 kHz and 120 watts correspond to R_{max} = 18 μm and $R_{max}/5$ = 3.6 μm. Thus, a point on the bubble surface travels a radial distance of 14.4 μm over the rarefaction period of 1.4 μs and assuming a constant radial velocity, a point at the bubble surface will travel at 10 m s^{-1} during expansion under present sonochemical conditions. If we assume a diffusion constant of 10^{-5} cm^2 s^{-1} or 10^{-3} μm^2 μs^{-1} for PFOS and PFOA, over a period of 1.4 μs a single molecule is expected to travel around 35 nm, which is much less than the bubble radial motion of 14.4 μm over the same period.

The differential volume between the average initial bubble, R_0 = 3.6 μm, and a bubble at its maximum radius, R_{max} = 18 μm, is $V_{diff} = (4/3)\ \pi\ (18^3 - 3.6^3) = 24200\ \mu m^3$. Using the high-frequency assumption that the rate of diffusion is significantly less than the rate of radial expansion, then all of the PFOS or PFOA molecules contained in the initial volume would be packed into a sheath of 35 nm in radius around the maximal bubble volume, $V_{sheath} = (4/3)\ \pi\ (18.035^3 - 18^3) = 143\ \mu m^3$. The ratio of the initial differential bubble volume to the bubble sheath volume, V_{diff}/V_{sheath} = 170. This suggests that the sonochemically induced increase in PFOS and PFOA surface activity may be partially due to high-velocity bubble oscillations enhancing the diffusion of the fluorochemicals to the bubble-water. Other effects such as acoustic microstreaming[24] may also be responsible for enhanced diffusion to the bubble interface and thus the sonochemical surface activity

The results here are seemingly at variance with recent work by Tronson et al.[33] and Sunartio et al.[34] which concluded that the Gibb's surface excess was not attained for non-volatile surfactants. Fyrillas and Szeri[28] predicted that high-velocity bubble oscillations would reduce the maximal surfactant bubble surface population. This is consistent with conclusions that relatively short acoustic bubble lifetimes (~ 100 μs), as compared to ionic surfactant equilibration times (> 1 ms), led to the Gibb's surface excess not being attained during ultrasonic irradiation. Examples of possible nonequilibrium sonochemical PFOS surface activites, K^{PFOS}, and possible nonequilibrium sonochemical max surface excesses, Γ_{Max}^{PFOS}, and their affects on the surface excess population, Γ_{ex}^{PFOS} (eq. 3), are presented in Figure 4.6. Variations in Γ_{Max}^{PFOS} lead to a vertical shift in the Γ_{ex}^{PFOS} vs. [PFOS] curve, with the expected sonochemical effect to be a decrease in Γ_{Max}^{PFOS} and thus an overall, concentration-independent decrease in Γ_{ex}^{PFOS}. Variations in K^{PFOS} lead to a horizontal shift in the Γ_{ex}^{PFOS} vs. [PFOS] curve. The experimental results presented here suggest an increase in K^{PFOS} and thus a shift in the direction of the ordinate. If a decrease in Γ_{Max}^{PFOS} and an increase in K^{PFOS} occur upon moving from equilibrium air-water interface partitioning to a sonochemical air-water interface partitioning, then under surface saturation conditions a decrease Γ_{ex}^{PFOS} would still be predicted. Therefore, the experimental results presented suggesting a sonochemical increase in surface activity, $K_{Sono} > K_{Eq}$, are not necessarily at variance with previous results suggesting the Gibb's surface excess was not attained for nonvolatile solutes. For example, in Figure 4.6c, simultaneous variations in both Γ_{Max}^{PFOS} and K^{PFOS} have been plotted. Decreasing Γ_{Max}^{PFOS} by a factor of ten also reduces Γ_{ex}^{PFOS} under lightly populated conditions by a factor of 10 (green line). Increasing K^{PFOS} by a factor of 10 (blue line) brings Γ_{ex}^{PFOS} to the equilibrium level (black line) for undersaturation conditons. Furthermore, when Γ_{Max}^{PFOS} is decreased by a factor of 10 and K^{PFOS} is increased by a factor of 100 (red line), the Γ_{ex}^{PFOS} then exceeds the predicted equilibrium adsorption limit for lightly populated conditions and is still below predicted equilibrium adsorption for saturation conditions.

Conclusions

The sonochemical degradation kinetics of PFOS and PFOA have been studied over the concentration range of 20 nM < $[PFOX]_I$ < 200 μM. The kinetics are fit to the Langmuir-Hinshelwood model using experimental rate maximums of V_{Max}^{-PFOA} = 2230 ± 560 nM min^{-1} and V_{Max}^{-PFOS} = 230 ± 60 nM min^{-1}. The corresponding sonochemical bubble surface activities for PFOS and PFOA are determined to be K_{Sono}^{PFOS} = 120,000 M^{-1} and K_{Sono}^{PFOA} = 28,500 M^{-1}, respectively. Competitive bubble surface adsorption is factored into the LH model in order to accurately model the kinetics of PFOA under saturation conditions. The sonochemical surface activities, K_{Sono}^{PFOX}, are 50 to 100 times greater than the predicted equilibrium air-water interfacial activities, K_{Eq}^{PFOX}, as determined via concentration-dependent surface tension measurements. The apparent enhancements in bubble surface activities has positive implications for the application of ultrasonic irradation as a treatment technology for dilute, < 1 μM, aqueous solutions of PFOS and

PFOA. At low concentrations, the efficacy of conventional chemical treatment methods is greatly reduced due to concentration effects. These results will also have implications for the sonochemical destruction of other pollutants where adsorption to the transiently cavitating bubble interface is expected to partially mediate absolute degradation rates.

Figures

Figure 4.1. PFOX sonochemical degradation initial concentration dependence. (358 kHz, 250 W L^{-1}, Ar, 10 ^{o}C). A) [PFOS]$_t$ / [PFOS]$_i$ vs. time in minutes. [PFOS]$_i$ = (●) 20 nM, (○) 14 μM, (▼) 30 μM, (▽) 39 μM, (■) 67 μM, and (□) 114 μM. B) [PFOA]$_t$ / [PFOA]$_i$ vs. Time (in minutes). [PFOA]$_i$ = (●) 20 nM, (○) 6.5 μM, (▼) 13.2 μM, (▽) 16.6 μM, (■) 30.5 μM, (□) 105 μM, and (◆) 220 μM

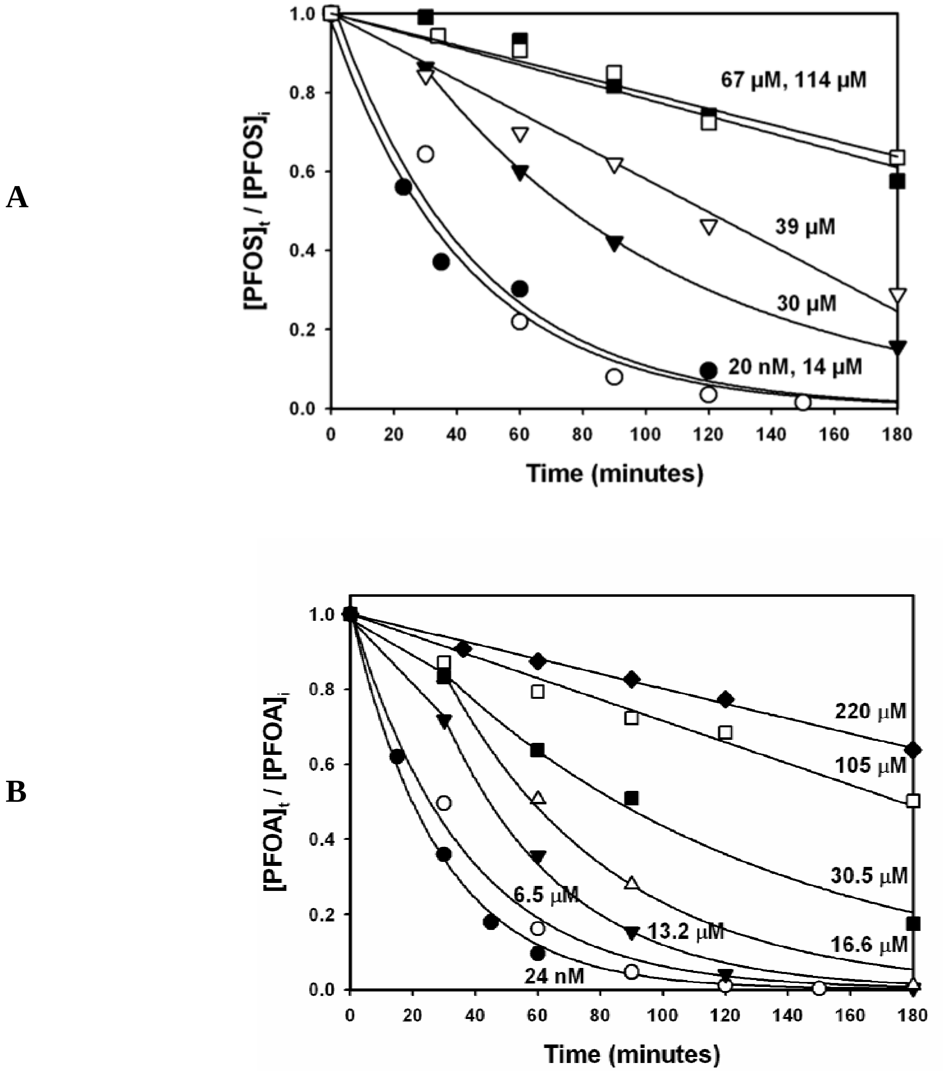

Figure 4.2. Equilibrium PFOX air-water interface partitioning. A) Plot of surface tension vs. aqueous PFOS and/or PFOA concentration. (●) PFOA, (●) PFOS, and (▼) PFOS & PFOA. B) Plot of surface excess vs. aqueous PFOS and/or PFOA concentration. (○) PFOA noncompetitive, (○) PFOS noncompetitive, (--) PFOA competitive, and (--) PFOS competitive

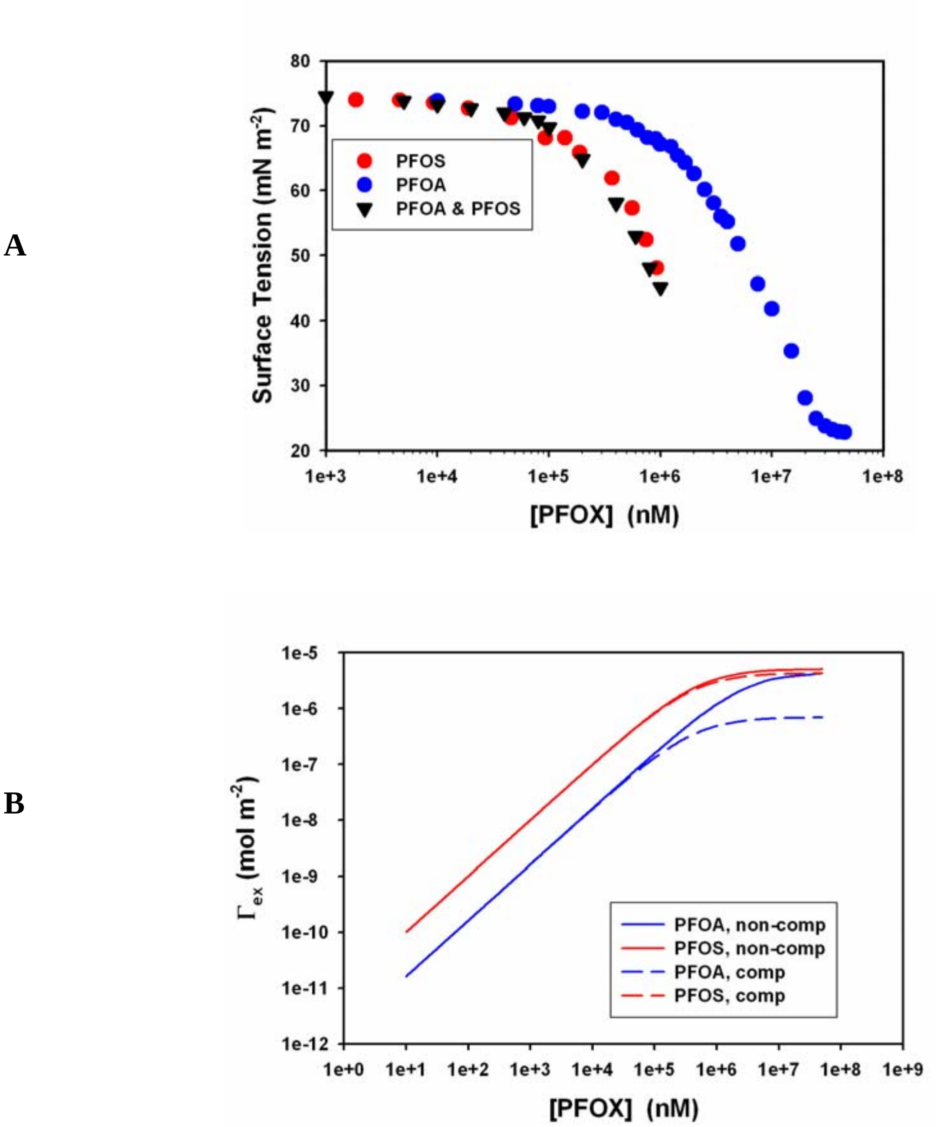

Figure 4.3. PFOX sonochemical degradation rate initial concentration dependence. PFOS and PFOA were simultaneously degraded under ultrasonic conditions: 358 kHz, 250 W L^{-1}, 10 °C, and argon. (○) PFOA and (○) PFOS. A) Linear-linear plot with the inset truncating off the final three data points. B) Log-log plot

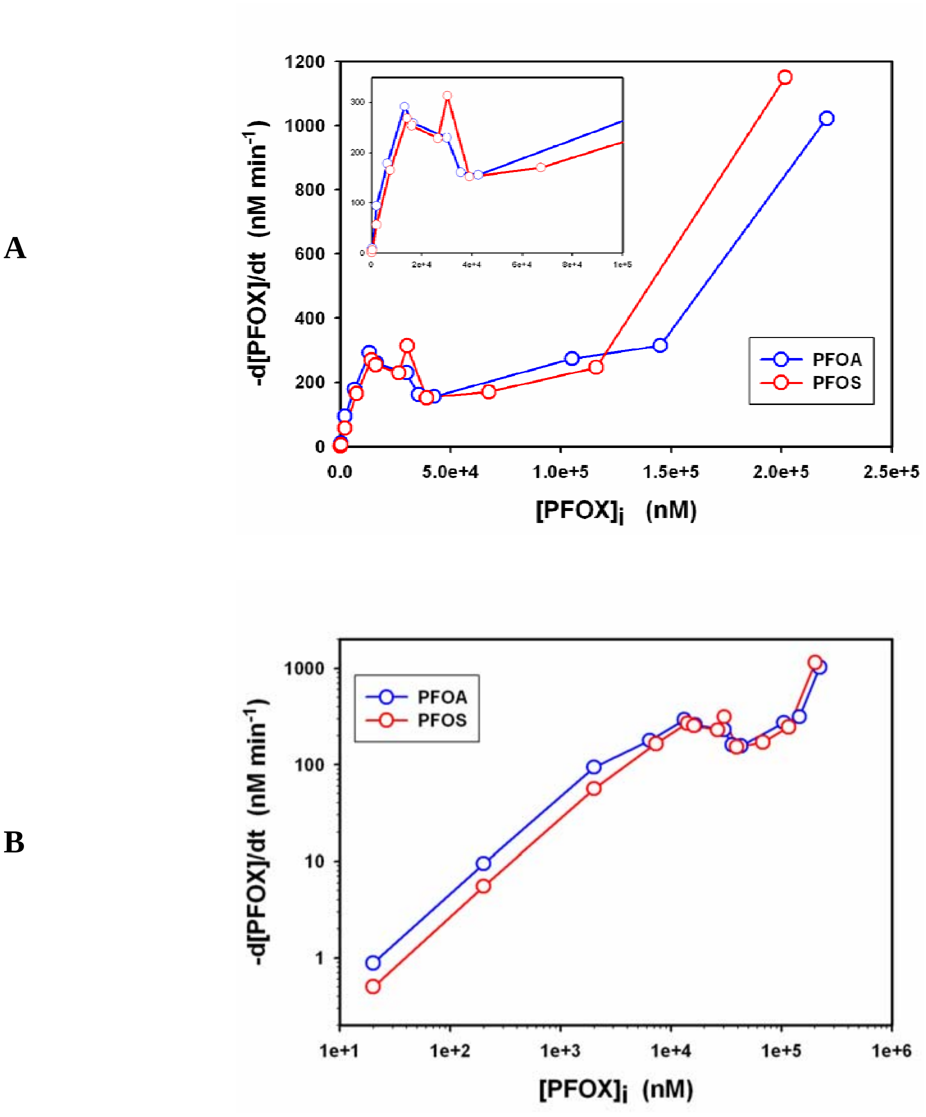

Figure 4.4. Kinetic modeling of PFOS sonolysis concentration-dependent kinetics. –[PFOS]/dt vs. [PFOX]$_i$ fitted by competitive Langmuir-Hinshelwood model, eq. 4.15: $V_{Max,app}^{-PFOS} =$ 230 nM min^{-1}. (●) Experimental, (—) $K_{Sono}^{PFOS} = K_{Eq}^{PFOS}$, (—) $K_{Sono}^{PFOS} = 10 \times K_{Eq}^{PFOS}$ and (—) $K_{Sono}^{PFOS} = 100 \times K_{Eq}^{PFOS}$

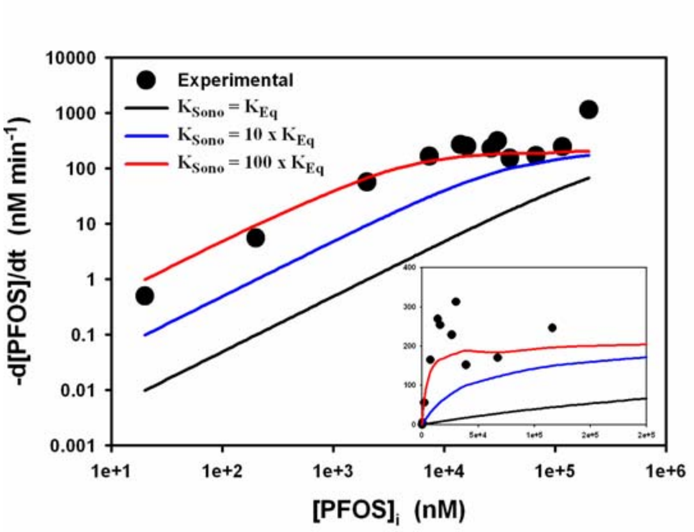

Figure 4.5. Kinetic modeling of PFOA sonolysis concentration-dependent kinetics. – [PFOA]/dt vs. $[PFOA]_i$ fitted by competitive Langmuir-Hinshelwood model (eq. 16): A) $V_{Max}^{-PFOA} =$ 240 nM min^{-1} and C) $V_{Max}^{-PFOA} =$ 2230 nM min^{-1}. (●) Experimental, **(—)** $K_{Sono}^{PFOA} = 100 \times K_{Eq}^{PFOA}$, **(—)** $K_{Sono}^{PFOA} = 100 \times K_{Eq}^{PFOA}$ and **(—)** $K_{Sono}^{PFOA} = 100 \times K_{Eq}^{PFOA}$

A

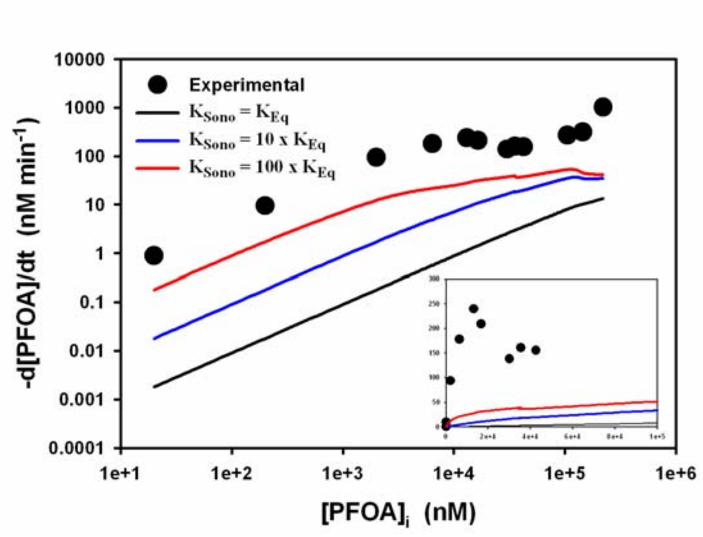

B

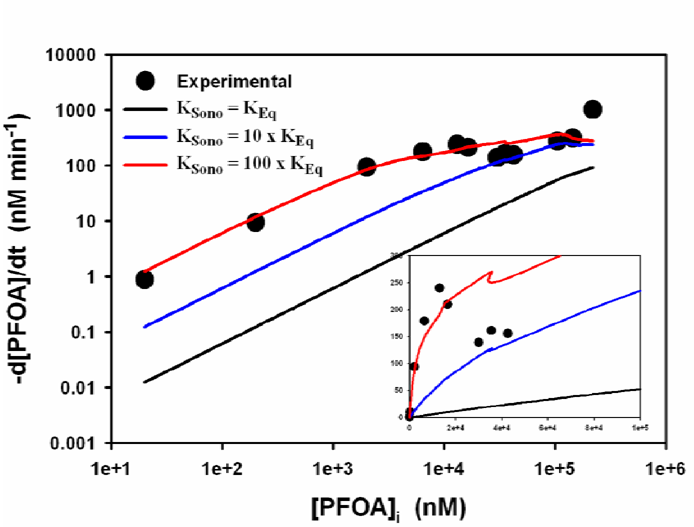

Figure 4.6. PFOS surface excess vs. PFOS bulk concentration (eq. 5): a) (○) Γ_{Max}^{PFOS}, (○) $10\times\Gamma_{Max}^{PFOS}$, and (○) $0.1\times\Gamma_{Max}^{PFOS}$, B) (○) K_{Eq}^{PFOS}, (○) $10\times K_{Eq}^{PFOS}$, and (○) $0.1\times K_{Eq}^{PFOS}$, and C) (○) Γ_{Max}^{PFOS} and K_{Eq}^{PFOS}, (○) $0.1\times\Gamma_{Max}^{PFOS}$ and K_{Eq}^{PFOS}, (○) $0.1\times\Gamma_{Max}^{PFOS}$ and $10\times K_{Eq}^{PFOS}$, and (○) $0.1\times\Gamma_{Max}^{PFOS}$ and $100\times K_{Eq}^{PFOS}$

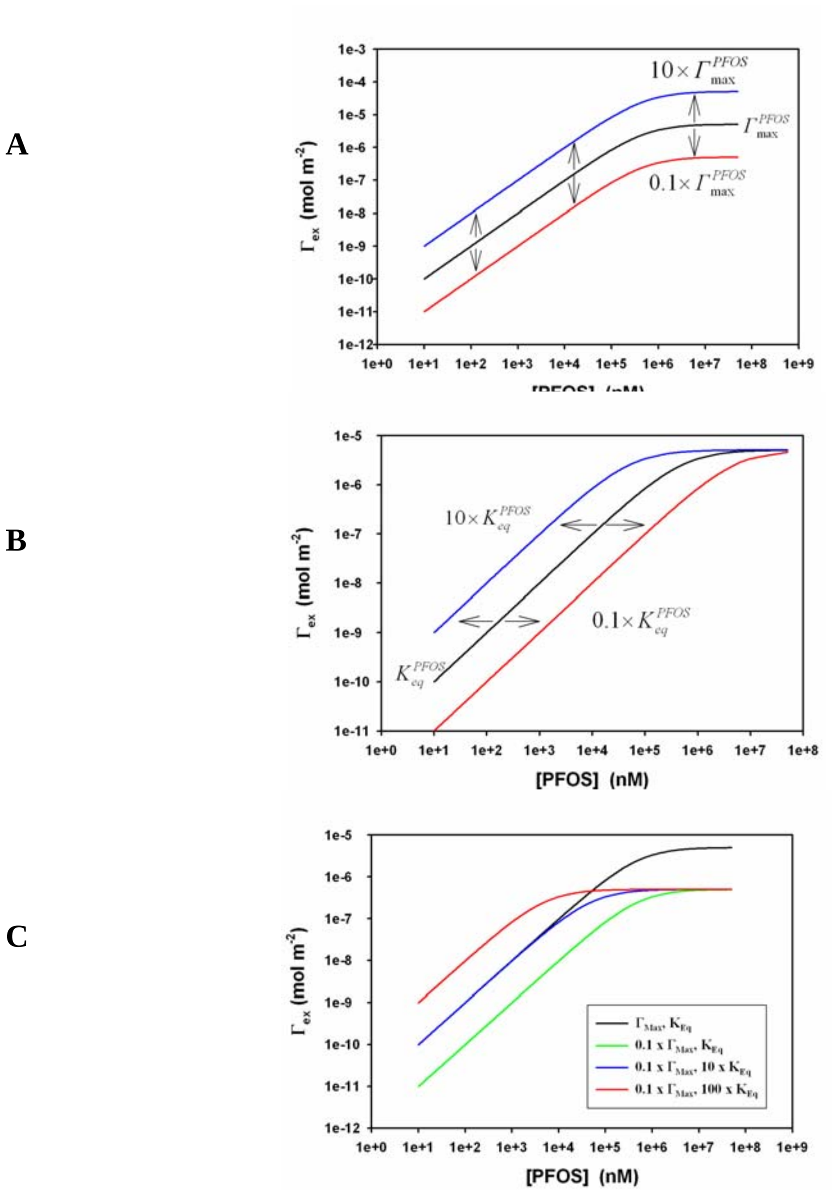

Tables

Table 4.1. Concentration-dependent PFOX sonochemical kinetics

[PFOA] (nM)	1st-Order (min^{-1})	0-Order (M min^{-1})	$\frac{-d[PFOA]}{dt}$ (M min^{-1})	[PFOS] (nM)	1st-Order (min^{-1})	0-Order (M min^{-1})	$\frac{-d[PFOS]}{dt}$ (M min^{-1})
20	0.044 ± 0.013		0.88	20	0.025 ± 0.005		0.5
200	0.047 ± 0.002		9.5	200	0.028 ± 0.006		5.5
2000	0.047 ± 0.005		94	2000	0.028 ± 0.005		56
6400	0.028		180	7300	0.023		165
13100	0.026	51	292	14000	0.019		269
16500	0.0184	39	259	16000	0.019	10	254
30000	0.0088	65	230	26400	0.01	56	229
35500		161	161	30200	0.012	69	313
42500		156	156	39000		152	152
105000		273	273	67300		170	170
145000		314	314	116000		250	250
221000		1022	1022	202000		1150	1150

Table 4.2. Sonochemical vs. equilibrium surface activity

	Frequency (kHz)	Applied Power Density (W L^{-1})	$\Gamma_{eq,\max}$ (mol m^{-2})	K_{eq} (M^{-1})	$V_{sono,\max}$	K_{Sono} (M^{-1})	$\frac{K_{Sono}}{K_{Eq}}$	Ref.
PFOS	354	250	5.1e-6	1,970	230 nM min^{-1}	121,000	60	this work
PFOA	354	250	4.5e-6	360	1660 nM min^{-1}	28,500	80	this work
SDS	47		6.9e-6[25]	400[25]	1 μM min^{-1}	5,000	12.5	[26]
SOS	47		6.4e-6[25]	22[25]	1.4 μM min^{-1}	8,000	410	[26]
Humic	20	14,000	4.6e-6[27]	1,180[27]		4e6	3,400	[29]

References

(1) 3M Company. *The Science of Organic Fluorochemistry*; Docket AR226-0547; Office of Pollution Prevention and Toxics, U.S. Environmental Protection Agency: Washington, D.C., 1999; p. 12.

(2) 3M Company. *Sulfonated perfluorochemicals in the environment: Sources, dispersion, fate and effects*; Docket AR226-0620; Office of Pollution Prevention & Toxics, U.S. Environmental Protection Agency: Washington, D.C., 2000; p. 51.

(3) 3M Company. *Removal of PFOA with Granular Activated Carbon: 3M Wastewater Treatment System Monitoring*; Docket AR226-1699; Office of Pollution Prevention & Toxics, U.S. Environmental Protection Agency: Washington, D.C., 2004; p. 5.

(4) Key, B. D.; Howell, R. D.; Criddle, C. S. *Environ. Sci. Technol.* **1998**, *32*, 2283.

(5) Schultz, M. M.; Higgins, C. P.; Huset, C. A.; Luthy, R. G.; Barofsky, D. F.; Field, J. A. *Environ. Sci. Technol.* **2006**, *40*, 7350.

(6) Schroder, H. F.; Meesters, R. J. W. *J. Chromatogr. A* **2005**, *1082*, 110.

(7) Hori, H.; Yamamoto, A.; Hayakawa, E.; Taniyasu, S.; Yamashita, N.; Kutsuna, S.; Kiatagawa, H.; Arakawa, R. *Environ. Sci. Technol.* **2005**, *39*, 2383.

(8) Chen, J.; Zhang, P. *Water Sci. Technol.* **2006**, *54*.

(9) Hori, H.; Hayakawa, E.; Einaga, H.; Kutsuna, S.; Koike, K.; Ibusuki, T.; Kiatagawa, H.; Arakawa, R. *Environ. Sci. Technol.* **2004**, *38*, 6118.

(10) Hori, H.; Nagaoka, Y.; Yamamoto, A.; Sano, T.; Yamashita, N.; Taniyasu, S.; Kutsuna, S.; Osaka, I.; Arakawa, R. *Environ. Sci. Technol.* **2006**, *40*, 1049.

(11) Yamamoto, T.; Noma, Y.; Sakai, S. I.; Shibata, Y. *Environ. Sci. Technol.* **2007**, *41*, 5660.

(12) Hori, H.; Hayakawa, E.; Koike, K.; Einaga, H.; Ibusuki, T. *J. Mol. Catal. A—Chem.* **2004**, *211*, 35.

(13) Dillert, R.; Bahnemann, D.; Hidaka, H. *Chemosphere* **2007**, *67*, 785.

(14) Moriwaki, H.; Takagi, Y.; Tanaka, M.; Tsuruho, K.; Okitsu, K.; Maeda, Y. *Environ. Sci. Technol.* **2005**, *39*, 3388.

(15) Jennings, B. H.; Townsend, S. N. *J. Phys. Chem.* **1961**, *65*, 1574.

(16) Destaillats, H.; Hung, H. M.; Hoffmann, M. R. *Environ. Sci. Technol.* **2000**, *34*, 311.

(17) Kotronarou, A.; Mills, G.; Hoffmann, M. R. *J. Phys. Chem.* **1991**, *95*, 3630.

(18) Petrier, C.; David, B.; Laguian, S. *Chemosphere* **1996**, *32*, 1709.

(19) Brennen, C. E. *Cavitation and Bubble Dynamics*; Oxford University Press: New York, 1995.

(20) Didenko, Y. T.; McNamara, W. B.; Suslick, K. S. *J. Am. Chem. Soc.* **1999**, *121*, 5817.

(21) Ciawi, E.; Rae, J.; Ashokkumar, M.; Grieser, F. *J. Phys. Chem. B* **2006**, *110*, 13656.

(22) Ashokkumar, M.; Grieser, F. *J. Am. Chem. Soc.* **2005**, *127*, 5326.

(23) Eddingsaas, N. C.; Suslick, K. S. *J. Am. Chem. Soc.* **2007**, *129*, 3838.

(24) Leighton, T. G. *The Acoustic Bubble*; Academic Press: London, 1994.

(25) Hung, H. M.; Hoffmann, M. R. *J. Phys. Chem. A* **1999**, *103*, 2734.

(26) Vecitis, C. D.; Park, H.; Cheng, J.; Mader, B. M.; Hoffmann, M. R. *J. Phys. Chem. C* **2008**, *112*.

(27) Henglein, A.; Kormann, C. *Int. J. Radiat. Biol.* **1985**, *48*, 251.

(28) Fyrillas, M. M.; Szeri, A. J. *J. Fluid Mech.* **1996**, *311*, 361.

(29) Kim, I. K.; Jung, O. J. *Bull. Korean Chem. Soc.* **2001**, *22*, 1093.

(30) O'Shea, K. E.; Aguila, A.; Vinodgopal, K.; Kamat, P. V. *Res. Chem. Intermed.* **1998**, *24*, 695.

(31) Sostaric, J. Z.; Riesz, P. *J. Am. Chem. Soc.* **2001**, *123*, 11010.

(32) Sostaric, J. Z.; Riesz, P. *J. Phys. Chem. B* **2002**, *106*, 12537.

(33) Tronson, R.; Ashokkumar, M.; Grieser, F. *J. Phys. Chem. B* **2003**, *107*, 7307.

(34) Sunartio, D.; Ashokkumar, M.; Grieser, F. *J. Am. Chem. Soc.* **2007**, *129*, 6031.

(35) Lopez-Fontan, J. L.; Gonzalez-Perez, A.; Costa, J.; Ruso, J. M.; Prieto, G.; Schulz, P. C.; Sarmiento, M. *J. Colloid Interface Sci.* **2006**, *294*, 458.

(36) Lopez-Fontan, J. L.; Sarmiento, F.; Schulz, P. C. *Colloid Polym. Sci.* **2005**, *283*, 862.

(37) Simister, E. A.; Lee, E. M.; Lu, J. R.; Thomas, R. K.; Ottewill, R. H.; Rennie, A. R.; Penfold, J. *J. Chem. Soc.—Faraday Trans.* **1992**, *88*, 3033.

(38) Shinoda, K.; Hato, M.; Hayashi, T. *J. Phys. Chem.* **1972**, *76*, 909.

(39) Langmuir, I. *J. Am. Chem. Soc.* **1916**, *38*, 2221.

(40) Glockner, V.; Lunkwitz, K.; Prescher, D. *Tenside Surf. Det.* **1989**, *26*.

(41) Lines, D.; Sutcliffe, H. *J. Fluor. Chem.* **1984**, *25*, 505.

(42) Lazerte, J. D.; Hals, L. J.; Reid, T. S.; Smith, G. H. *J. Am. Chem. Soc.* **1953**, *75*, 4525.

(43) Hals, L. J.; Reid, T. S.; Smith, G. H. *J. Am. Chem. Soc.* **1951**, *73*, 4054.

(44) Krusic, P. J.; Marchione, A. A.; Roe, D. C. *J. Fluor. Chem.* **2005**, *126*, 1510.

(45) Krusic, P. J.; Roe, D. C. *Anal. Chem.* **2004**, *76*, 3800.

(46) Ashokkumar, M.; Hall, R.; Mulvaney, P.; Grieser, F. *J. Phys. Chem. B* **1997**, *101*, 10845.

(47) Lee, J.; Kentish, S. E.; Ashokkurnar, M. *J. Phys. Chem. B* **2005**, *109*, 5095.

(48) Ashokkumar, M.; Hodnett, M.; Zeqiri, B.; Grieser, F.; Price, G. J. *J. Am. Chem. Soc.* **2007**, *129*, 2250.

(49) Price, G. J.; Ashokkumar, M.; Hodnett, M.; Zequiri, B.; Grieser, F. *J. Phys. Chem. B* **2005**, *109*, 17799.

(50) Eller, A.; Flynn, H. G. *J. Acoust. Soc. Am.* **1965**, *37*, 493.

(51) Colussi, A. J.; Hung, H. M.; Hoffmann, M. R. *J. Phys. Chem. A* **1999**, *103*, 2696.

(52) Lunkenheimer, K.; Czichocki, G.; Hirte, R.; Barzyk, W. *Colloid Surf. A—Physicochem. Eng. Asp.* **1995**, *101*, 187.

(53) Tuckermann, R. *Atmos. Environ.* **2007**, *41*, 6265.

Chapter 5

Reductive Defluorination of Aqueous Perfluorinated Alkyl Surfactants: Effects of Ionic Headgroup and Chain Length

Sections reprinted with permission from Park, H.; Vecitis, C. D.; Cheng, J.; Choi, W.; Mader, B. T.; Hoffmann, M. R. *Journal of Physical Chemistry A* **2009**, *113*, 4, 690–696.

Abstract

Perfluorinated chemicals (PFCs) are distributed throughout the environment. In the case of perfluorinated alkyl carboxylates and sulfonates, they can be classified as persistent organic pollutants since they have relatively high water solubilities and are resistant to oxidation. With this in mind, we report on the reductive defluorination of perfluorobutanoate, PFBA ($C_3F_7CO_2^-$), perfluorohexanoate, PFHA ($C_5F_{11}CO_2^-$), perfluorooctanoate, PFOA ($C_7F_{15}CO_2^-$), perfluorobutane sulfonate, PFBS ($C_4F_9SO_3^-$), perfluorohexane sulfonate, PFHS ($C_6F_{13}SO_3^-$), and perfluorooctane sulfonate, PFOS ($C_8F_{17}SO_3^-$), by aquated electrons, e_{aq}^-, that are generated from the UV photolysis (λ = 254 nm) of iodide. The ionic headgroup ($-SO_3^-$ vs. $-CO_2^-$) has a significant effect on the reduction kinetics and extent of defluorination (F-Index; $-[F^-]_{produced}/[PFC]_{degraded}$). Perfluoroalkylsulfonate reduction kinetics and the F-index increase linearly with increasing chain length. In contrast, perfluoroalkylcarboxylate chain length appears to have a negligible effect on the observed kinetics and the F-index. H/F ratios in the gaseous fluoroorganic products are consistent with measured F-indexes. Incomplete defluorination of the gaseous products suggests a reductive cleavage of the ionic headgroup occurs before complete defluorination. Detailed mechanisms involving initiation by aquated electrons are proposed.

Introduction

Fluorinated chemicals (FCs), such as fluorotelomer alcohols, partially fluorinated amphiphiles, perfluoroalkyl carboxylates, and perfluoroalkylsulfonates, have been widely used for water-proofing textiles, as protective coatings on metals, in aqueous film-forming foams (AFFFs), in semi-conductor etching, and as lubricants. Atmospheric oxidation[1,2] and bio-transformation[3,4] can convert partially fluorinated chemicals into environmentally persistent perfluorochemicals (PFCs). For example, perfluorooctane sulfonate (PFOS) and perfluorooctanoate (PFOA) have been detected globally in surface waters[5,6] due to atmospheric[7] and oceanic transportation[8].

Perfluorochemicals are chemically inert due to relatively high organic bond strengths (e.g., 413.0 kJ/mol for $F_3C\text{-}CF_3$; 530.5 kJ/mol for $F\text{-}C_2F_5$)[9] and fluorine's electronegativity making them resistant to conventional advanced oxidation processes (AOPs)[10–13]. For example, hydroxyl radical ($^{\bullet}OH$) with a reduction potential of $E° = 2.73$ V[14] reacts with a typical hydrocarbon octanoate with a second-order rate constant that is $>10^9\ M^{-1}s^{-1}$ [15], however, the corresponding second-order rate constants, when the compounds are perfluorinated, have an upper limit of $< 10^5\ M^{-1}s^{-1}$ (e.g., PFOA and PFOS)[16]. Direct electron transfer oxidation processes (e.g., $S_2O_8^{2-}$/UV[13] and $PW_{12}O_{40}^{3-}$/UV[12]) and aqueous pyrolysis (i.e., sonolysis)[17,18] have shown to be more effective for PFC remediation. Perfluorocarboxylate reaction rate constants with sulfate radical ($SO_4^{\bullet -}$) are estimated to be on the order of $10^4\ M^{-1}s^{-1}$ [19,20.] At this level, the reaction rate constants are orders of magnitude lower than the sulfate radical constants with hydrocarbons[21].

Reductive remediation of perfluorocarboxylates and perfluorosulfonates is feasible[22–24]. For example, PFOS and PFHS can be reduced by elemental iron (Fe(0), E = - 0.447 V)[14] in water under extreme conditions (350 °C, 20 MPa)[23,24]. Aromatic[25,26], benzylic[27], olefinic[28,29], and tertiary[30–32] fluoroorganics readily undergo reductive defluorination by chemical and electrochemical methods. Studies on linear fluorochemicals containing only secondary[20] and primary[33] C-F bonds are limited due to low ($E < -2.7$ V) reduction potentials[34,35]. Reductive fluoride elimination is influenced by a number of chemical properties, such as C-F bonding character (e.g., σ vs. π character)[26], electron density[36], redox potential[35], anion radical stability[25], ionic head group[16], $–(CF_2)_n–$ chain length[20], and electron-donating reagent strength[37]. The activation energies of aqueous electron reactions with halo-organics are invariable and small (6 to 30 kJ/mol) due to tunneling effects[38]. However, fluoroorganic reduction rates are lower than other organohalogens since fluorine has no low-lying vacant d-orbital to accept an electron. Low PFC water solubility has limited most reductive defluorination studies to organic solvents[39].

A systematic study on the reductive remediation of aqueous PFCs ($C_3F_7CO_2^-$, $C_5F_{11}CO_2^-$, $C_7F_{15}CO_2^-$, $C_4F_9SO_3^-$, $C_6F_{13}SO_3^-$, and $C_8F_{17}SO_3^-$) has yet to be completed. We here utilize the aquated electron (e_{aq}^-, $E°_{aq/e} = - 2.9$ V), a powerful reductant, to decompose a number of perfluoroalkyl carboxylates and perfluoroalkyl sulfonates of varying chain (hydrophobic tail) length (e.g., C3 to C8). Aquated electrons are generated from UV-photolysis of aqueous iodide solutions via charge-transfer-to-solvent (CTTS) states[40]. The kinetics and mechanism of aqueous PFC reduction is significantly affected by ionic headgroup speciation and fluorinated tail length.

Experimental Details

Perfluorooctanoate (PFOA: $C_7F_{15}CO_2NH_4$, 3M), perfluorohexanoate (PFHA: $C_5F_{11}CO_2H$, > 97%, Fluka), perfluorobutanoate (PFBA: $C_3F_7CO_2H$, > 98%, Aldrich), perfluorooctane sulfonate (PFOS: $C_8F_{17}SO_3K$, 3M), perfluorohexane sulfonate (PFHS: $C_6F_{13}SO_3K$, > 98%, Fluka), and perfluorobutane sulfonate (PFBS: $C_4F_9SO_3K$, 3M Company) were used as received. PFC stock solutions were prepared to be 500 mg/L and the pH was adjusted to between 6 and 8 with HCl or NH_4OH. A 1 mol/L KI (Fisher) aqueous stock solution was freshly prepared every week and stored in the dark.

PFC and KI stock solutions were diluted with Milli-Q water to 30 mL. Photolysis was completed in a Pyrex glass reactor with a quartz window and irradiated with 254 nm light source (UVP, 8 W). Argon or air was continuously purged through the aqueous solution or through the headspace. A 0.5 mL sample aliquot was taken at different time points during photolysis, and if necessary, diluted prior to analysis. The incident photon flux was determined to be $5.17(\pm 0.06) \times 10^{-5}$ mol L^{-1} min^{-1} by iodide/iodate actinometry using the intrinsic quantum yield of iodide/iodate as a reference[38].

Initial PFC and possible aqueous-phase intermediate analysis was completed by HPLC-MS (Agilent 1100 LC and Agilent Ion Trap) with a Betasil C18 column (Thermo-Electron) of dimensions 2.1 mm ID, 100 mm length and 5 μm-particle size. A 2 mM aqueous ammonium acetate:methanol gradient mobile phase at a flow rate of 0.3 mL min^{-1} was used for separation. The samples were analyzed by the MS/MS (Agilent, MSD Trap) in negative mode monitoring for the molecular ions of PFOS (m/z = 499), PFHS (m/z = 399), and PFBS (m/z = 299), and decarboxylated ions of PFOA (m/z = 369), PFHA (m/z = 269), and PFBA (m/z = 169). The nebulizer gas pressure was 40 PSI, drying gas flow rate and temperature were 9 L min^{-1} and 325 ºC, the capillary voltage was set at + 3500 V and the skimmer voltage was – 15 V. HPLC analytical procedures are detailed elsewhere[18].

Ion chromatography (Dionex DX-500) was used for the analysis of fluoride and other ionic intermediates. 0.5 mL aliquots were transferred from the reactor to disposable PolyVial sample vials (PolyVial) and sealed with filter caps (PolyVial) and loaded onto an AS-40 autosampler. The 0.5 ml sample was injected and anions were separated on an IonPac AS11-HC anion exchange column and quantified by conductivity measurement.

The gaseous fluorointermediates produced were analyzed by GC-MS. The reactor headspace was continuously purged with argon. The purge gas containing the reaction intermediates was circulated over a thermal desorption tube (CarboTrap, Supelco) to adsorb the intermediates. After completion of the reaction, the purge gas was turned off and the tubes were sealed to atmosphere. GC-MS analysis consisted of thermal desorption of the intermediates from the tube (OI Analytical), and analysis of the desorbed gases by GC-MS (Agilent 6890 GC and 5973 MSD).

Results and Discussion

Figure 5.1 shows the time course for the reductive decomposition of PFOS and PFOA during the photolysis ($\lambda = 254$ nm) of an aqueous iodide solution in the presence of argon and air ($[\text{PFOS}]_i = 0.20\ \mu\text{M}$, $[\text{PFOA}]_i = 0.24\ \mu\text{M}$, $[\text{I}^-]_i = 10$ mM). The quantum yield for the generation of aquated electrons from iodide photolysis at 248 nm (eq. 5.1) is 28%[39]. In the presence of air, PFOS and PFOA are degraded (Figure 5.1) due to the rapid reaction ($k_3 = 1.9\times10^{10}\ \text{M}^{-1}\ \text{s}^{-1}$)[15] of the aquated electron with dissolved oxygen (~ 0.2 mM) (eq. 5.3).

$$\text{I}^- + h\nu \rightarrow \text{I}^{-*}_{\text{CTTS}} \rightarrow \text{I}^\bullet + \text{e}^-_{\text{aq}} \qquad (5.1)$$

$$e^-_{aq} + I^\bullet \rightarrow I^- \tag{5.2}$$

$$e^-_{aq} + O_2 \rightarrow O_2^- \tag{5.3}$$

$$e^-_{aq} + PFOX^- \rightarrow PFOX^{\bullet 2-} \tag{5.4}$$

However, in the presence of Ar (i.e., in the absence of air) PFOS and PFOA initial decomposition (eq. 5.4, where X = S and A for sulfonate and carboxylate, respectively) follows pseudo-first-order kinetics. Under these conditions, the rate of PFOS reduction is two times greater than that of PFOA ($k_{app}^{-PFOS} = 6.5 \times 10^{-3}$ min^{-1}; $k_{app}^{-PFOA} = 2.9 \times 10^{-3}$ min^{-1}). The relative photoreduction rates ($k_{app}^{-PFOS} / k_{app}^{-PFOA}$) are consistent with those observed in pulse radiolysis[16] where k_4^{-PFOS} and k_4^{-PFOA} for reduction by aquated electrons are reported to be 7.3×10^7 M^{-1} s^{-1} and 5.1×10^7 M^{-1} s^{-1}, respectively. A more recent laser flash photolysis study[20] reported $k_4^{-PFOA} = 1.7 \times 10^7$ M^{-1} s^{-1}.

The quantum yields for the photoreduction of PFOS and PFOA are 11.8×10^{-4} and 6.4×10^{-4}, respectively. The relatively low quantum yields (~ 0.1%) indicate that there are quenching reactions for aquated electrons. Photodetachment of an aquated electron produces iodine atom ($I^\bullet$, eq. 5.1). $I^\bullet$ complexes with a neighboring iodide forming the diiodide radical anion (I_2^-, eq. 5,5') with an equilibrium constant, $K_5 > 1.2 \times 10^4$. The complexation is diffusion controlled and $[I^-]_{ss} >> [e^-]_{ss}$ such that $k_5 >> k_2$ and $I_2^-/I^\bullet = 120$. The diffusion-controlled reaction ($k_6 = 3.2 \times 10^9$ M^{-1} s^{-1}) between two I_2^- molecules (eq. 5.6) produces triiodide (I_3^-) and I^-.

$$I^\bullet + I^- \longleftrightarrow I_2^- \tag{5.5, 5.5'}$$

$$I_2^- + I_2^- \rightarrow I_3^- + I^- \tag{5.6}$$

Aquated electron quenching may occur via $I^{\bullet}$ carriers (eq. 5.7) or by way of hydrogen production (eq. 5.8).

$$e^-_{aq} + I_2^{\bullet -}/I_3^- \rightarrow I^-/I_2^{\bullet -} + I^- \tag{5.7}$$

$$e^-_{aq} + H^+ \rightarrow H^{\bullet};\ H^{\bullet} + e^-_{aq} + H^+ \rightarrow H_2 \tag{5.8}$$

As shown in Figure 5.2a, the steady-state triiodide concentration, $[I_3^-]_{ss}$, is almost negligible in aqueous solutions without PFOX (i.e., in the absence of dissolved oxygen) and increases to micromolar levels upon addition of PFOX, suggesting the $I^{\bullet}$ carrier quenching is the predominant mechanism. Minimal pH changes during the reactions (Figure 5.2b) is consistent with $I^{\bullet}$ carrier quenching. $H^{\bullet}$, intermediates in eq. 5.8, may also be quenched by $I^{\bullet}$ carriers. In particular in the absence of PFOX and oxygen, pH rises up to 10–11 immediately after light irradiation, probably due to proton consumption by e_{aq}^- (eq. 5.8). The PFOA photolysis also continuously increases the pH, whereas the pH at the PFOS photolysis is decreased soon after initial increase. The bell-shaped pH change is ascribed to the initial proton consumption and the post-release of fluoride ion (i.e., pK_a (HF) = 3.45). This indicates that the pH changes are primarily caused by the fluoride production and could be used as an indicator of the defluorination.

Reaction of the initial perfluorinated alkyl carboxylate or sulfonate with e_{aq}^- yields the corresponding radical anion ($C_nF_{2n+1}X^{\bullet 2-}$; n = 8, X = SO_3 for $PFOS^{\bullet 2-}$; n = 7, X = CO_2 for $PFOA^{\bullet 2-}$, eq. 5.4). The radical anion will quickly decompose via fluoride elimination[27,41] to yield the perfluoroalkyl radical ($C_nF_{2n}X^{\bullet -}$, eq. 5.9).

$$C_nF_{2n+1}X^{\bullet 2-} \rightarrow C_nF_{2n}X^{\bullet -} + F^- \tag{5.9}$$

$$C_nF_{2n}X^{\bullet -} + e^-_{aq} \rightarrow C_nF_{2n}X^{2-} \tag{5.10}$$

$$C_nF_{2n}X^{\bullet -} + I^{\bullet} \underset{hv}{\rightleftarrows} C_nF_{2n}IX^{-} \qquad (5.11, 5.11')$$

$$C_nF_{2n}IX^{-} + e^{-}_{aq} \rightarrow C_nF_{2n}X^{\bullet -} + I^{-} \qquad (5.12)$$

$$C_nF_{2n}X^{2-} \rightarrow C_nF_{2n-1}X^{-} + F^{-} \qquad (5.13)$$

$$C_nF_{2n}X^{2-} + H^{+}/H_2O \rightarrow C_nF_{2n}HX^{-} \qquad (5.14)$$

$$C_nF_{2n}X^{\bullet -} + H^{\bullet} \rightarrow C_nF_{2n}HX^{-} \qquad (5.15)$$

The electrophilic perfluoroalkyl radicals[42–44] may react further with e_{aq}^{-} to yield carbanions ($C_nF_{2n}X^{2-}$, eq 10) or with $I^{\bullet}$ carriers (i.e., $I^{\bullet}$, $I_2^{\bullet -}$, $I_3^{\bullet -}$) to yield the perfluoroalkyl iodide carboxylate or sulfonate ($C_nF_{2n}IX^{-}$, eq. 5.11). The perfluoroalkyl iodide carboxylates and sulfonates will be converted back to perfluoroalkyl radicals via photolytic homolysis of the C-I bond (eq 5.11') or via reaction with e^{-}_{aq} to yield the radical and I^{-} (eq. 5.12)[45]. In organic solvents, the carbanion intramolecularly defluorinates to give an olefin (eq 5.13).[27,35] However, in the presence of water, the carbanion, which is a strong base, will be protonated. An overall H/F exchange may also occur via reaction of a fluoroalkyl radical anion ($C_nF_{2n}X^{\bullet -}$) with an $H^{\bullet}$ (eq. 5.15). If an H/F exchange product retains the anionic carboxylate or sulfonate terminal group, it will remain in the aqueous phase and proceed through sequential H/F exchanges. Subsequent e_{aq}^{-} reductions with partially defluorinated intermediates ($C_nF_{2n}IX^{-}$, $C_nF_{2n-1}X^{-}$ or $C_nF_{2n}HX^{-}$) should be faster than the initial defluorination step[27].

A systematic study of perfluorochemical decomposition was completed by reducing the shorter-chained PFCs (PFHS, PFBS, PFHA, and PFBA, where H = hexane and B = butane) under the same photolytic conditions. Figure 5.3a and b show the time-dependent reactions of all six PFCs with the aquated electron. The three perfluoroalkyl carboxylates have similar pseudo-first-order degradation rates, $k_{app}^{-PFOA} \approx k_{app}^{-PFHA} \approx k_{app}^{-PFBA} \approx 1.3 \times 10^{-3}$ min^{-1} (Figure 5.3a), and the carboxylate kinetics are plotted on the sulfonate curve as a dashed line for comparison (Figure 5.3b). In contrast, the perfluoroalkyl sulfonates kinetics are dependent on chain length, $k_{app}^{-PFOS} > k_{app}^{-PFHS} > k_{app}^{-PFBS}$ and the rate decreases with decreasing chain length (3.0×10^{-3}, 1.2×10^{-3}, and 4.0×10^{-4} min^{-1} for PFOS, PFHS, and PFBS, respectively). Accordingly, quantum yields for the degradation of the carboxylates are independent of chain length, i.e., PFBA (7.05×10^{-4}) ≈ PFHA (6.94×10^{-4}) ≈ PFOA (6.36×10^{-4}), whereas those for the sulfonates are chain length dependent, i.e., PFOS (11.8×10^{-4}) > PFHS (5.71×10^{-4}) > PFBS (2.41×10^{-4}) (Table 5.1).

The aqueous electron-mediated reduction of perfluorochemicals eventually eliminates fluoride (F^-) and thus fluoride measurements give insight into the overall mechanism and extent of reduction. The time-dependent F^- production during degradation of the perfluorocarboxylates and the perfluorosulfonates are shown in Figures 5.4a and b, respectively. Similar to the decomposition kinetics, the perfluorocarboxylate F^- production has no chain-length dependence ($[F^-] = 5 \sim 12$ μM at 2.5 h-photolysis), whereas the perfluorosulfonate F^- production is dependent on chain length; F^- production decreases with decreasing chain length ($[F^-]$ = 58, 23, and 5 μM at 2.5 h-photolysis for PFOS, PFHS, and PFBS, respectively). Alternatively, the F^- yield can be evaluated using the *F-index* (i.e., $-[F^-]_{produced}/[PFC]_{degraded}$). F-indices for all PFCs are observed to grow linearly over the course of the reaction. For the three carboxylates, the F-index is between 1 and 2, suggesting a reductive mechanism independent of chain length. For the sulfonates, the F-index is related to the number of carbons in the hydrophobic tail, with approximately one defluorination per carbon (i.e., 9, 6, and 3 for PFOS, PFHS, and PFBS, respectively). In both cases, defluorination is incomplete, suggesting loss of partially defluorinated species to the gas phase, which implies loss of the sulfonate or carboxylate ionic headgroup prior to complete defluorination.

The data from Figures 5.3 and 5.4 has been compiled in Figure 5.5. k_{app}^{-PFC}, and the F-index for all six PFCs are plotted as a function of fluorocarbon chain length. It appears that the carboxylates have a similar degradation mechanism since both the kinetics and F-indices show no chain-length dependence. Minimal defluorination suggests that the carboxylate group is lost shortly after the initial reduction or simultaneously with the reduction. In the case of hydrocarbon carboxylates,[46] the aquated electron-mediated reduction occurs at the carbonyl group with subsequent loss of HO^- and CO, yielding an alkyl radical, or in this case a fluoroalkyl radical (R_F•, eq. 5.16).

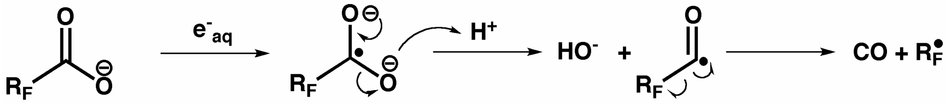

(5.16)

An initial defluorination may be required at the alpha carbon to the carbonyl to favor the decarboxylation mechanism. A similar mechanism may be active for the desulfonation of the perfluoroalkyl sulfonates. In contrast to the carboxylates, a larger number of reductive defluorinations is required prior to loss of the ionic headgroup, suggesting initial defluorination occurs at carbons away from the sulfonate group.

Gaseous intermediates produced during PFC reduction were trapped in thermal desorption tubes and analyzed by GC-MS. A number of intermediates were identified, which were composed of carbon, fluorine, hydrogen, and iodine (Figure 5.6 and Table 5.2). The perfluoroalkyl carboxylate gaseous intermediates were primarily composed of C-F bonds, consistent with F-indices. The perfluoroalkyl sulfonate intermediates had a greater degree of H/F exchange (i.e., degree of reduction), which is also consistent with F-indices for these compounds. The agreement between H/F exchange and the F-index suggests initial defluorination is primarily followed by protonation of the carbanion intermediate (eq. 5.14) or perfluororadical reaction with H-atom (eq. 5.15), with minor olefinization (eq. 5.13). It is of note that the reduction products of the perfluorinated chemicals in aprotic solvents are primarily olefins. Also, the sulfonates have a larger number of unique gaseous intermediates as compared to the carboxylates. For example, PFOS has a more diverse set of intermediates ranging from C_1 to C_8 and 3 times the total number of intermediates as PFOA (Table 5.2).

A large majority of the gases produced are iodinated and the noniodinated minority generally contains an olefin. On average, a single $I^{\bullet}$ is incorporated into a gaseous fluorointermediate suggesting partitioning out of solution quickly follows neutral fluororadical iodination. For example, the reaction of the fluoroalkyl radical ($R_F\bullet$) produced in eq. 5.16 with $I^{\bullet}$ results in a product that has a high tendency to partition into the vapor phase (eq. 5.17).

$$R_F^{\bullet} + I^{\bullet} \text{ carriers} \rightarrow R_FI_{(aq)} \rightarrow R_FI_{(g)} \tag{5.17}$$

The absence of vapor-phase intermediates with higher degrees of iodination may be due to subsequent photolytic cleavage or reduction of C-I bonds by aquated electron (eqs. 5.11' and 5.12, respectively) formed from the aqueous fluoro-intermediates. It should be noted that a C-I bond (bond strength, 209 kJ/mol) is weaker than a C-F bond (bond strength, 460 kJ/mol). In addition, perfluorooctyl iodide ($C_8F_{17}I$) is observed as the heaviest intermediate during PFOS photolysis, whereas perfluorohexyl iodide ($C_6F_{13}I$)—*not* $C_7F_{15}I$— is detected during PFOA photolysis. This suggests the presence of a transient perfluorooctyl radical ($C_8F_{17}^{\bullet}$) intermediate during PFOS photolysis and perfluorohexyl radical ($C_6F_{13}^{\bullet}$) generated from PFOA photolysis (eq. 5.17). The sulfonate elimination from an intact fluorocarbon tail is also observed during PFHS photolytic reduction (e.g., $C_6F_{13}I$, $C_6F_{12}HI$) and PFBS reduction (e.g., $C_4F_4H_4$). In addition, the loss of the carboxylate group plus a tail carbon is observed during PFHA photolysis (e.g., C_4F_9I). However, in the case of PFBA, a C_3 intermediate is detected, likely due to the altered properties as the CF_2-CF_2 chain length shortens.

In summary, the ionic head group, carboxylate vs. sulfonate, has a significant effect on the kinetics and mechanism of perfluoroalkyl surfactant reduction by aqueous electrons. The fluorocarbon tail length of the perfluorinated alkyl sulfonates significantly affects the reduction rate and extent of defluorination, implying the existence of multiple reaction sites across the fluorocarbon tail. In contrast, perfluorinated alkyl carboxylates have invariable reaction rates with aqueous electrons and similar degrees of defluorination implying a similar initial reaction site near the ionic headgroup. Ionic headgroup cleavage and loss of the subsequent neutral to the gas phase is likely cause of incomplete defluorination. Detailed studies utilizing a more quantitative intermediate analysis to better understand defluorination kinetics and mechanism are being investigated.

Figures

Figure 5.1. Pseudo-first-order plots of PFOX UV$_{254\text{ nm}}$ KI photolysis. Irradiation of an aqueous KI-PFOX solution in the presence and absence of oxygen (i.e., air vs. Ar). PFOS and PFOA are identically 100 ppb, i.e., $[\mathrm{PFOA}]_0 = 0.24$ μM; $[\mathrm{PFOS}]_0 = 0.20$ μM; and $[\mathrm{KI}]_0 = 10$ mM

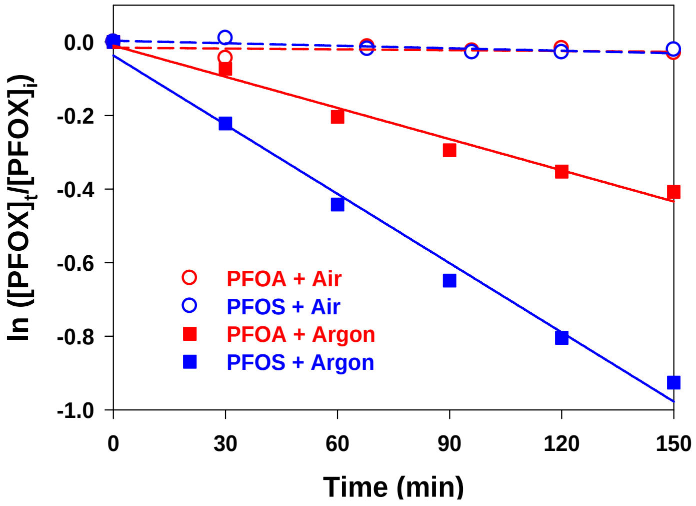

Figure 5.2. I_3^- production and pH change during PFOX UV-KI photolysis. A) triiodide production, and B) pH change during the photolysis of aqueous iodide-PFOX solutions. $[PFOS]_0$ = 20 μM; $[PFOA]_0$ = 24 μM; $[KI]_0$ = 10 mM; λ = 254 nm and in the presence of Ar

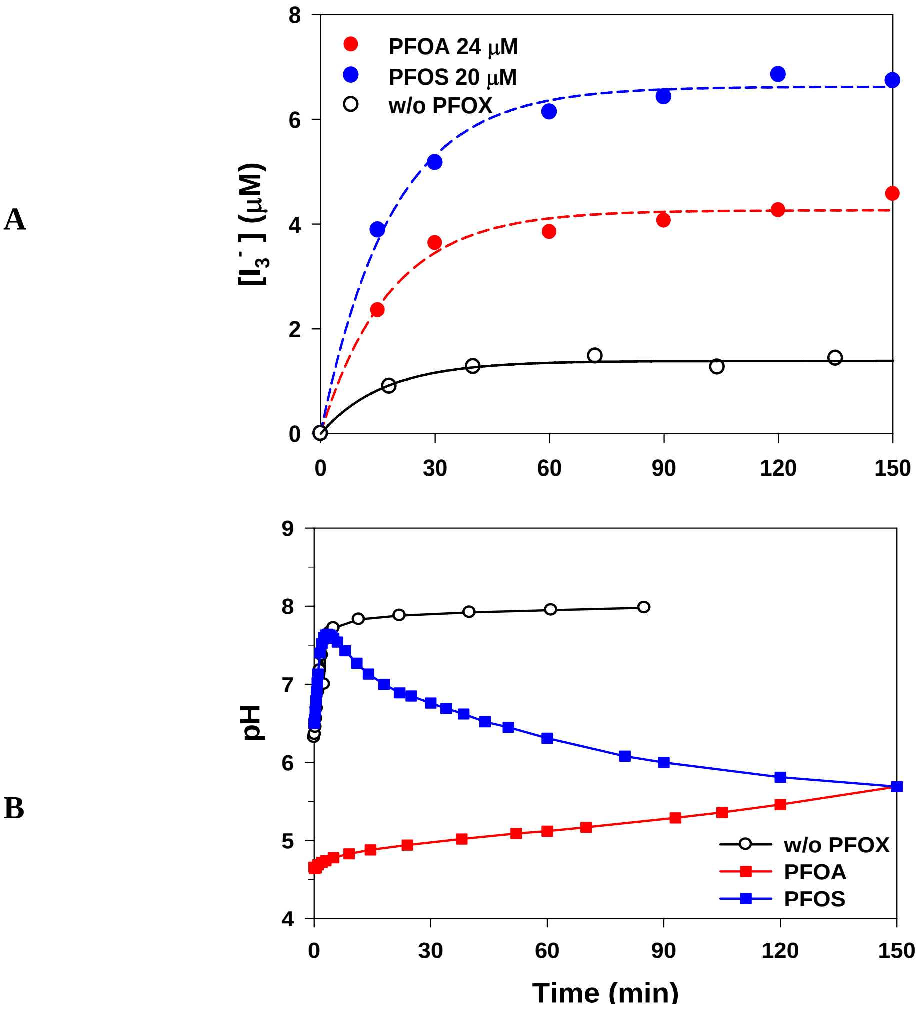

Figure 5.3. PFXA and PFXS (X = O, H, B) degradation during UV-KI photolysis. λ = 254 nm irradiation of aqueous KI solution in the presence of Ar. All PFCs are identically 10 ppm, i.e., $[PFOS]_0$ = 20 μM; $[PFHS]_0$ = 25.1 μM; $[PFBS]_0$ = 33.4 μM; $[PFOA]_0$ = 24 μM; $[PFHA]_0$ = 31.9 μM; $[PFBA]_0$ = 46.0 μM; and $[KI]_0$ = 10 mM

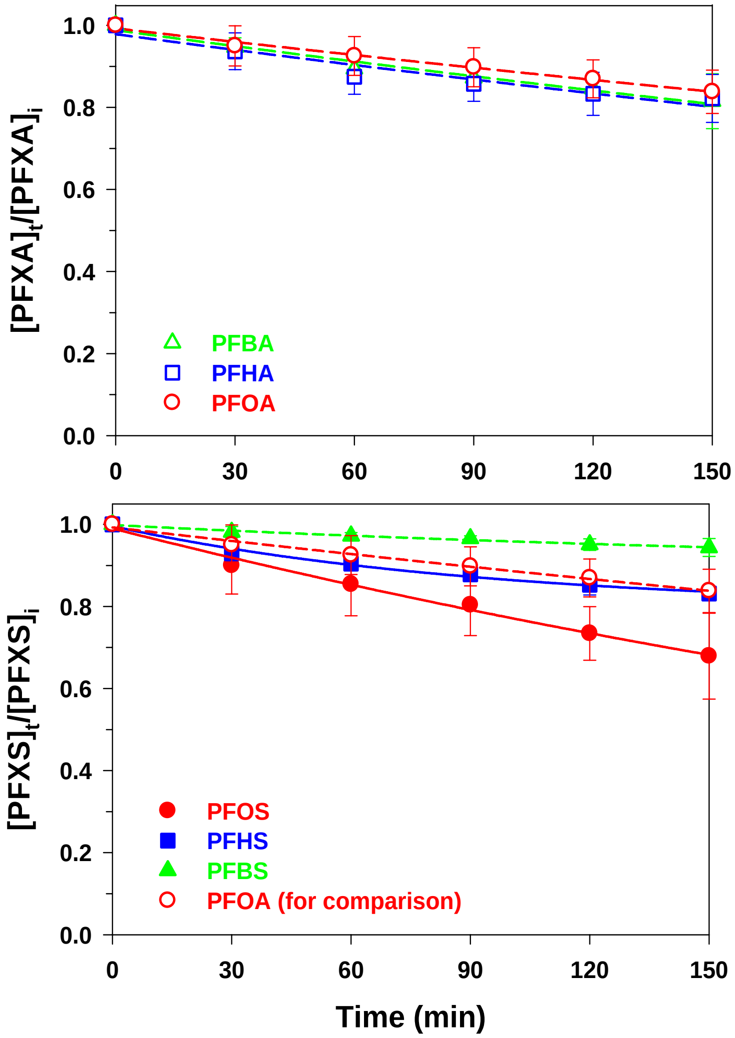

Figure 5.4. F$^-$ production during PFXA and PFXS (X = O, H, B) UV-KI photolysis. A) PFXA (X = O, H, B), and B) PFXS (X = O, H, B) photolysis. Experimental conditions are identical to those of Figure 5.3

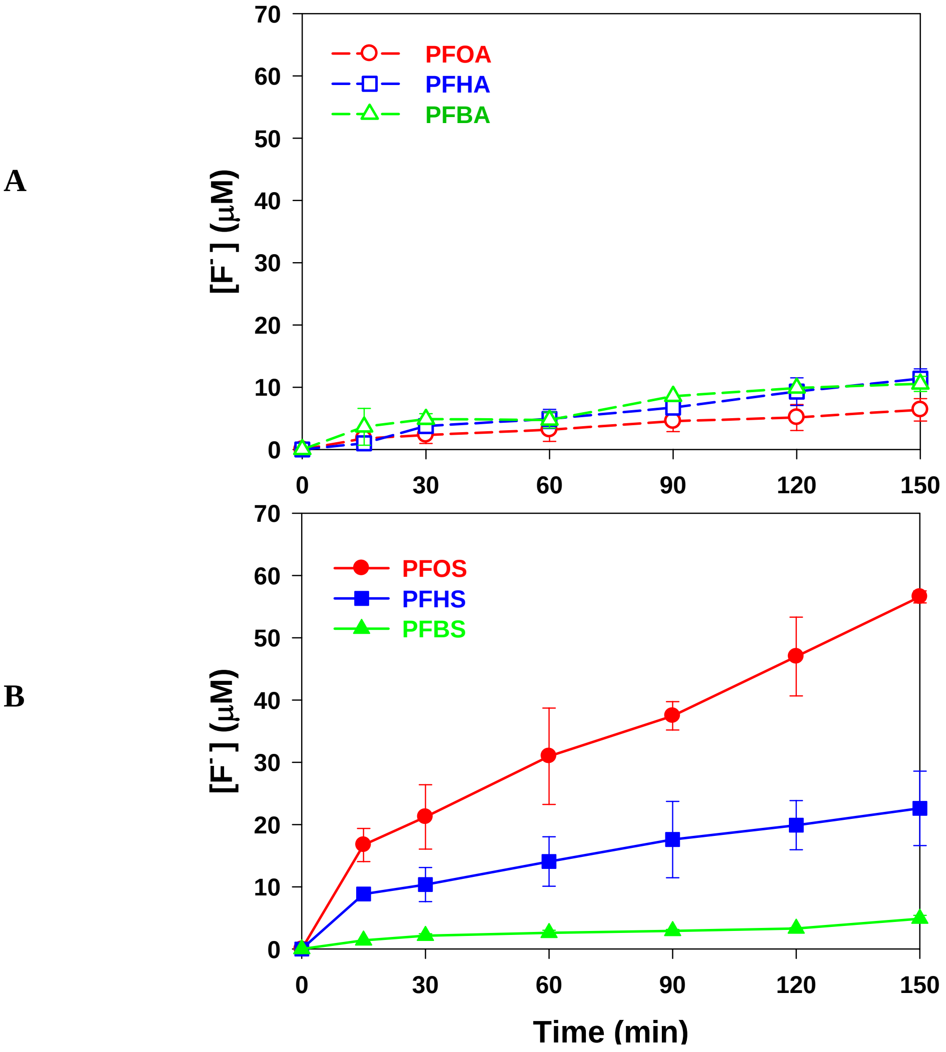

Figure 5.5. Effects of chain length on FC UV-KI degradation rates and F-index. Experimental conditions are identical to those of Figure 5.3

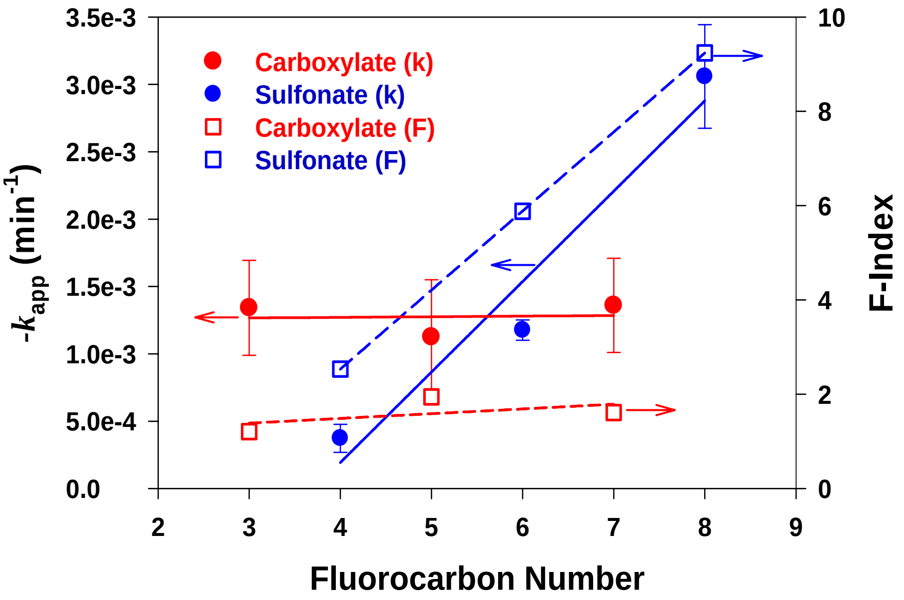

Figure 5.6. Gaseous products during PFOX UV-KI photolysis. Experimental conditions identical to those of Figure 5.3. A) Representative PFOA GC-MS Spectrum, B) Representative PFOS GC-MS

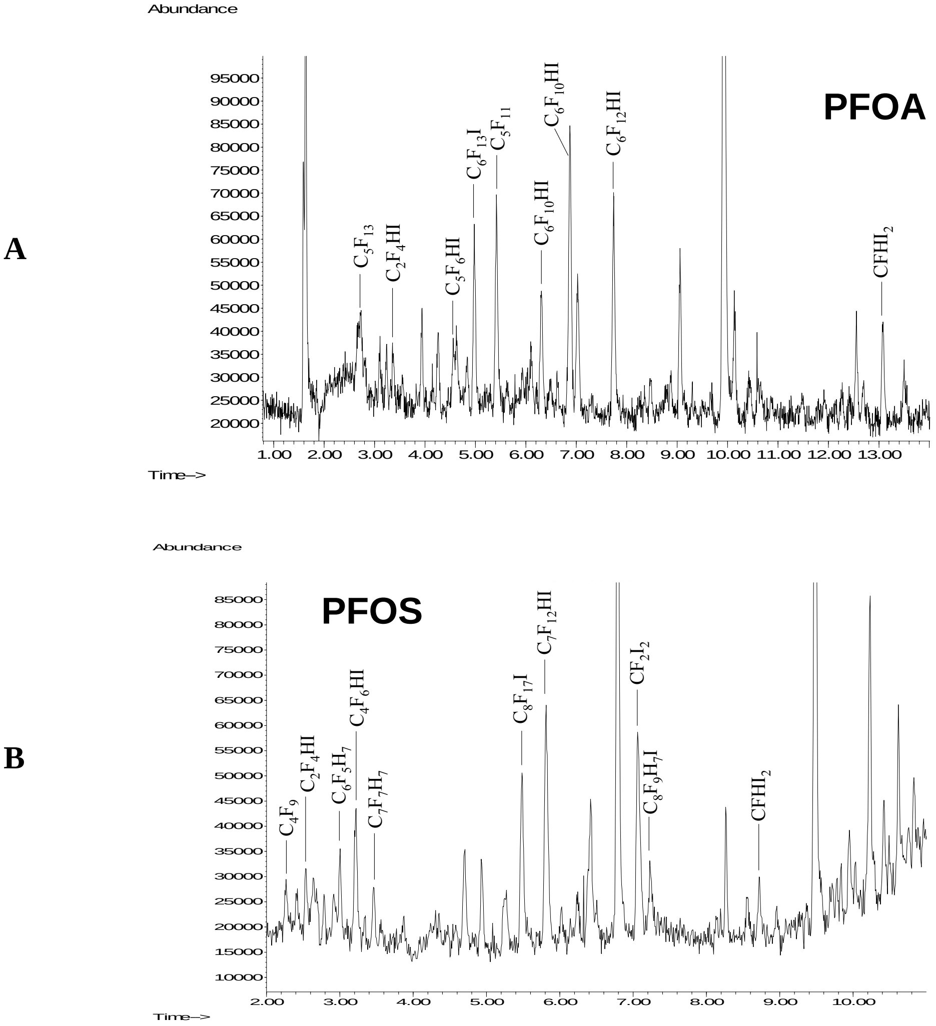

Tables

Table 5.1. Fluorochemical UV-KI photolysis kinetics and F-index. Apparent first-order rate constants, quantum yields, and F-indexes for the decomposition of perfluoroalkylcarboxylates and perfluoroalkylsulfonates by aqueous iodide photolysis[a]

PFC	Formula	k (min^{-1})	QY	F-Index[b]
PFBA	$CF_3(CF_2)_2CO_2^-$	1.3×10^{-3}	7.1×10^{-4}	1.2
PFHA	$CF_3(CF_2)_4CO_2^-$	1.1×10^{-3}	6.9×10^{-4}	1.9
PFOA	$CF_3(CF_2)_6CO_2^-$	1.4×10^{-3}	6.4×10^{-4}	1.6
PFBS	$CF_3(CF_2)_3SO_3^-$	4.0×10^{-4}	2.4×10^{-4}	2.5
PFHS	$CF_3(CF_2)_5SO_3^-$	1.2×10^{-3}	5.7×10^{-4}	5.9
PFOS	$CF_3(CF_2)_7SO_3^-$	3.0×10^{-3}	1.2×10^{-3}	9.2

a) See Figure 5.3 for detailed experimental conditions.
b) $-[F^-]_{Produced}/[PFC^-]_{Degraded}$

Table 5.2. Gaseous products during fluorochemical UV-KI photolysis. The gases are separated by carbon number and iodation

	PFBS $C_4F_9SO_3^-$		PFHS $C_6F_{13}SO_3^-$		PFOS $C_8F_{17}SO_3^-$	
#C	**Iodide**	**Non-Iodide**	**Iodide**	**Non-Iodide**	**Iodide**	**Non-Iodide**
8					C8F17I C8F9H8I C8F9H7I C8F6H3I	C8F13H4 C8F13H3
7					C7F12HI C7F9H6I	C7F7H7 C7F6H9 C7F4H10
6			C6F13I C6F12HI C6F3H8I	C6F7H5 C6F5H5		C6F5H7
5			C5F8HI C5F6HI C5F4H4I2 C5FH4I	C5F2H8	C5F7H2I C5F3HI	
4		C4F4H4	C4F6H3I C4F6HI C4F5H2I	C4F4H4	C4F6HI C4F5H2I C4H9I	C4F9 C4F4H2
3	C3F2I2 C3F2I C3FH2I C3FHI		C3F6HI		C3F6HI C3F4H3I	
2	C2FI C2H5I	C2F3H3	C2F4I2 C2F3H2I C2H5I C2H4I		C2F4HI C2F3HI2 C2H4I2 C2H3I2 C2H2I2 C2H5I	
1	CH2I2 CH3I		CF2I2 CH3I		CF2I2 CFHI2 CH2I2 CH3I	

	PFBA $C_3F_7CO_2^-$		PFHA $C_5F_{11}CO_2^-$		PFOA $C_7F_{15}CO_2^-$	
#C	**Iodide**	**Non-Iodide**	**Iodide**	**Non-Iodide**	**Iodide**	**Non-Iodide**
8						
7						
6					C6F13I C6F12HI C6F10HI	C6F5H7
5					C5F6HI	C5F13 C5F11
4			C4F9I			
3	C3F6HI			C3F9 C3F7		
2	C2F5I C2F4I2 C2F4HI C2H6I				C2F4HI	
1	CH3I		CFHI2 CH3I CH2I2		CFHI2 CH3I CH2I2	

References

(1) D'Eon, J. C.; Hurley, M. D.; Wallington, T. J.; Mabury, S. A. *Environ. Sci. Technol.* **2006**, *40*, 1862.

(2) Martin, J. W.; Ellis, D. A.; Mabury, S. A.; Hurley, M. D.; Wallington, T. J. *Environ. Sci. Technol.* **2006**, *40*, 864.

(3) Xu, L.; Krenitsky, D. M.; Seacat, A. M.; Butenhoff, J. L.; Anders, M. W. *Chem. Res. Toxicol.* **2004**, *17*, 767.

(4) Tomy, G. T.; Tittlemier, S. A.; Palace, V. P.; Budakowski, W. R.; Braekevelt, E.; Brinkworth, L.; Friesen, K. *Environ. Sci. Technol.* **2004**, *38*, 758.

(5) Scott, B. F.; Moody, C. A.; Spencer, C.; Small, J. M.; Muir, D. C. G.; Mabury, S. A. *Environ. Sci. Technol.* **2006**, *40*, 6405.

(6) Skutlarek, D.; Exner, M.; Farber, H. *Environ. Sci. Pollut. Res.* **2006**, *13*, 299.

(7) Shoeib, M.; Harner, T.; Vlahos, P. *Environ. Sci. Technol.* **2006**, *40*, 7577.

(8) Yamashita, N.; Kannan, K.; Taniyasu, S.; Horii, Y.; Petrick, G.; Gamo, T. *Mar. Pollut. Bull.* **2005**, *51*, 658.

(9) The Science of Organic Fluorochemistry. Office of Pollution Prevention and Toxics; Docket AR226-0547; U.S. Environmental Protection Agency: Washington, D.C., 1999; p. 12.

(10) Schroder, H. F.; Meesters, R. J. W. *J. Chromatogr. A* **2005**, *1082*, 110.

(11) Dillert, R.; Bahnemann, D.; Hidaka, H. *Chemosphere* **2007**, *67*, 785.

(12) Hori, H.; Hayakawa, E.; Einaga, H.; Kutsuna, S.; Koike, K.; Ibusuki, T.; Kiatagawa, H.; Arakawa, R. *Environ. Sci. Technol.* **2004**, *38*, 6118.

(13) Hori, H.; Yamamoto, A.; Hayakawa, E.; Taniyasu, S.; Yamashita, N.; Kutsuna, S. *Environ. Sci. Technol.* **2005**, *39*, 2383.

(14) Wardman, P. *J. Phys. Chem. Ref. Data* **1989**, *18*, 1637.

(15) Buxton, G. V.; Greenstock, C. L.; Helman, W. P.; Ross, A. B. *J. Phys. Chem. Ref. Data* **1988**, *17*, 513.

(16) Szajdzinska-Pietek, E.; Gebicki, J. L. *Res. Chem. Intermed.* **2000**, *26*, 897.

(17) Moriwaki, H.; Takagi, Y.; Tanaka, M.; Tsuruho, K.; Okitsu, K.; Maeda, Y. *Environ. Sci. Technol.* **2005**, *39*, 3388.

(18) Vecitis, C. D.; Park, H.; Cheng, J.; Mader, B. T.; Hoffmann, M. R. *J. Phys. Chem. A* **2008**, *112*, 4261.

(19) Kutsuna, S.; Hori, H. *Int. J. Chem. Kinet.* **2007**, *39*, 276.

(20) Huang, L.; Dong, W. B.; Hou, H. Q. *Chem. Phys. Lett.* **2007**, *436*, 124.

(21) Neta, P.; Huie, R. E.; Ross, A. B. *J. Phys. Chem. Ref. Data* **1988**, *17*, 1027.

(22) Yamamoto, T.; Noma, Y.; Sakai, S. I.; Shibata, Y. *Environ. Sci. Technol.* **2007**, *41*, 5660.

(23) Hori, H.; Nagaoka, Y.; Yamamoto, A.; Sano, T.; Yamashita, N.; Taniyasu, S.; Kutsuna, S.; Osaka, I.; Arakawa, R. *Environ. Sci. Technol.* **2006**, *40*, 1049.

(24) Hori, H.; Nagaoka, Y.; Sano, T.; Kutsuna, S. *Chemosphere* **2008**, *70*, 800.

(25) Shoute, L. C. T.; Mittal, J. P.; Neta, P. *J. Phys. Chem.* **1996**, *100*, 3016.

(26) Shoute, L. C. T.; Mittal, J. P.; Neta, P. *J. Phys. Chem.* **1996**, *100*, 11355.

(27) Combellas, C.; Kanoufi, F.; Thiebault, A. *J. Phys. Chem. B* **2003**, *107*, 10894.

(28) Corvaja, C.; Farnia, G.; Formenton, G.; Navarrini, W.; Sandona, G.; Tortelli, V. *Journal of Physical Chemistry* **1994**, *98*, 2307.

(29) Watson, P. L.; Tulip, T. H.; Williams, I. *Organometallics* **1990**, *9*, 1999.

(30) Burdeniuc, J.; Chupka, W.; Crabtree, R. H. *J. Am. Chem. Soc.* **1995**, *117*, 10119.

(31) Macnicol, D. D.; Robertson, C. D. *Nature* **1988**, *332*, 59.

(32) Scherer, K. V.; Ono, T.; Yamanouchi, K.; Fernandez, R.; Henderson, P.; Goldwhite, H. *J. Am. Chem. Soc.* **1985**, *107*, 718.

(33) Anbar, M.; Hart, E. J. *J. Phys. Chem.* **1965**, *69*, 271.

(34) Pud, A. A.; Shapoval, G. S.; Kukhar, V. P.; Mikulina, O. E.; Gervits, L. L. *Electrochim. Acta* **1995**, *40*, 1157.

(35) Marsella, J. A.; Gilicinski, A. G.; Coughlin, A. M.; Pez, G. P. *J. Org. Chem.* **1992**, *57*, 2856.

(36) Chen, X. D.; Lemal, D. M. *J. Fluor. Chem.* **2006**, *127*, 1158.

(37) Ono, T.; Fukaya, H.; Hayashi, E.; Saida, H.; Abe, T.; Henderson, P. B.; Fernandez, R. E.; Scherer, K. V. *J. Fluor. Chem.* **1999**, *97*, 173.

(38) Rahn, R. O.; Stephan, M. I.; Bolton, J. R.; Goren, E.; Shaw, P.-S.; Lykke, K. R. *Photochem. Photobiol.* **2003**, *78*, 146.

(39) Sauer, M. C.; Crowell, R. A.; Shkrob, I. A. *J. Phys. Chem. A* **2004**, *108*, 5490.

(40) Lehr, L.; Zanni, M. T.; Frischkorn, C.; Weinkauf, R.; Neumark, D. M. *Science* **1999**, *284*, 635.

(41) Andrieux, C. P.; Combellas, C.; Kanoufi, F.; Saveant, J. M.; Thiebault, A. *J. Am. Chem. Soc.* **1997**, *119*, 9527.

(42) Avila, D. V.; Ingold, K. U.; Lusztyk, J.; Dolbier, W. R.; Pan, H. Q. *J. Am. Chem. Soc.* **1993**, *115*, 1577.

(43) Avila, D. V.; Ingold, K. U.; Lusztyk, J.; Dolbier, W. R.; Pan, H. Q.; Muir, M. *J. Am. Chem. Soc.* **1994**, *116*, 99.

(44) Zhang, L.; Dolbier, W. R.; Sheeller, B.; Ingold, K. U. *J. Am. Chem. Soc.* **2002**, *124*, 6362.

(45) Dolbier, W. R. *Chem. Rev.* **1996**, *96*, 1557.

(46) Hart, E. J.; Anbar, M. *The Hydrated Electron*; Wiley-Interscience: New York, 1970.

Chapter 6

Mass Spectrometric Detection of Oxidation Products and Intermediates of Aqueous Aerosol Iodide and/or Thiosulfate Reaction with Gaseous Ozone

Sections reprinted with permission from Enami, S.; Vecitis, C. D.; Cheng, J.; Hoffmann, M. R.; Colussi, A. J. *Journal of Physical Chemical A* **2007**, *111*, 50, 13032–13037.

Abstract

The intermediates ISO_3^- (m/z = 207) and $IS_2O_3^-$ (m/z = 239) generated in aqueous ($NaI/Na_2S_2O_3$) microdroplets traversing dilute O_3 gas plumes are detected via online electrospray mass spectrometry within ~ 1 ms, and their stabilities gauged by collisionally induced dissociation. The simultaneous detection of anionic reactants and the $S_2O_6^{2-}$, HSO_4^-, IO_3^-, and I_3^- products, as a function of experimental conditions, provides evidence for air-water interfacial reactions, as compared to strictly bulk aqueous reactions. For example, O_3(aq) reacts ~ 3 times faster with I^- than with $S_2O_3^{2-}$ in bulk solution; only $S_2O_3^{2-}$ is significantly depleted in the interfacial layers of $[I^-]/[S_2O_3^{2-}] = 10$ microdroplets below $[O_3(g)]$ ~ 50 ppm. This suggests that either interfacial kinetics are at variance with bulk aqueous kinetics and/or I^- mediates that ozone oxidation of $S_2O_3^{2-}$.

Introduction

Atmospheric aerosols absorb and scatter solar radiation[1] and mediate important chemical processes[2,3,4,5]. For example, atmospheric SO_2 and NO_x can be oxidized in the gas-phase, but acid rain results from their faster processing in aqueous aerosol droplets[6,7,8.] However, the analysis of gas-aerosol reaction mechanisms and kinetics is assumed to follow concepts derived from studies performed in bulk aqueous solution[9,10]. However, the possibility of unique reaction mechanisms and enhanced chemical kinetics of air-water interfacial reactions, as well as the reduced water activity in atmospheric aerosol particles, should prevent the simple extrapolation of bulk data to the aerosol phase. The minimal examination of reactions specific to the air-water interface is a result of the technical difficulties associated with producing radially small aerosol particles under atmospherically relevant conditions in the laboratory and probing their chemical transformations while suspended in reactive atmospheres. Most studies, with a few exceptions[11,12,13], have monitored the uptake of reactive gases by stationary trains of ~10– 100 μm droplets[14] that would have exceedingly large settling velocities (~1 km day^{-1}), short residence times (i.e., negligible number densities in the atmosphere), and relatively low surface-area-to-volume ratios[15].

Here, we report experiments in which the chemical composition of aqueous droplets (r = 0.5 to 3.0 microns) undergoing chemical reaction with a reactive gas is directly monitored by electrospray mass spectrometry (ES-MS) in ~ 1–10 ms time frames. The fast oxidations of I^-(aq) and $S_2O_3^{2-}$(aq) by O_3(g), which proceed at nearly diffusionally controlled rates in bulk solution[16], are studied by spraying droplets across O_3/air gas plumes. We detect and quantify anion reactants and products, as well as the previously postulated short-lived reaction intermediates ISO_3^- and $IS_2O_3^-$. Our results show that this technique is capable of tracking chemical reactions in the condensed phase during fast aerosol-gas reactions. ES-MS has been previously used for online monitoring of thermal, electrochemical and photochemical reactions[17,18,19,20,21,22,23,24,25,26,27,28].

Experimental

The experimental setup is shown in Figures 6.1a and b. Aqueous solutions were pumped (50 μL min^{-1}) into the reaction chamber through a grounded stainless steel needle injector (~ 50 μM radius bore)[29]and pneumatically sprayed by means of coaxially flowing nebulizer gas. The difference between the exit velocities of the liquid jet (10.6 cm s^{-1}) and nebulizer gas (2.65×10^4 cm s^{-1}) is so large that the drag imposed on the liquid breaks it apart into micrometer size droplets. The terminal velocities of the microdroplets produced are ~ 10^2–10^3 cm s^{-1},[30] which lead to transit times around 1 to 10 ms across the ~ 0.5 cm wide ozone plume. The droplets are produced by fragmentation of electrically neutral solutions from a grounded injector, and are charged via statistical fluctuations that scale with $(\text{drop size})^{-1/2}$ [31]. The ensemble of spray droplets is on average neutral, but individual droplets carry charges that follow a Gaussian distribution, as expected for a random process. For example, this phenomenon is the basis of the classical oil drop experiment performed by Millikan to determine the magnitude of the elementary charge[32] and leads to the charge of sea-sprayed aerosols. The finer sea water aerosol droplets, which will remain airborne the longest after generation during bubble bursting, are reported to be negatively charged[33]. It should be emphasized that charge separation during pneumatic nebulization of liquids does not produce highly charged droplets (10 to 100 charges per droplet vs. 10,000 charges per droplet) such as those created during electrospray ionization using high-field nozzles[34]. The spray droplets eventually contract through solvent evaporation, a process regulated by ambient temperature and relative humidity, thereby increasing electrostatic repulsion among excess surface charges. In highly charged droplets, Coulomb explosions may occur, producing a distribution of smaller, charged droplets. Once charged droplets near radii on the nm scale, ion evaporation may occur, yielding hydrated, gas-phase ions[35]. Similar events will proceed in both sea-sprayed marine aerosols as they rise into the dry atmosphere, and our spray chamber as the droplets are electrostatically extracted into a high-temperature, high-flow-rate, dry-nitrogen gas stream. The drying events will generate smaller aerosols and eventually gas-phase ions whose chemical distribution is enriched in tensio- or surface active species. Thus, the ESMS technique effectively samples the interfacial layers of droplets.

Ozone was generated by flowing ultrapure O_2(g) (0.1 L/min, Air Liquide) through a commercial ozonizer (Ozone Solution), diluted tenfold with ultrapure N_2(g) (0.9 L/min) and quantified by UV absorption spectrophotometry (HP 8452) at 250 and 300 nm [absorption cross-sections $\sigma(250\ \text{nm}) = 1.1 \times 10^{-17}$, $\sigma(300\ \text{nm}) = 3.9 \times 10^{-19}$ $\text{cm}^2\ \text{molecule}^{-1}$ at 298 K][36] prior to entering the reaction chamber. In the text, the reported [O_3(g)] values, which correspond to the concentrations actually sensed by droplets in the reaction chamber, are estimated to be ~ 10 times smaller than the values determined from UV absorbances due to further dilution by the N_2 drying gas (Fig. 6.1a, 10 L/min). Gas flows were regulated by calibrated mass flow controllers (MKS). Typical instrumental parameters were as follows: drying gas temperature, 340 ^{o}C; Nebulizer pressure, 28 psi; collector capillary voltage, +3.5 kV; fragmentor voltage, 22 V. Solutions were prepared with MilliQ water that had been previously purged with ultrapure $N_2(g)$ for at least 30 min. NaI (> 99 %), Na_2SO_3 (> 98 %) and $Na_2S_2O_3$ (> 99.999 %) were obtained from Sigma-Aldrich. Solution pH was measured with a calibrated pH meter (VWR, SB21).

Results and Discussion

We have recently shown that I^- is rapidly oxidized to I_3^- and IO_3^- by $O_3(g)$ at ppm levels in this experimental setup[37]. Thiosulfate is expected to react with $O_3(g)$ at similar rates[38]. Since I_2/I_3^- also react rapidly with $S_2O_3^{2-}$, it should be possible to observe the transient intermediates $I_2S_2O_3^{2-}$ and $IS_2O_3^-$ proposed by Raschig a century ago to account for their slow conversion into tetrathionate (see also Table 6.1)[39,40,41,42,43.]

$$I_2 + I^- \rightleftarrows I_3^- \tag{6.1, 6.1'}$$

$$I_2 + S_2O_3^{2-} \rightleftarrows I_2S_2O_3^{2-} \tag{6.2, 6.2'}$$

$$I_3^- + S_2O_3^{2-} \rightleftarrows I_2S_2O_3^{2-} + I^- \tag{6.3, 6.3'}$$

$$I_2S_2O_3^{2-} \rightleftarrows IS_2O_3^- + I^- \tag{6.4, 6.4'}$$

$$IS_2O_3^- + S_2O_3^{2-} \rightarrow I^- + S_4O_6^{2-} \tag{6.5}$$

A similar mechanism has been proposed for the I_2/I_3^- + HSO_3^-/SO_3^{2-} reaction, which proceeds via the ISO_3^- intermediate[44,45,46,47.] The absorption spectra assigned by Packer and Anderson to the $I_2S_2O_3^{2-}$ and $IS_2O_3^-$ intermediates detected in their pulse radiolysis experiments[48], were found to be blue-shifted relative to those of I_3^- and I_2.

Identification of anion products and intermediates

Figure 6.2 shows the mass spectra of aqueous $Na_2S_2O_3$ microdroplets in the absence and presence of $O_3(g)$. Signals at m/z = 112, 135, and 293, which are ascribed to $S_2O_3^{\cdot -}$, $NaS_2O_3^-$, and $Na_3(S_2O_3)_2^-$, respectively, are observed in the absence of $O_3(g)$. We detect the radical monoanion $S_2O_3^{\cdot -}$, rather than the closed-shell dianion $S_2O_3^{2-}$ (m/z = 56) in the ESMS of $Na_2S_2O_3$, in accord with previous reports[49,50]. Apparently, $S_2O_3^{2-}$(g) has negative electron affinity due to electrostatic repulsion between vicinal localized charges in $S=S(O)(O^-)_2$. The ready detection of $S_2O_8^{2-}$, in which charges are localized farther apart, supports this interpretation. Therefore, field ejection of $S_2O_3^{2-}$ from charged droplets[51] likely involves concerted electron transfer to the solvent, i.e.: $S_2O_3(H_2O)_n^{2-} \rightarrow S_2O_3^- + (H_2O)_n^-$. Thus, we consider $S_2O_3^{\cdot -}$ to be a valid marker of $S_2O_3^{2-}$ under present conditions. In the presence of O_3(g), new signals at m/z = 80, 97, 119, and 261 appear, which correspond to $S_2O_6^{2-}$, HSO_4^-, $NaSO_4^-$, and $Na_3(SO_4)_2^-$, respectively.

Figure 6.3 shows a mass spectrum of $NaI/Na_2S_2O_3$ microdroplets reacting with O_3(g). The m/z = 175 and 381 signals correspond to IO_3^- and I_3^-, while the signals at m/z = 207 and 239 are assigned to the I-S species ISO_3^- and $IS_2O_3^-$, respectively. The m/z = 207 signal, accompanied by m/z = 97, 175, and 381 signals, is also produced in the reaction of NaI/Na_2SO_3 microdroplets with O_3(g). All product signals disappear at once upon discontinuing O_3(g) injection.

The identity of S-containing species was confirmed from the relative intensities of their M and M+2 signals. Intensity ratios: M/M+2 = 100/4.4, 100/8.8, and 100/17.6 are expected for natural ^{34}S-abundance compounds containing one, two, and four S-atoms, respectively. The measured (112)/(114) = 100/9.9, (207)/(209) = 100/5.6, and (239)/(241) = 100/10.3 ratios are therefore consistent with species containing two, one, and two S-atom(s), respectively, and exclude $S_4O_6^{2-}$, $I_2S_2O_6^{2-}$ or $I_2S_4O_6^{2-}$ species. We infer that the m/z = 207 and 239 signals correspond to ISO_3^- and $IS_2O_3^-$, respectively.

Reaction Mechanism

Further information is gained by studying the dependence of signal intensities on [O_3(g)]. Reactant anion signal intensities at m/z = 112 ($S_2O_3^-$), 127 (I^-) and 135 ($NaS_2O_3^-$) decline with increasing [O_3(g)], as shown in Figure 6.4a. Product and intermediate anion signal intensities at m/z = 80 ($S_2O_6^{2-}$), 97 (HSO_4^-), 119 ($NaSO_4^-$), 175 (IO_3^-), 381 (I_3^-), 207 (ISO_3^-), and 239 ($IS_2O_3^-$) are all enhanced upon increasing [O_3(g)], as shown in Figure 6.4b and c. Note the upward inflections observed at ~ 50 ppm O_3(g) in Figures 6.4b and c.

Figure 6.5 shows a plot of the [HSO_4^-]/[$S_2O_6^{2-}$] ratio as function of [O_3(g)]. A nonvanishing value below ~ 50 ppm O_3(g) is a direct indication that $S_2O_6^{2-}$ and HSO_4^- are primary species produced in competing pathways, eqs. 6.10a and b in Table 6.1[52]. The marked increase of this ratio at higher [O_3(g)], however, shows that further HSO_4^- is produced in the oxidation of reactive byproducts. This interpretation is confirmed by the inertness of 0.1 mM $S_2O_6^{2-}$ toward O_3, together with the lack of HSO_4^- (m/z = 97) production below 420 ppm O_3(g). Neither does a 0.25 mM $S_4O_6^{2-}$ solution, prepared by titration of 0.5 mM $S_2O_3^{2-}$ with I_3^-:[53]

$$I_3^- + 2S_2O_3^{2-} \rightarrow 3I^- + S_4O_6^{2-} \qquad (6.6)$$

and subsequently sprayed in the reaction chamber, react with O_3(g). The m/z = 112 ($S_4O_6^{2-}$) and 97 (HSO_4^-) signal intensities remain constant below 520 ppm O_3(g).

Figure 6.6 shows how ISO_3^-, $IS_2O_3^-$, HSO_4^-, and IO_3^- signal intensities vary with [O_3(g)], and indicates that HSO_4^-, IO_3^-, ISO_3^-, and $IS_2O_3^-$ are later generation species whose rates of formation have a stronger, direct dependence on [O_3(g)] than those of $S_2O_6^{2-}$ and I_3^-.

We recently found that in this setup the oxidation of I^- by $O_3(g)$ yields iodate, IO_3^-, and triiodide, I_3^- (R12-14)[29]. I_3^- is in equilibrium with I^- and I_2[54,55,56,57] (R1). I_3^- and/or I_2 can then react with HSO_3^- or $S_2O_3^{2-}$ according to reactions R2-R3 and R7-R8[28,32]. The fact that we do not observe $I_2SO_3^{2-}$ (m/z = 167) or $I_2S_2O_3^{2-}$ (m/z = 183) in NaI/Na_2SO_3 or NaI/$Na_2S_2O_3$ droplets in contact with $O_3(g)$ implies that their decomposition lifetimes are much shorter than ~ 1 to 10 ms under present conditions (eqs. 6.4' and 6.9); in accord with Margerum et al.[32] $I_2S_2O_3^{2-}$ is thermodynamically stable ($k_2/k_{-2} = K_2 = 3.2 \times 10^7$ M^{-1}), but kinetically reactive ($k_4/k_{-4} = K_4 = 0.245$ M). The dissociation equilibrium constant of $I_2S_2O_3^{2-}$, $K_4 = 0.245$ M, is ~ 100 times larger than that of I_3^-, $k_{-1}/k_1 = 1.39 \times 10^{-3}$ M.[58] Our results do not exclude, however, the participation of hypoiodous acid, HOI, which is considered to be more reactive than I_2 or I_3^- as oxidant.

$$HOI + S_2O_3^{2-} + H^+ \rightarrow IS_2O_3^- + H_2O \qquad (6.15)$$

The dependence of $IS_2O_3^-$ (m/z = 239) signal intensity in 30 μM $Na_2S_2O_3$ droplets as a function of [NaI] in the range of 1–300 μM, at constant $[O_3(g)] = 300$ ppm, is shown in Figure 6.7a. The observed exponential growth to a maximum is qualitatively consistent with the proposed mechanism of formation. Figure 6.7b shows the dependence of $IS_2O_3^-$ (m/z = 239) signal intensity in 30 μM NaI droplets as a function of $[Na_2S_2O_3]$ in the range of 1–300 μM, at constant $[O_3(g)] = 350$ ppm. In contrast with the behavior observed in Figure 6.7a, $IS_2O_3^-$ peaks at $[Na_2S_2O_3]$ ~ 100 μM. This response implies that $S_2O_3^{2-}$ participates both in the formation and destruction of $IS_2O_3^-$, and is consistent with the increasing role of eq. 6.5 at higher $[Na_2S_2O_3]$[32]. From the reported value of $k_5 = 1.29 \times 10^6$ M^{-1} s^{-1}, we estimate that the half-life of $IS_2O_3^-$ in eq. 6.5 is ~ 5 ms at $[Na_2S_2O_3]$ ~ 100 μM, which provides a direct measure of our temporal window. The rapid hydrolysis of

ISO_3^-, eq. 6.16, regenerates I^-,[44] and may be responsible for the results shown in Figure 6.8a.

Interfacial Reaction Kinetics

Figure 6.8 shows the dependence of $[I^-]$ and $[S_2O_3^{2-}]$ vs. $[O_3(g)]$ in three different solutions: $[NaI]_0 = [Na_2S_2O_3]_0 = 30\ \mu M$ (a), $[NaI]_0 = 10 \times [Na_2S_2O_3]_0 = 300\ \mu M$ (b), and $[Na_2S_2O_3]_0 = 10 \times [NaI]_0 = 300\ \mu M$ (c). $S_2O_3^{2-}$ undergoes significant oxidation in all cases over the entire $[O_3(g)]$ range covered in these experiments. In contrast, I^- oxidation begins above $[O_3(g)] \sim 50$ ppm in the a and b mixtures, and is fully inhibited in c. Since $O_3(aq)$ reacts ~ 3 times faster with I^- than with $S_2O_3^{2-}$ in the bulk (see Table 6.1) these observations imply that the interfacial layers of the droplets are predominantly populated by $S_2O_3^{2-}$ and/or that reactivities at the air-water interface are significantly different than in the bulk. Considering that the ratio of signal intensities, $I(S_2O_3^-)/I(I^-) = 1.2 \pm 0.1$, in equimolar $Na_2S_2O_3$/NaI solutions is a direct measure of the relative affinities of $S_2O_3^{2-}$ and I^- for the interfacial layers of microdroplets, we must conclude that their relative reactivities toward $O_3(g)$ are indeed reversed relative to the bulk. Note that decrease of I^- at $[O_3(g)] \geq 50$ ppm in Figure 6.8a coincides with the onset of the $IS_2O_3^-$ and ISO_3^- in Figure 6.4c, supporting the proposed involvement of the products of I^- oxidation in their mechanism of formation.

Intermediate Stability

We probed the thermal stability of the ISO_3^-, $IS_2O_3^-$, and I_3^- in the gas-phase via collisional-induced dissociation experiments, in which the variation of ion signal intensities were recorded as function of fragmentor voltage (FV). FV is the electrical potential difference between the capillary exit and the first skimmer, a region where ions are accelerated up to excess kinetic energies given by: KE = FE × q_i = ½ m_i v_i^2 (q_i is the charge, m_i the mass, and v_i the excess velocity of ion *i*, respectively). Molecular ions convert their excess KE into internal (vibrational/rotational) excitation during impact with (N_2) bath gas molecules prior to undergoing collisionally induced dissociation (CID)[59]. Figure 6.9a shows the dependence of m/z = 127 (I^-), 207 (ISO_3^-), 239 ($IS_2O_3^-$) and 381 (I_3^-) signal intensities on FV. The monotonous increase of the I^- signal reveals that ion collection efficiencies generally increase with FV. The maxima observed in the case of ISO_3^-, $IS_2O_3^-$, and I_3^- indicates, therefore, the onset of fragmentation. Curve deconvolution into two sigmoids, followed by the conversion of laboratory (KE) to center-of-mass (CEM) kinetic energies—CEM = m/(m + M) KE, where m = 28 is the molecular mass of the N_2 collider gas and M = 207, 239, or 381, the molecular masses of the various anions—leads to the fragmentation curves shown in Figure 6.9b. Threshold CEM energies are consistent with the reported values for BDE(I^-−I_2) = 1.31 eV[60], and BDE(I^-−SO_3) = 1.67 eV[61]. The fact that $IS_2O_3^-$ and ISO_3^- have similar stabilities in the gas-phase suggests the presence of weak I-S bonds in both species[32].

Figures

Figure 6.1. Diagram of electrospray and overall reactor setup. A) Schematic diagram of electrospraying chamber and $O_3(g)$ injection system. B) An overview of the experimental setup. MFC stands for mass flow controller

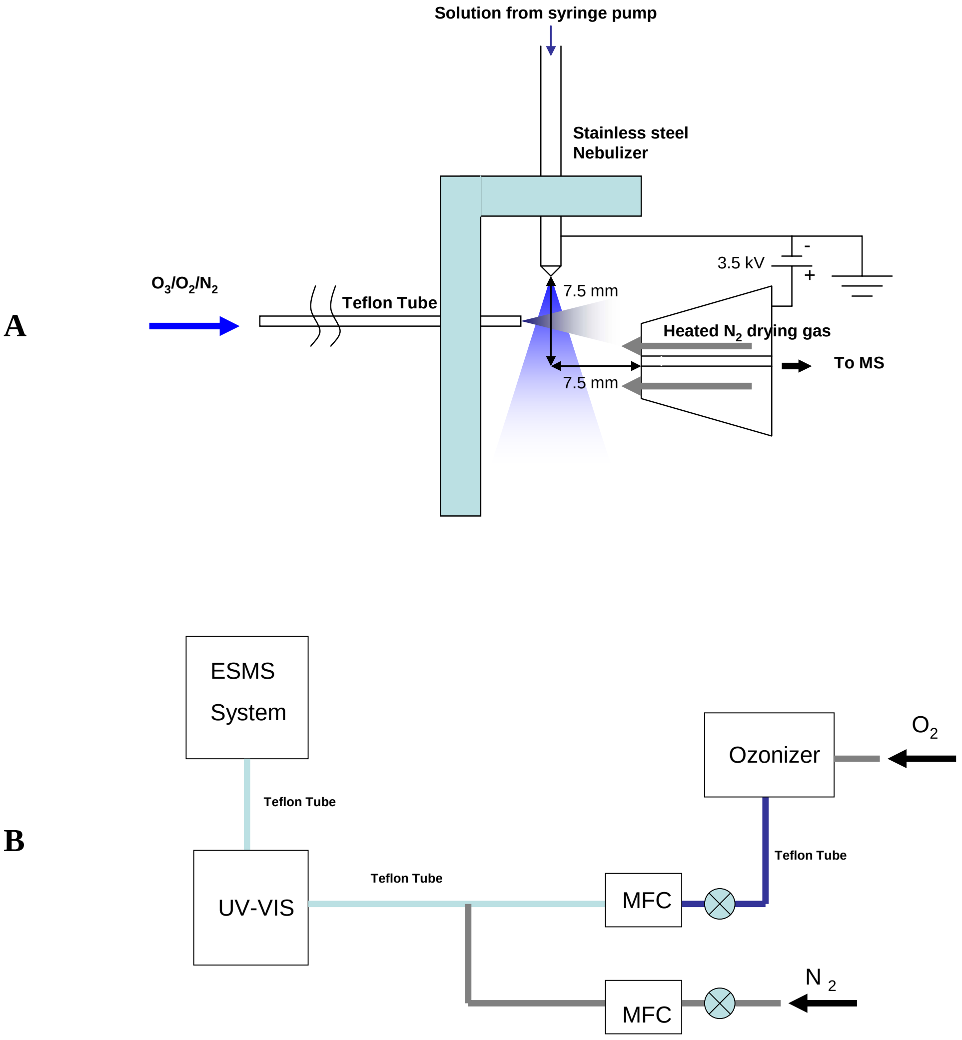

Figure 6.2. ESI-MS of aqueous $Na_2S_2O_3$ and gaseous O_3 reaction products. (100 µM $Na_2S_2O_3$, pH 6.2) droplets in the presence of 640 ppm O_3(g) (—), and in its absence (—). A) m/z = 112 ($S_2O_3^-$); B) 135 ($NaS_2O_3^-$); C) 293 [$Na_3(S_2O_3)_2^-$]; P) 80 ($S_2O_6^{2-}$); Q) 97 (HSO_4^-); R) 119 ($NaSO_4^-$); S) 261 [$Na_3(SO_4)_2^-$]

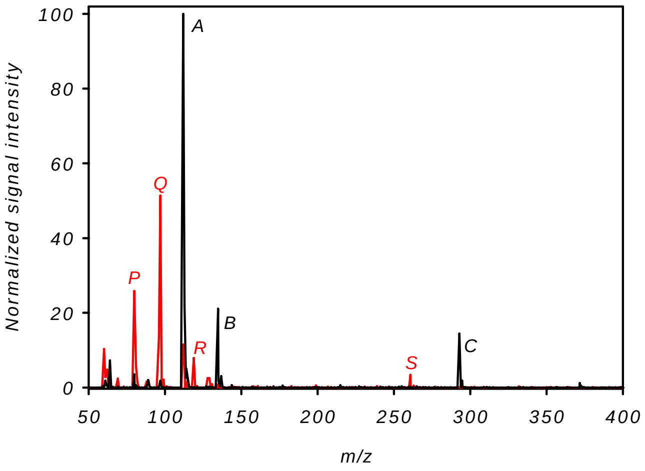

Figure 6.3. ESI-MS of aqueous $Na_2S_2O_3$-NaI droplets and gaseous O_3 reaction products. (100 µM $Na_2S_2O_3$ + 100 µM NaI, pH 6.2) microdroplets in the presence of 760 ppm O_3(g) (—), and in its absence (—). D) m/z = 127 (I^-); E) 277 (NaI_2^-); U) 159 (IO_2^-), V) 175 (IO_3^-); W) 381 (I_3^-); X) 207 (ISO_3^-); Y) 239 ($IS_2O_3^-$); Z) 255 ($IS_2O_4^-$)

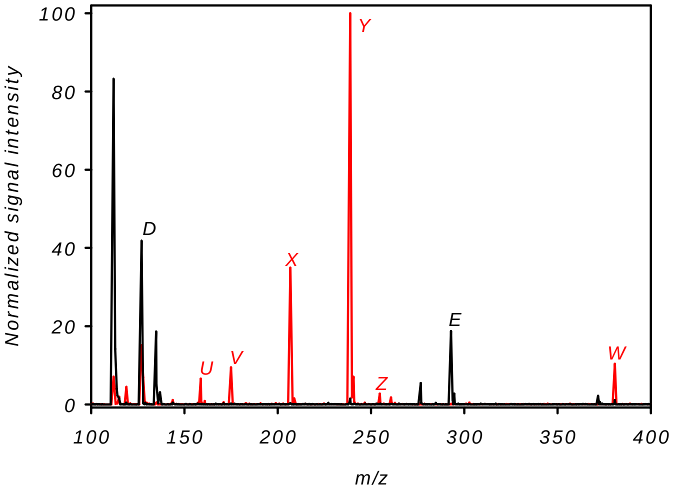

Figure 6.4. $Na_2S_2O_3$-$NaI_{(aq,drop)}$ and $O_{3(g)}$ reaction products vs. [$O_{3(g)}$]. (100 μM $Na_2S_2O_3$ + 100 μM NaI, pH 6.2) A) ESMS signal intensities at m/z = 112 ($S_2O_3^-$, ●), 127 (I^-, ○), and 135 ($NaS_2O_3^-$, ▲) vs. [O_3(g)]. B) ESMS signal intensities at m/z = 80 ($S_2O_6^{2-}$, Δ), 97 (HSO_4^-, ○), 175 (IO_3^-, ■), and 381 (I_3^-, □) vs. [O_3(g)]. C)ESMS signal intensities at m/z = 207 (ISO_3^-, ◊), 239 ($IS_2O_3^-$, ♦) vs. [O_3(g)]

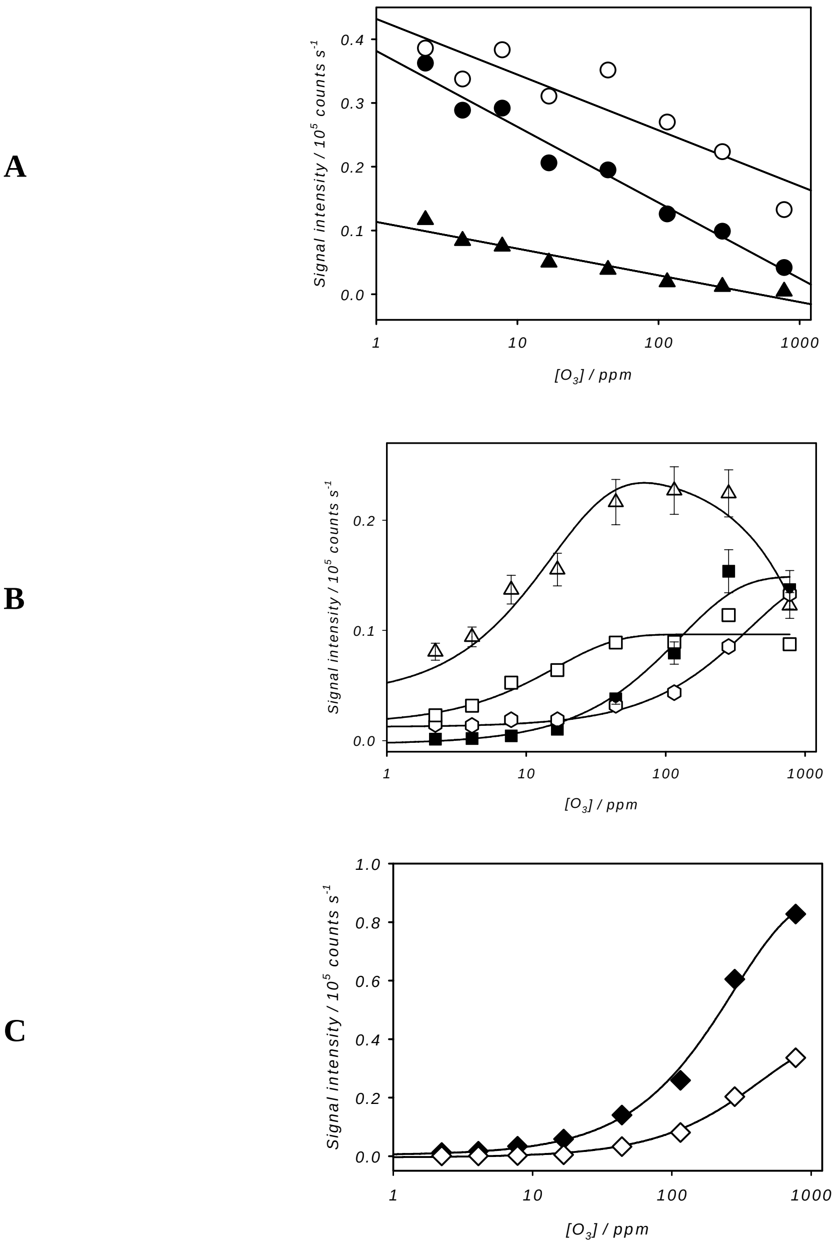

Figure 6.5. ESI-MS $HSO_4^-/S_2O_6^{2-}$ signal ratio vs. $[O_3(g)]$. Ratio of signal intensities at m/z = 97 and 80: $I(HSO_4^-)/I(S_2O_6^{2-})$ vs. $[O_3(g)]$ in (100 μM $Na_2S_2O_3$ + 100 μM NaI, pH 6.2) microdroplets

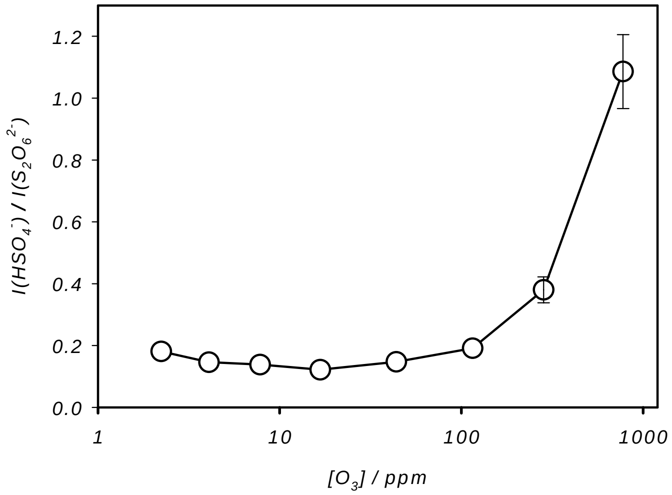

Figure 6.6. $Na_2S_2O_3$-$NaI_{(aq,drop)}$ and $O_{3(g)}$ reaction products vs. $[O_{3(g)}]$. Normalized ESI-MS signal intensities I at m/z = 97 (HSO_4^-), 175 (IO_3^-), 207 (ISO_3^-), and 239 ($IS_2O_3^-$) vs. $[O_3(g)]$ in (100 μM $Na_2S_2O_3$ + 100 μM NaI, pH 6.2) microdroplets

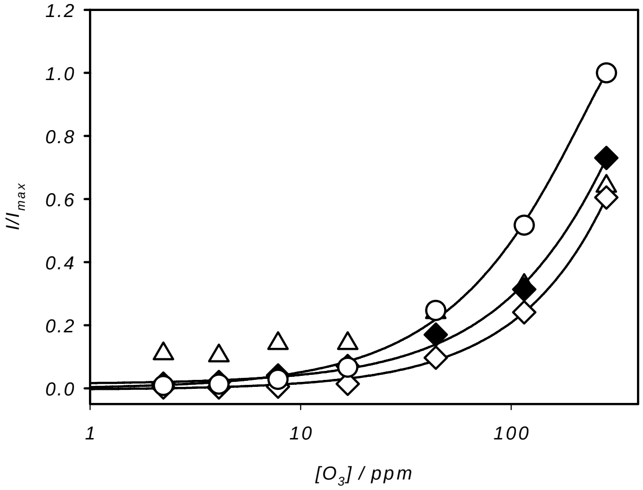

Figure 6.7. $IS_2O_3^-$ signal intensities vs. [$Na_2S_2O_3$] and [NaI]. A) [$Na_2S_2O_3$]$_0$ in ($Na_2S_2O_3$ + 30 μM NaI, pH 6.2) microdroplets at [O_3(g)] = 350 ppm, and B) [NaI]$_0$ in (30 μM $Na_2S_2O_3$ + NaI, pH 6.2) microdroplets at [O_3(g)] = 300 ppm

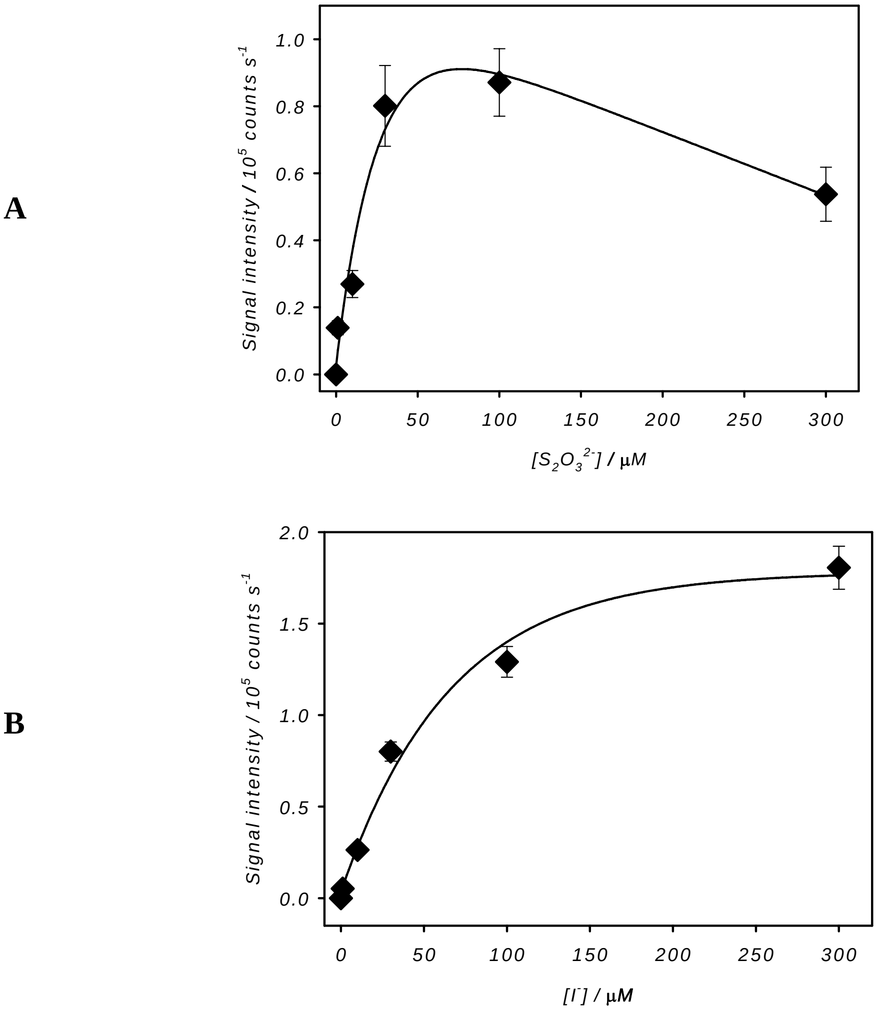

Figure 6.8. Normalized I^- and $S_2O_3^-$ ESI-MS signal intensities vs. $[O_{3(g)}]$. A) m/z = 127 (I^-) ($[NaI]_0 = [Na_2S_2O_3]_0 = 30\ \mu M$) (Δ), ($[NaI]_0 = 300$, $[Na_2S_2O_3]_0 = 30\ \mu M$) (○), and ($[NaI]_0 = 30$, $[Na_2S_2O_3]_0 = 300\ \mu M$) (●), and B) m/z = 112 ($S_2O_3^-$) in: ($[NaI]_0 = [Na_2S_2O_3]_0 = 30\ \mu M$) (▽), ($[NaI]_0 = 300$, $[Na_2S_2O_3]_0 = 30\ \mu M$) (□), and ($[NaI]_0 = 30$, $[Na_2S_2O_3]_0 = 300\ \mu M$) (■)

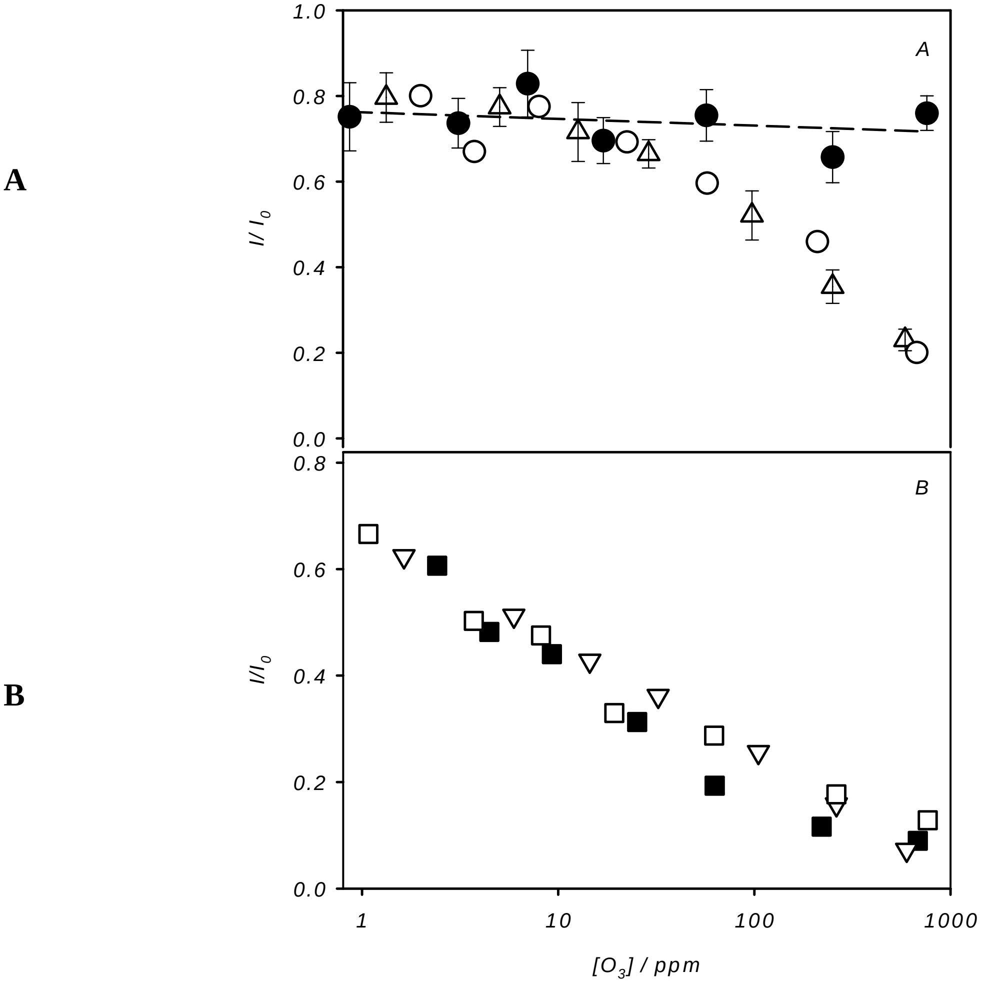

Figure 6.9. Collision-induced dissociation of $Na_2S_2O_3$-$NaI_{(aq)}$ and $O_{3(g)}$ products. A) ($[NaI]_0 = [Na_2S_2O_3]_0 = 100$ μM) microdroplets at $[O_3(g)] = 410$ ppm. I^- (○); ISO_3^- (▼); $IS_2O_3^-$ (▲); I_3^- (◊). B) ESI-MS signal intensities vs. center of mass energy. I_3^- (◊); ISO_3^- (▼); $IS_2O_3^-$ (▲)

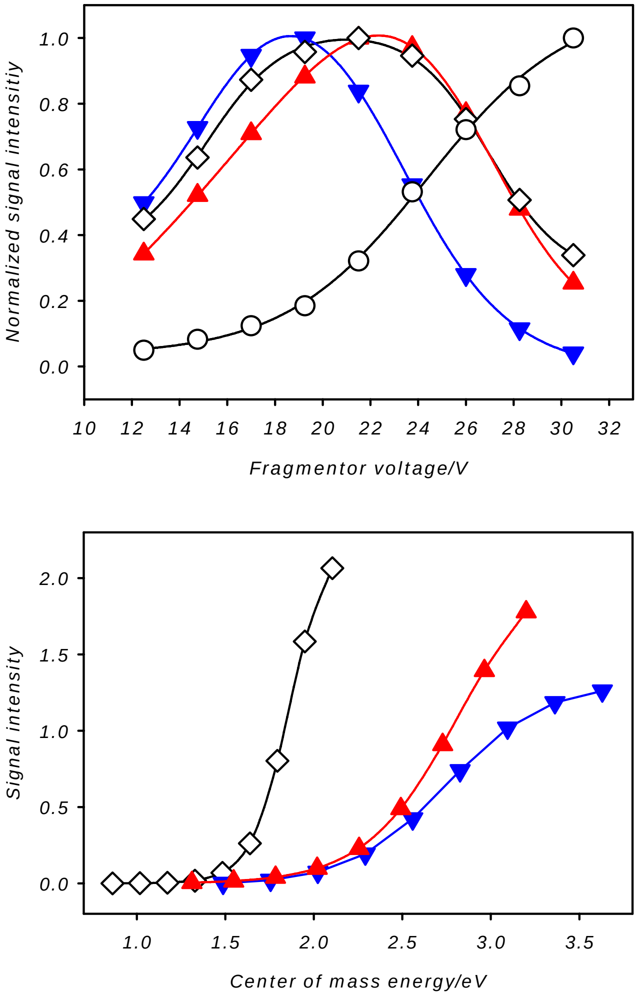

Tables

Table 6.1. Kinetic data for $Na_2S_2O_3$-$NaI_{(aq)}$ and $O_{3(g)}$ reactions at 298 K

eq#	Reaction	Rate or equilibrium constants (M, s units)	Ref.
6.1	$I_2 + I^- \rightleftarrows I_3^-$	$721\ M^{-1}$	56
6.2	$I_2 + S_2O_3^{2-} \rightleftarrows I_2S_2O_3^{2-}$	$7.8 \times 10^9\ M^{-1}\ s^{-1}$	41
6.2’		$2.5 \times 10^2\ s^{-1}$	
6.3	$I_3^- + S_2O_3^{2-} \rightleftarrows I_2S_2O_3^{2-} + I^-$	$4.2 \times 10^8\ M^{-1}\ s^{-1}$	41
6.3’		$9.5 \times 10^3\ s^{-1}$	
6.4	$I_2S_2O_3^{2-} \rightleftarrows IS_2O_3^- + I^-$	0.245 M	41
6.4’			
6.5	$IS_2O_3^- + S_2O_3^{2-} \rightarrow I^- + S_4O_6^{2-}$	$1.3 \times 10^6\ M^{-1}\ s^{-1}$	41
6.6	$I_3^- + 2S_2O_3^{2-} \rightarrow 3I^- + S_4O_6^{2-}$	N/A	41
6.7	$I_2 + HSO_3^- \rightarrow I_2SO_3^{2-} + H^+$	$1.7 \times 10^9\ M^{-1}\ s^{-1}$	
6.8	$I_3^- + HSO_3^- \rightarrow I^- + I_2SO_3^{2-} + H^+$	$1.5 \times 10^7\ M^{-1}\ s^{-1}$	44
6.9	$I_2SO_3^{2-} \rightarrow ISO_3^- + I^-$	N/A	44
6.10a	$S_2O_3^{2-} + O_3 \rightarrow S_2O_6^{2-}$	$3.7 \times 10^8\ M^{-1}\ s^{-1}$	38
6.10b	$\rightarrow SO_4^{2-} + SO_2$		
6.11	$SO_2 + H_2O \rightleftarrows HSO_3^- + H^+$	$1.3 \text{ x } 10^{-2}\ M$	62
6.12	$I^- + O_3 + H^+ \rightarrow HOI + O_2$	$1.2 \times 10^9\ M^{-1}\ s^{-1}$	16
6.13	$HOI + 2O_3 \rightarrow IO_3^- + 2O_2 + H^+$	$3.6 \times 10^4\ M^{-1}\ s^{-1}$	63
6.14	$HOI + I^- + H^+ \rightarrow I_2 + H_2O$	$4.4 \times 10^{12}\ M^{-2}\ s^{-1}$	64
6.15	$HOI + S_2O_3^{2-} + H^+ \rightarrow IS_2O_3^- + H_2O$	N/A	
6.16	$ISO_3^- + H_2O \rightarrow I^- + SO_4^{2-} + 2H^+$	$298\ s^{-1}$	44

References

---

(1) Satheesh, S. K.; Moorthy, K. K. *Atmos. Environ*. **2005**, *39*, 2089.

(2) Herrmann, H.; *Chem. Rev.* **2003**, *103*, 4691.

(3) Reid, J. P.; Sayer, R. M. *Chem. Soc. Rev*. **2003**, *32*, 70.

(4) Nissenson, P.; Knox, C. J. H.; Finlayson-Pitts, B. J.; Phillips, L. F.; Dabdub, D. *Phys. Chem Chem. Phys.* **2006**, *8*, 4700.

(5) Pilinis, C.; Pandis, S. N.; Seinfeld, J. H. *J. Geophys. Res.* **1995**, *100*, 18739.

(6) Hoffmann, M. R.; Edwards, J. *J. Phys. Chem.* **1975**, *79*,2096.

(7) Mcardle, J. V.; Hoffmann, M. R. *J. Phys. Chem*. **1983**, *87*, 5425.

(8) Hoffmann, M. R. *Atmos. Environ*. **1986**, *20*, 1145.

(9) Hunt, S. W.; Roeselova, M.; Wang, W.; Wingen, L. M.; Knipping, E. M.; Tobias, D. J.; Dabdub, D.; Finlayson-Pitts, B. J. *J. Phys. Chem. A,* **2004***, 102,* 11559.

(10) Hu, J. H.; Shi, Q.; Davidovitz, P.; Worsnop, D. R.; Zahniser, M. S.; Kolb, C. E., *J. Phys.Chem*. **1995**, *99*, 8768.

(11) Schütze, M.; Herrmann, H. *Phys. Chem. Chem. Phys.* **2006**, *4*, 60.

(12) Tolocka, M. P.; Saul, T. D.; Johnston, M. V. *J. Phys. Chem. A* **2004**, *108*, 2659.

(13) González-Labrada, E.; Schmidt, R.; DeWolf, E. *Chem.Comm*. **2006**, *23*, 2471.

(14) Davidovits, P.; Kolb, C. E.; Williams, L. R.: Jayne, J. T.; Worsnop, D. R. *Chem. Rev*. **2006**, *106*, 1323.

(15) Finlayson-Pitts, B. J.; Pitts, J.N. *Chemistry of the upper and lower atmosphere,* Academic Press: San Diego, California, **2000**; p. 364.

(16) Liu, Q.; Schurter, L. M.; Muller, C. E.; Aloisio, S.; Francisco, J. D.; Margerum, D.W. *Inorg. Chem.* **2001**, *40*, 4436.

(17) Espenson, H. E.; Tan, H.; Mollah, S.; Houk, R. S.; Eager, M. D. *Inorg. Chem.* **1998**, *37*, 4621.

(18) Bakhtiar, R.; Hop, C. E. C. A. *J. Phys. Org. Chem*. **1999**, *12*, 511.

(19) Arakawa R.; Liu, J.; Mizuno, K.; Inoue, H.; Doe H.; Matsuo, T. *Int. J. Mass Spectrom*. **1997**, *160*, 371. **B.** Arakawa, R.; Tachiyashiki, S.; Matsuo, T. *Anal. Chem*. **1995**, *67*, 4133. **C.** Arakawa, R.; Mimura, S.; Mastsubayashi, G.; Matsuo, T. *Inorg. Chem*. **1996**, *35*, 5725. **D.** Arakawa, R.; Matsuda, F.; Mastsubayashi, G. *Am. Soc. Mass Spectrom*. **1997**, *8*, 713 .

(20) Aliprantis, A. O.; Canary, J. W. *J. Am. Chem. Soc*. **1994**, *116*, 6985.

(21) Brum, J.; Dell'Orco, P.; Lapka, S.; Muske, K.; Sisko, J. *Rapid Commun. Mass Spectrom*. **2001**, *15*, 1548.

(22) Zechel, D. L.; Konermann, L.; Withers, S. G.; Douglas, D. J. *Biochemistry* **1998**, *37*, 7664.

(23) Xu, X.; Lu, W.; Cole, R. B. *Anal. Chem*. **1996**, *68*, 4244.

(24) Brum, J.; Dell'Orco, P. *Rapid Commun. Mass Spectrom*. **1998**, *12*, 741.

(25) Volmer, D. A. *J. Chromatogr. A* **1998**, *794*, 129.

(26) Santos, L. S.; Knaack, L.; Metzger, J. O. *Int. J. Mass. Spec.* **2005**, *246*, 84.

(27) Ding, W.; Johnson, K. A.; Kutal, C.; Amster, I. J. *Anal. Chem.* **2003,** *75*, 4624.

(28) Thomas, M. C.; Mitchell, T. W.; Blanksby, S. J. *J. Am. Chem. Soc*. **2005,** *128*, 58.

(29) Cheng. J.; Vecitis, C. D.; Hoffmann, M. R.; Colussi, A. J. *J. Phys. Chem. B.* **2006**, *110*, 25598.

(30) Kahen, K.; Jorabchi, K.; Gray, C.; Montaser, A. *Anal. Chem.* **2004**, *76*, 7194.

(31) Dodd, E. E. *J. Appl. Phys.* **1953**, *24*, 73.

(32) Millikan, R. A. *Science* **1910**, *32*, 436.

(33) Reiter, R. *J. Geophys. Res.* **1994**, *99*, 10807.

(34) Fenn, J. B. *J. Am. Soc. Mass Spectrom.* **1993**, *4*, 524.

(35) Kebarle, P. *J. Mass Spectrom.* **2000**, *35*, 804.

(36) Sander, S. P., et al. *Chemical Kinetics and Photochemical Data for Use in Stratospheric Modeling, Evaluation 15*; Jet Propulsion Laboratory: Pasadena, CA, **2006**.

(37) Enami, S.; Vecitis, C. D.; Cheng. J.; Hoffmann, M. R.; Colussi, A. J. *J. Phys. Chem. A,* **2007**, *111*, 50, 13032.

(38) Muller, B.; Heal, M. R., *Phys. Chem. Chem. Phys.* **2002**, *4*, 3365.

(39) Raschig, F. *Chem. Ztg.* **1908**, *32*, 1203.

(40) Raschig, F. *Ber. Dtsch. Chem. Ges.* **1915**, *48*, 2088.

(41) Scheper, W. M.; Margerum, D. W. *Inorg. Chem.* **1992**, *31*, 5466.

(42) Dodd, G.; Griffith, R. O. *Trans. Faraday. Soc.* **1949**, *45*, 546.

(43) Awtrey, A.; Connick, R. E. *J. Am. Chem. Soc.* **1951**, *73*, 1341.

(44) Yiin B. S.; Margerum, D. W. *Inorg. Chem.* **1990**, *29*, 1559.

(45) Landolt, H. *Ber. Dtsch. Chem. Ges.* **1886**, *19*, 1317.

(46) Bunau, G.V.; Eigen, M. *Z. Physik. Chem. (Frankfurt)* **1962**, *32*, 27.

(47) Inoue, H.; Sudo, Y. *Kogyo Kagaku Zasshi* **1967,** *70*, 123.

(48) Packer, J. E.; Anderson, R. F. *Aust. J. Chem.* **1997,** *50*, 435.

(49) Stewart, I. I.; Barnett, D. A.; Horlick, G. *J. Anal. Atom. Spec.* **1996**, *11*, 877.

(50) Agnes, G. R.; Stewart, I. I.; Horlick, G. *Appl. Spec.* **1994**, *48*, 1347.

(51) Kebarle, P. *J. Mass Spectrom.* **2000**, *35*, 804.

(52) *Gmelins Handbuch der anorganischen Chemie*, *Schwefel*, Teil B, Lieferung 2;

Verlag: Weinheim; 1960, p. 896, and references therein.

(53) Harris, W. E.; Daniel, C. Q*uantitative Chemical Analysis,* 3rd ed.; Freeman: New York, **1991**.

(54) Myers, O. E. *J. Chem. Phys*. **1958**, *28*, 1027.

(55) Ramette, R. W.; Sandford, Jr., R. W. **1965**, *87*, 5001.

(56) McIndoe, J. S.; Tuck, D. G. *Dalton Trans*. **2003**, *2*, 244.

(57) Troy, R. C.; Kelly, M. D.; Nagy, J. C.; Margerum, D. W. *Inorg. Chem.* **1991,** *30,* 4838.

(58) Ramette, R. W.; Sandford, R. W. *J. Am. Chem. Soc*. **1965**, *87*, 5001.

(59) Schneider B. B.; Chen. D. Y. *Anal. Chem*. **2000**, *72*, 791.

(60) Nizzi, K. E., Pommerening, C. A., Sunderlin, L. S., *J. Phys. Chem. A*, **1998**, *102*, 7674.

(61) Hao, C., Gilbert, T. M., Sunderlin, L. S., *Can. J. Chem.* **2005**, *83*, 2013

(62) Sillén, G. H.; Martell, A. E. *Stability Constants of Metal-Ion Complexes*, Special Publication 17; Chemical Society: London, **1964**.

(63) Bichsel, Y.; von Gunten, U.; *Environ. Sci. Technol*. **1999**, *33*, 4040.

(64) Eigen, M.; Kustin, K. *J. Am. Chem. Soc.* **1962**, *84*, 1355.

Chapter 7

Mass Spectrometric Detection of Ozonation Products and Intermediates of Aqueous Aerosol Iodide and/or Sulfite: Implications for Interfacial Kinetics and Iodide-Mediated Sulfite Oxidation

Sections reprinted as rights of author from Enami, S.; Vecitis, C. D.; Cheng, J.; Hoffmann, M. R.; Colussi, A. J. *Chemical Physics Letters*. **2008**, *455*, 316–320.

Abstract

The oxidations of sulfite and iodide in the interfacial layers of aqueous droplets exposed for ~ 1 to 10 ms to O_3(g) are investigated by online mass spectrometry of electrostatically ejected anions. S(IV) oxidation losses in Na_2SO_3 microdroplets are proportional to [S(IV)] [O_3(g)] up to ~ 90% conversion. In contrast, although I^- is more abundant than HSO_3^- in the interfacial layers of equimolar (Na_2SO_3 + NaI) microdroplets and ~ 3 times more reactive than HSO_3^- toward O_3(aq) in bulk solution, it is converted with minimal loss to I_3^- and IO_3^-, plus a persistent ISO_3^- intermediate. These observations reveal unanticipated interfacial gradients, reactivity patterns, and transport phenomena that had not been taken into account in previous treatments of fast gas-liquid reactions and may be of importance for gas-aerosol reactions in the Marine Boundary Layer.

Introduction

The number density, size, and optical and chemical properties of atmospheric aerosols significantly impact the Earth's climate[1]. Aerosols absorb/scatter solar radiation[2], but also support key chemical processes[3,4,5]. For example, SO_2(g) is a pervasive anthropogenic contaminant, which largely partitions into aqueous aerosol droplets[6,7], where it is assumed to be rapidly oxidized by the sparingly water-soluble O_3(g)[8] in a process that mediates tropospheric sulfur chemistry[9,10,11]. The oxidation of SO_2 by O_3 has been thoroughly investigated in bulk water[12,13] and aqueous sulfuric acid[14,15,16]. Since SO_3^{2-} is far more reactive than HSO_3^- [$pK_a(HSO_3^-) = 6.30$][17], overall reaction rates markedly increase above pH ~ 6.

Gas-liquid reactions have been previously investigated by monitoring the uptake of reactive gases by stationary trains of ~ 10–100 μm droplets at relatively low pressures (~ 10–50 Torr)[18] or on coated-wall Knudsen flow reactors[19], and the results interpreted on the basis of continuous models parametrized with kinetic and transport data in bulk fluids[20]. However, there is now firm evidence that air/liquid interfaces are unique reaction media. Enhanced reactivity[18, 21], selective anion enrichment[22], and higher acidity[23], have been predicted for these interfaces. These predictions remain to be thoroughly evaluated[24]. Recently we reported experiments in which the composition of the interfaces of aqueous halide microdroplets undergoing chemical reaction with O_3(g) was monitored by mass spectrometry with millisecond time resolution[25,26]. Here we report a kinetic and mechanistic study of interfacial S(IV)/I^- + O_3(g) aerosol chemistry that further illustrates the peculiarities of these systems.

Experimental

Experiments were performed in the spraying chamber of a commercial electrospray mass spectrometer (HP-1100). Sodium iodide and/or bisulfite solutions (10–100 μM) were directly infused (50 μL min^{-1}) into the chamber through a grounded stainless steel needle injector (100 μm internal diameter, 150 μm external diameter) surrounded by a coaxial sheath (250 μm internal diameter) issuing 0.5 L min^{-1} of nebulizer N_2 gas. The difference between the exit velocities of the liquid jet (10.6 cm s^{-1}) and nebulizer gas (2.65×10^4 cm s^{-1}) is so large that the drag imposed on the liquid breaks it apart into microdroplets. The terminal velocities reached by these microdroplets are between 10^2 and 10^3 cm s^{-1} [27]. The transit times of microdroplets across the ~ 0.5 cm intersection with the ozone plume are 1 ms < τ < 10 ms. It should be emphasized that the pneumatically generated spray from the grounded nozzle injector is comprised of a normal distribution of weakly charged droplets centered at zero charge, as expected from statistical charge separation in the fragmentation of a neutral liquid jet[25,26]. This mechanism naturally discriminates against the production of highly charged droplets. Charged droplets of either sign can be electrostatically extracted into the mass spectrometer by applying a suitable bias (+/- 3-4 kV) at its inlet port.

After leaving the reaction zone, microdroplets rapidly evaporate, leading to sudden volume reduction and concomitant surface charge repulsion. Such droplets become mechanically unstable when Coulombic repulsive forces overtake liquid cohesive forces, casuing the droplets to ‘explode’ by shedding their interfacial films to produce smaller droplets. This phenomenon repeats itself until nanometer droplets are formed. Ions will be field-ejected from the outer layers of these last-generation nanodroplets[28]. This analytical technique therefore reports the composition of the nanodroplets produced from the outer interfacial layers of microdroplets that had reacted with O_3(g). Typical instrumental parameters were as follows: drying gas temperature, 340 ^oC; nebulizer pressure, 30 PSI; collector capillary voltage, +3.5 kV; fragmentor voltage, 19 V. Further experimental details and results were reported elsewhere[25,29].

Ozone was generated by flowing O_2(g) (0.1 L/min, Air Liquid America Co.) through a commercial ozonizer (Ozone Solutions), diluted tenfold with ultrapure N_2(g) (0.9 L/min), and quantified by UV absorption spectrophotometry (HP 8452) [using absorption cross-sections $\sigma(250\text{ nm}) = 1.1 \times 10^{-17}\text{ cm}^2\text{ molecule}^{-1}$, and $\sigma(300\text{ nm}) = 3.9 \times 10^{-19}\text{ cm}^2\text{ molecule}^{-1}$ at 298 K][30] prior to being injected into the chamber. Actual [O_3(g)] in the reaction chamber is about 10 times smaller than the values determined in this manner, due to further dilution by the hot (250^o C) N_2 drying gas (10 L/min). Gas flows were regulated by mass flow controllers (MKS). Solutions were prepared with MilliQ water that had been previously purged with ultrapure N_2(g) for at least 30 min to prevent reactant autooxidation. NaI (> 99 %) and Na_2SO_3 (> 98 %) were obtained from Sigma-Aldrich. Solution pH was measured with a calibrated pH meter (VWR, SB21). Molecular formula assignments of S-containing species could be confirmed from the (M+2)/M ratios associated with natural abundance sulfur isotopes: $^{34}S/^{32}S = 0.044$.

Results and Discussion

The typical data obtained from these experiments is shown in Figure 7.1, which displays the mass spectra of aqueous Na_2SO_3 microdroplets in the absence and presence of ozone. Signals at m/z = 61, 81, and 97, which are ascribed to HCO_3^- (from atmospheric CO_2), HSO_3^-, and HSO_4^- (a pervasive byproduct of S(IV) autooxidation), respectively, are observed in the absence of O_3(g) (Figure 7.1, lower panel)[31]. Upon addition of O_3(g),

HSO_4^- is significantly enhanced, and new signals appear at m/z = 119 ($NaSO_4^-$) and m/z = 261 [$Na_3(SO_4)_2^-$] (Figure 7.1, upper panel), indicating extensive S(IV) → S(VI) processing. The dependences of HSO_3^- and HSO_4^- interfacial concentrations on [O_3(g)] in microdroplets that had been exposed to O_3(g) for ~ 1 to 10 ms are shown in Figure 7.2a.

The reactant conversion vs. [O_3(g)] data of Figure 7.2a cannot be analyzed using integrated kinetic equations for constant volume batch reactors, such as those employed in conventional studies, in which concentrations are expressed as explicit functions of time.[32] The chemical events probed in present experiments actually occur in a few-nm-thick open films that exchange ionic solutes with the droplets interior and O_3(g) with the gas-phase, in ~ 1 to 10 ms time frames. The analysis of gas-liquid reactions has been conventionally carried out via coupled partial differential equations associated with diffusional transport in homogeneous media separated by sharp boundaries[33]. Such methodology may not be appropriate to our films, because diffusional transport applies to large molecular assemblies spread over lengths much longer than mean free paths, and the medium in which transport takes place is no longer homogeneous or isotropic close to the interface, where compositional gradients arise even in the absence of chemical reaction.[29] Therefore, the issue of whether our findings correspond to surface or bulk reactive transformations should be decided by an in-depth evaluation of the data rather than by strict compliance with previously established models[33].

By assuming that the interfacial liquid films are in solubility or collisional equilibrium with O_3(g) (i.e., [O_3(int)] $\propto$ [O_3(g)]), we can tentatively treat them as unidimensional flow reactors where reactive losses are offset by reactant inflow from the underlying layers.

$$d[S(IV)]/dt = \{[S(IV)] - [S(IV)]_0\}\ \tau^{-1} = - k_R\ [S(IV)]^n\ [O_3(g)] + \{[S(IV)]_0 - [S(IV)]\}\tau_t^{-1} \tag{7.1}$$

In eq. 7.1, τ is the average contact time between microdroplets and $O_3(g)$, τ_t is the average time for bulk S(IV) to replenish a partially depleted film, k_R is an effective reaction rate constant, and *n* is a phenomenological kinetic order that reflects the influence of mass transport over a particular range of experimental conditions[24,34] Figure 7.2b shows that $\gamma = [HSO_3^-]/[HSO_3^-]_0$ closely follows a single exponential decay to a nonzero limiting value: $\gamma = \gamma_\infty + \gamma_0 \exp\{(- \beta\ [O_3(g)]\}$, which is consistent with an interfacial chemical reaction largely unperturbed by S(IV) transport from the droplets core below ~ 500 ppm $O_3(g)$. However, the fact that $\gamma_\infty \sim 0.1$ at ~ 1200 ppm $O_3(g)$ indicates that conversion is ultimately limited by mass transfer. Accordingly, a $[S(IV)]_0 - [S(IV)])/[S(IV)]^n$ vs. $k_R\,[\tau/(1 + \tau\ \tau_t^{-1})]\ [O_3(g)]$ plot (from eq. 7.1]) is linearized with $n = 1.0 \pm 0.1$ ($r^2 = 0.998$) independent of $[S(IV)]_0$ (Figure 7.2c). A kinetic order *n* significantly smaller than 1 would have indicated that the interfacial film is competitively replenished by intradroplet transport. The oxidation of I^- under similar conditions yields, for example: $n = 0.67 \pm 0.03$.[25] These results are quite reproducible under various experimental conditions, although we have no direct control of the droplet size distribution.

Figure 7.3 shows the mass spectra of NaI/Na_2SO_3 microdroplets in the absence (Figure 7.3, lower panel) and presence (Figure 7.3, upper panel) of $O_3(g)$. The m/z = 175 and 381 product signals correspond to IO_3^- and I_3^-, whereas the dominant m/z = 207 signal is assigned to the ISO_3^- intermediate. HSO_4^-, IO_3^-, and ISO_3^- signal intensities monotonically increase at higher $[O_3(g)]$ (Figure 7.4). In contrast, I_3^- displays a broad maximum at ~80 ppm $O_3(g)$. These processes likely proceed via the set of reactions shown in Table 7.1. The fact that I_3^- signals peak and then decline with $[O_3(g)]$, while IO_3^- signals keep increasing, follows from I^- and O_3 competition for the HOI precursor, eqs. 7.1, 7.10, and 7.11 in Table 7.1 (Scheme 7.1). We found that I^- signals are larger than those of HSO_3^- in an equimolar NaI/Na_2SO_3 solution, and also larger than in a NaI solution of the same concentration. In other words, I^- competes favorably with HSO_3^- for the air/water interface, even at sub-millimolar bulk concentrations and in the absence of $O_3(g)$. Thus, I^- is enriched near the air-water interface proper, while HSO_3^- lies behind in the deeper layers under stationary conditions. The differential affinity of the various anions for the interfacial region is a phenomenon that has not been taken into account in previous work on gas-liquid reactions.

Considering that S(IV) mixtures at pH 6.6 (which consist of 0.7 HSO_3^- + 0.3 SO_3^{2-}) react with a composite second-order rate constant: $k^{II}[S(IV) + O_3] \sim 4 \times 10^8\ M^{-1}\ s^{-1}$, that is ~ 3 times smaller than $k^{II}(I^- + O_3) = 1.2 \times 10^9\ M^{-1}\ s^{-1}$ in bulk solution, the fact that I^- is oxidized to IO_3^-, I_3^-, and ISO_3^- without apparent loss of interfacial I^- is an unexpected result (Figure 7.4b). The IO_3^- and I_3^- yields: $Y(X) = [S(X^-)\ f_x^{-1}]/[S(I^-)_0 - S(I^-)]$, measured in NaI/Na_2SO_3 solutions at $[O_3(g)] = 210$ ppm, [NaI] = 10 μM, are also anomalous because they increase with $[Na_2SO_3]$, eventually exceeding unity (Figure 7.5). S(X)s are ESMS signal intensities, and f_xs the relative response factors ($f_{IO_3^-} = S(IO_3^-)/S(I^-) = 0.80$, and $f_{I_3^-} = S(I_3^-)/S(I^-) = 0.76$) determined under present experimental conditions.

It is apparent that the interfacial layers are efficiently replenished with I^- from the droplet's core during reaction with $O_3(g)$, and that this process is enhanced in the presence of S(IV). This phenomenon arises from interfacial anion fractionation. As O_3

penetrates the droplets, it largely reacts with I^- first, but increasingly so with HSO_3^- further inside, thereby minimizing I^- depletion from the underlying region that eventually resupplies the outermost layers. [S(IV)] × [I^-] also peaks in this region, maximizing ISO_3^- production, whose hydrolysis, eq. 7.6, regenerates I^- and contributes to buffering interfacial I^- concentrations (Scheme 7.1). The ISO_3^- intermediate may derive from I_2/I_3^- via reactions R2-R5[35,36,37,38], but more likely from HOI via eq. 7.12. The fact that ISO_3^- signals are ~ 20 times more intense than those of IO_3^- and I_3^- under most conditions supports the efficient scavenging of HOI, the initial precursor of IO_3^- and I_3^- by S(IV), reactions R10–R12.

In summary, we have shown that it is possible to monitor fast reactions in the interfacial layers of aqueous microdroplets during exposure to a reactive gas by mass spectrometry. The larger propensity of I^- vs. HSO_3^- for the air-water interface influences their reactions with O_3(g) via a combination of physical and chemical processes. Mutually inert solutes can compete for reactive gases in ways that are beginning to be understood.

Figures

Figure 7.1. ESI-MS of aqueous Na_2SO_3 droplets and gaseous O_3 reaction products. 0.1 mM $Na_2SO_3(aq)$ solutions at pH 6.8 in the presence of 670 ppm $O_3(g)$ (—), and in the absence of $O_3(g)$ (—)

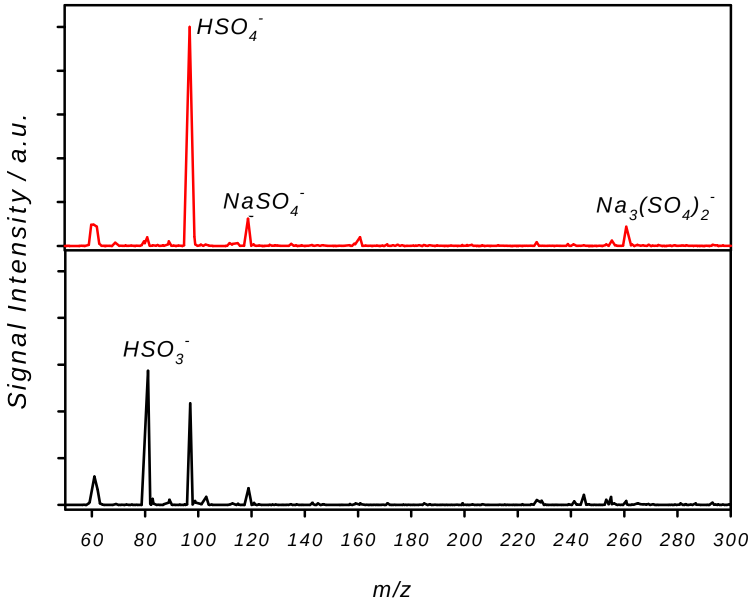

Figure 7.2. HSO_3^- and HSO_4^- absolute and relative ESI-MS signals vs. $[O_{3(g)}]$. A) Mass spectral signal intensities: HSO_3^- (●), HSO_4^- (○) versus $[O_3(g)]$ in microdroplets produced by spraying 0.1 mM Na_2SO_3 aqueous solutions at pH 6.8. B) Single exponential plot of HSO_3^- losses. C) Linearized kinetic plot of HSO_3^- losses

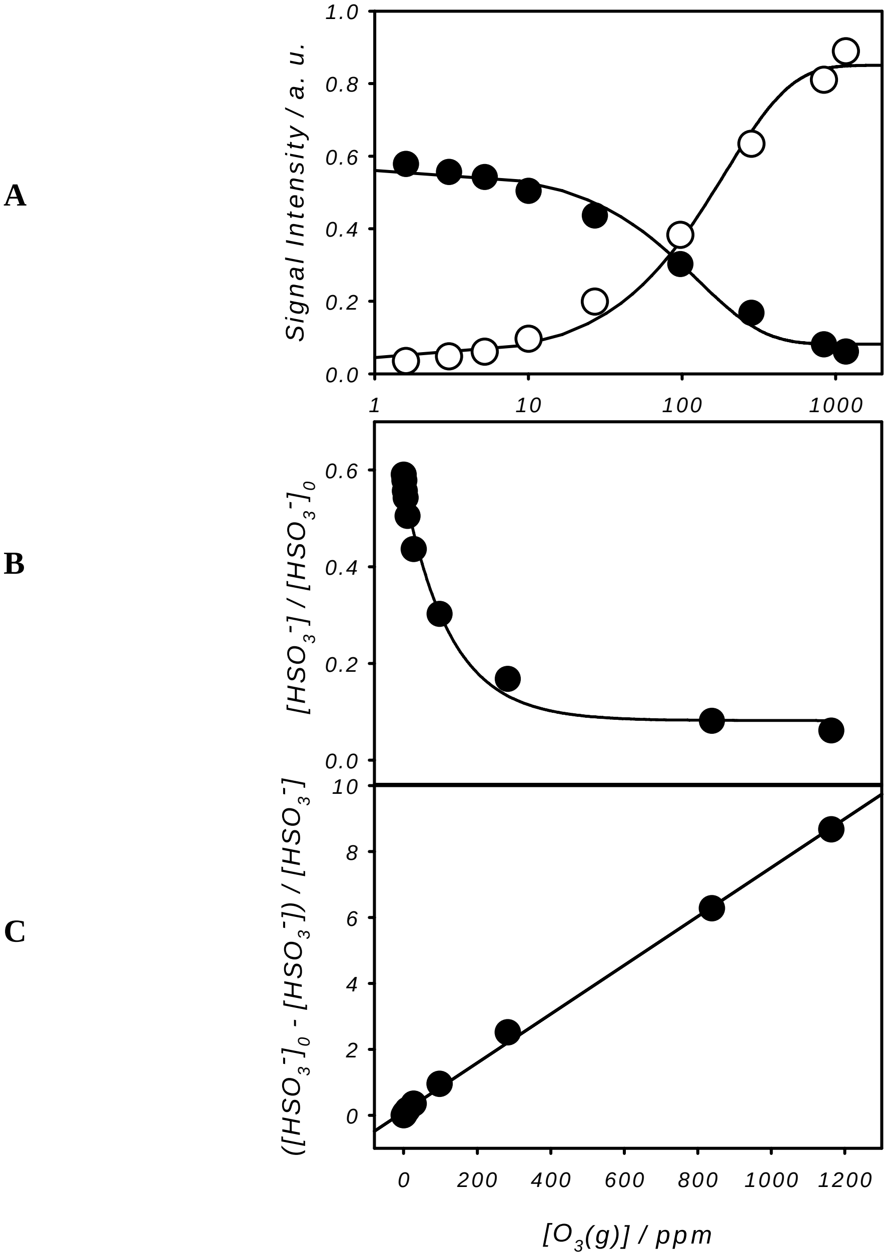

Figure 7.3. ESI-MS of aqueous Na_2SO_3-NaI droplets and gaseous O_3 reaction products. (0.1 mM Na_2SO_3 + 0.1 mM NaI) aqueous solutions at pH 6.6 in the presence of 50 ppm $O_3(g)$ (—), and in the absence of $O_3(g)$ (—). See also Figure 7.1 for further spectral assignments

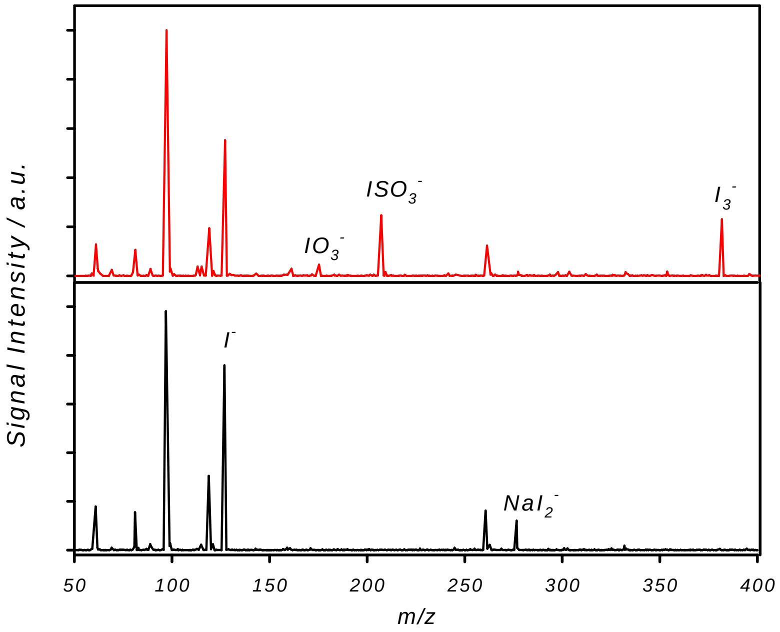

Figure 7.4. A) Mass spectral intensities of HSO_3^- (○), HSO_4^- (●). B) I^- (□), IO_3^- (× 10, Δ), I_3^- (× 10, ▼). C) ISO_3^- (♦) signals vs. [O_3(g)] in microdroplets produced by spraying (0.1 mM Na_2SO_3 + 0.01 mM NaI) aqueous solutions at pH 6.6

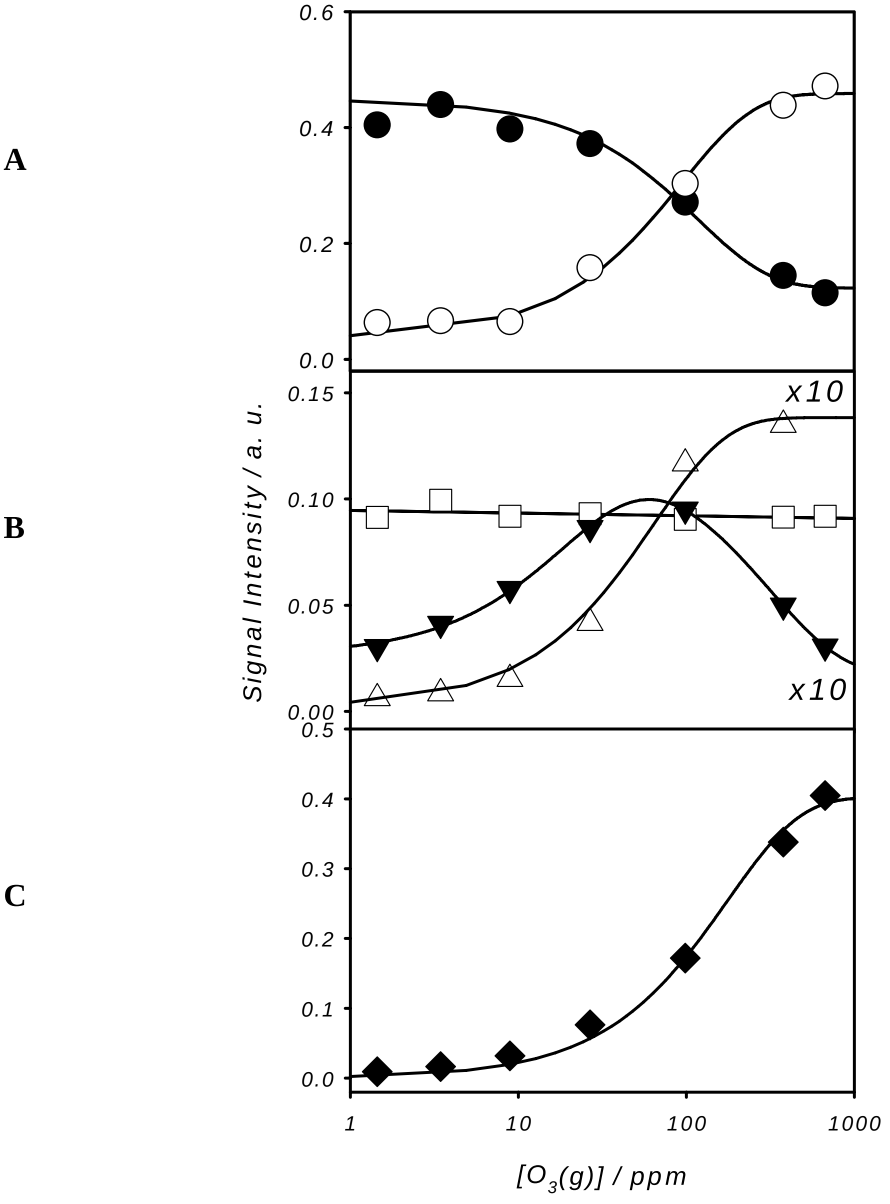

Figure 7.5. IO_3^- and I_3^- iodide-normalized yields vs. $[Na_2SO_3]$. IO_3^- (Δ) and I_3^- (▼) yields based on interfacial I^- losses (see text for definition of yield) vs. $[Na_2SO_3]$ in microdroplets produced by spraying (Na_2SO_3 + 0.01 mM NaI) aqueous solutions at pH 6.6 in 210 ppm $O_3(g)$

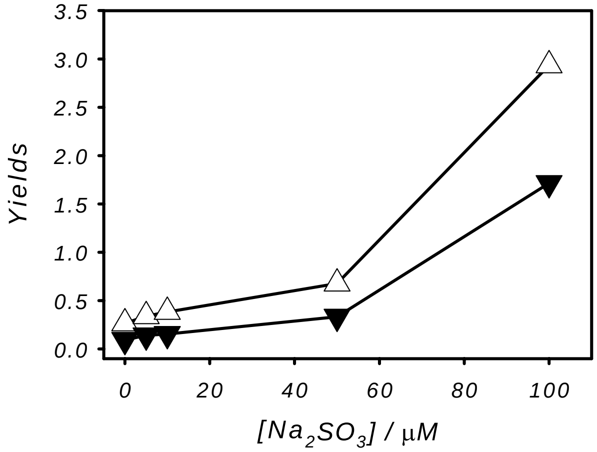

Schemes

Scheme 7.1. Catalytic cycle for iodide-mediated ozone oxidation of sulfite

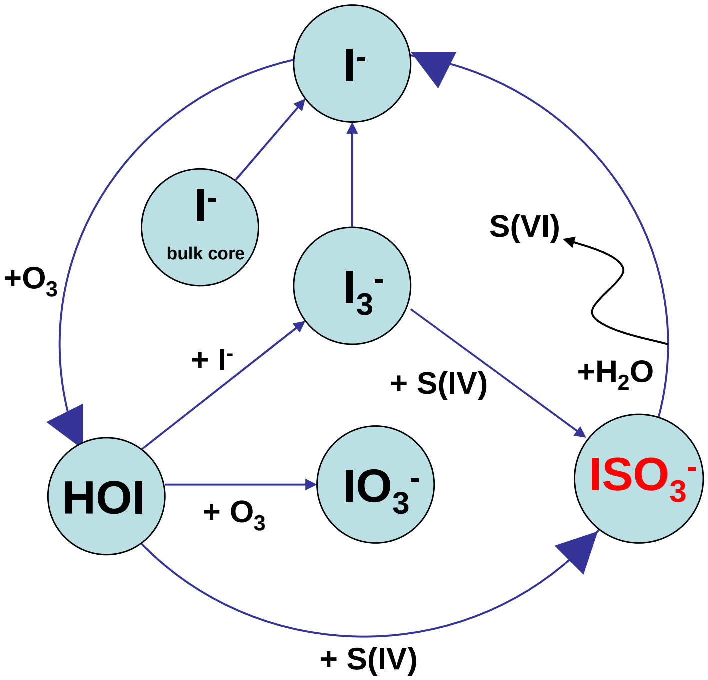

Tables

Table 7.1. Kinetic data for Na_2SO_3-$NaI_{(aq)}$ and $O_{3(g)}$ reactions at 298 K

eq#	Reaction	Rate, equilibrium constants in M, s units	Ref.
7.1	$I_2 + I^- \rightleftarrows I_3^-$	$721\ M^{-1}$	39
7.2	$I_2 + SO_3^{2-} \rightarrow ISO_3^- + I^-$	$3.1 \text{ x } 10^9\ M^{-1}\ s^{-1}$	35
7.3	$I_3^- + SO_3^{2-} \rightarrow ISO_3^- + 2I^-$	$2.9 \times 10^8\ M^{-1}\ s^{-1}$	35
7.4	$I_2 + HSO_3^- \rightarrow I^- + ISO_3^- + H^+$	$1.7 \times 10^9\ M^{-1}\ s^{-1}$	35
7.5	$I_3^- + HSO_3^- \rightarrow 2I^- + ISO_3^- + H^+$	$1.5 \times 10^7\ M^{-1}\ s^{-1}$	35
7.6	$ISO_3^- + H_2O \rightarrow I^- + SO_4^{2-} + 2H^+$	$298\ s^{-1}$	35
7.7	$SO_3^{2-} + O_3 \rightarrow SO_4^{2-} + O_2$	$1.5 \times 10^9\ M^{-1}\ s^{-1}$	9
7.8	$HSO_3^- + O_3 \rightarrow HSO_4^- + O_2$	$3.7 \text{ x } 10^5\ M^{-1}\ s^{-1}$	9
7.9	$I^- + O_3 + H^+ \rightarrow HOI + O_2$	$1.2 \times 10^9\ M^{-1}\ s^{-1}$	40
7.10	$HOI + 2O_3 \rightarrow IO_3^- + 2O_2 + H^+$	$3.6 \times 10^4\ M^{-1}\ s^{-1}$	41
7.11	$HOI + I^- + H^+ \rightarrow I_2 + H_2O$	$4.4 \times 10^{12}\ M^{-2}\ s^{-1}$	42
7.12	$HOI + SO_3^{2-} + H^+ \rightarrow ISO_3^- + H_2O$	N/A	N/A

References

---

(1) Pilinis, C.; Pandis, S. N.; Seinfeld J. H. *J. Geophys. Res.* **1995**, *100*, 18739.

(2) Satheesh, S. K.; Moorthy, K. K.; *Atmos. Environ.* **2005**, *39*, 2089.

(3) Herrmann, H. *Chem. Rev.* **2003**, *103*, 4691.

(4) Reid, J. P.; Sayer, R. M.; *Chem. Soc. Rev.* **2003**, *32*, 70.

(5) Nissenson, P.; Knox, C. J. H.; Finlayson-Pitts, B. J.; Phillips, L. F.; Dabdub, D. *Phys. Chem Chem. Phys.* **2006**, *8*, 4700.

(6) Finlayson-Pitts, B. J.; Pitts, J. N. *Chemistry of the upper and lower atmosphere*, Academic Press; San Diego, CA, **2000**.

(7) Martin, L. R.; Damschen, D. E. *Atmos. Environ.* **1981**, *15*, 1615.

(8) Shorter, J. A.; De Bruyn, W. J.; Hu, J.; Swartz, E.; Davidovits, P.; Worsnop, D. R.; Zahniser, M. S.; Kolb, C. E. *Environ. Sci. Technol.* **1995**, *29*, 1171.

(9) Hoffmann, M. R.; *Atmos. Environ.* **1986**, *20*, 1145.

(10) Tie, X.; Brasseur, G.; Emmons, L.; Horowitz, L.; Kinnison, D.; *J. Geophys. Res.* **2001**, *106*, 22931.

(11) Tie, X.X.; Madronich, S.; Walters, S.; Edwards, S. P.; Ginoux, P.; Mahowald, N.; Zhang, R. Y.; Lou, C.; Brasseur, G.. *J. Geophys. Res.* **2005**, *110*, D03204.

(12) Lagrange, J.; Pallares, C.; Wenger, G.; Lagrange, P. *J. Geophys. Res.* **1994**, *99*, 14595.

(13) Botha, C. F.; Hahn, J.; Pienaar, J. J.; van Eldik, R. *Atmos. Environ.* **1994**, *28*, 3207.

(14) Tarbuck, T. L.; Richmond, G. L. *J. Am. Chem. Soc.* **2006**, *128*, 3256.

(15) Boniface, J.; Shi, Q.; Li, Y. Q.; Cheung, J. L.; Rattigan, O. V.; Davidovits, J.;

Worsnop, D. R.; Jayne, J. T.; Kolb, C. E. *J. Phys. Chem. A* **2000**, *104*, 7502.

(16) Rattigan, O. V.; Boniface, J.; Swartz, E.; Davidovits, P.; Jayne, J. T.; Kolb, C. E.; Worsnop, D. R. *J. Geophys. Res.* **2000**, *105*, 29065.

(17) Liu, Q.; Schurter, L. M.; Muller, C. E.; Aloisio, S.; Francisco, J. S.; Margerum, D. W. *Inorg. Chem.* **2001**, *40*, 4436.

(18) Davidovits, P.; Kolb, C. E.; Williams, L. R.; Jayne, J. T.; Worsnop, D. R. *Chem. Rev.* **2006**, *106*, 1323.

(19) Underwood, G.. M.; Li, P.; Usher, C. R.; Grassian, V. H. *J. Phys. Chem. A* **2000**, *104*, 819.

(20) Schutze, M.; Herrmann, H. *Phys. Chem. Chem. Phys*. **2002**, *4*, 60.

(21) Boniface, J.; Shi, Q.; Li, Y. Q.; Cheung, J. L.; Rattigan, O. V; Davidovits, P.; Worsnop, D. R.; Jayne, J. T.; Kolb, C. E. *J. Phys. Chem. A* **2000**, *104*, 7502.

(22) Knipping, E. M.; Lakin, M. J.; Foster, K. L.; Jungwirth, P.; Tobias, D. J.; Gerber, R. B.; Dabdub, D.; Finlayson-Pitts, B. J. *Science* **2000**, *288*, 301.

(23) Buch, V.; Milet, A.; Vácha, R.; Jungwirth, P.; Devlin, J. P. *Proc. Natl. Acad. Sci. U. S. A.* **2007**, *104*, 7342.

(24) Smith, G.. D.; Woods III, E.; DeForest, C. L.; Baer, T.; Miller, R. E. *J. Phys. Chem. A* **2002**, *106*, 8085.

(25) Enami, S.; Vecitis, C. D.; Cheng. J.; Hoffmann, M. R.; Colussi, A. J. *J. Phys. Chem. A* **2007**, *111*, 8749.

(26) Enami, S.; Vecitis, C. D.; Cheng. J.; Hoffmann, M. R.; Colussi, A. J. *J. Phys. Chem. A* **2007**, *111*, 13032.

(27) Kahen, K.; Jorabchi, K.; Gray, C.; Montaser, A. *Anal. Chem.* **2004**, *76*, 7194.

---

(28) Kebarle, P.; *J. Mass Spectrom.* **2001**, *35*, 804.

(29) Cheng, J.; Vecitis, C. D.; Hoffmann, M. R.; Colussi, A. J. *J. Phys. Chem. B* **2006**, 110 25598.

(30) Sander, S. P. et al. *Chemical Kinetics and Photochemical Data for Use in Stratospheric Modeling; Evaluation* 15; Jet Propulsion Laboratory: Pasadena, CA, **2006**.

(31) Stewart, I. I.; Barnett, D. A.; Horlick, G.. J. *Anal. Atom. Spec.* **1996**, *11*, 877.

(32) Benson, S. W. *The Foundations of Chemical Kinetics*; McGraw-Hill: New York, **1960**.

(33) Danckwerts, P. V., *Gas-Liquid Reactions*; McGraw-Hill: New York, **1970**.

(34) Hanson, D. R.; Ravishankara, A. R. *J. Phys. Chem.* **1994**, *98,* 5728.

(35) Yiin, B. S.; Margerum, D. W. *Inorg. Chem.* **1990**, *29* 1559.

(36) Landolt, H., *Ber. Dtsch. Chem. Ges.* **1886**, *19,* 1317.

(37) Bunau, G.. V.; Eigen, M. *Z. Physik. Chem.* (Frankfurt) **1962**, *32,* 27.

(38) Inoue, H.; Sudo, Y.; *Kogyo Kagaku Zasshi* **1967**, *70,* 123.

(39) Troy, R. C.; Kelly, M. D.; Nagy, J.C.; Margerum, D.W. *Inorg. Chem.* **1991**, *30*, 4838.

(40) Magi, L.; Schweitzer, F.; Pallares, C.; Cherif, S.; Mirabel, P.; George, C. *J. Phys. Chem. A* **1999**, *101*, 4943.

(41) Bichsel, Y.; von Gunten, U. *Environ. Sci. Technol.* **1999**, *33*, 4040.

(42) Eigen, M.; Kustin, K. *J. Am. Chem. Soc.* **1962**, *84*, 1355.

Chapter 8

Iodide-Mediated Gaseous Ozone Oxidation of Aerosol Bromide and Chloride as a Possible Source of Gaseous Marine Halogens

Sections reprinted with permission from Enami, S.; Vecitis, C. D.; Cheng, J.; Hoffmann, M. R.; Colussi, A. J. *Journal of Physical Chemistry A* **2007**, *111*, 8749-8752.

Abstract

A few gaseous bromine molecules per trillion (ppt) cause the complete destruction of ozone in the lower troposphere during the polar sunrise and about half of the losses associated with the 'ozone hole' in the stratosphere. Recent field measurements of BrO in the free troposphere suggest an even more global role of atmospheric bromine. Models quantifying ozone trends by assuming atmospheric inorganic bromine (Br_y) stems exclusively from long-lived bromoalkane gases significantly underpredict BrO measurements. This discrepancy implies a tropospheric background level of ~ 4 ppt Br_y of unknown origin. Here we report that I^- efficiently mediates the oxidation of Br^- and Cl^- in aqueous droplets exposed to gaseous ozone. Br^- and Cl^-, which are kinetically unreactive towards O_3 in comparison to I^-, and were previously deemed unlikely direct precursors of atmospheric halogens, are readily converted into IBr_2^- and ICl_2^- in the presence of I^- and gaseous ozone. Fine sea salt aerosol particles ($r < 1$ micron) are reported to be enriched in I^- and Br^- and may be a global source of photoactive gaseous halogen compounds in the atmosphere even in the absence of sunlight.

Introduction

Bromine critically affects atmospheric ozone at all altitudes, playing a crucial role in the ozone depletion events (ODEs) observed in the polar lower troposphere during early spring[1-3]. Despite its lower abundance, bromine is 45–70 times more efficient than chlorine as a catalyst of stratospheric ozone depletion[4]. The mechanism of atmospheric bromine production from its primary seawater bromide source is not fully understood[5]. It has been generally assumed that gaseous inorganic bromine (Br_y) is released in the stratosphere by the short wavelength photolysis of long-lived source gases, such as biogenic methyl bromide and anthropogenic halons[6]. However, recent field (surface station, balloon, and satellite) BrO measurements, which are broadly consistent with each other, significantly exceed model predictions based on those BrO source assumptions[7–9] The implication is that some Br_y is directly delivered to the free troposphere, possibly carried by sea salt aerosol itself[8,10–12]. Marine aerosols appear to be plausible vehicles for halogen activation since a fraction of the sea spray aerosols are fine ($r < 1$ micron) particles that remain suspended long enough to undergo chemical processing.

Polar ODEs require the presence of appreciable levels ($\gtrsim$10 ppt) of rapidly photolyzable Br_2(g) in the boundary layer at the end of the polar winter night[13-15]. Since ODEs are also observed under pristine Antarctic conditions, the conversion of marine Br^- into Br_2(g) should involve an oxidant that persists in the dark, such as O_3. The inertness of Br^- and Cl^- towards O_3 is circumvented in sea salt as compared to NaCl and NaBr alone[16]. That significantly more Br_2(g) is emitted from sea salt than from pure NaBr exposed to O_3(g) implies that Br^- oxidation is catalyzed or mediated by a minor component of the sea salt[17]. I^- is one viable sea salt component since it reacts at diffusion-controlled rates with ozone. Halogen activation may also occur to some extent on the surface of sea ice, which has been reported to catalyze a number of atmospherically relevant reactions.

The enrichment of seawater anions such as Br^- and I^- in fine marine aerosol particles would be expected to enhance the possible halogen activation[18–20]. Relative anion populations, f_i, at the interface of droplets produced from equimolar solutions were recently shown to increase exponentially with ionic radius r_i, i.e.: $f_i \propto \exp(\beta\, r_i)$, $f_{I^-}/f_{Br^-} = 5.2$, $f_{Br^-}/f_{Cl^-} = 3.4$.[21] This correlation reveals that anion fractionation at the air/water interface is simply another manifestation of the Hofmeister effects generally observed at aqueous interfaces in contact with less polarizable media.[22] The enrichment of Br^- and I^- in fine aerosol particles of greater surface-area-to-volume ratios would be expected to enhance oxidation kinetics by ozone, which partitions weakly to the aqueous phase from the gas phase, via reactions at the air-water interface.

We investigated this possibility in laboratory experiments where the reaction products of aqueous halide droplets sprayed into an $O_3(g)$ plume are monitored via online electrospray mass spectrometry (ESMS) of the evaporated anions (Figure 6.1).

Small drops are usually charged, even when produced by fragmentation of electrically neutral liquids, due to statistical fluctuations that scale with $(\text{drop size})^{-1/2}$ [23]. For example, submicron marine aerosol drops are, on average, negatively charged[24]. Water evaporation regulated by ambient relative humidity will eventually shrink the suspended droplets, subsequently increasing electrostatic repulsion among excess surface charges. Coulomb explosions may ensue if charge density is great enough and highly charged droplets lose interfacial charge and mass into smaller droplets[25]. These events, if replicated by the subsequent droplets, generate small particles that are enriched (i.e., net enrichment $\propto (f_i)^m$, where m is the number of successive Coulomb explosions) in Br^- and I^-. This mechanism provides a physicochemical (i.e., abiotic)[1,26] explanation for anion enrichment in aerosol particles, as well as for its inverse dependence on particle size and statistical variations among individual particles of similar size[19]. Anion enrichment may also be partially due to droplet acidification resulting in protonation and then gasification of the weaker acids. Smaller particles drawing mass and surface charge from larger units is consistent with observations that Br^- is enriched in submicron particles while depleted in larger specimens[2].

Figure 8.1a shows the extent of I^- oxidation in aqueous NaI microdroplets injected in $O_3(g)$ gas mixtures at atmospheric pressure. Interfacial I^- concentration decreases by ~ 50% after exposure to $[O_3(g)] \simeq 100$ ppm for $\simeq 1$ to 10 ms (i.e., I^- reacts with O_3 with an apparent pseudo-first-order rate constant, $k^I \sim 10^3\ s^{-1}$, that can be formally calculated from the reaction rate constant in bulk solution: $k^{II}(I^- + O_3)_{aq} = 1.2 \times 10^9\ M^{-1}\ s^{-1}$ [28], and $[O_3(aq)] \sim 1\ \mu M$ (from Henry's law constant $H = 0.01\ M\ atm^{-1}$ for O_3 in water at 298 K). I^- oxidation proceeds at rates R_{-I^-} given by: $R_{-I^-} \propto [I^-]^n\ [O_3(g)]$. The actual n value may be obtained from the fact that at steady state: $IF(I^-) - [I^-]\ \tau^{-1} - k_R\ [I^-]^n\ [O_3(g)] = 0$, where $IF(I^-)$ is the I^- inflow to the reaction zone, i.e., the intersection between the droplets and the $O_3(g)$ plumes in Figure 6.1, τ is the transit time through this zone, k_R the overall reaction rate constant, and n the effective kinetic order of $[I^-]$ in eq. 8.1[29]. Since: $IF(I^-) - [I^-]_0\ \tau^{-1} = 0$ at $[O_3(g)] = 0$, a plot of $([I^-]_0 - [I^-])/[I^-]^n$ vs. $[O_3(g)]$ should be linear. The data of Figure 8.1a are linearized provided that $\langle n \rangle = 0.67 \pm 0.03$ in the range $1 \leq [NaI]/\mu M \leq 30$ ($[I^-] = 0.5\ \mu M$ in seawater) (Figure 8.1b). In this context $0.5 \leq \langle n \rangle \leq 1$ is an empirical parameter that encodes the competition between mass transfer and chemical reaction at the gas-liquid interface. We actually verified that $\langle n \rangle \rightarrow 1$ as $[I^-] \rightarrow 500$ μM, as expected for a surface-specific gas-liquid reaction[30,31]. From these experiments, we estimate that it takes ~ 40 minutes to oxidize 50% of the iodide contained in microdroplets suspended in typical ~ 40 ppb (parts per billion) atmospheric $O_3(g)$ concentrations. R_{-I^-} is independent of bulk pH in the range 4.0 to 7.0. However, this calculation assumes that ozone is only reacting with I^- in the aerosols, which is a poor assumption given that a similar or greater concentration of more surface-active organics that will also react at diffusion-controlled rates with ozone will be found in the marine aerosols.

The simultaneous detection of iodate, IO_3^- (m/z = 175), and triiodide, I_3^- (m/z = 381), as products of I^- oxidation by O_3 in this system implies that their putative precursor, the HOI intermediate formed in eq. 8.1

$$I^- + O_3 + H^+ = HOI + O_2 \tag{8.1}$$

also has a reactive half-life shorter than ~ 1 to 10 ms. This finding is, however, at odds with estimates based on bulk solution kinetic data and conditions. From $k^{II}(HOI + O_3)_{aq} = 3.6 \times 10^4\ M^{-1}\ s^{-1}$ [32], $k^{II}(HOI + I^- + H^+)_{aq} = 4.4 \times 10^{12}\ M^{-2}\ s^{-1}$ [33], $[O_3(aq)] \sim 1$ μM, $[I^-] \sim 10$ μM, at pH ~ 7 we estimate HOI half-lives toward oxidation by O_3 ($t_{1/2} = 19$ s) and reaction with I^- ($t_{1/2} = 0.16$ s) that are significantly longer than 1 ms. As expected from Scheme 8.1, the $[IO_3^-]/[I_3^-]$ ratio is an increasing function of $[O_3(g)]$ (Figure 8.2). Relative interfacial anion concentrations were derived from ESMS signal intensities S corrected by the response factors: $[IO_3^-]/[I^-] = 0.80 \times S(IO_3^-)/S(I^-)$, and $[I_3^-]/[I^-] = 0.76 \times S(I_3^-)/S(I^-)$, determined under present experimental conditions. Note that the detected I_3^-, which is presumably involved in the fast equilibrium: $I_2 + I^- \leftrightarrow I_3^-$ ($K_{eq} = 740\ M^{-1}$), must actually desorb from microdroplets in which [I^-] necessarily exceeds the μM range. Thus, while I^- is oxidized to HOI immediately after the droplets enter the O_3(g) plume, subsequent chemistry takes place in the increasingly concentrated aqueous media resulting from rapid solvent evaporation due to high (10 L/min) and hot (250° C) dry N_2 cross-flows [25]. Similar conditions are expected to develop, albeit at a slower pace, in the marine aerosol as they rise into the dry atmosphere[34]. IO_3^- and I_3^- yields calculated from interfacial I^- losses (m/z = 127) circumstantially exceed unity, revealing that interfacial layers are competitively replenished with I^- from the droplets core. These results suggest that the rates and mechanisms of chemical reactions at aerosol interfaces cannot be directly inferred from those in bulk solution[35].

We confirmed that aqueous Br^- and Cl^- are inert toward O_3 under present conditions, in line with reported rate constants $k^{II}(Br^- + O_3)_{aq} = 248\ M^{-1}\ s^{-1}$ [28], and $k^{II}(Cl^- + O_3)_{aq} = 0.1\ M^{-1}\ s^{-1}$, that are $\gtrsim 10^7$ times smaller than $k^{II}(I^- + O_3)_{aq}$ in bulk solution. However, ozonation experiments performed on (NaI + NaBr) and (NaI + NaCl) solutions readily yield the trihalide anions IBr_2^- and ICl_2^- (Figures 8.3a and 8.3b). IBr_2^- and ICl_2^- production rates increase with [O_3(g)] (Figure 8.4) while Br^- inhibits I^- depletion and depresses IO_3^- and I_3^- formation (Figure 8.5). IBr_2^- and ICl_2^- are, therefore, the products of Br^- and Cl^- oxidation by I-containing intermediates, such as HOI or the primary adduct I-OOO$^-$, that are considerably more reactive than O_3. Since rate constants for the reactions of halide anions with HOI are similar ($I^- \sim Br^- \sim 10\ Cl^-$)[36] the huge selectivity of the stronger oxidizer O_3 for I^- vs. Br^-/Cl^- is counterintuitive. Note that spin conservation requires the formation of excited $O_2(^1\Delta_g)$ in eq. 8.1. This restriction is more likely to be lifted by I^- than by Br^- or Cl^- via heavy atom enhancement of crossing rates into the triplet manifold that leads to ground state $O_2(^3\Sigma_g)^{37}$. By mitigating spin conservation constraints, eq. 8.1 becomes the gateway to the I^--mediated production of Br_2 (and Cl_2) from sea salt (Scheme 8.1). The efficiency of this cycle (i.e., the $[Br_2]/[IO_3^-]$ ratio) is expected to be a direct function of $[Br^-]/[O_3]$ at the droplets interface. Since Cl^- will always be present in large excess ($[Cl^-]/[Br^-]/[I^-] = 1.1 \times 10^6/1680/1$ in seawater) sea salt particles exposed to $O_3(g)$ will generate IBr_2^- and ICl_2^- rather than I_3^-, depending on actual interfacial halide and $[O_3(g)]$, and some Br^- will remain even after extensive atmospheric processing. Scheme 8.1 actually provides a plausible mechanism for buffering the $[IO_3^-]/[I^-]$ ratio[38].

Present experiments and analysis suggest that I^- may be the ‘minor component’ that enhances O_3 uptake and concomitant Br_2 formation in sea salt.[17] The iodide-mediated oxidation cycle in Scheme 8.1 qualifies as the previously unidentified dark process that may liberate dihalogens such as IBr(g), ICl(g), or even $Cl_2(g)$ and $Br_2(g)$ from sea salt into the boundary layer during the polar winter night[15]. The accumulation of these species on aerosol surfaces or in the atmosphere would prime the sudden destruction of O_3 at polar sunrise due to their quick photolysis ($\tau_{1/2} \sim 1$ to 2 min)[1]. The proposed mechanism of marine halide ozone oxidation should operate over the oceans worldwide, rather than just around coastal regions, at rates that may be locally modulated by wind speed, relative humidity, and atmospheric ozone concentration[8]. The fast halogen activation rates demonstrated by our experiments may exceed aerosol transport rates. In summary, fine marine aerosols are expected to be naturally enriched in I^- and Br^-, and the oxidation of these species by reactive gases such as ozone may release gaseous halogen species into the atmosphere even in the absence of sunlight. Further experiments will be completed to evaluate this process under more environmental conditions.

Figures

Figure 8.1. Normalized iodide concentrations $[I^-]/[I^-]_0$ vs. $[O_3(g)]$ A) (▼): 1 μM. (●): 10 μM. (▲) : 30 μM NaI) droplets. B) Linearized plot of the data of Figure 8.1a. See text. (▼): 1 μM; (●): 10 μM; (▲) : 30 μM NaI

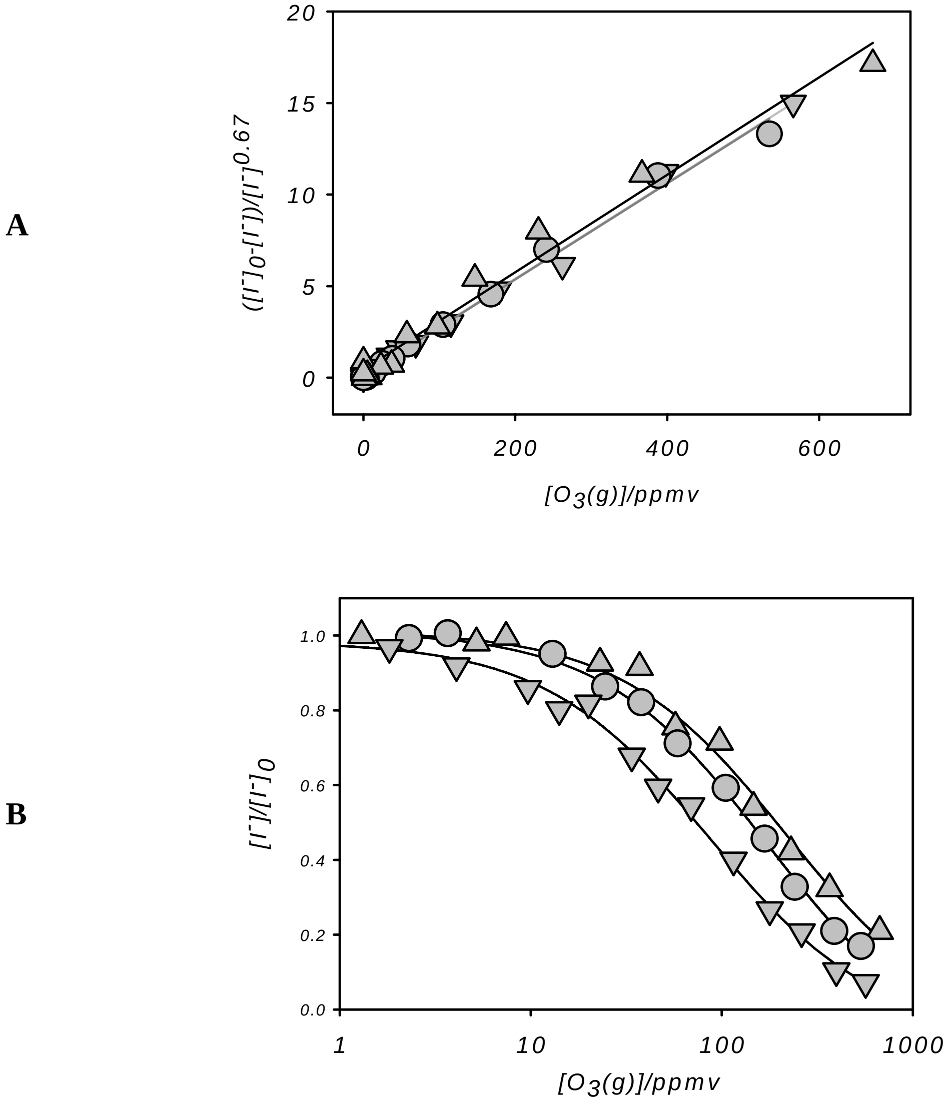

Figure 8.2. $[IO_3^-]/[I_3^-]$ ratio as function of $[O_3(g)]$. (▼): 1 μM; (●): 10 μM; (▲) :30 μM NaI. The straight line corresponds to a linear $[IO_3^-]/[I_3^-]$ vs. $[O_3(g)]$ dependence

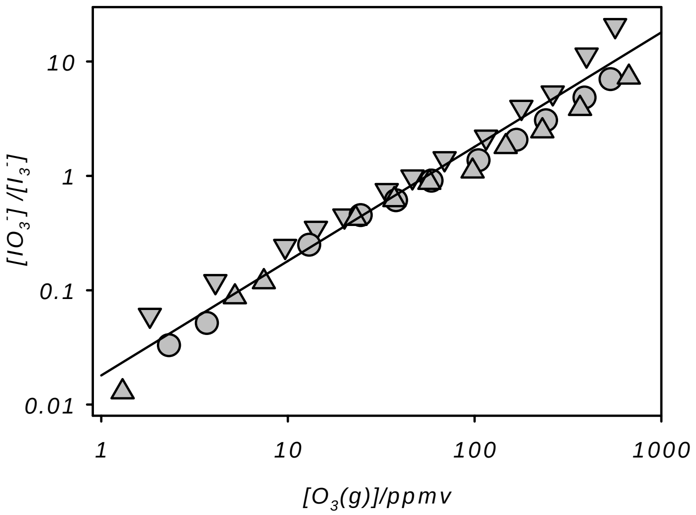

Figure 8.3. Aqueous NaBr-NaI or NaCl-NaI and $O_{3(g)}$ reaction products. A) Negative ion mass spectra of aqueous (10 μM NaI + 100 μM NaBr) droplets. **Blue trace**: Mass spectrum in 1 atm N_2. Peak 1: m/z = 127 (I^-). Peak group 2: m/z = 181, 183, and 185 ($NaBr_2^-$). **Red trace**: Mass spectrum in [840 ppm O_3(g) + 1 atm N_2] gas mixtures. Peak X: m/z = 175 (IO_3^-). Peak group Y: m/z = 285 ($I^{79}Br^{79}Br^-$), m/z = 287 ($I^{79}Br^{81}Br^-$), m/z = 289 ($I^{81}Br^{81}Br^-$). Peak Z: m/z = 381 (I_3^-). B) Negative ion mass spectra of aqueous (10 μM NaI + 10 mM NaCl) droplets. **Blue trace**: mass spectrum in 1 atm N_2. Peak 1: m/z = 127 (I^-). Peak group 2: m/z = 151, 153, 155, and 157 ($Na_2Cl_3^-$). Peak group 3: m/z = 209 to 217 ($Na_3Cl_4^-$). **Red trace**: mass spectrum in [690 ppm O_3(g) + 1 atm N_2] gas mixtures. Peak X: m/z = 175 (IO_3^-). Peak group W: m/z = 197 ($I^{35}Cl^{35}Cl^-$), m/z = 199 ($I^{35}Cl^{37}Cl^-$), m/z = 201 ($I^{37}Cl^{37}Cl^-$)

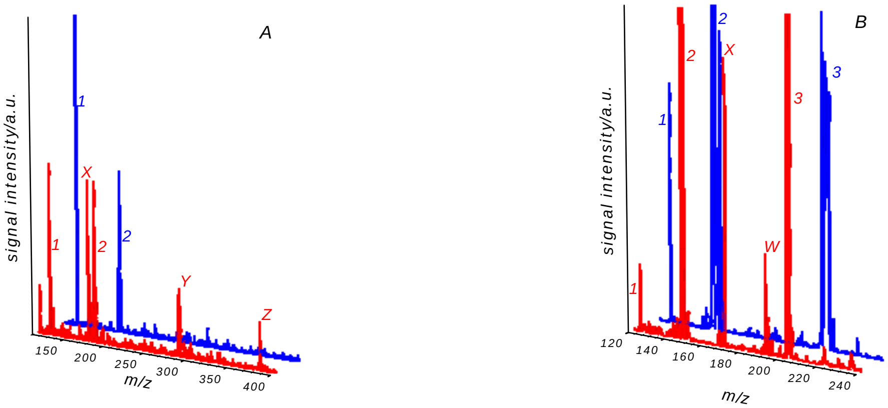

Figure 8.4. Aqueous NaBr-NaI or NaCl-NaI and $O_{3(g)}$ reaction products vs. $[O_{3(g)}]$. (▲): m/z = 287 ($I^{79}Br^{81}Br^-$) from ([NaI] = 10 μM + [NaBr] = 5 mM) droplets. (▼): m/z = 197 ($I^{35}Cl^{35}Cl^-$) from (10 μM NaI + 10 mM NaCl) droplets

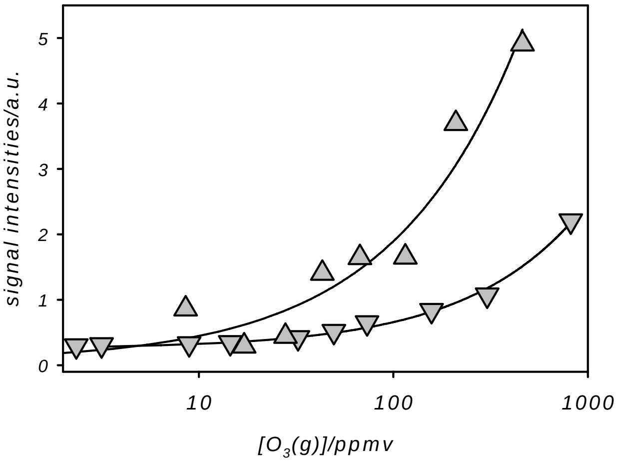

Figure 8.5. Aqueous NaBr-NaI and NaI and $O_{3(g)}$ reaction products vs. $[O_{3(g)}]$. (○): experiments in 10 μM NaI. (●): experiments in (10 μM NaI + 1 mM NaBr). ○: m/z = 127 (I^-); △: m/z = 175 (IO_3^-); ▽: m/z = 381 (I_3^-)

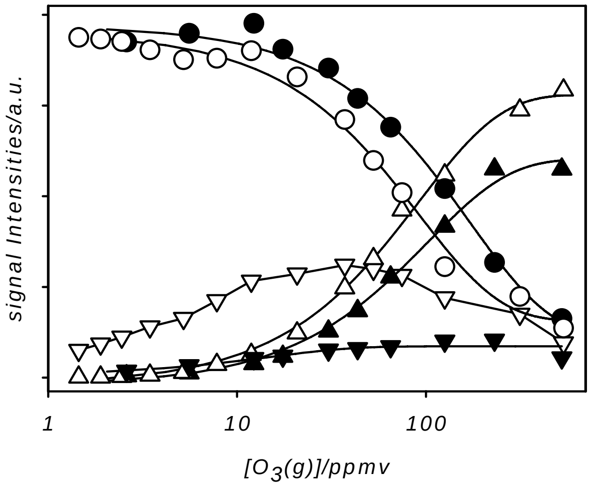

Scheme 8.1. Representation of iodide-mediated ozone oxidation of chloride and bromide

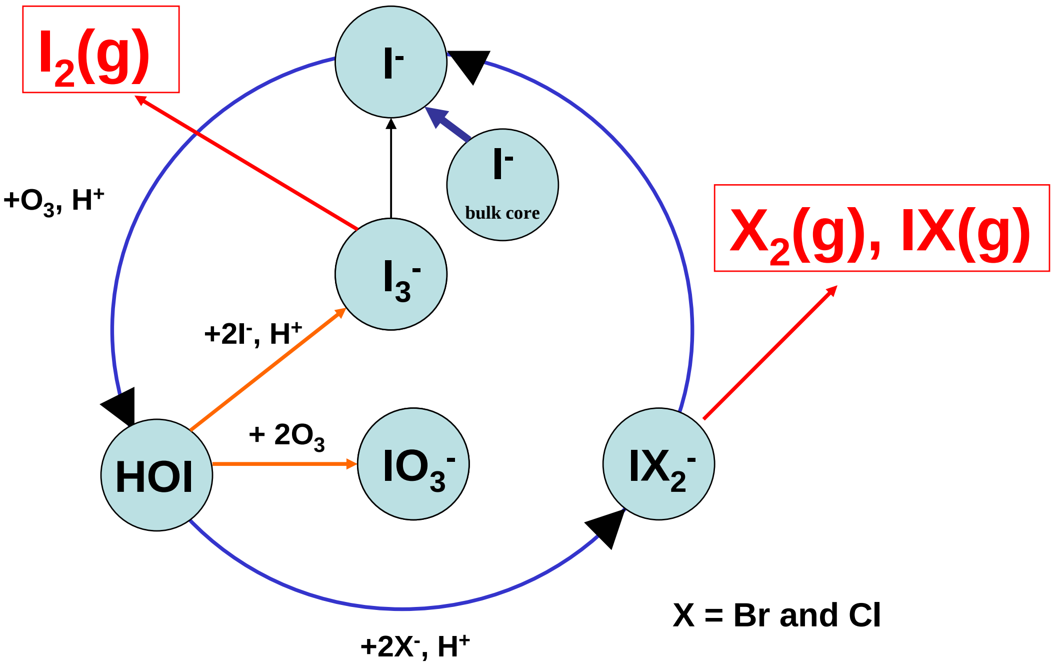

References

(1) Barrie, L. A.; Bottenheim, J. W.; Schnell, R. C.; Crutzen, P. J.; Rasmussen, R. A. *Nature* **1988**, *334*, 138.

(2) Sander, R.; Keene, W. C.; Pszenny, A. A. P.; Arimoto, R.; Ayers, G. P.; Baboukas, E.; Cainey, J. M.; Crutzen, P. J.; Duce, R. A.; Honninger, G.; Huebert, B. J.; Maenhaut, W.; Mihalopoulos, N.; Turekian, V. C.; Van Dingenen, R. *Atmos. Chem. Phys.* **2003**, 1301.

(3) Yang, X.; Cox, R. A.; Warwick, N. J.; Pyle, J. A.; Carver, G. D.; O'Connor, F. M.; Savage, N. H. *J. Geophys. Res.* **2005**, *110*, D23311.

(4) Sinnhuber, B. M.; Sheode, N.; Sinnhuber, M.; Chipperfield, M. P. *Atmos. Chem. Phys. Discuss.* **2006**, 6497.

(5) Simpson, W. R.; Von Glasow, R.; Riedel, K.; Anderson, P.; Ariya, P.; Bottenheim, J. W.; Burrows, J.; Carpenter, L.; Friess, U.; Goodsite, M. E.; Heard, D.; Hutterli, M.; Jacobi, H. W.; Kaleschke, L.; Neff, B.; Plane, J.; Platt, U.; Richter, A.; Roscoe, H.; Sander, R.; Shepson, P. B.; Sodeau, J.; Steffen, A.; Wagner, T.; Wolff, E. *Atmos. Chem. Phys. Discuss.* **2007**, *7*, 4285.

(6) World Metereological Organization (WMO), *Global Ozone Research and Monitoring Project*, *Scientific Assessment of Ozone Depletion: 2002, Report No. 47*; Geneva, 2003.

(7) Sioris, C. E.; Kovalenko, L. J.; McLinden, C. A.; Salawitch, R. J.; Van Roozendael, M.; Goutail, F.; Dorf, M.; Pfeilsticker, K.; Chance, K.; von Savigny, C.; Liu, X.; Kurosu, T. P.; Pommereau, J. P.; Bosch, H.; Frerick, J. *J. Geophys. Res.* **2006**, *111*, D14301.

(8) Dorf, M.; Butler, J. H.; Butz, A.; Camy-Peyret, C.; Chipperfield, M. P.; Kritten, L.; Montzka, S. A.; Simmes, B.; Weidner, F.; Pfeilsticker, K. *Geophys. Res. Lett.* **2006**, *33*, L24803.

(9) Schofield, R.; Johnston, P. V.; Thomas, A.; Kreher, K.; Connor, B. J.; Wood, S.; Shooter, D.; Chipperfield, M. P.; Richter, A.; von Glasow, R.; Rodgers, D. C. *J. Geophys. Res.* **2006**, *111*, D22310.

(10) Salawitch, R. J. *Nature* **2006**, *439*, 275.

(11) Salawitch, R. J.; Weisenstein, D. K.; Kovalenko, L. J.; Sioris, C. E.; Wennberg, P. O.; Chance, K.; Ko, M. K. W.; McLinden, C. A. *Geophys. Res. Lett.* **2005**, *32*, L05811.

(12) von Glasow, R.; von Kuhlmann, R.; Lawrence, M. G.; Platt, U.; Crutzen, P. J. *Atmos. Chem. Phys.* **2004**, *4*, 2481.

(13) Li, S. M.; Yokouchi, Y.; Barrie, L. A.; Muthuramu, K.; Shepson, P. B.; Bottenheim, J. W.; Sturges, W. T.; Landsberger, S. *J. Geophys. Res.* **1994**, *99*, 25415.

(14) Foster, K. L.; Plastridge, R. A.; Bottenheim, J. W.; Shepson, P. B.; Finlayson-Pitts, B. J.; Spicer, C. W. *Science* **2001**, *291*, 471.

(15) Hara, K.; Osada, K.; Matsunaga, K.; Iwasaka, Y.; Shibata, T.; Furuya, K. *J. Geophys. Res.* **2002**, *107*, D4361.

(16) Finlayson-Pitts, B. J. *Chem. Rev.* **2003**, *103*, 4801.

(17) Mochida, M.; Hirokawa, J.; Akimoto, H. *Geophys. Res. Lett.* **2000**, *27*, 2629.

(18) Lewis, E. R.; Schwartz, S. E. *Sea Salt Aerosol Production: Mechanisms, Methods, Measurements and Models—A Critical Review*, Vol. Geophysical Monograph 152; American Geophysical Union: Washington, D.C., **2004**.

(19) Murphy, D. M.; Thomson, D. S.; Middlebrook, A. M. *Geophys. Res. Lett.* **1997**, *24*, 3197.

(20) Murphy, D. M.; Cziczo, D. J.; Froyd, K. D.; Hudson, P. K.; Matthew, B. M.; Middlebrook, A. M.; Peltier, R. E.; Sullivan, A.; Thompson, D. S.; Weber, R. J. *J. Geophys. Res.* **2006**, *111*, D23S32.

(21) Cheng, J.; Vecitis, C.; Hoffmann, M. R.; Colussi, A. J. *J. Phys. Chem. B* **2006**, *110*, 25598.

(22) Pegram, L. M.; Record, M. T. *J. Phys. Chem. B* **2007**, *111*, 5411.

(23) Dodd, E. E. *J. Appl. Phys.* **1953**, *24*, 73.

(24) Reiter, R. *J. Geophys. Res.* **1994**, *99*, 10807.

(25) Kebarle, P. *J. Mass Spectrom.* **2000**, *35*, 804.

(26) Carpenter, L. J.; Hopkins, J. R.; Jones, C. E.; Lewis, A. C.; Parthipan, R.; Wevill, D. J. *Environ. Sci. Technol.* **2005**, *39*, 8812.

(27) Simpson, W. R.; Alvarez-Aviles, L.; Douglas, T. A.; Sturm, M.; Domine, F. *Geophys. Res. Lett.* **2005**, *32*, L04811.

(28) Liu, Q.; Schurter, L. M.; Muller, C. E.; Aloisio, S.; Francisco, J. S.; Margerum, D. W. *Inorg. Chem.* **2001**, *40*, 4436.

(29) Colussi, A. J.; Baghal-Vayjooee, M. H.; Benson, S. W. *J. Am. Chem. Soc.* **1978**, *100*, 3214.

(30) Davidovits, P.; Kolb, C. E.; Williams, L. R.; Jayne, J. T.; Worsnop, D. R. *Chem. Rev.* **2006**, *106*, 1323.

(31) Hanson, D. R. *J. Phys. Chem. B* **1997**, *101*, 4998.

(32) Bichsel, Y.; von Gunten, U. *Environ. Sci. Technol.* **1999**, *33*, 4040.

(33) Eigen, M.; Kustin, K. *J. Am. Chem. Soc.* **1962**, *84*, 1355.

(34) Gao, Y.; Chen, S. B.; Yu, L. E. *Atmos. Environ.* **2007**, *41*, 2019.

(35) Hunt, S. W.; Roeselova, M.; Wang, W.; Wingen, L. M.; Knipping, E. M.; Tobias, D. J.; Dabdub, D.; Finlayson-Pitts, B. J. *J. Phys. Chem. A* **2004**, *108*, 11559.

(36) Vogt, R.; Sander, R.; von Glasow, R.; Crutzen, P. J. *J. Atmos. Chem.* **1999**, *32*, 375.

(37) Muñoz, F.; Mvula, E.; Braslavsky, S. E.; von Sonntag, C. *J. Chem. Soc. Perkin Trans. 2* **2001**, 1109.

(38) Bruchert, W.; Helfrich, A.; Zinn, N.; Klimach, T.; Breckenheimer, M.; Chen, H.; Lai, S.; Hoffmann, T.; Bettmer, J. *Anal. Chem.* **2007**, *79*, 1714.

Chapter 9

Solar-Powered Electrochemical Production of Molecular Hydrogen from Water

Sections reprinted with permission from Park, H.; Vecitis, C. D.; Choi, W.; Weres, O.; Hoffmann, M. R. *Journal of Physical Chemistry C* **2008**, *112*, 4, 885–889.

Abstract

Electrochemical water splitting powered by conventional electricity or photovoltaic arrays produces molecular hydrogen at the cathode while organic compound oxidation under mild conditions takes place at the anode in competition with the production of oxygen. An electrolytic cell, which is based on the coupling of bismuth-doped titanium dioxide anodes (BiO_x-TiO_2) with stainless steel cathodes (SS), is characterized in terms of hydrogen production efficiency and organic compound degradation. In the solar-powered PV-electrochemical system, the production of molecular oxygen at the anode is suppressed by the simultaneous oxidation and mineralization of organic compounds dissolved in water. In addition, the anodic oxidation of organic substrates has a synergistic effect on hydrogen production at the cathode that results in a 53% increase in the energy efficiency for H_2 generation at circum-neutral pH in the presence of dilute electrolyte solutions.

Introduction

At the present time, the majority of industrial-scale hydrogen is produced by steam-methane reformation (SMR), even though the high temperature conversion of methane to hydrogen results in the concomitant production of carbon monoxide and carbon dioxide at a weight ratio of CO_2 to H_2 equal to 2.5. As a consequence, SMR has a relatively large carbon footprint. Carbon-free water electrolysis is considered to be less attractive given the rising costs of electricity[1-3]. However, the direct utilization of solar light for hydrogen production through photocatalytic[4] or photo-electrochemical[5,6] water splitting may provide an economically viable alternative source of hydrogen in the future.

There have been several previous reports of electrolysis systems powered nominally by photovoltaic arrays[7-9]. The PV arrays are used to convert solar light to electricity in order to power alkaline (e.g., 27% KOH at pH 14.7) electrolyzers for producing hydrogen gas. However, these systems are thought to be impractical in that the cost of hydrogen is greater than conventional DC-electrolysis, which in turn, is more expensive than SMR.

Narayanan et al. describe a DC-powered hybrid system that drives a methanol fuel cell in reverse[10], while Soler et al. report on a solar-powered photo-Fenton process that produces hydrogen noncatalytically under severe condition with a limited number of organic substrates[11]. Mathieson et al. described a hybrid electrolytic system that functions via the induced corrosion of the anode to release the corresponding metal ions to solution, which lead to the coagulation and subsequent removal of high-molecular-weight organic compounds from water[12]. Drew et al. reported TiO_2/Ru-Pt hybrid catalyst for boosting fuel cell performance[13].

In this letter, we report on a hybrid photovoltaic electrochemical reactor that results in the simultaneous production of molecular hydrogen via water splitting at stainless steel cathodes, while organic substrates are oxidized at metal-doped TiO_2 anodes (Scheme 9.1). Semiconductor electrodes have been used to drive the electrochemical splitting of water into hydrogen and oxygen. However, we have previously demonstrated that the oxidation of water via an overall four-electron oxidation can be suppressed by using anodes made with niobium-doped polycrystalline TiO_2 particles attached to metallic titanium plates[14]. Metal-doped TiO_2 electrodes preferentially oxidize water to hydroxyl radical due to the formation of surface titanol (>TiOH) groups on hydrated titanium dioxide surfaces at current efficiencies approaching 50%. In addition, the surface-bound hydroxyl radicals on the semiconductor anodes can be utilized to preferentially oxidize a wide variety of organic and inorganic substrates[14]. In this letter, we characterize the electrochemistry of a mixed-metal oxide anode that is based on a mixture of bismuth oxide and Bi-doped TiO_2 that is coupled to a stainless-steel cathode and powered by a photovoltaic panel.

The BiO_x-TiO_2-coated titanium anode[15] and stainless steel cathode were immersed in an electrolyte solution (e.g., 50 mM NaCl) in a reactor with a total volume of either 200 mL in a single electrode couple or 20 L with multiple electrode couples. Organic substrates were mixed into the background electrolyte solutions or added during the course of electrolysis. A constant cell voltage or current was applied to the electrodes either with a DC power supply (HP 6263B and 6260B) or with a commercial amorphous silicon PV panel (Silicon Solar, Inc.) that has a power rating of 6.4 W with a peak output potential, E_{peak} = 8–10V, and a peak current of I_{peak} = 0.95A for an active surface area of 1280 cm^2 (Scheme 9.1). The theoretical maximum solar-to-electric energy efficiency is estimated to be 4.5% according to the specifications of the PV manufacturer. Solar radiation was monitored by a pyranometer (Apogee) connected to a data-logger (Campbell Scientific). Cell voltage (E_{cell}) and current (I_{cell}) were monitored with a digital multimeter (Fluke). The current efficiencies and the energy efficiencies are obtained as follows in eqs. 9.1 and 9.2.

$$\text{Current efficiency (\%)} = \frac{\#\text{ molecules produced } (\mathrm{H_2}, \mathrm{O_2}, \text{ or } \mathrm{CO_2}) \text{ or degraded (phenol)}}{\#\text{ electrons}} \times n \times 100 \tag{9.1}$$

$$\mathrm{H_2}\text{ production energy efficiency (\%)} = \frac{(39\mathrm{W}\cdot\mathrm{h/g} \times \mathrm{H_2}\text{ rate} \times 2\mathrm{g/mol})}{\mathrm{E_{cell}} \times I_{\mathrm{cell}}} \times 100 \tag{9.2}$$

where n = 2 and 4 for hydrogen and oxygen production cathodic current (CE) efficiencies, respectively. For anodic current efficiencies, n = 1 for one-electron oxidation of phenol, and n = 14/3 for complete mineralization from phenol carbon to carbon dioxide.

The electrolytic reactors were sealed to the atmosphere and the headspace gas was extracted at a known rate by a peristaltic pump. The extracted headspace gas was pulled through a stainless steel membrane into the vacuum chamber (5.0×10^{-6} torr), evacuated by a membrane pump and a turbo pump (Pfeiffer Vacuum), where it was ionized by high-energy electrons and analyzed by quadrupole mass spectrometry (Balzers). The volume percent of the headspace was calculated by assuming that the observed signal intensity was directly proportional to the ion current measured by the mass spectrometer (i.e., the transfer of all gases through the membrane and their 70 eV electron ionization cross-sections were roughly equivalent). This assumption is validated by the fact that ambient air was measured to be 77% nitrogen, 17% oxygen, 5% water vapor, and 1% argon.

Aqueous organic compounds including intermediates were analyzed by high performance liquid chromatography (HPLC, Agilent 1100 series) with separation on a

C18 column. The eluent composition was 55% Milli-Q water (0.1 wt% acetic acid) and 45% acetonitrile at flow rate of 0.7 mL min^{-1}. Analyte concentrations were monitored by UV-Vis spectrophotometry. Total organic carbon measurements were made with an OI Analytical Aurora Model 1030 TOC analyzer coupled to an autosampler (OI Analytical Model 1096).

The composite BiO_x-TiO_2 anodes, when coupled with stainless steel (SS) cathodes have an inherent potential ranging from + 0.2 to + 0.5 V, due to the formation of a space-charge layer within the TiO_2 particles bound to the titanium substrate. Water splitting and current flow commence at an applied cell voltage of + 2.0 V, with an observed a linear correlation between the measured rates of H_2 and O_2 production, eq. 9.3 (Figure 9.1).

$$2\,H_2O \xrightarrow{E>+2.1\,V} 2\,H_2 + O_2 \tag{9.3}$$

The H_2/O_2 mole ratio for the electrolysis of pure water (i.e., without added substrates) depends on the background electrolyte. In the case of sodium sulfate (50 mM), the observed H_2/O_2 mole production ratio is 5.2, while in the presence of sodium chloride (50 mM) the corresponding mole ratio (H_2/O_2) is increased to 7.6 (Figure 9.1). The sharp departures from a theoretical 2 to 1 mole ratio for water splitting indicate that electrochemical reaction products or intermediates other than oxygen are being formed at the semiconductor anode. These reactions include the oxidation of surface-bound hydroxyl groups of hydrated TiO_2 to produce hydroxyl radicals (i.e., eq. 9.4, as depicted in Scheme 9.1), as well as the oxidation of the background electrolyte (e.g., Cl^-; eq. 9.5).

$$\mathbf{> Ti - OH \rightarrow > Ti - OH^{\bullet} + e^{-}} \tag{9.5}$$

At applied potentials greater than 2.0 V, the one-electron oxidation of chloride ($E°(Cl^{•}/Cl^{-})$ = 2.55 V vs. NHE) and sulfate ($E°(SO_4^{•-}/SO_4^{2-})$ = 2.43 V vs. NHE) are competitive with water oxidation.

When powered by a photovoltaic (PV) panel, the cell voltage (E_{cell}) of the reactor increases to +4 V with a corresponding current (I_{cell}) close to 0.9 A (i.e., 30 mA cm^{-2}), as shown in Figure 9.2. The voltage and current of the electrodes are nearly constant under steady sunlight irradiation at a measured solar flux of 1100 $W{\cdot}m^{-2}$. The hybrid PV-electrochemical reactor system produces hydrogen at a rate of 0.18 mmol min^{-1} and oxygen at rate of 0.028 mmol min^{-1}, which corresponds to a ratio of the rates of production (i.e., a H_2/O_2 mole ratio) that is near 7.

With the addition of phenol, the hydrogen production rate is enhanced by 20 to 30% and the oxygen production rate is slightly decreased. The overall energy efficiency for H_2 production ranges from 30 to 40% depending on the PV panel output energy. The DC-powered current efficiency for the hybrid electrolysis ranges from 70 to 95%, while the corresponding energy efficiencies for H_2 production range from 36 to 61%, depending on operating conditions (Table 9.1). These values compare favorably with industrial-scale electrolysis employing alkaline or proton exchange membrane electrolyzers with reported energy efficiencies ranging from 56 to 73%. Our hybrid PV- and DC-powered systems operate at comparable efficiencies; however, they have distinct advantages over commercial electrolytic devices, in that the hybrid system is efficient at low electrolyte concentrations at circum-neutral pH under ambient temperature and pressure. The overall solar-to-hydrogen energy efficiency is thereby limited by the actual solar light energy-to-electric power conversion efficiency (ε) of the specific PV system that is used to drive electrolytic water splitting with semiconductor electrodes.

In the case of phenol, oxidative degradation (> 99%) is achieved within 10 min ($t_{1/2}$ ~ 1 min) (Figure 9.2). The electrolytic oxidation follows first-order kinetics with the eventual conversion of the phenolic carbon into CO_2. This overall process can be repeated with each successive addition of phenol to the hybrid PV-electrolytic reactor. The phase-delay for the detectable production of carbon dioxide relative to the disappearance of phenol indicates that carbon-containing intermediates are produced and are involved in further competitive reactions at the semiconductor anode. Reaction intermediates found during electrolysis at a constant current density of 14 mA cm^{-2} with NaCl as the background electrolyte included mono-, di-, and tri-chlorophenol (Figure 9.3). When added individually, the chlorinated phenols are destroyed in the following order of relative electrochemical reactivity: 2,4,6-trichlorophenol (3.74) > 2,6-dichlorophenol (1.84) > 2,4-dichlorophenol (1.38) > phenol (1.0) > 2-chlorophenol (0.78) > 4-chlorophenol (0.57) (Table 9.1), where the numbers in parenthesis represent reaction rates relative to phenol. The trichlorophenol reaction intermediate undergoes a sequential dechlorination through a cyclopentene intermediate, followed by production of simple aliphatic acids that are formed after ring opening. The aliphatic acid intermediates are then oxidized to CO_2 by surface-bound hydroxyl radicals that are produced at the anode (R1 in Scheme 9.1). Due to the competitive reactions of phenol and intermediates at the anode, the one-electron oxidation current efficiency for the oxidation of phenol is 10%, even though the cathodic current efficiency for hydrogen production is close to 70%. Production of the intermediate chlorinated phenols is consistent with the formation of chlorine radicals such as $Cl^{\bullet}$ and $Cl_2^{\bullet-}$ at the semiconductor anode (R3) when NaCl is used as the background electrolyte. Furthermore, the overall degradation of the chlorinated phenol intermediates leads to the generation of carbon dioxide. For phenol, the total amount of carbon, from carbon dioxide in the PV-connected (30 min, Figure 9.2) and the DC-powered (100 min, Figure 9.3) systems corresponds to around 25% of the phenolic carbon with the time-scale for CO_2 release depending on the initial substrate concentration and reaction conditions (e.g., NaCl concentration). The remainder of the phenolic carbon is present in solution as HCO_2^-, $C_2O_4^{2-}$, HCO_3^-, and CO_3^{2-}.

When phenol is added to the electrochemical reactor, the cell-voltage increases from 4.0 V to 4.2 V, while, at the same time, the cell current appears to be invariant when powered by the PV panel (Figure 9.2). It is clear from the data presented in Figure 9.2 that the addition of phenol increases the hydrogen rate under constant solar radiation (~ 1100 W m^{-2}). Hydrogen production rates are also enhanced with the addition of maleic acid, oxalic acid, catechol, salicylic acid, and a variety of chlorinated phenols as shown in Table 9.1. As depicted in Scheme 9.1, R5 is thermodynamically favored over R4 ($E(Cl_2^{\bullet-}/2Cl^-) = +2.3$ V; $E(H_2O/H_2,OH^- = -0.41$ V at pH 7), and competes with R4 for electron at the cathode. However, the added organic compounds react with the intermediate radical species such as $HO^{\bullet}$, $Cl^{\bullet}$, $Cl_2^{\bullet-}$ (R6), which are produced at the anode (R1 & R3) and reduced at the cathode. Since phenol and the other organic substrates react with $HO^{\bullet}$, $Cl^{\bullet}$, and $Cl_2^{\bullet-}$ in solution, as opposed to the cathode surface, more electrons are available for water or proton reduction at the cathode (R4), thereby resulting in increasing H_2 production energy efficiencies of 30 to 53% at lower I_{cell}. In contrast, aliphatic acids increase the observed H_2 production energy efficiencies by a smaller amount (~ 10%) due to their slower oxidation kinetics and lesser radical (e.g., $Cl_2^{\bullet -}$) reaction rates.

We envision that hybrid PV electrochemical systems could be used for solar-powered water purification, coupled with the generation of a potentially useful and energy rich byproduct. Also, solar light could be directly irradiated to the anode connected to PV to boost the organic oxidation and give much greater synergy effects on the hydrogen production.

Tables

Table 9.1. Electrochemical organic oxidation and hydrogen production[a]

Substrate	k_{obs}[b] (min^{-1})	E_{cell}[c] (V)	H_2[d] (10^{-6} mol/min)		I_{cell} (A)[e]		Energy Efficiency (%)[f]		
			before	after	before	after	before	after	Δ[g]
Maleic acid	-	3.07	70	75	0.29	0.29	45.7	49.4	8.0
Oxalate	-	3.05	71	78	0.30	0.30	45.0	49.6	10.2
Phenol	0.21	3.10	66	86	0.38	0.32	33.0	50.5	53.1
Catechol	0.13	3.25	104	126	0.44	0.42	42.5	54.2	27.3
Hydroquinone	0.96	-	-	-	-	-	-	-	-
Salicylic acid	0.087	3.17	51	63	0.34	0.32	27.8	36.4	31.2
2-ClPhOH	0.17	3.14	67	81	0.34	0.30	36.8	50.2	36.3
4-ClPhOH	0.12	3.18	80	100	0.32	0.30	46.0	61.3	33.3
2,4-ClPhOH	0.29	-	-	-	-	-	-	-	-
2,6-ClPhOH	0.39	-	-	-	-	-	-	-	-
2,4,6-ClPhOH	0.79	-	-	-	-	-	-	-	-

a. 50 mM NaCl used as an electrolyte

b. Observed degradation rates of aqueous pollutants at constant current density of 14 mA cm^{-2}

c. Constant cell voltage

d. Hydrogen production rate before and after addition of substrate (1 mM) at a given voltage

e. Cell current before and after addition of substrate (1 mM) at a given voltage

f. Energy efficiency (EE) for hydrogen production = $(39 W \cdot h/g\text{-}H_2 \times H_2 \text{ rate} \times 2 g/mol\text{-}H_2)/(E_{Cell} \times I_{Cell}) \times 100\%$

g. $\Delta = (\text{EE after} - \text{EE before})/\text{EE before} \times 100\%$

Figures

Figure 9.1. Electrochemical H_2 and O_2 production. A) Real-time profiles of H_2 and O_2 as a function of cell voltage (E_{cell}). B) Effects of E_{cell} on cell current (I_{cell}). C) I_{cell} vs. the H_2 and O_2 production rates in different supporting electrolyte medium (Na_2SO_4 vs. NaCl). 50 mM NaCl or 50 mM

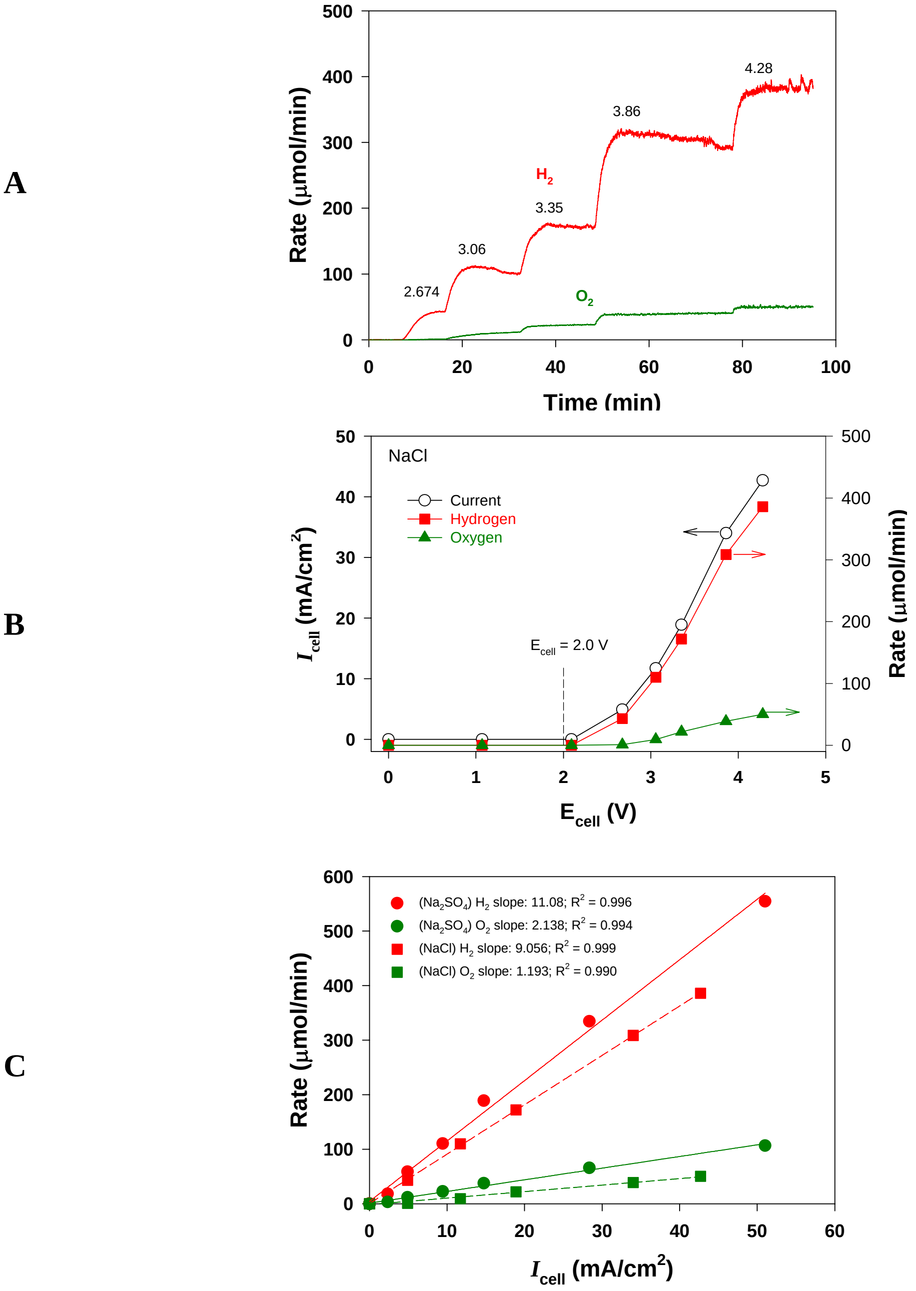

Figure 9.2. Outdoor field test of PV-electrochemical system (April 18th, 2007) on the roof of W.M. Keck Laboratories at the California Institute of Technology. Upper panel: Measurements of temperature and solar radiation (I_S). Middle panel: Measurements of E_{cell} and I_{cell}. Bottom panel: Measurements of phenol degradation (C_t/C_0), CO_2 generation, and hydrogen production. 1 mM of phenol was injected 6 times separately during the electrolysis with 50 mM NaCl

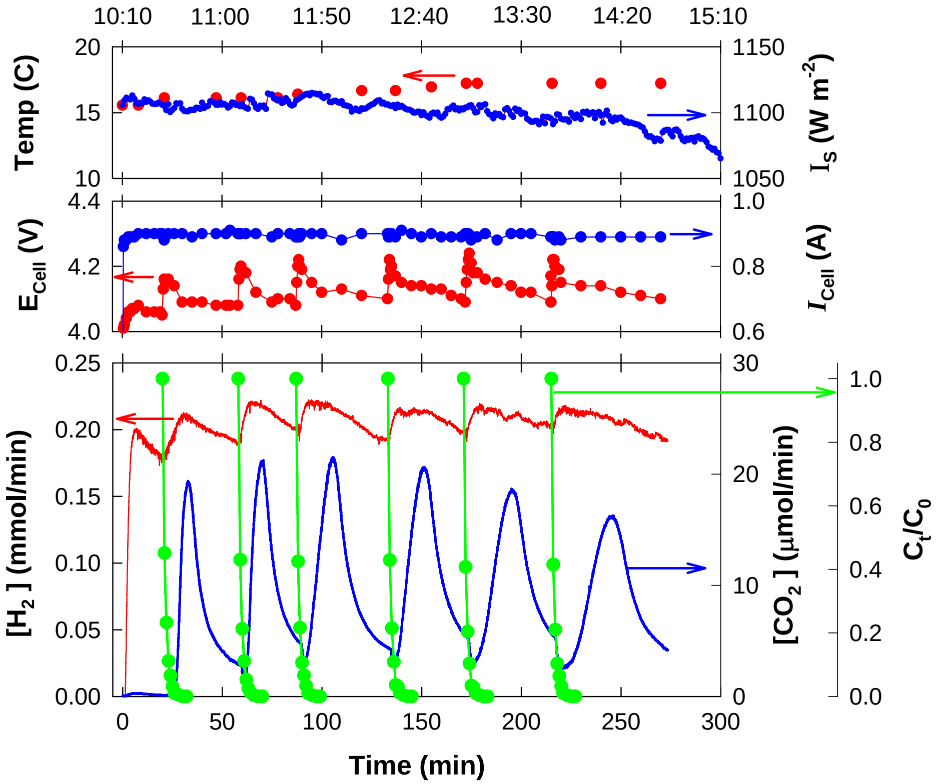

Figure 9.3. Products of electrolytic degradation of 1 mM phenol. TOC change and carbon balance at constant current (14 mA cm^{-2}). Phenol (●), 2-chlorophenol (🔴), 4-chlorophenol (🟢), 2,4-dichlorophenol (🟡), 2,6-dichlorophenol (🔵), 2,4,6-trichlorophenol (🟣), CO_2 (—), TOC (■), and carbon balance (□)

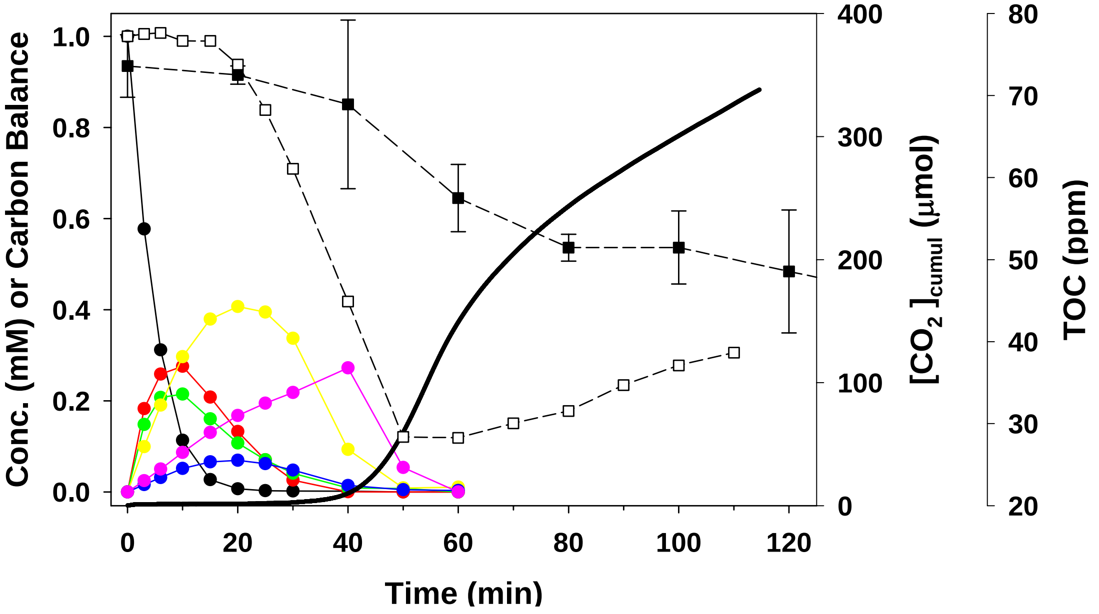

Scheme 9.1. Schematic diagram of the electrochemical setup

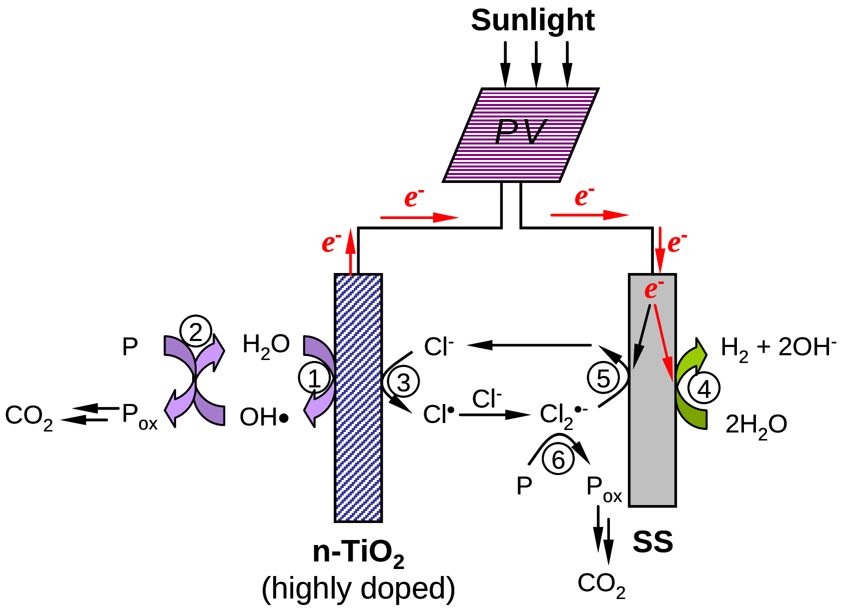

References

1. Turner, J. A. *Science* **2004**, *305*, 972.
2. *Solar and Wind Technologies for Hydrogen Production*, available at http://www.hydrogen.energy.gov/congress_reports.html.
3. Ivy, J. *Summary of Electrolytic Hydrogen Production: Milestone Completion Report*, available at www.nrel.gov/hydrogen/pdfs/36734.pdf.
4. Maeda, K.; Teramura, K.; Lu, D. L.; Takata, T.; Saito, N.; Inoue, Y.; Domen, K. *Nature* **2006**, *440*, 295.
5. Grätzel, M. *Nature* **2001**, *414*, 338.
6. Khaselev, O.; Turner, J. A. *Science* **1998**, *280*, 425.
7. Friberg, R. *Int. J. Hydrogen Energy* **1993**, *18*, 853.
8. Ahmad, G. E.; El Shenawy, E. T. *Renewable Energy* **2006**, *31*, 1043.
9. Lehman, P. A.; Chamberlin, C. E.; Pauletto, G.; Rocheleau, M. A. *Int. J. Hydrogen Energy* **1997**, *22*, 465.
10. Narayanan, S. R.; W., C.; Jeffries-Nakamura, B.; Valdez, T. I. *Hydrogen Generation by Electrolysis of Aqueous Organic Solutions*; U.S. Patent 6,368,492; Apr. 9, **2002**.
11. Soler, L.; Macanas, J.; Munoz, M.; Casado, J. *Int. J. Hydrogen Energy* **2006**, *31*, 129.
12. Mathieson, G.; Langdon, A.; Jamieson, G. *Dev. Chem. Eng. Mineral Process* **2006**, *14*, 71.
13. Drew, K.; Girishkumar, G.; Vinodgopal, K.; Kamat, P.V. *J. Phys. Chem. B* **2005**, *109*, 11851.

14. Kesselman, J. M.; Weres, O.; Lewis, N. S.; Hoffmann, M. R. *J. Phys. Chem. B* **1997**, *101*, 2637.

15. Weres, O. *Electrode with Surface Comprising Oxides of Titanium and Bismuth and Water Purification Process Using This Electrode;* U.S. Patent 0,000,774 A1; Jan. 4, **2007**.

Chapter 10

Electrochemical Anodic Oxidation of Organic Compounds Coupled with the Cathodic Production of Molecular Hydrogen

Sections reprinted with permission from Park, H.; Vecitis, C. D.; Hoffmann, M. R.
Journal of Physical Chemistry A **2008**, *112*, 33, 7616-7626.

Abstract

A Bi-doped TiO_2 anode, which is prepared from a mixed-metal oxide coating deposited on Ti metal, coupled with a stainless steel cathode is shown to be efficient for conventional water splitting. In this hybrid photovoltaic/electrochemical system, a photovoltaic (PV) cell is used to convert solar light to electricity, which is then used to oxidize a series of phenolic compounds at the semiconductor anode to carbon dioxide, with the simultaneous production of molecular hydrogen from water/proton reduction at the stainless steel cathode. Degradation of phenol in the presence of a background NaCl electrolyte produces chlorinated phenols as reaction intermediates which are subsequently oxidized completely to carbon dioxide and low-molecular-weight carboxylic acids. The anodic current efficiency for the complete oxidation of phenolic compounds ranges from 3 to 17%, while the cathodic current efficiency and the energy efficiency for hydrogen gas generation ranges from 68 to 95% and from 30 to 70%, respectively.

Introduction

Hydrogen is under consideration as a viable alternative and renewable energy source. This is partially due to the increasing price of fossil fuels and a growing demand for fuels that are carbon-free and therefore environmentally benign[1–3]. In the United States alone, the hydrogen market was estimated to have an economic value of $798 million in 2005; this number is expected to rise to $1,600 million in 2010[3]. Hydrogen is produced primarily by steam-methane reformation (SMR). SMR accounts for 95% and 48% of all hydrogen produced in the U.S. and in the world, respectively. However, the SMR process has a large carbon footprint in the form of carbon dioxide and carbon monoxide emissions. For example, the carbon released during SMR is 2.5 times by mass greater than the hydrogen produced.

Electrochemical water splitting (i.e., electrolysis) provides a zero-carbon alternative to SMR. However, the major component of the cost of electrolytic hydrogen production is not the energy efficiency, but the price of electricity. In this regard, the U.S. Department of Energy (DOE) has established a target energy efficiency of 76% (corresponding to \$2.75/GGE H_2) for electrolytic hydrogen generation (e.g., alkaline electrolyzers or proton exchange membrane electrolyzers) by 2015. The current average for commercial electrolyzers is 62%[4]. In order to reduce the overall cost of the electrolysis, low-cost, renewable energy sources, such as solar light, should be utilized as an energy source. Alternatively, the overall costs could also be reduced by implementation of a dual-purpose electrolytic system that couples hydrogen generation with energy-intensive water or wastewater treatment.

The underlying concept of solar-light driven (PV) electrolysis for hydrogen production has been previously suggested and evaluated[5–9]. The primary objective is to produce hydrogen as a storable fuel of high energy density for the dark generation of electricity. This approach is an alternative to a battery-based storage system. However, the PV-electrolyzer-hydrogen systems were determined to be economically impractical as compared to the PV-electricity-battery systems, due to inefficiencies of converting electrons to hydrogen. Thus it is suggested to simultaneously treat wastewater by electrolysis to improve overall energy efficiencies. Hybrid systems which electrolytically produce hydrogen while simultaneously oxidizing organic substrates have also been reported[10–12]. However, the previously reported systems operate noncatalytically, with much lower efficiencies, and require severe conditions (e.g., $pH < 2$, molar ranges of reagents), making them nonpractical.

Therefore, in order to address the goal of PV-driven electrolytic hydrogen production with simultaneous oxidation of wastewater constituents, we have combined a stainless-steel (SS) cathode for reductive hydrogen production with a Bi-doped TiO_2 anode for oxidative organic destruction. It was determined that the hybrid electrolysis system operates catalytically (addition of organics increases H_2 production efficiencies) under mild conditions (50 mM salt) with relatively high efficiencies (30% to 70% H_2 energy efficiencies).

The details of the electrochemistry give insight into these processes. The anode generates oxidizing radical species (e.g., $OH^\bullet$, $Cl^\bullet$) (eq. 10.1), which subsequently react with aqueous pollutants while the cathode splits water into hydrogen (eq. 10.2). Oxygen evolution via water oxidation (eq. 10.3) is normally the complementary reaction to H_2

production (eq. 10.2) and thus the generation of radical species (eq. 10.1) at the anode results in nonstoichiometric water splitting (i.e., $H_2/O_2 > 2$).

$$H_2O \rightarrow OH^{\bullet} + H^{+} + e^{-} \quad (E° = 2.74 \text{ V vs. NHE}) \qquad (10.1)$$

$$2H_2O + 2e^{-} \rightarrow H_2 + 2OH^{-} \quad (E° = 0 \text{ V}) \qquad (10.2)$$

$$2H_2O \rightarrow O_2 + 4H^{+} + 4e^{-} \quad (E° = 1.23 \text{ V}) \qquad (10.3)$$

$$C_xH_yO_z + (x + 0.25y - 0.5z)\, O_2 \rightarrow xCO_2 + 0.5\, yH_2O \qquad (10.4)$$

Previously, we developed a Nb^{4+}-doped polycrystalline TiO_2 anode, which generated hydroxyl radical via one-electron oxidation of water at average current efficiencies of 50%[13-16]. However, a newer, more robust, and longer lived semiconductor anode based on a mixed metal oxide of BiO_x-TiO_2 has been developed. This anode operates at current efficiencies in the range of 20 to 30%[17]. In this study, a BiO_x-TiO_2 anode is coupled with stainless steel cathode and powered by a photovoltaic (PV) array to oxidize organic substrates while simultaneously generating molecular hydrogen (Scheme 10.1)[18,19]. Phenol is used as a model chemical substrate as phenolic compounds are a common contaminant present in industrial (solvents) and municipal (detergent by-products) wastewater[20,21].

Experimental Methods

Electrodes

The anode was prepared as follows: 1) A Ti metal sheet (Ti-Gr.2 sheet, 0.50 mm thick) was cleaned using SiC paper (120 to 240 grit) before coating with a sequence of substrates (Scheme 10.2a). 2) An initial metal oxide coating containing Ir and Ta oxides at an Ir:Ta = mole ratio of 0.67:0.33 is deposited and annealed to the Ti metal base. 3) A second metal oxide coating of Bi-doped SnO_2 at a Sn:Bi mole ratio of 0.9:0.1 is applied and annealed. 4) A third layer of Bi-doped TiO_2 at a Ti:Bi mole ratio of 0.96:0.04 is applied and annealed at high temperature. 5) The final step involves the deposition of the anodically active overcoat that also contains Bi-doped TiO_2 at a Ti:Bi mole ratio of 0.9:0.1. Each successive step of coating requires a specific heat-treatment regime at different temperatures and durations. More details are provided elsewhere[17]. Two types of anode-cathode couples were used for the experiments reported herein. The first couple is composed of a single anode with an active area of contact with the electrolyte solution of 10.0×2.0 cm^2, and two-piece stainless-steel (SS) cathodes (Hastelloy C-22) of the same size on both sides (i.e., a sandwich configuration) of the Bi-doped TiO_2 anode, at a separation distance of 2 mm. The second configuration involves a small pilot-scale reactor consisting of 5 anode plates (5 pieces × 800 cm^2/piece) and 6 stainless steel cathode plates that face each other with a distance of separation of 2 mm (Scheme 10.2b).

Electrolysis Experiments

The BiO_x-TiO_2 anode and SS cathode couple was immersed in an aqueous electrolyte solution of 50 mM NaCl (200 mL or 20 L) and was stirred under continuous purging with air or nitrogen as a background carrier gas. The target substrates (e.g., phenol) were mixed in with a background electrolyte or added during the course of electrolysis. A constant cell voltage or current was applied to the electrodes with a DC power supply (HP 6263B and 6260B). For the PV-powered electrolyses, a commercial thin film, amorphous silicon PV (Silicon Solar, Inc.) with a peak power output of 6.4 W ($PV_{peak} = E_{peak} \times I_{peak}$; $E_{peak} = 8 – 10$ V; $I_{peak} = 0.95$A) and with active surface area of 1280 cm^2 was used (Scheme 9.1). Incident solar radiation was monitored and recorded with a pyranometer (Apogee) connected to a datalogger (Campbell Scientific). Cell voltage (E_{cell})

and cell current (I_{cell}) were measured by multimeters (Fluke). The current efficiencies (CEs) and the energy efficiencies (EEs) for hydrogen production (i.e., higher heating value) were obtained by the following equations 10.5–10.9

$$\text{CE (\%)} = \frac{\text{Number of molecules produced (H}_2\text{, O}_2\text{, or CO}_2\text{) or degraded (phenol)}}{\text{Number of electrons flowed}} \times \text{n} \times 100 \tag{10.5}$$

$$\text{DC or PV-powered Electrolytic H}_2\text{ EE} = \left(\frac{(39\ \text{W} \cdot \text{h/g} \times \text{H}_2\ \text{rate} \times 2\ \text{g/mol})}{\text{E}_{\text{cell}} \times I_{\text{cell}}} \right) \times 100\% \tag{10.6}$$

$$\text{PV}_{\text{cell}} = \text{E}_{\text{cell}} \times I_{\text{cell}}\ \text{(applied to the cell reactor)} \tag{10.7}$$

$$\text{Solar-to-PV}_{\text{cell}}\ \text{EE} = \left(\frac{\text{PV}_{\text{cell}}\ \text{(W)}}{\text{Solar Flux (W cm}^{-2}\text{)} \times \text{PV Area (cm}^{2}\text{)}} \right) \times 100\% \tag{10.8}$$

$$\text{Solar-to-H}_2\ \text{EE} = \left(\text{Electrolytic H}_2\ \text{EE} \times \text{Solar-to-PV EE} \right) \times 100\% \tag{10.9}$$

where n = 2 and 4 for hydrogen and oxygen production in cathodic current efficiencies (CCEs), respectively. For the anodic current efficiencies (ACEs), n = 1 for one-electron oxidation of phenol (ACE-I), and n = 14/3 for complete oxidation from carbon at phenol to carbon at carbon dioxide (ACE-II).

Analytical Procedures

The reactor was sealed from the ambient atmosphere. At a given rate, the headspace gas of the reactor was extracted with a peristaltic pump and extracted by a differentially pumped membrane inlet into a low-pressure cell with a quadrupole mass spectrometry (Balzers) via a turbo pump (Pfeiffer; 5.0×10^{-6} torr). The volume percent of various gases in the headspace was calculated assuming that the percent was directly proportional to the ion current measured by the mass spectrometer, and that the transfer of all gases through the membrane and their 70 eV electron ionization cross-sections were approximately equivalent. This assumption was validated in part since ambient air was measured to be 77% nitrogen, 17% oxygen, 5% water vapor, and 1% argon.

Aqueous organic compounds including intermediates were analyzed by a high-performance liquid chromatography (HPLC, Agilent 1100 series) with a C18 column. The eluent was composed of 55% Milli-Q water (0.1 wt% acetic acid) and 45% acetonitrile at flow rate of 0.7 mL/min. Analyte concentration was monitored by UV-Vis spectrophotometry. Total organic carbon was determined (TOC, OI Analytical Aurora Model 1030) with an autosampler (OI Analytical Model 1096).

Results and Discussion

Electrolytic Nonstoichiometric Water Splitting

Figure 10.1 shows a typical DC-powered electrolysis at the BiO_x-TiO_2 anode coupled to the stainless-steel cathode couple in the presence of sodium chloride as a supporting electrolyte. Water splitting is initiated at 2.0V which is approximately 0.8 V higher than the ideal potential ($E° = 1.23$ V). The rates of H_2 production and O_2 production increase with increasing cell voltage (E_{cell}). Furthermore, cell currents (I_{cell}) also increase in a linear fashion with increasing E_{cell} above 2.1V. The rates of formation of H_2 and O_2, respectively, are 9.0 μmol/min per mA/cm^2 and 1.3 μmol/min per mA/cm^2, which correspond to nonstoichiometric H_2 to O_2 ratios between 6 and 7, depending on the specific experimental conditions. This indicates additional anodic reactions (eq. 10.1) as well as water oxidation (eq. 10.3) takes place simultaneously at the anode. Water oxidation at the surface of a semiconducting, metal oxide (MO) anode like TiO_2 is known to proceed by the coupling of two surface-bound hydroxyl radicals (eq. 10.10 & 10.11).

$$\equiv\text{Ti-OH} + H_2O \rightarrow \equiv\text{Ti-OH}[OH^{\bullet}]_{ad} + H^+ + e^- \qquad (10.10)$$

$$2\equiv\text{Ti-OH}[OH^{\bullet}]_{ad} \rightarrow 2\equiv\text{Ti-OH} + O_2 + 2H^+ + 2e^- \qquad (10.11)$$

The current efficiencies for the hydrogen production at the SS cathode are close to 70% while those for the oxygen production at the BiO_x-TiO_2 anode are in the range of 10 to 25% (Figure 10.1c). In spite of an initial N_2 atmosphere, H_2O_2 can be produced via superoxide/hydroperoxyl radical pathway at the cathode (eqs. 10.12 to 10.14) due to oxygen reduction.

$$O_2 + e^- \rightarrow O_2^- \text{ (at the SS)} \qquad (10.12)$$

$$O_2^- + H^+ \rightarrow HOO^{\bullet} \ (pK_a = 4.88) \qquad (10.13)$$

$$2\ HOO^{\bullet} \rightarrow H_2O_2 + O_2 \qquad (10.14)$$

The cathodic reaction 10.12 will limit the current efficiency for the hydrogen production. The energy efficiencies, which are expressed in terms of Higher Heating Values (HHV) for H_2 production, are in the range of 35 to 60% (Figure 10.1d). This value decreases with increasing applied power. However, the energy efficiency can be improved, either by reducing the ohmic potential drop in the cell by increasing electrolyte concentration, or by coating noble metal (e.g., Pt) on the stainless-steel cathode.

Electrochemical Oxidation of Organic Compounds

The electrochemical oxidation and complete degradation of phenol at current density of $I = 14$ mA/cm^2 is shown in Figure 10.2. Phenol is completely degraded following first-order kinetics with an apparent half-life of $t_{1/2} = 4.25$ min. The end-product of phenol oxidation, CO_2, is initially detected after 38 min of electrolysis (Figure 10.2a). Under these conditions, the H_2 production rate (i.e., 95 μmol/min) is reduced slightly to 90 μmol/min, concomitant with initiation of CO_2 production, while the O_2 production rate remains steady at 15 μmol/min. As phenol degrades, mono-, di-, and trichlorinated phenols are formed as intermediates by stepwise chlorination of the parent phenol. The chlorinated phenols are completely decomposed within 1 h (Figure 10.2b and Scheme 10.2). When added separately, the chlorinated phenols are degraded with similar kinetics to phenol in following order of electrochemical reactivity: 2,4,6-trichlorophenol (3.74) > 2,6-dichlorophenol (1.84) > 2,4-dichlorophenol (1.38) > phenol (1.0) > 2-chlorophenol (0.78) > 4-chlorophenol (0.57). The numbers in parenthesis are observed reaction rates relative to phenol. At around 40 min of electrolysis, trichlorophenol begins to degrade rapidly (Figure 10.2a) and at the same time carbon dioxide release begins (Figure 10.2a). The total organic carbon (TOC) concentration also begins to decrease dramatically at this time (Figure 10.2c), consistent with CO_2 production. It is notable that after 2 h electrolysis the total amount of CO_2 released accounts for 25% of the initial amount of carbon present in phenol, while carbon removal based on TOC measurements is close to 34%. The “apparent carbon deficit” (~ 9%) consists of dissolved carbonate (CO_3^{2-}) and bicarbonate (HCO_3^-), which are removed by acidification prior to actual TOC measurements.

The phenol oxidation intermediates observed during the electrolytic degradation of phenol vary depending on the composition of anode surface and on the nature of the supporting electrolyte. In the case of Na_2SO_4, oxygenated or hydroxylated phenols such as catechol, hydroquinone, and benzoquinone are observed as the primary aromatic intermediates[22–26]. In contrast, for NaCl, a carbon-based anode produces chlorinated phenols as intermediates and SnO_2/Ti and IrO_2/Ti anodes produce nonchlorinated intermediates[27]. The electrolysis with NaCl as a background electrolyte is reported to generate active chlorine species, such as chlorine radical ($Cl^{\bullet}$), dichloride radical anion ($Cl_2^{\bullet-}$), and hypochlorous acid/hyperchlorite ($HOCl/OCl^-$) via surface-bound hydroxyl radical mediated pathways (eqs. 10.15–10.18).

$$\equiv Ti\text{-}OH[OH^{\bullet}]_{ad} + Cl^- \rightarrow \equiv Ti\text{-}OH + Cl^{\bullet} + HO^- \quad (10.15)$$

$$Cl^{\bullet} + Cl^- \rightarrow Cl_2^{\bullet-} \ (K = 1.4 \times 10^5\ M^{-1}) \quad (10.16)$$

$$\equiv Ti\text{-}OH[OH^{\bullet}]_{ad} + Cl^- \rightarrow \equiv Ti\text{-}OH + HOCl + e^- \quad (10.17)$$

$$HOCl \rightarrow OCl^- + H^+ \ (pK_a = 7.46) \quad (10.18)$$

The rate constants for the reaction of hydroxyl radical, chlorine radical, dichloride radical anion, and HClO with phenol are $6.6\times10^9\ M^{-1}s^{-1}$,[28] $2.5\times10^{10}\ M^{-1}$s-1, $2.5\times10^8\ M^{-1}s^{-1}$, and $2.2\times10^4\ M^{-1}s^{-1}$ [29,30], respectively. As a consequence, phenol and its oxidation intermediates have a variety of degradation pathways, including surface-bound/free hydroxyl radicals, chlorine radicals, dichloride radical anions, hypochlorite ions, and possibly hydrogen peroxide as well.

As the current density is increased from 7 to 38 mA/cm^2, the half life ($t_{1/2}$) for phenol oxidation along with the anodic current efficiency (ACE-II) for complete oxidation of phenol carbon (formal charge -2/3) to carbon dioxide (formal charge +4) decreases (Figure 10.3). The faster phenol oxidation rates yield shorter CO_2 release phase-delays of 60 to 15 min. However, the amount of carbon dioxide released during the course of the electrolysis and the anodic current efficiency (ACE-I) for one-electron oxidation of phenol ($PhOH \rightarrow PhOH^+ + e^-$) is not altered significantly (Figure 10.3c). In addition, cathodic current efficiency (CCE) for hydrogen production is almost invariable in the range of 50 to 70%.

The initial concentration of phenol markedly affects the apparent degradation rate. The half life grows linearly with concentration over the range of 0.5 to 2.0 mM (Figure 10.4) and increases by two orders of magnitude at higher concentrations (i.e., $t_{1/2}$ = 1.28 min at 0.5 mM and $t_{1/2}$ = 150 min at 10 mM). As the concentration of phenol is increased, a greater number of reaction intermediates are produced, which in turn compete with phenol for oxidants. This should result in both a decrease in $t_{1/2}$ and a lengthening of the release onset time of carbon dioxide. The anodic current efficiency (ACE-I) is lowered somewhat to 8% at concentrations above 1.0 mM, while the ACE-II ranges from 5 to 10%. On the other hand, CCE is invariable (~ 68%) to increasing the initial phenol concentration. This indicates that anodic radical production and subsequent organic oxidation has minimal effects on the hydrogen production as long as substrates are initially present in the medium. A comparison of hydrogen production with and without organic substrates suggests addition of aqueous pollutants synergistically enhances the H_2 production rate[18,19].

The electrolytic efficiency of Na_2SO_4 vs. NaCl as background electrolyte was also compared. The phenol degradation rate in NaCl is two orders of magnitude faster than that in Na_2SO_4 (Figure 10.5). Sodium phosphate and carbonate have similar effects to sodium sulfate as background electrolytes. However, the cathodic H_2 production efficiency using Na_2SO_4 as an electrolyte is 23% greater than NaCl. When 50 mM NaCl is added to a 50 mM Na_2SO_4 solution at increasing concentrations, the phenol degradation efficiency increases while the H_2 production efficiency decreases (i.e., CCE at 50 mM Na_2SO_4 = 95%; CCE at 50 mM Na_2SO_4 + 50 mM NaCl = 73%; CCE at 50 mM

NaCl = 68%). This indicates the anode is oxidatively active during generation of chlorine radical species and suggests these chlorine radicals can interrupt H_2 production.

During the course of electrolysis of water and electrolyte alone, the pH of solution rises initially from pH 6 to 10 and then remains constant throughout. After current is removed, the pH decreases to 9.5 (Figure 10.6). In contrast, when electrolysis takes place in the presence of phenol, the pH increases initially to 11 and then decreases quickly to pH 7 after 20 min, and then remains in the circum-neutral range (~ pH 7.5) during the latter stages of electrolysis. The cathodic reduction of protons results in a rise in the measured pH. However, the progressive oxidation of phenol eventually produces organic acids such as oxalic, maleic, and formic acid, which account for the subsequent drop in pH. Eventually, these daughter acids are further degraded at the anode surface by surface-bound hydroxyl radicals to aqueous CO_2 (e.g., $CO_2{\cdot}H_2O$, HCO_3^-, CO_3^{2-}) with the subsequent release of gaseous CO_2 accounting for the slight increase of the pH after 38 min of electrolysis (Scheme 10.2). This is the time that measurable CO_2 is released from the reactor (Figure 10.2a vs. Figure 10.6).

At pH 10, phenol is partially deprotonated ($pK_a = 9.98$) while the BiO_x-TiO_2 anode due to the presence of Lewis acid metals (e.g., Bi) at the surface should be positively charged despite the predominance of TiO_2 (pH_{zpc} of TiO_2 ~ 6.8). Thus, the ability of phenol to react directly at the anode surface at pH 10 is possible but the degree of interaction is unlikely to be strong. In contrast, substrates that are able to strongly adsorb to the anode via surface complexation should be oxidized quickly and immediately release CO_2 by multi-electron transfers instead of sequential one-electron transfers. This conjecture is confirmed by the results shown in Figure 10.7 for the oxidation of catechol ($pKa_1 = 9.45$;

$pKa_2 = 12.8$)[31]. Catechol functions as a monodentate or a bidentate ligand binding at one or two surface titanol groups. Thus as soon as the electrolysis is initiated, CO_2 is immediately released from solution and continues over the 2 hour period of electrolysis. Salicylic acid ($pK_{a1} = 2.97$; $pKa_2 = 13.74$) also shows the same behavior. Both compounds have been observed to chelate TiO_2 surfaces (as depicted on the right-hand side of Figure 10.7)[31,32], and multiple electrons can be transferred to the anode within seconds after the initiation of electrolysis. Nevertheless, the first-order rate constants for degradation of catechol and salicylic acid are lowered by approximately 50% compared to phenol ($k_{catechol}/k_{phenol} = 0.59$; $k_{salicylic\ acid}/k_{phenol} = 0.41$). In the case of phenol, oxidation primarily occurs on homogeneously distributed phenol molecules (and intermediates) in the bulk solution, whereas in the cases of catechol and salicylic acid, the oxidation preferentially occurs to the adsorbed molecules rather than the ones remaining in the bulk. This should result in immediate and complete oxidation of the adsorbed phenol molecules, but a slower oxidation rate of the phenol molecules in the bulk solution.

Solar Powered Electrolysis and Scale-Up

Figure 10.8 shows the hydrogen production and organic oxidation results of a PV-driven hybrid reactor system under two different solar light irradiation conditions. The total incident solar light radiation energy of A ($\mathbf{I}_{S,B}$) is measured at 0.107 ± 0.005 W/cm^2, while that of B ($\mathbf{I}_{S,A}$) is around 0.100 ± 0.005 W/cm^2. The overall reaction scheme is similar to that in Figure 10.2a. As soon as the PV is connected to the electrode couples, hydrogen and oxygen are produced and phenol is degraded, following apparent first-order kinetics. Carbon dioxide is released during the latter stages of the electrolysis. The difference of incident solar energy only affects the rate of hydrogen production; the phenol degradation rate, the oxygen generation rate, and the carbon dioxide release time-delay are almost invariable. At the condition B, the energy efficiency for the hydrogen production is around 30%. According to manufacturer, a theoretical maximum power of the PV_{peak} is 6.4 W corresponding to 4.5% of the average solar light radiation energy ($\mathbf{I}_{S,0}$ = 1100 W/m^2). However, when the PV is directly connected to the electrode couple, the power applied to the electrolysis (PV_{cell}) was 3.5 W (3.9V×0.9A). This corresponds to 55% of the PV_{peak} and 2.5% of the $I_{S,0}$.

To investigate the effect of solar flux on the PV power and the H_2 production, the PV-connected hybrid reactor was tested on a cloudy day. As shown in Figure 10.9, $\mathbf{I}_S$, E_{cell}, and I_{cell} vary over the range of 0.1 W/cm^2 to 0.08 W/cm^2, 4.1 V to 3.7 V, and 0.7 A to 0.9 A, respectively. The $\mathbf{I}_S$ continually decreases over the period of time from 15 min to 50 min of electrolysis, and the PV_{cell} and the H_2 production rate also follow the trend. However, upon addition of phenol to the reactor at 52 min, the H_2 production rate substantially increases in spite of a continued decrease in $\mathbf{I}_S$ and PV_{cell}. The H_2 production rate begins to decrease again after reaching a rate maximum of ~ 0.21 mmol/min. This behavior was observed again after a subsequent phenol addition at around 80 min. The synergistic effect of phenol addition on H_2 production efficiency has been qualitatively described elsewhere[18]. Briefly, oxidants such as $HO^{\bullet}$, $Cl^{\bullet}$, $Cl_2^{\bullet-}$, and HClO/ClO$^-$ produced at the anode can act as electron shuttles consuming electrons at the cathode. Reactive oxidant reduction is thermodynamically favored over proton/water reduction. When organics such as phenol are added to the system, they consume oxidants and a greater fraction of cathodic electrons are available for proton/water reduction. Our observations show this can increase H_2 production energy efficiencies by as much as 30 to 53% at low I_{cell}.

The PV_{cell} is correlated to the $\mathbf{I}_S$ with and without phenol addition (Figure 10.10a). Without phenol addition (i.e., pure electrolysis), the PV_{cell} efficiency (= $PV_{\mathrm{cell}}/\mathbf{I}_S \times 100\%$) is determined to be 2.0 to 2.8 %. The lower efficiency than supplier-reported (PV_{peak} = 4.5%) is probably due to overestimation of the array performance by the supplier and a conversion efficiency loss by the heating of the array and ohmic drop within the reactor[33]. The PV_{cell} efficiency increases linearly by 1.5 times from 2.37% to 3.58% by addition of phenol. The presence of phenol molecules also affects the electrolytic H_2 energy efficiency and behavior. As PV_{cell} increases in the absence of organics, the electrolytic H_2 production increases linearly with an average efficiency of 22% (= H_2 energy/PV_{cell} in Figure 10.10b). However, in the presence of phenol, the H_2 production energy efficiencies do not correlate with PV_{cell}. Prior to phenol addition, the electrolytic H_2 energy efficiency is around 20%. After phenol addition, PV_{cell} decreases to 2.1×10^{-3} W/cm^2 and H_2 production efficiencies increase to nearly 40%. The overall solar-to-H_2 energy efficiency (= H_2 energy/$\mathbf{I}_S \times 100\%$) also displays a similar trend. In the absence of phenol, the overall efficiency is around 0.67% (Figure 10.10c). The addition of phenol increases the overall efficiency from 0.53% (5.5×10^{-4} W cm^{-2}/ 1.03×10^{-1} W cm^{-2}) to 1.0% (8.1×10^{-4} W cm^{-2}/8.1×10^{-2} W cm^{-2}), which is similar to the efficiency observed in Figure 10.8.

For evaluation of a sub-pilot scale electrolysis, a 20 L batch reactor was prepared using 5 anodes (each, 800 cm^2) and 6 cathodes of the same dimensions arranged in an alternative fashion (Scheme 10.2b). At a total power of 60 W (3 V×20 A), carbon dioxide production is observed after 20 min, and the hydrogen production rate is 3.5×10^{-3} mol/min with an energy efficiency of 28% (Figure 10.11a). The degradation half-life of 1 mM phenol is < 2 min. Based on these operation conditions, we can estimate the PV area required (i.e., PV_{cell} efficiency = $PV_{cell}/(\mathbf{I}_{S,0} \times \text{PV area}) \times 100\%$) to treat variable volumes of wastewater contaminated with 1 mM phenol (Figure 10.11b). It is clear that water-treatment capacity is strongly related to the PV area and efficiency. For example, treatment of 16 metric tons of water (i.e., 1.6 kg phenol) daily (i.e., operation for 9 h/day) requires a 62 m^2 PV panel operating at 10% efficiency. In addition, hydrogen is obtained as a potentially useful byproduct. Hydrogen production rates are affected both by the water treatment capacity and H_2 energy efficiency (Figure 10.11c). Small-scale reactors are usually better than large reactors for energy efficiency. At a H_2 energy efficiency of 60%, the treatment of 16 tons of water with a PV of 10% efficiency will yield around 1 kg of H_2.

Technical Consideration.

Electrodes

Commercial electrolytic water splitting typically employs Pt group metals (PGM) as anodes and Ni-based alloy (e.g., Ni-Zn, Ni-Al, Ni-Co, Ni-Mo-Cd)[34-36], stainless steel[36], or noble metals (e.g., Pt, Au) as cathodes, and operates at extreme conditions such as high electrolyte concentrations (> 1.0 mol/L), high pH (> 1.0 mol/L KOH), and high pressure. The main reason for employing the Pt-based anode is that Pt catalyzes the four-electron oxidation of water (10.3). However, for the electrochemical oxidation of organic compounds (10.4), the anode should preferentially generate surface-bound or homogeneous radical species (e.g., $HO^\bullet$, $Cl^\bullet$).

A variety of anodes, such as single metal oxides (e.g., PbO_2[24,25,37-41], SnO_2[24,37,39,42], IrO_2[42,43], RuO_2[43]), multiple metal oxides (e.g., Ta_2O_5/IrO_2[44], Bi-PbO_2/Pt[40], PbO_2/SnO_2[45], $IrO_2/RuO_2/TiO_2$[46]), and boron-doped diamond (BDD)[47] have been utilized for the electrolytic treatment of aqueous chemical contaminants. For example, PbO_2 coated on titanium substrate has been widely studied; however, the likely release of lead ions and long-term anodic stability issues are drawbacks to the practical application of PbO_2 anodes. The BDD electrode has also been the subject of a number of studies due to its great stability and wide potential window[47]; yet the high price of synthetic diamond hinders application even at the pilot scale. Application of Pt-based anodes is impractical due to formation of polymeric surface films during phenol oxidation, which reduces energy efficiencies[22,48,49]. In comparison, the BiOx-TiO_2 anode employed in this study is found to be very stable and results in decent current efficiencies in the range of 25 to 36% for oxidation of propylene glycol[17]. In addition, it has been manufactured at the sub-pilot scale with electrode areas nearing a square meter at relatively low costs. Various cathodes are available for use in combination with the BiOx-TiO_2 anode. From an economical point of view, SS is the most feasible in cost, stability, and availability. Surface treatment of SS (e.g., Ni or Pt-coating) may catalyze electron transfer to protons/water and increase H_2 energy efficiencies[50,51]. However, a great increase is not expected, since energy efficiencies are already in the range of 30% to 70%.

Technical Comparison

It should be noted that the PV-electrolysis-water-treatment system used in this study has many differences as compared to the commercial PV-electrolyzer systems. First, few experimental studies on hybrid PV-electrolyzer technologies for H_2 production and organic oxidation operating at such mild conditions (atmospheric pressure, pH 6 to 11, 50 mM salt) have been reported. For example, Ahmad and Shenway evaluated a PV-driven electrolysis system for hydrogen production with reported electrolysis efficiencies of 60% (similar to our system) under much harsher conditions (27% KOH solution; ~ 4.8 mol/L; pH 14.7)[6]. Comparison of the solar-to-H_2 energy efficiency is not reliable due to different overall purpose and conditions. A high-powered and efficient PV usually has a high solar-to-H_2 efficiency. Photovoltaic arrays of 5–9 kW PV_{peak} and 8.1–8.4% PV_{cell} efficiency, coupled with alkaline electrolyzer (30% KOH) of 62 to 77% electrolytic H_2 efficiency, have overall solar-to-H_2 efficiency of 3.6 to 6.2%[33,52]. The alkaline electrolyzer of similar electrolytic H_2 efficiency (60%) has a much lowered solar-to-H_2 energy efficiency of 1.5% when coupled to a lower power PV (PV_{peak} = 53 W)[6]. Due to the extremely high electrolyte concentration, which is a usual condition for optimal efficiency during alkaline electrolysis, it is impractical for application to water treatment. In comparison, our system operates over a similar efficiency range (electrolytic H_2 energy efficiency of 30% to 70%; solar-to-H_2 energy efficiency ~ 1.0%) with a low-power PV (PV_{peak} = 6.4 W) at two-orders of magnitude lower electrolyte concentrations (2×10^{-2} to 5×10^{-2} mol/L).

Second, PV-electrolyzer systems on a lab or pilot scale have been considered and examined as alternatives to a system of PV-electricity-battery. The systems are typically composed of PV arrays for converting solar light to electricity, alkaline electrolyzers for producing hydrogen using the electricity, hydrogen storage tanks, and fuel cells for producing electricity from the stored hydrogen (and oxygen). Therefore, the primary goal of theses studies is to utilize hydrogen as a storable medium for the dark generation of electricity. However, the PV-electrolyzer systems, which produce hydrogen, are found to be economically impractical compared to conventional PV-electricity-battery combinations. For example, total annual cost of the electricity from the electrolyze-based systems is around 3 times and 4 times higher than those of the battery-based systems due to energy losses during electrolysis and fuel-cell processes[8]. The hydrogen produced from a typical PV-electrolyzer system is also more expensive than SMR. On the other hand, if the hydrogen production can be combined with costly wastewater treatment, then PV-electrolyzer systems may become economically viable[53,54].

This hybrid system should be distinguished from reported electrochemical hybrid systems for hydrogen production and chemical oxidation in terms of practical operation and efficiency. Most hybrid systems operate with limited number of organic chemicals at lower efficiencies. For example, the DC-powered electrolytic hydrogen production from methanol was reported, but the system only works with methanol (i.e., a reversed direct methanol fuel cell process)[12]. A hybrid system of electro-assisted photo-Fenton oxidation and cathodic hydrogen production was described, yet the system operates only for a limited number of substrates under limited conditions and needs post-electrolysis treatment to separate the consumed reagents[10]. In contrast, our system has been proven to decompose and mineralize a variety of phenolic compounds (e.g., phenol, mono-, di-, trichlorinated phenols, catechol, hydroquinone, resorcinol, salicylic acids, etc.), aliphatic acids (e.g., maleic acid, malonic acid, oxalic acid, fumaric acid, polypropylene, etc.), and dyestuffs (methyl orange, ortho-methyl red, para-methyl red, methylene blue, acid orange 7, rhodamine B, etc.)[18,19]. These chemicals are commonly found in industrial and domestic wastewaters.

Application

Some issues would limit the applications of the presented hybrid system to a conventional water treatment facility. First the electrolyte (i.e., NaCl), which is intrinsically necessary for the electrolysis. However, the sodium chloride is the most abundant constituent of a water/wastewater stream, in the range 1 to 9300 kg/day[21], and wastewater inflows have a high conductivity in the range of 620 to 3550 μS/cm[55]. In addition, this hybrid is found to work efficiently even at 21 mM NaCl (~ 1.2 g/L)[17]. The other is that the electrolysis could produce some toxic byproducts. However, no chlorinated gases such as methyl chloride, dichloromethane, chloroform, tetrachloride, phosgene, vinyl chloride, or chlorine were detected during the electrolysis in the presence of phenol. The chlorinated phenols produced are very rapidly converted to carbon dioxide (e.g., $k_{2,4,6\text{-ClPhOH}} / k_{\text{PhOH}} > 3.7$), water, and chloride.

Separation and purification of the evolved gas stream is absolutely necessary. However, it is not a difficult challenge. Proton-exchange membranes such as Nafion or porous ceramic separators (e.g., fine glass frit) can be put between the anode and cathode. Since oxygen and carbon dioxide are produced at the anode, both gases are effectively separated from hydrogen produced at the cathode provided that there is an appropriate membrane separating the two compartments. In addition, even if hydrogen is mixed with carbon dioxide, CO_2 can be readily removed just by chemical absorption process (e.g., flowing carbon dioxide gas through amine solution), which is a typical CO_2 separation process in gas turbine power plants.

Current water and wastewater treatment plants involving a series of water treatment processes include pre-treatment steps to screen out solid debris and large particle suspended solids, physical separation such as small particle coagulation, flocculation and sedimentation, floatation and clarification, biological treatment for removal of biological oxygen demand, and advanced oxidation treatment such as UV/ozone process for disinfection and reduction of chemical oxygen demand. Therefore no unit process itself could replace the overall wastewater treatment processes. Our PV-electrolytic system would replace conventional UV/ozone steps as an advanced oxidation or disinfection alternative.

Figures

Figure 10.1. Time profiles of a DC-powered hydrogen and oxygen production rate. A) As a function of cell voltage (E_{cell}) at BiOx-TiO_2 anode and stainless steel (SS) cathode in 50 mM NaCl solution. B) Effects of E_{cell} on cell currents (I_{cell}) and the rates of hydrogen and oxygen production. C) The rates and current efficiencies of hydrogen production and oxygen production as a function of I_{cell}. D) Effects of applied power on energy efficiencies for hydrogen production

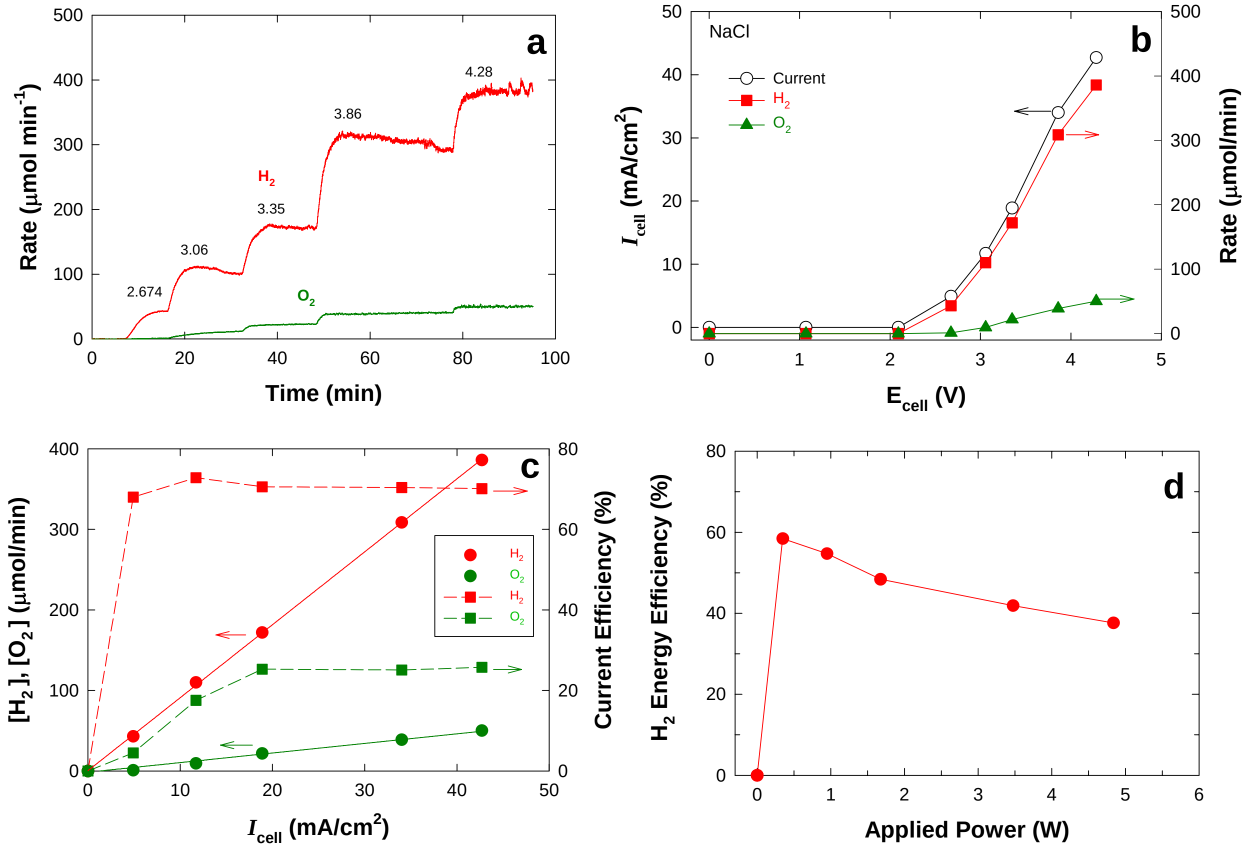

Figure 10.2. Electrochemical oxidation of phenol to CO_2 and simultaneous generation of H_2 and O_2. A) At $I_{cell} = 14$ mA/cm^2. B) Time profiles of intermediates generated during the oxidation of phenol. C) Time profiles of accumulation of carbon dioxide and TOC decrease. [phenol]$_0$ = 1 mM (0.2 L); [NaCl] = 50 mM; nitrogen purged continuously

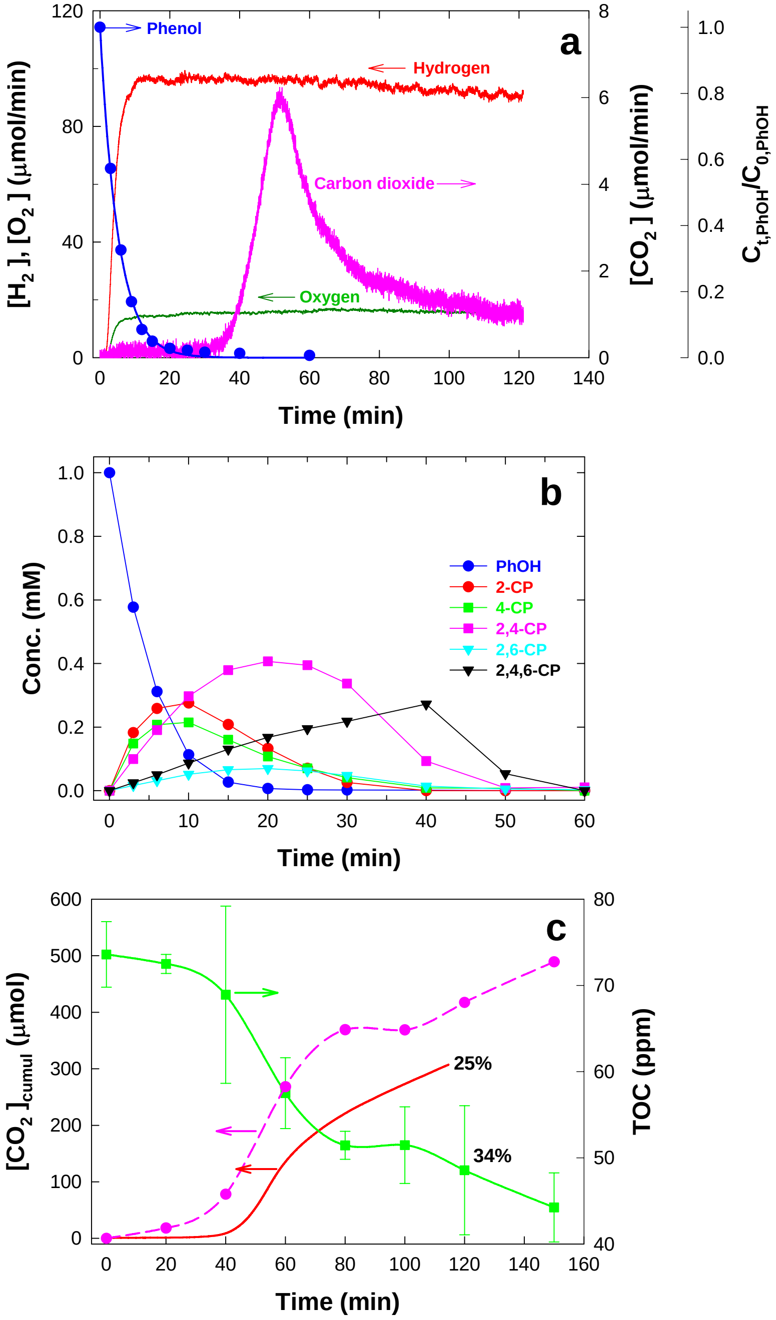

Figure 10.3. Effects of I_{cell} on observed electrochemistry. A) degradation of phenol, B) release of carbon dioxide, and C) half life time ($t_{1/2}$) for degradation of phenol, anodic efficiencies (AE-I, AE-II: see experimental section), and cathodic efficiencies (CE). Experimental conditions identical to those of Figure 10.2

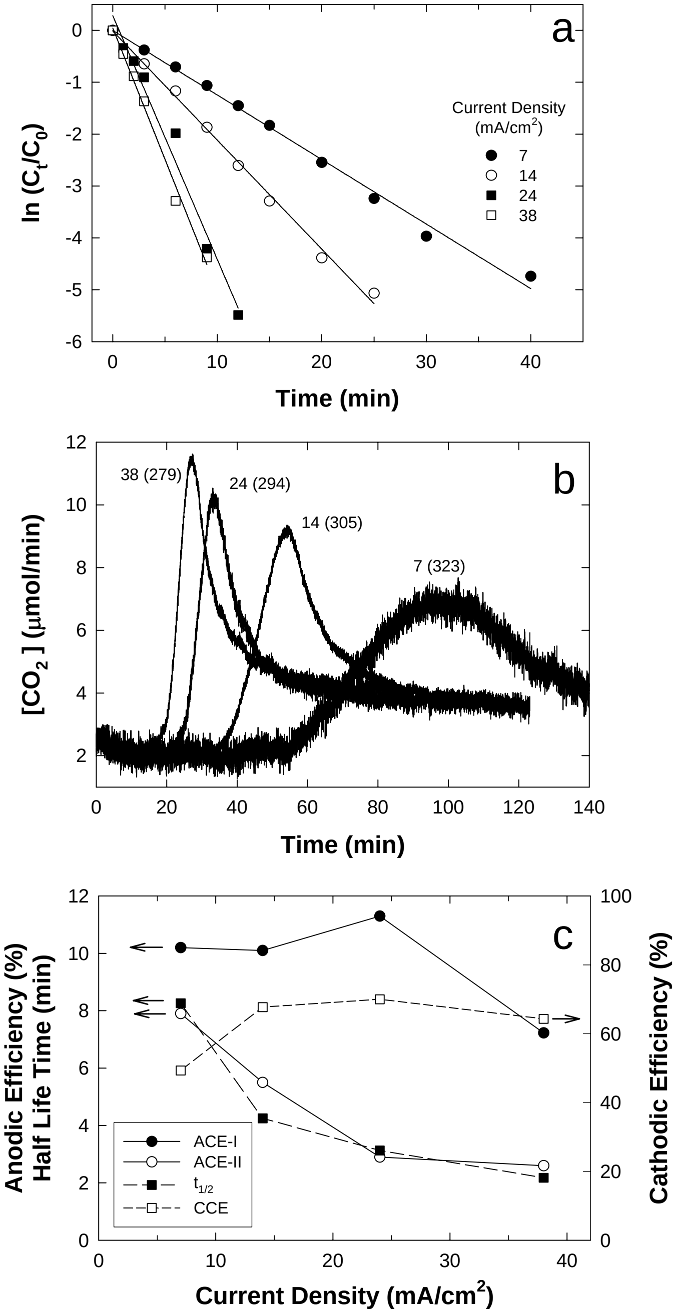

Figure 10.4. Effects of phenol concentration on electrochemistry. A) degradation of phenol, B) release of carbon dioxide, and C) half life time ($t_{1/2}$) for degradation of phenol, anodic efficiencies (AE-I, AE-II), and cathodic efficiencies (CE). $I_{\mathrm{cell}} = 14$ mA/cm^2

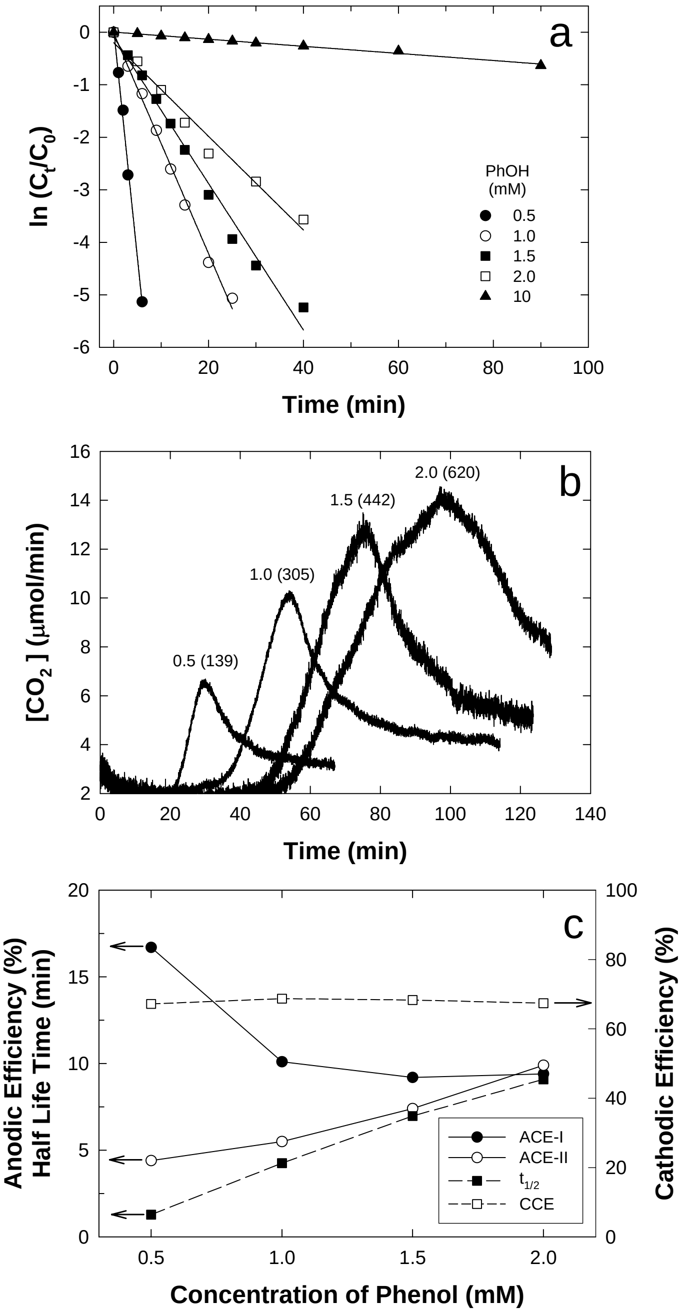

Figure 10.5. Effect of NaCl concentration on the electrochemistry. Degradation rate (*k*) of phenol (■) and the current efficiency for hydrogen production (●) in 50 mM Na_2SO_4. For comparison, effect of 50 mM NaCl without Na_2SO_4 was also shown for k (□) and hydrogen production (○). The current efficiency for hydrogen = (number of H_2 molecules × 2) / (number of electrons) × 100%

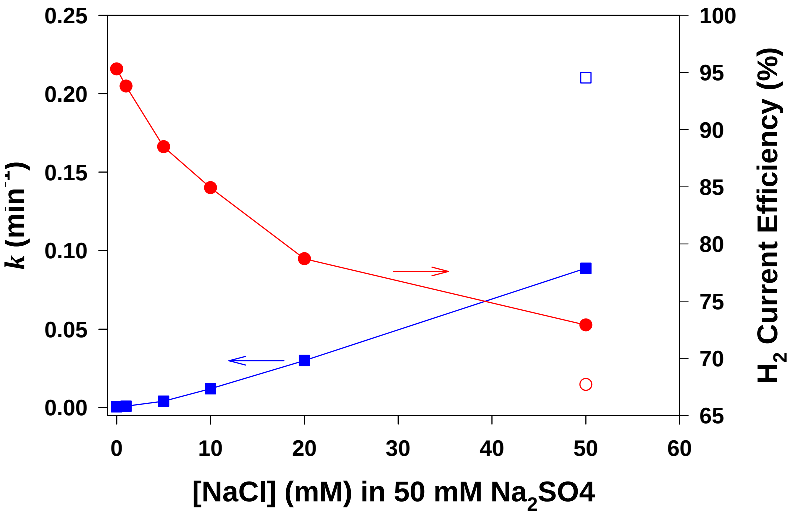

Figure 10.6. Time profiles of pH change during the course of electrolysis. I_{cell} = 14 mA/cm^2 in the absence and presence of 1 mM phenol

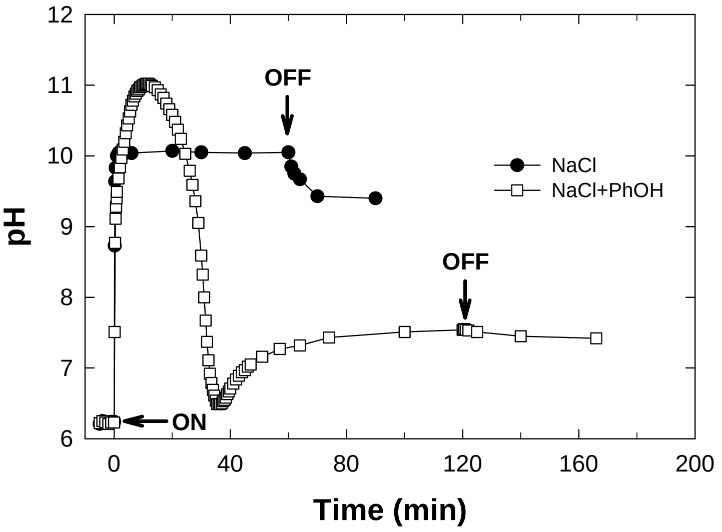

Figure 10.7. H_2 and CO_2 production during electrochemical catechol oxidation. 1 mM catechol at I_{cell} = 12.8 mA/cm^2

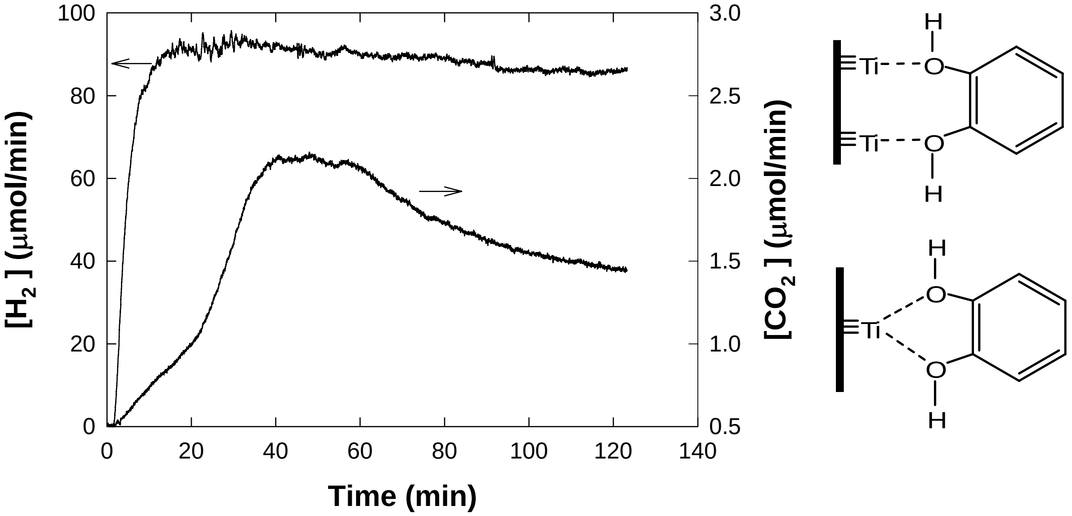

Figure 10.8. H_2 and CO_2 production during PV-electrochemical catechol oxidation. A 6.4W-rated photovoltaic cell with area of 1280 cm^2 is directly connected to the anode-cathode couple. Hydrogen A and B indicates the hydrogen production at incident solar energy of 1.00±0.01 and 1.07±0.01 W/cm^2, respectively

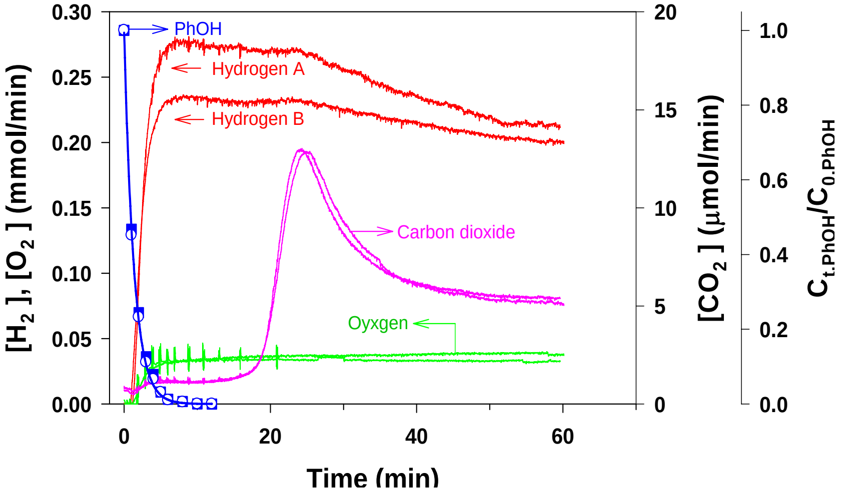

Figure 10.9. Solar-powered electrolysis with phenol addition on a cloudy day. (April 13th, 2007). A 6.4W-rated photovoltaic cell with area of 1280 cm^2 is directly connected to the anode-cathode couple. **I**$_S$: solar light radiation energy (W/cm^2); E$_{cell}$: cell voltage (V); I_{cell}: cell current (A). 1 mM phenol was successively added at 52 min and 87 min of electrolysis, as indicated by dotted lines

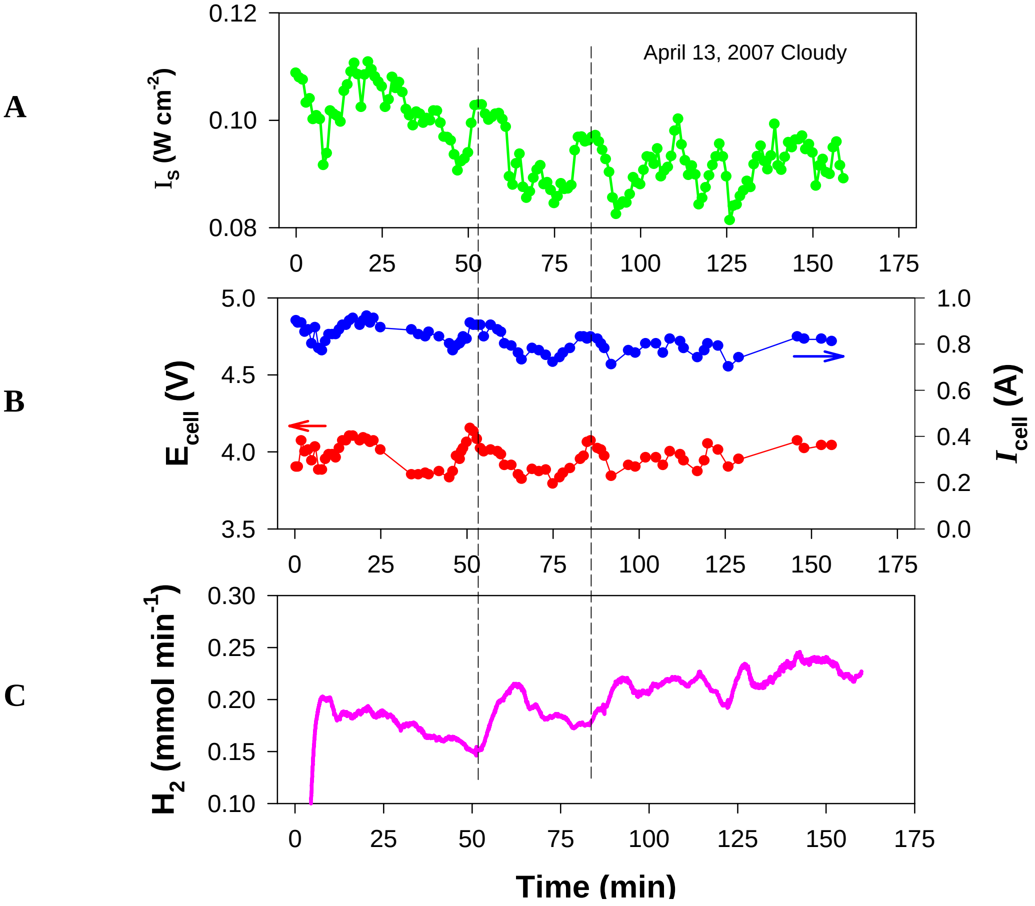

Figure 10.10. Relationships between I_S, PV_{cell}, and H_2 energy. A) $\mathbf{I}_S$ vs. PV_{cell} B) PV_{cell} vs. H_2 energy, and C) $\mathbf{I}_S$ vs. H_2 energy without and with phenol addition during electrolysis

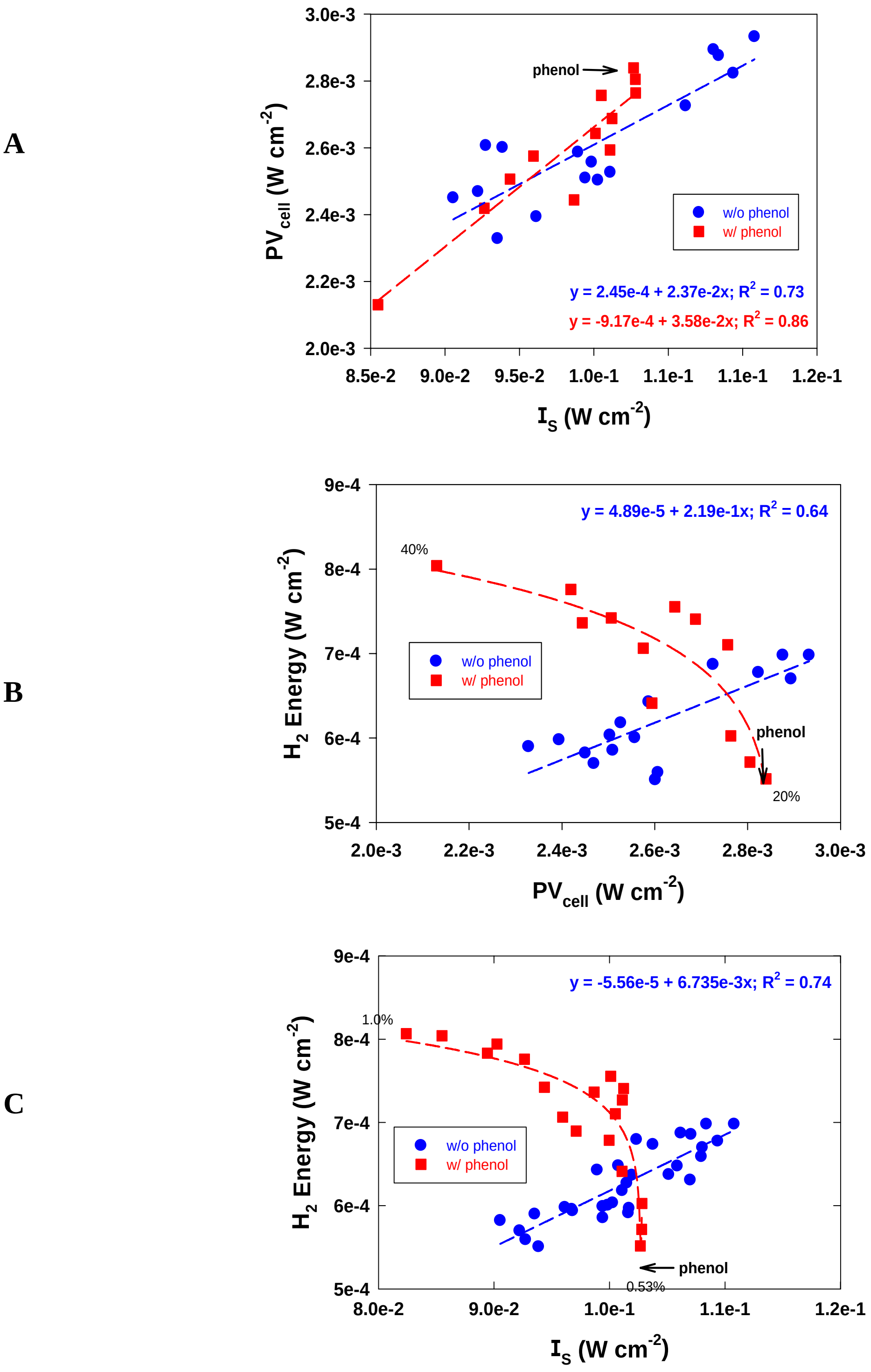

Figure 10.11. Electrolysis in a sub-pilot scale, 20 L reactor. A) A DC-powered electrochemical oxidation of phenol to carbon dioxide and generation of hydrogen in a sub-pilot scaled reactor (20L) at E_{cell} = 3V and I_{cell} = 20A. $[\text{phenol}]_0$ = 1 mM. B) Correlation between water treatment capacity and required PV area with different efficiencies. C) Effects of water treatment capacity on the amount of hydrogen obtainable with different energy efficiencies at a PV_{cell} of 10%

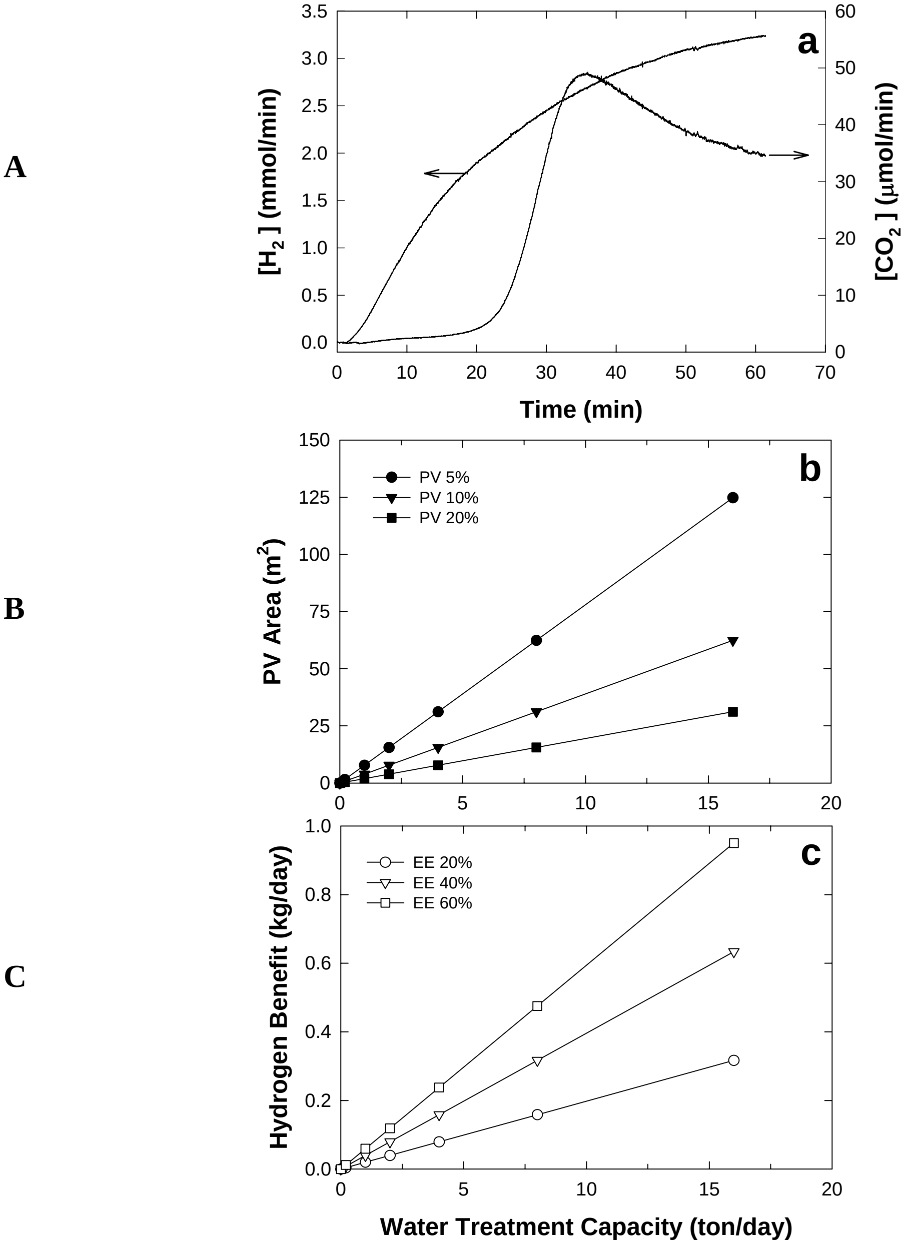

Schemes

Scheme 10.1. A) Composition and preparation procedure of BiOx-TiO_2/Ti anode. B) A bundle of BiOx-TiO_2 anode and stainless-steel (SS) cathode couples for a sub-pilot scaled electrolysis (20L)

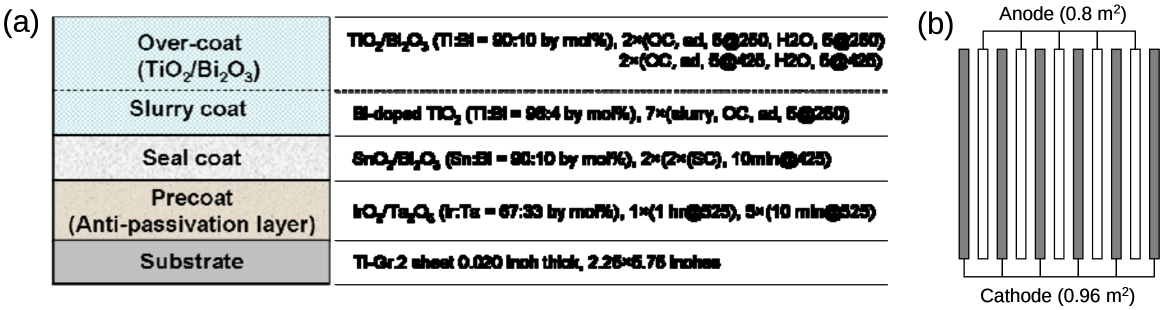

(a)

Over-coat (TiO_2/Bi_2O_3)	TiO_2/Bi_2O_3 (Ti:Bi = 90:10 by mol%), 2×(OC, ad, 5@250, H2O, 5@250) 2×(OC, ad, 5@425, H2O, 5@425)
Slurry coat	Bi-doped TiO_2 (Ti:Bi = 96:4 by mol%), 7×(slurry, OC, ad, 5@250)
Seal coat	SnO_2/Bi_2O_3 (Sn:Bi = 90:10 by mol%), 2×(2×(SC), 10min@425)
Precoat (Anti-passivation layer)	IrO_2/Ta_2O_5 (Ir:Ta = 67:33 by mol%), 1×(1 hr@525), 5×(10 min@525)
Substrate	Ti-Gr.2 sheet 0.020 inch thick, 2.25×5.75 inches

Scheme 10.2. Proposed reaction pathway for electrochemical degradation of phenol

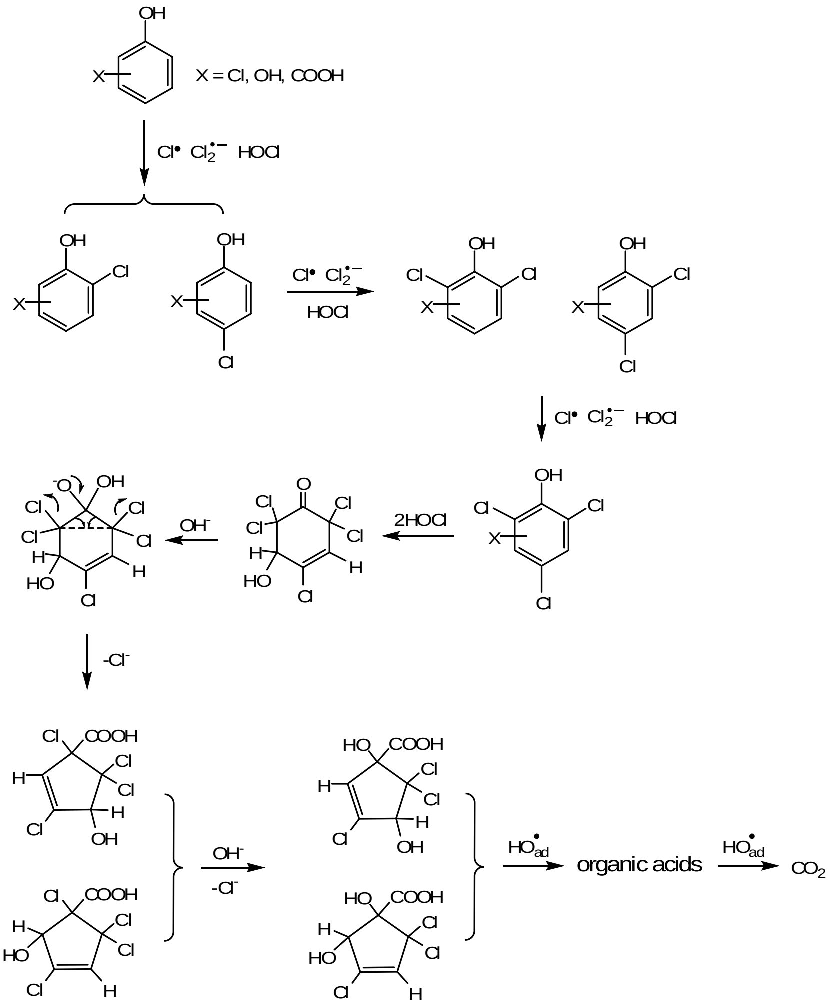

Tables

Table 10.1. Comparison of PV-electrolysis energy efficiencies (EEs)

PV_{peak}	Electrode	Electrolyte	Purpose	Average solar-to-PV EE[a]	Average electrolytic H_2 EE[b]	Average solar-to-H_2 EE[c]	Ref
5 kW_p	-	30wt% KOH	H_2 storage & fuel cell	8.4%	62%	3.6%	Hollmuller
53W_p	Ni/Ni	27wt% KOH	H_2 storage & fuel cell	-	60%	1.5%	Ahmad
9.2 kW_p	Bipolar alkaline electrolyzer		H_2 storage & fuel cell	8.1%	77%	6.2%	Lehman
6.4W_p	BiO_x-TiO_2/SS	0.27wt% NaCl	Hybrid	2.5%	30 – 60%	1.0%	This study

a. PV_{cell} / $\mathbf{I}_S$
b. H_2 energy / PV_{cell}
c. H_2 energy / $\mathbf{I}_S$

References

(1) *International Energy Outlook 2006*; Energy Information Administration.

(2) Penner, S. S. *Energy* **1998**, *23*, 71.

(3) *2005 Hydrogen Market, Hydrogen R&D and Commercial Implication in the U.S. and E.U.*, available at http://www.researchandmarkets.com/reports/301714.

(4) *Solar and Wind Technologies for Hydrogen Production*, available at http://www.hydrogen.energy.gov/congress_reports.html.

(5) Korposki, B.; Levene, J.; Harrison, K.; Sen, P. K.; Novachek, F. *Electrolysis: Information and Opportunities for Electric Power Plants*, available at http://www.osti.gov/bridge.

(6) Ahmad, G. E.; El Shenawy, E. T. *Renewable Energy* **2006**, *31*, 1043.

(7) Turner, J. A. *Science* **1999**, *285*, 687.

(8) Friberg, R. *Int. J. Hydrogen Energy* **1993**, *18*, 853.

(9) Szyszka, A. *Int. J. Hydrogen Energy* **1998**, *23*, 849.

(10) Soler, L.; Macanas, J.; Munoz, M.; Casado, J. *Int. J. Hydrogen Energy* **2006**, *31*, 129.

(11) Mathieson, G.; Langdon, A.; Jamieson, G. *Dev. Chem. Eng. Mineral Process* **2006**, *14*, 71.

(12) Narayanan, S. R.; W., C.; Jeffries-Nakamura, B.; Valdez, T. I. *Hydrogen Generation by Electrolysis of Aqueous Organic Solutions*; U.S. Patent 6,368,492; Apr. 9, **2002**.

(13) Kesselman, J. M.; Weres, O.; Lewis, N. S.; Hoffmann, M. R. *J. Phys. Chem. B* **1997**, *101*, 2637.

(14) Weres, O.; Hoffmann, M. R. *Electrode, Electrode Manufacturing Process and Electrochemical Cell*, U.S. Patent 5,419,824, **1995**.

(15) Weres, O.; Hoffmann, M. R. *Electrochemical Method and Device for Generating Hydroxyl Free Radicals and Oxidizing Chemical Substances Dissolved in Water*; U.S. Patent 5,364,508; Nov. 15, 1994.

(16) Weres, O.; Hoffmann, M. R. *Electrochemical Device for Generating Hydroxyl Free Radicals and Oxidizing Chemical Substances Dissolved in Water*; U.S. Patent 5,439,577; Aug. 8, 1995.

(17) Weres, O. *Electrode with Surface Comprising Oxides of Titanium and Bismuth and Water Purification Process Using This Electrode*; U.S. Patent 0,000,774 A1; Jan. 4, 2007.

(18) Park, H.; Vecitis, C. D.; Choi, W.; Weres, O.; Hoffmann, M. R. *J. Phys. Chem. C* **2008**, *112*, 885.

(19) Park, H.; Vecitis, C. D.; Hoffmann, M. R. *J. Phys. Chem. C* **2008**, (accepted).

(20) Glassmeyer, S. T.; Furlong, E. T.; Kolpin, D. W.; Cahill, J. D.; Zaugg, S. D.; Werner, S. L.; Meyer, M. T.; Kryak, D. D. *Environ. Sci. Technol.* **2005**, *39*, 5157.

(21) Barber, L. B.; Murphy, S. F.; Verplanck, P. L.; Sandstrom, M. W.; Taylor, H. E.; Furlong, E. T. *Environ. Sci. Technol.* **2006**, *40*, 475.

(22) Gattrell, M.; Kirk, D. W. *J. Electrochem. Soc.* **1993**, *140*, 903.

(23) Canizares, P.; Martinez, F.; Diaz, M.; Garcia-Gomez, J.; Rodrigo, M. A. *J. Electrochem. Soc.* **2002**, *149*, D118.

(24) Kotz, R.; Stucki, S.; Carcer, B. *J. Appl. Electrochem.* **1991**, *21*, 14.

(25) Tahar, N. B.; Savall, A. *J. Electrochem. Soc.* **1998**, *145*, 3427.

(26) Boudenne, J. L.; Cerclier, O.; Bianco, P. *J. Electrochem. Soc.* **1998**, *145*, 2763.

(27) Korbahti, B. K.; Salih, B.; Tanyolac, A. *J. Chem. Technol. Biotechnol.* **2002**, *77*, 70.

(28) Buxton, G. V.; Greenstock, C. L.; Helman, W. P.; Ross, A. B. *J. Phys. Chem. Ref. Data* **1988**, *17*, 513.

(29) Hasegawa, K.; Neta, P. *J. Phys. Chem.* **1978**, *82*, 854.

(30) Gallard, H.; von Gunten, U. *Environ. Sci. Technol.* **2002**, *36*, 884.

(31) Araujo, P. Z.; Morando, P. J.; Blesa, M. A. *Langmuir* **2005**, *21*, 3470.

(32) Tunesi, S.; Anderson, M. *J. Phys. Chem.* **1991**, *95*, 3399.

(33) Hollmuller, P.; Joubert, J. M.; Lachal, B.; Yvon, K. *Int. J. Hydrog. Energy* **2000**, *25*, 97.

(34) Los, P.; Rami, A.; Lasia, A. *J. Appl. Electrochem.* **1993**, *23*, 135.

(35) Navarro-Flores, E.; Chong, Z. W.; Omanovic, S. *J. Mol. Catal. A* **2005**, *226*, 179.

(36) Radhakrishnamurthy, P.; Sathyanarayana, S.; Reddy, A. K. N. *J. Appl. Electrochem.* **1977**, *7*, 51.

(37) Rodgers, J. D.; Jedral, W.; Bunce, N. I. *Environ. Sci. Technol.* **1999**, *33*, 1453.

(38) Bonfatti, F.; Ferro, S.; Lavezzo, F.; Malacarne, M.; Lodi, G.; De Battisti, A. *J. Electrochem. Soc.* **2000**, *147*, 592.

(40) Iniesta, J.; Exposito, E.; Gonzalez-Garcia, J.; Montiel, V.; Aldaz, A. *J. Electrochem. Soc.* **2002**, *149*, D57.

(41) Kaba, L.; Hitchens, G. D.; Bockris, J. O. *J. Electrochem. Soc.* **1990**, *137*, 1341.

(42) Comninellis, C.; Nerini, A. *J. Appl. Electrochem.* **1995**, *25*, 23.

(43) Kim, K. W.; Lee, E. H.; Kim, J. S.; Shin, K. H.; Jung, B. I. *J. Electrochem. Soc.* **2002**, *149*, D187.

(44) Fino, D.; Jara, C.; Saracco, G.; Specchia, V.; Spinelli, P. *J. Appl. Electrochem.* **2005**, *35*, 405.

(45) Gherardini, L.; Michaud, P. A.; Panizza, M.; Comninellis, C.; Vatistas, N. *J. Electrochem. Soc.* **2001**, *148*, D78.

(46) Rajkumar, D.; Kim, J. G.; Palanivelu, K. *Chem. Eng. Technol.* **2005**, *28*, 98.

(47) Panizza, M.; Cerisola, G. *Electrochim. Acta* **2005**, *51*, 191.

(48) Koile, R. C.; Johnson, D. C. *Anal. Chem.* **1979**, *51*, 741.

(49) Boudenne, J. L.; Cerclier, O.; Galea, J.; VanderVlist, E. *Appl. Catal. A.* **1996**, *143*, 185.

(50) Whalen, J. J.; Weiland, J. D.; Searson, P. C. *J. Electrochem. Soc.* **2005**, *152*, C738.

(51) Dominey, R. N.; Lewis, N. S.; Bruce, J. A.; Bookbinder, D. C.; Wrighton, M. S. *J. Am. Chem. Soc.* **1982**, *104*, 467.

(52) Lehman, P. A.; Chamberlin, C. E.; Pauletto, G.; Rocheleau, M. A. *Int. J. Hydrog. Energy* **1997**, *22*, 465.

(53) *Phenolic Wastewater Treatment Alternatives*; Air Force Engineering and Service Center: Tyndall AFB FL Engineering and Services Lab, **1980**.

(54) Jones, O. A. H.; Green, P. G.; Voulvoulis, N.; Lester, J. N. *Environ. Sci. Technol.* **2007**, *41*, 5085.

(55) Conn, K. E.; Barber, L. B.; Brown, G. K.; Siegrist, R. L. *Environ. Sci. Technol.* **2006**, *40*, 7358.

Chapter 11

Enhancement of Cathodic H_2 Production Efficiencies by Simultaneous Anodic Oxidation of Organics: Role of Substrate and Active Chlorine Species

Sections reprinted with permission from Park, H.; Vecitis, C. D.; Hoffmann, M. R.
J*ournal of Physical Chemistry A* **2009**, *113*.

Abstract

The need for alternative energy sources with minimal-to-no carbon footprint is growing. A solar-powered electrochemical system which produces hydrogen via water splitting using organic pollutants as sacrificial electron donors is a possible solution. The hybridization of a BiO_x-TiO_2/Ti anode with a stainless-steel cathode powered by a photovoltaic (PV) array has been shown to achieve this process. The electrochemical degradation kinetics of a variety of organic substrates is investigated as a function of a background electrolyte NaCl vs. Na_2SO_4. The observed substrate (S) degradation kinetics ($-k_{\mathrm{obs}}^{\mathrm{S}}$) are found to correlate well with the cell current (I_{cell}) and the H_2 production energy efficiency (EE) in the presence of NaCl as the background electrolyte. In the case of Na_2SO_4, no correlation is observed and the degradation rates are greatly reduced in comparison to NaCl. This suggests the primary chemical oxidant is electrolyte-dependent. $-k_{\mathrm{obs}}^{\mathrm{S}}$s are found to be proportional to bimolecular rate constants of $\mathrm{Cl}_2^{\bullet -}$ with the substrate ($k_{\mathrm{Cl}_2^{\bullet -} + \mathrm{S}}$) and to substrate-induced ΔEEs (EE with substrate – EE without substrate) in the presence of NaCl. The ΔEE correlation arises from the active chlorine species acting as an electron shuttle, which compete with H_2 production for cathodic electrons. In the presence of the organic substrates, the active chlorine species are quenched, increasing the fraction of electrons utilized for the H_2 production.

Introduction

As the cost of fossil fuels increases, the development of alternative, renewable, and environmentally benign (i.e., carbon-free) sources of energy is paramount[1,2]. Hydrogen, as a potential alternative fuel, has a higher energy density (per kg) than gasoline or alcohols and a viable storage capacity under high pressures. Electrochemical water splitting (i.e., electrolysis) for H_2 generation has a negligible carbon footprint compared to steam methane reformation (SMR), which is the predominant H_2 production method today. At present, commercial-scale water electrolyzer efficiencies range from 50 to 75% efficient[3–5]. yet the cost of electrolytic hydrogen production technology is continuing to rise because of rising electricity costs. In order to lower the cost of electrolytic H_2 production, it may prove beneficial to couple electrochemical water treatment with hydrogen generation. The hybridization of these two processes should result in a single, cooperative, and more cost-effective electrochemical process. Conventional water and wastewater treatment operations are known to be energy-intensive and correspond to > 20% of local energy expenditures for water-scarce municipalities[6].

Solar-powered electrolytic systems have been developed to couple hydrogen production with the simultaneous remediation of environmentally relevant organic pollutants[7,8]. In these systems, a photovoltaic (PV) cell is used to convert solar light into DC current, which in turn powers the electrochemical cell. At a multi-component, hetero-junction anode, organic compounds are converted primarily to carbon dioxide and lower-molecular-weight organic acids. At a stainless-steel (SS) cathode, hydrogen is produced via water or proton reduction. Anodic oxygen evolution (i.e., water oxidation) is circumvented by the generation of oxidizing radical species resulting in a nonstoichiometric water splitting (i.e., overall H_2/O_2 mole ratios of 6 to 8). Anodic current efficiencies for the one-electron oxidation and for the complete mineralization of phenol range from 7 to 17% and 3 to 10%, respectively. The cathodic current and energy efficiencies for hydrogen generation range from 50 to 70% and 30 to 60%, respectively.

In addition, the oxidation of organics substrates (e.g., phenol) appears to increase 1) the rate of H_2 production, 2) the H_2 production energy efficiency by 50%, and 3) the cell voltage (E_{cell}) by 0.1–0.2 V in the photovoltaic (PV)-connected system[7,8]. The relative degree of the apparent "substrate-induced synergy effect" is dependent on the supporting electrolyte. For example, sodium chloride has a large efficiency enhancement effect, whereas sodium sulfate has minimal effect. In addition, the degradation rate of phenol in sodium chloride is faster by more than two orders of magnitude than that in sodium sulfate.

Sodium chloride is often utilized as a supporting electrolyte in electrochemical water treatment[9–23] NaCl improves .e anodic oxidation efficiency for phenol[10,11,13,15,16], glucose[12,17], p-cresol[9], propylene glycol[22], trichlosan[14], oxalic acid[18], dyestuffs[20,21], and endocrine disruptors[23], compared to sodium sulfate[10,12,23], sodium bicarbonate[9], and sodium nitrate[23]. In some cases, chlorinated substrates enhance anodic efficiencies due to the liberation of chlorine during the course of electrolysis[24]. Active chlorine species such as $Cl^{\bullet}$, $Cl_2^{\bullet-}$, and ClO^{-} are generated at the anode surface and act as indirect oxidants for organic or inorganic reductants. However, the impact of reactive chlorine intermediates on cathodic reactions has not been studied in detail (e.g., the impact of reaction chlorine species on hydrogen production rates in this study). With this in mind, we have compared a variety of substrates in terms of relative anodic oxidation efficiencies and the corresponding effects on cathodic hydrogen production using NaCl or Na_2SO_4 as the supporting electrolytes.

Experimental Details

Chemical Reagents

All chemicals were reagent or HPLC grade. Phenol (PhOH, J.T.Baker), catechol (CC, Sigma), hydroquinone (HQ, J.T.Baker), 2-chlorophenol (2CP, Aldrich), 4-chlorophenol (4CP, Aldrich), 2,4-dichlorophenol (24CP, TCI), 2,6-dichlorophenol (26CP, TCI), 2,4,6-trichlorophenol (246CP, TCI), salicylic acid (SA, Aldrich), benzoic acid (BA, J.T.Baker), methanol (EMD), sodium formate (Aldrich), sodium acetate (Aldrich), maleic acid (Sigma), malonic acid (Sigma), sodium oxalate (Aldrich), and sodium hypochlorite (NaOCl, VWR) were used as received. NaCl (J.T.Baker), Na_2SO_4 (EMD), or CO_2(g)-purged $NaHCO_3$ was used as a supporting electrolyte.

Electrodes

A BiO_x-TiO_2-Ti(0) electrode was used as the primary anode. Details of the anode preparation are provided elsewhere[7,8,22]. In summary, the electrode consists of a series of metal oxide coatings on a titanium metal substrate. They include a pre-coating, sealing coating, slurry coating, and over-coating. Each step of coating requires a specific heat treatment regime with different temperatures and times. A single thin anode with an active area of 25.5 cm^2 and two stainless-steel (SS) cathodes (Hastelloy C-22) of equal size were used as the electrodes. A cathode was placed on both sides of the double-sided anode with a separation distance of 2 mm.

Electrolytic Reactions

The double-sided BiO_x-TiO_2-Ti(0) anode coupled with SS cathodes was immersed in aqueous electrolyte solutions of either sodium chloride or sodium sulfate (200 mL). The electrolyte solution was stirred during continuous purging with air or nitrogen as a background carrier gas. The target substrates were added to the background electrolyte at t = 0 or added subsequently during the course of electrolysis. A constant cell voltage or current was applied to the electrodes with a DC-power supply (HP 6263B and 6260B). The current efficiencies (eq. 11.1) and the energy efficiencies (eq. 11.2) were obtained using the following equations.

$$\text{Current efficiency (\%)} = \frac{\text{Number of molecules produced } (H_2, O_2, \text{ or } CO_2) \text{ or degraded (phenol)}}{\text{Number of electrons flowed}} \times n \times 100 \qquad (11.1)$$

where n = 2 and 4 for cathodic hydrogen and anodic oxygen production, respectively. For anodic current efficiencies, n = 1 for one-electron oxidation of phenol, and n = 14/3 for the complete oxidation of phenol carbon to carbon-dioxide carbon.

$$H_2 \text{ energy efficiency (\%)} = \frac{(39\text{W}\cdot\text{h/g} \times H_2 \text{ rate} \times 2\text{g/mol})}{E_{\text{cell}} \times I_{\text{cell}}} \times 100 \qquad (11.2)$$

Chemical Analyses

The electrolytic reactor was sealed to the atmosphere. The gas in the headspace was extracted using a peristaltic pump and pushed through a membrane inlet and then pulled into a mass spectrometer (MS) under a vacuum (5.0×10^{-6} torr) generated with a turbo pump (Pfeiffer). The extracted gases were ionized by 70 eV electron impact and subsequently analyzed by quadrupole mass spectrometry (Balzers). The volume percent of the headspace was calculated assuming that it was directly proportional to the ion current measured by the mass spectrometer (i.e., the transfer of all gases through the membrane and their 70 eV electron ionization cross-sections were approximately equivalent). This assumption was validated by the fact that ambient air was determined to be 77% nitrogen, 17% oxygen, 5% water vapor, and 1% argon.

Aromatic compounds and their reaction intermediates were analyzed by a high-performance liquid chromatography (HPLC, Agilent 1100 series) using a C18 column for separation. The eluent was composed of 55% Milli-Q water (0.1 wt% acetic acid) and 45% acetonitrile at flow rate of 0.7 mL/min.

Results and Discussion

Substrate-Specific Reaction Rates

A time profile of H_2 and O_2 production at the BiO_x-TiO_2-Ti(0)/SS electrode couple is shown in Figure 11.1 for a background electrolyte concentration of 50 mM NaCl. In the absence of phenol (i.e., conventional water electrolysis), the initial H_2 production rate was observed to range from 90 to 100 μmol min^{-1}. Under steady-state conditions, however, the H_2 production rate declined slightly to 80 μmol min^{-1}. In contrast, with the addition of phenol to the reaction mixture, the H_2 production rate increased again to 110 μmol min^{-1}. The apparent substrate enhancement of the H_2 production rate is maintained for a short period after the incremental addition of phenol, and then it relaxes back to the state-state condition as the rate of CO_2 production is maximized. On the other hand, the addition of an oxidizable substrate has little impact on the rate of O_2 production.

Other phenolic substrates—such as catechol, hydroquinone, salicylic acid, 2-chlorophenol, and 4-chloropenol—exhibit similar behavior as shown in Figure 11.2a, whereas maleic acid, malonic acid, and oxalic acid have a lesser rate enhancement than the phenolic substrates. Lower molecular weight compounds such as methanol, formate, and acetate do not show any synergistic effects on the hydrogen production rates.

The addition of phenol to the electrolytic system lowers the cell current from 0.38 A to 0.32 A under a constant DC cell voltage of 3.1 V in spite of an increase in hydrogen production by 20 μmol min^{-1} (Table 11.1). Maleic acid, oxalic acid, catechol, salicylic acid, and the chlorinated phenols also increase the hydrogen production efficiency, while concurrently lowering cell current. When the electrolytic cell is powered by a PV array, then the cell voltage is increased from 4.0 V to 4.2 V upon addition of phenol, while the cell current remains constant[7]. Therefore, the substrate synergistic effect on the hydrogen production energy efficiency is twofold: the hydrogen production rates are increased and the cell currents are decreased at a constant DC cell voltage. The addition of aromatic substrates results in an increase in the apparent energy efficiencies by 30 to 50%, whereas the addition of maleic or oxalic acid increases the efficiencies by only 8 to 10% (Table 11.1).

The degradation of the phenolic substrates follows pseudo-first-order kinetics. The observed reaction rate constants ($-k_{\mathrm{obs}}^{\mathrm{S}}$) appear to be dependent on the chemical structure under similar electrolytic conditions (I_{cell} = 0.375A; 50 mM NaCl).

$$\frac{\mathrm{d[S]}}{\mathrm{dt}} = -k_{\mathrm{obs}}^{\mathrm{S}}[\mathrm{S}] \tag{11.3}$$

For example, the degradation rates of hydroquinone and 2,4,6-trichlorophenol are 4.6 and 3.7 times faster than phenol, respectively (Figure 11.2b & Table 11.1). On the other hand, the degradation rates of salicylic acid and benzoic acid are 2 and 250 times slower than phenol, respectively. It appears that the presence of a aromatic ring substituent such as a chlorine (-Cl) and/or hydroxyl group (-OH) enhances the apparent degradation rates, while carboxyl groups (-COOH/-COO$^-$) decrease the observed rates relative to phenol[25,26].

NaCl and NaSO$_4$ as Background Electrolytes

To investigate the nature of the substrate-induced synergistic effects, sodium sulfate was used as the electrolyte and compared with sodium chloride in terms of the electrochemical hydrogen production and substrate degradation rates. The hydrogen production energy efficiencies in the sodium sulfate range from 50 to 80%, depending on the applied power. The efficiencies are 10 to 20% higher than those observed for sodium chloride (Figure 11.3a). However, upon addition of phenol to the sodium sulfate electrolyte, the hydrogen production rate decreases slightly with no apparent synergy (Figure 11.3b). The electrolytic degradation rates of phenol, salicylic acid, and benzoic acid with Na$_2$SO$_4$ as the background electrolyte are lower than those with a NaCl electrolyte system (Figure 11.3c vs. Figure 11.2b; Table 11.1). For example, the degradation rate of *0.1 mM* phenol in sodium sulfate is 37 times lower than that of *1 mM* phenol in sodium chloride ($-k_{\text{obs}}^{\text{PhOH}}$ (in NaCl) $/-k_{\text{obs}}^{\text{PhOH}}$ (in Na$_2$SO$_4$) = 37) (implying the degradation rate of 1 mM phenol in sodium sulfate should be much lower). The degradation of salicylic acid also shows a similar rate difference, e.g., $-k_{\text{obs}}^{\text{SA}}$ (in NaCl) $/-k_{\text{obs}}^{\text{SA}}$ (in Na$_2$SO$_4$) = 19. However, the variation of the observed degradation rates with structure of the organic substrates is substantially less in Na$_2$SO$_4$ than NaCl (e.g., $-k_{\text{obs}}^{\text{SA}}/-k_{\text{obs}}^{\text{PhOH}} = 0.41$ and $-k_{\text{obs}}^{\text{BA}}/-k_{\text{obs}}^{\text{PhOH}} = 0.0045$ in NaCl; $-k_{\text{obs}}^{\text{SA}}/-k_{\text{obs}}^{\text{PhOH}} = 0.81$ and $-k_{\text{obs}}^{\text{BA}}/-k_{\text{obs}}^{\text{PhOH}} = 0.13$ in Na$_2$SO$_4$). These results suggest that the primary oxidant (e.g., $SO_4\cdot^-$, ·OH radical or surface bound holes, h$^+$) in the Na$_2$SO$_4$ electrolytic system is of lower concentration and/or less discriminating in terms of likely reaction sites.

A change in the supporting electrolyte also affects the extent of pH change during the course of electrolysis. After initiation of electrolysis in a pure sodium chloride solution, the pH immediately rises from 6 to 10, and then is maintained at a steady state throughout continued electrolysis (Figure 11.4a)[8]. After terminating the electrolysis, the pH decreases to 9.5. However, in the presence of phenol, the pH increases to 11 during the initial stages of electrolysis and subsequently declines to a value below pH 7 as small organic acids are produced. Upon continued electrolysis, the pH increases slightly to circum-neutral range (~ pH 7.5). Electrolytic hydrogen production consumes protons and/or generates hydroxide ions resulting in increase of pH. However, continued oxidation of phenol results in the formation of ring-opening intermediates leading to the production of short-chained organic acids such as oxalic acid and maleic acid, which may serve to lower the pH.

The pH vs. time profile during the electrolysis of pure sodium sulfate is similar to that observed in pure NaCl electrolyte. On the other hand, the pH vs. time profile during the electrolytic oxidation of phenol in a background sodium sulfate electrolyte (Na_2SO_4 + phenol) is clearly different than that observed during electrolysis in Na_2SO_4 alone. In addition, the pH vs. time profile for Na_2SO_4 electrolysis has a different shape than that observed in the case of the electrolytic oxidation of phenol in the presence of sodium chloride electrolyte. In particular, the pH does not return to the circum-neutral range at any time during the electrolysis. The degradation rates of substrates during sodium sulfate electrolysis are much slower than those in the sodium chloride (Figure 11.2b vs. 11.3c; Table 11.1). The apparent pH-lowering effect during NaCl electrolysis is due to the production of the short-chained organic acids. However, in the case of Na_2SO_4

electrolytic phenol oxidation, the short-chain carboxylates are either not electrolysis intermediates or not produced on the timescale of the current electrolysis experiments. This is consistent with the observation that CO_2 is not produced during the course of phenol electrolysis in the presence of sodium sulfate.

Primary Reactive Intermediate Species

The presence of titanol groups (i.e., >TiOH) on the hydrated, anodic TiO_2 surface implies that the initiation of the oxidation proceeds via formation of either a surface-bound hydroxyl radical (>Ti-OH$^\bullet$) or a free hydroxyl radical ($^\bullet$OH) (A1 in Table 11.2). The initiation of the cathodic reaction proceeds via the one electron-reduction of dissolved oxygen molecules (A7 and E1), protons, or water (E2). However, further reactions may have many parallel or sequential steps in which the supporting electrolyte is either directly or indirectly involved the subsequent reactions. For example, the electrochemical oxidation of organic substrates in the presence of a sodium chloride electrolyte has six or more possible oxidation pathways. They include direct electron transfer from the substrate to surface-bound OH$^\bullet$, and indirect homogeneous reactions with free OH$^\bullet$, Cl$^\bullet$, $Cl_2^{\bullet-}$, HClO/ClO$^-$, and H_2O_2 (Table 11.2).

>TiOH$^\bullet$/OH$^\bullet$

Figures 11.5a and b show the correlation between the normalized pseudo-first-order electrolysis rates for the substrates ($k^{o}_{obs} = -k^{S}_{obs} / -k^{PhOH}_{obs}$) and the relative bimolecular reaction rate constants of $^\bullet$OH and $Cl_2^{\bullet-}$ with respect to phenol ($k^{o}_{OH} = k_{OH+S} / k_{OH+PhOH}$; $k^{o}_{Cl_2^-} = k_{Cl_2^-+S} / k_{Cl_2^-+PhOH}$)[27–29]. The k^{o}_{obs} vs. k^{o}_{OH} data are not correlated. This suggests that hydroxyl radicals are not the primary oxidant involved in the anodic reactions. The steady-state concentration of OH radicals (i.e., [$^\bullet$OH] = [>Ti-OH$^\bullet$] + [free $^\bullet$OH]) can be estimated assuming that 20% of applied current generates oxygen (i.e., $I_{\mathrm{an}}^{\mathrm{O_2}} = 0.2 I_{\mathrm{an}}$) and the reaction of OH radical with Cl$^-$ is the dominant OH$^\bullet$ pathway ($k_{\mathrm{OH+Cl^-}}[\mathrm{Cl^-}] >> k_{\mathrm{OH+ClO^-}}[\mathrm{ClO^-}] + k_{\mathrm{OH+S}}[\mathrm{S}]$). The assumption of $I_{\mathrm{an}}^{\mathrm{O_2}} / I_{\mathrm{an}} = 0.2$ is valid, since typical H_2/O_2 ratio is approximately 7 and the cathodic hydrogen production current efficiency is 70% (i.e., $H_2/O_2 = 7$; $I_{\mathrm{cell}} = I_{\mathrm{an}} = I_{\mathrm{ca}}$; $I_{\mathrm{ca}}^{\mathrm{H_2}} / I_{\mathrm{ca}} = 0.7$; $I_{\mathrm{an}}^{\mathrm{O_2}} = 2 \times I_{\mathrm{ca}}^{\mathrm{H_2}}$, thus $I_{\mathrm{an}}^{\mathrm{O_2}} / I_{\mathrm{an}} = 0.2$).

$$\frac{d[\mathrm{OH^\bullet}]}{dt} = \frac{4I_{\mathrm{an}} - I_{\mathrm{an}}^{\mathrm{O_2}}}{4\mathrm{FV}} - (k_{\mathrm{OH+Cl^-}}[\mathrm{Cl^-}] + k_{\mathrm{OH+ClO^-}}[\mathrm{ClO^-}] + k_{\mathrm{OH+S}}[\mathrm{S}])[\mathrm{OH^\bullet}] \qquad (11.4)$$

$$[\mathrm{OH^\bullet}]_{\mathrm{SS}} = \frac{4I_{\mathrm{an}} - I_{\mathrm{an}}^{\mathrm{O_2}}}{4\mathrm{FV}(k_{\mathrm{OH+Cl^-}}[\mathrm{Cl^-}]_{\mathrm{SS}})} \qquad (11.5)$$

At I_{cell} = 0.375A and in the presence of 50 mM NaCl, the steady-state hydroxyl radical concentration is estimated to be 1.6×10^{-15} mol cm^{-2} at the anode surface (corresponding to 8.6×10^{-15} mol L^{-1} if all OH$^\bullet$ were released to solution). This number is seven orders of magnitude smaller than the typical site density of >Ti-OH groups on colloidal TiO_2 (i.e., assuming 5 hydroxy sites nm^{-2}), which is equivalent to 1×10^{-8} mol-OH cm^{-2} [30]. Thus, once produced, the surface-bound or free hydroxyl radical immediately reacts with chloride ion to yield Cl$^\bullet$. The low >TiOH$^\bullet$ concentration also yields a large number of potential binding sites for a substrate sorption to the TiO_2 surface and direct electron transfer reactions may occur simultaneously with homogeneous oxidations.

Cl$^\bullet$

The possible active chlorine species include Cl$^\bullet$, $Cl_2^{\bullet-}$, HClO, and ClO$^-$. In aqueous solution, the active chlorine species will be in equilibrium with each other and their redox potentials are as follows: E°($Cl^•/Cl^-$) > E°($Cl_2^{•-}/2Cl^-$) > E°($HClO/0.5Cl_2$) > E°($Cl^-/HClO$) > E°(Cl^-/ClO^-) (D1–D3)[31]. From a thermo-chemical perspective, $Cl^•$ is the most reactive species towards one electron oxidation. It has a similar reactivity when compared to $^•OH$ radical (E°($OH^•/H_2O$) = 2.7 V)[29]. And the $Cl^•$ second-order rate constants for reaction with a wide range of aliphatic organic compounds (RH) are well correlated (k_{OH+RH} vs. k_{Cl+RH}).[32] $Cl^•$ readily undergoes rapid addition, hydrogen-abstraction, and direct electron transfer reactions with aromatics at second-order rate constants ranging from 10^8 to 10^9 M^{-1} s^{-1}. $Cl^•$ is generated through a transient adduct of Cl^- with the >Ti-$OH^•$ group at the anode surface, or by direct hole oxidation of >$TiOHCl^-$ surface groups and subsequent protonation of the adduct (A4). Assuming all reactions are diffusion controlled, the $Cl^•$ branching ratio depends on the Cl^- concentration relative to S concentration; at low [Cl^-]/[S] < 1 , the reaction of $Cl^•$ with substrates is predominant, whereas at high [Cl^-]/[S] > 1 concentration, $Cl_2^{•-}$ formation should occur preferentially[32,33]. The relatively high Cl^- concentration (50 mM) as compared to substrates (~ 1 mM) in our system pushes $Cl^•$ branching towards $Cl_2^{•-}$ formation. The nondetection of $Cl_{2(g)}$ is consistent with $Cl_2^{•-}$ formation (i.e., B3 and B5 are negligible).

$Cl_2^{•-}$

At high background chloride concentrations, [Cl^-]/[S] > 1, $Cl_2^{•-}$ should dominate the active chlorine species. When k^o_{obs} values are plotted against known $k^o_{Cl_2^{•-}+S}$ values for phenol, salicylic acid, hydroquinone, and benzoic acid, an excellent linear correlation is obtained ($R^2 > 0.99$), as shown in Figure 11.5b. This strongly indicates that the dichloride radical anion is a primary oxidant species during electrolysis with sodium chloride. The dichloride radical anion is in equilibrium with $Cl^{\bullet}$ and Cl^{-} (B4: $K_{eq} = 1.4\times10^{5}$ M^{-1}; $[Cl^{-}] =$ 50 mM, $[Cl_2^{\bullet-}]/[Cl^{\bullet}] = 7\times10^{3}$) and the forward reaction is diffusion controlled[28,34,35]. Like $Cl^{\bullet}$, $Cl_2^{\bullet-}$ reacts with organics via hydrogen abstraction, electrophilic addition, and direct electron transfer mechanisms. However, $Cl_2^{\bullet-}$ bimolecular oxidation kinetics is typically two to four orders of magnitude slower than $Cl^{\bullet}$. $Cl_2^{\bullet-}$ reacts with the aliphatic compounds primarily through a hydrogen abstraction mechanism with rate constants ranging from $< 10^{3}$ to 10^{6} M^{-1} s^{-1} [36,37]. The H-abstraction rates are controlled by the C-H bond dissociation energy. In addition, deprotonated substrates are less reactive than their protonated counterparts. For example, the reaction rate of $Cl_2^{\bullet-}$ with formic acid is two to three orders of magnitude greater than with formate (Table 11.1), consistent with H-abstraction being the predominant mechanism. $Cl_2^{\bullet-}$ oxidation mechanisms and kinetics are also affected by size (i.e., steric hindrance) and electron donating/withdrawing character of aromatic substituents.

The reaction of $Cl_2^{\bullet-}$ with aromatic compounds involves H-atom abstraction, direct electron transfer or electrophilic addition, with rate constants ranging from 10^{6} to 10^{9} $M^{-1}s^{-1}$. A previously reported Hammett plot of para-substituted phenols indicates that electron-withdrawing substituents such as -COOH and -CN decrease the rate relative to phenol, whereas electron-donating substituents such as $-OCH_3$, $-COO^{-}$, and -OH, increase the rate relative to phenol[36]. The results suggest an electrophilic addition or direct electron transfer mechanism, which would benefit from increased electron density, are active. Figure 11.5d shows a plot between k^{o}_{obs} and the corresponding Hammett (σ) constants. The observed V behavior suggests $Cl_2^{\bullet-}$ oxidation has two branching pathways[38,39]. The negative correlation ($-0.4 < \sigma < 0.2$, $R^2 > 0.93$) is in agreement with previous pulse radiolysis results, suggesting a Cl-addition or direct electron transfer pathway. Once $\sigma > 0.2$, $k^{\mathrm{o}}_{\mathrm{obs}}$ is positively correlated with σ, indicating a change in the $Cl_2^{\bullet-}$ oxidation mechanism. The addition of bulky Cl-subtituents may sterically hinder $Cl_2^{\bullet-}$ from an intimate encounter with the phenol retarding a Cl-addition or direct electron transfer pathway. Steric hindrance could explain why Cl-addition/electron transfer is no longer the primary pathway, but can not explain the rate increase. The subsequent addition of electron withdrawing groups removes electron density from the ring and weakens the remaining Ar-H bonds. $Cl_2^{\bullet-}$ H-abstraction rates with aliphatics are directly proportional to the C-H bond strength. This would suggest a $Cl_2^{\bullet-}$ H-abstraction mechanism is present in the positive correlation regime. Another plausible explanation is that the increased electron-withdrawing character will reduce the pK_a and a shift in branching pathway is the result of aqueous speciation (i.e, phenol vs. phenoxide).

HOCl/OCl$^-$

Hypochlorous acid (HOCl) or hypochlorite (ClO^-) can be electrochemically produced via a number of mechanisms: direct hole oxidation of >Ti-OHCl$^{\bullet-}$ at the anode surface (A5), $Cl_2^{\bullet-}$-oxidation of H_2O (B7), or by reaction of $Cl_2^{\bullet-}$ and >Ti-OH$^{\bullet}$/OH$^{\bullet}$ (here no distinction between surface-bound and free OH radical) (B8). Many investigators argue that hypochlorous acid (E° = 1.63V) and hypochlorite ion (E° = 0.90V) are the primary oxidants in the electrochemical degradation of organics in a sodium chloride medium[9,10,12,18,24]. In this study, the production of hypochlorite was only observed during the electrolysis of NaCl in the absence of organics (Figure 11.6a). During NaCl electrolysis, hypochlorite increases in concentration reaching a plateau of 5 mM after 1 h of electrolysis. Absence of HOCl/OCl$^-$ accumulation in the presence of phenol would suggest a HOCl/OCl$^-$ loss mechanism via substrate oxidation. However, as shown in Figure 11.5c there is no correlation between the normalized electrochemical oxidation rates ($k^{\mathrm{o}}_{\mathrm{obs}}$) and the normalized bimolecular rate constants of HOCl with substrates ($k^{\mathrm{o}}_{\mathrm{HOCl}}$). Additionally, HOCl has relatively slow second-order rate constants with phenol (e.g., $k_{\mathrm{HOCl+PhOH}} = 2.19 \times 10^4$ M^{-1} s^{-1} and $k_{\mathrm{Cl_2^{\bullet-}+PhOH}} / k_{\mathrm{HOCl+PhOH}} = 1.14 \times 10^5$) and becomes even slower with OH- or Cl-addition (i.e., 10^1 to 10^3 M^{-1} s^{-1}, $k_{\mathrm{Cl_2^{\bullet-}+HQ}} / k_{\mathrm{HOCl+HQ}} = 3.11 \times 10^6$)[40]. An alternative mechanism is proposed by examining the pathways for HOCl production which involve $\mathrm{Cl_2}^{\bullet-}$ as an intermediate (B7, B8). Substrate addition will consume $\mathrm{Cl_2}^{\bullet-}$ subsequently inhibiting the HOCl production pathways. The alternative mechanism HOCl inhibition through intermediate $\mathrm{Cl_2}^{\bullet-}$ consumption is consistent with kinetic correlations and time-dependent HOCl observation.

The effect of the hypochlorite on electrochemistry was investigated by spiking the reactor to 5 mM NaOCl during electrolysis of 50 mM NaCl at a constant cell voltage (E_{cell} = 3.17 V, Figure 11.6b). Immediately after addition, the hydrogen production rate decreased, then slowly recovered and eventually exceeded the initial production rate. The oxygen production rate increased upon NaOCl addition and retained a higher production rate during continued electrolysis. The addition of sodium hypochlorite also increased the cell current from 0.38 A to 0.44 A. A subsequent NaOCl addition yielded similar results (i.e, the cell current increases again from 0.43 A to 0.50 A). After continued electrolysis, a slight decrease in cell current is observed (e.g., 0.44 A to 0.43 A; 0.50 A to 0.48 A).

$\mathrm{Cl^{I}O^-}$ can be electrochemically oxidized to chlorate ion ($\mathrm{Cl^{V}O_3^-}$) with simultaneous generation of oxygen (B20) or reduced to chloride ion (D3). The oxidative pathway (B20) increases the overall oxygen production, while the reductive pathway (D3) competitively reduces the hydrogen production (E2) leading to initial decrease of the hydrogen production rate. The oxidative pathway (B20) yields a greater electron flow through the circuit and increases the cell current and the hydrogen production rate as the electrolysis proceeds. It was reported that chlorate anion (ClO_3^-) is produced either when hypochlorous acid is hydrolyzed (B20)[12] or when Cl_2 gas is released at a boron-doped diamond electrode[41].

H_2O_2

Hydrogen peroxide (H_2O_2) can be produced by an anodic surface recombination pathway (A3), through hydroxyl radical recombination (B8), or hydroperoxy radical recombination (A7c). The oxidation of substrates such as phenol with NaCl as an electrolyte does not produce any hydroxylated intermediates (e.g., catechol, hydroquinone, resorcinol); instead, only chlorinated phenols such as 2-/4-chlorophenol, 2,4-/2,6-dichlorophenol, and 2,4,6-trichlorophenol were observed as intermediates[7,8]. This suggests that even if hydrogen peroxide is produced, it contributes little to the oxidation of the substrates. Hydrogen peroxide can be oxidized by the hydroxyl radical (B9, $k = 2.7 \times 10^7\ M^{-1}\ s^{-1}$) or $Cl_2^{\bullet-}$ (B12, $k = 1.4 \times 10^5\ M^{-1}\ s^{-1}$) to hydroperoxyl radical ($HOO^\bullet$), which is further oxidized by $Cl_2^{\bullet-}$ to oxygen (B13) at diffusion-limited rates ($k = 3 \times 10^9\ M^{-1}\ s^{-1}$). In addition, hydrogen peroxide may also react with chloride ion under present conditions yielding HOCl (B14). Despite the bulk alkaline pH (Figure 11.4a), the near-surface region (i.e., within electrical double layer) of the metal-doped TiO_2 anode should have a lower pH due to the presence of surface-bound Lewis acid metals, driving reaction B14 and subsequent reaction of H_2O_2 and HClO (B15) to yield O_2.

Primary Electrochemical Oxidant

Most studies of the electrochemical degradation of phenolic compounds with NaCl argue that the primary oxidant is $HClO/ClO^{-}$[9,10,12,18,24], which has been reported to chlorinate phenol[42,43]. In contrast, we argue that $Cl_2^{\bullet-}$ is the primary oxidant and that $HClO/ClO^{-}$ plays a only minor role, if any, in the overall oxidation mechanism. $Cl_2^{\bullet-}$ has a greater one-electron oxidation potential than $HClO/ClO^{-}$ by 0.5/1.0 eV, and its reaction rate constants with organics are approximately five orders of magnitude greater. In addition, the relative bimolecular rate constants of $Cl_2^{\bullet-}$ with various substrates correlate well with the observed reaction kinetics (Figure 11.5d). On the other hand there is no correlation between relative HOCl rate constants and the observed kinetics (Figure 11.5c). Additionally, $Cl_2^{\bullet-}$ consumption during substrate oxidation (C5a) will inhibit HOCl production (B7, B8) consistent with experimental results.

NaCl electrolysis without substrate produces active chlorine species at the anode, which can be reduced at the cathode (Scheme 11.1) yielding a null chemical cycle. Thus, the chlorine species act as an electron relay between the anode and the cathode, ultimately limiting H_2 production rates. Upon substrate addition during electrolysis at a constant cell voltage (E_{cell}) the active chlorine species rapidly oxidizes the substrates, inhibiting the electron-shuttle pathway consistent with the observed decrease in I_{cell}. Despite the lower I_{cell}, H_2 production increases because a greater fraction of the cathodic electrons are available for H_2O/H^{+} reduction, as they are no longer scavenged by active chlorine. If the substrates are not oxidized by the chlorine species, hydrogen production is not enhanced. This argument explains why the extent of synergism is substrate-specific and dependent upon the substrate oxidation kinetics (i.e., depletion of active chlorine electron scavengers).

For example, the substitution-dependent trend of the observed pseudo-first-order rates in sodium chloride is $-k_{\mathrm{obs}}^{\mathrm{PhOH}} > -k_{\mathrm{obs}}^{\mathrm{2\text{-}CP}} > -k_{\mathrm{obs}}^{\mathrm{4\text{-}CP}} \sim -k_{\mathrm{obs}}^{\mathrm{CC}} > -k_{\mathrm{obs}}^{\mathrm{SA}} >> -k_{\mathrm{obs}}^{\mathrm{BA}}$, which parallels the apparent order of synergistic effects (i.e., ΔEE), PhOH > 2-CP > 4-CP > SA > CC >> BA. Figure 11.7 shows the linear correlations of $-k_{\mathrm{obs}}$ vs. $-\Delta I_{\mathrm{cell}}$ and $-k_{\mathrm{obs}}$ vs. ΔEE with $R^2 = 0.90$ and 0.91, respectively. This indicates that the substrate oxidation kinetics significantly influences the cathodic hydrogen production. The minimal synergism observed for catechol, in spite of relatively fast electrolytic degradation, can be attributed to a different reaction mechanism. Due to neighboring aromatic -OH groups, catechol adsorbs strongly to the metal oxide surface. Catechol oxidation is likely due to direct electron transfer of the adsorbed (i.e., chelated) catechol to a hole at the anode surface. If the chloride radical anion is, in fact, the primary active chlorine species, then the substrate-dependent reaction rate can be readily interpreted. For example, $-k_{\mathrm{obs}}^{\mathrm{HQ}}$ is 4.5 times higher than $-k_{\mathrm{obs}}^{\mathrm{PhOH}}$ and $k_{\mathrm{Cl_2^{\bullet-}+HQ}}$ is 5.6 times higher than $k_{\mathrm{Cl_2^{\bullet-}+PhOH}}$, while $-k_{\mathrm{obs}}^{\mathrm{SA}} / -k_{\mathrm{obs}}^{\mathrm{PhOH}}$ is 0.41 and $k_{\mathrm{Cl_2^{\bullet-}+SA}} / k_{\mathrm{Cl_2^{\bullet-}+PhOH}}$ is 0.44. The slow reaction rate of $\mathrm{Cl_2^{\bullet-}}$ with aliphatic substrates is consistent with the lack of synergy.

Effects of Variable Reaction Parameters

An increase in the concentration of the active chlorine species should affect the electrolytic degradation rates and, subsequently, the rates of hydrogen production at the cathode. When the sodium chloride concentration was increased from 0 to 50 mM in a background sodium sulfate electrolyte (50 mM), $-k_{\mathrm{obs}}^{\mathrm{PhOH}}$ was observed to increase linearly (Figure 11.8a). Since $-k_{\mathrm{obs}}^{\mathrm{S}}$ is the product of the true first-order rate constant ($k_{\mathrm{Cl}_2^{\bullet -}+\mathrm{S}}$) and the concentration of the reactive chlorine species ($N_{\mathrm{Cl2\bullet -ss}}$) which can be varied experimentally, the intrinsic contribution of the active chlorine species to the degradation of phenol, α, can be estimated simply by plotting $-k_{\mathrm{obs}}^{\mathrm{S}}$ vs. [NaCl].

$$\frac{\mathrm{d[S]}}{\mathrm{dt}} = -k_{\mathrm{obs}}^{\mathrm{S}} \times [\mathrm{S}] = k_{\mathrm{Cl}_2^{\bullet -}+\mathrm{S}} \times \mathrm{N}_{\mathrm{Cl}_2^{\bullet -}} \times [\mathrm{S}] \tag{11.6}$$

$$-k_{\mathrm{obs}}^{\mathrm{S}} = k_{\mathrm{Cl}_2^{\bullet -}+\mathrm{S}} \times \mathrm{N}_{\mathrm{Cl}_2^{\bullet -}} = \alpha[\mathrm{NaCl}] \tag{11.7}$$

$$\frac{-k_{\mathrm{obs}}^{\mathrm{S}}}{[\mathrm{NaCl}]} = \alpha \tag{11.8}$$

α is determined to be 1.8 M^{-1} min^{-1} with a $R^2 > 0.99$ at 1 mM phenol, 50 mM $\mathrm{Na_2SO_4}$, and I_{cell} = 14.7 mA cm^{-2}. However, when oxidation rates of 50 mM NaCl + 50 mM $\mathrm{Na_2SO_4}$ are compared to 50 mM NaCl (without $\mathrm{Na_2SO_4}$), the latter is found to be higher than the former by a factor of two. This indicates that when present together, the two electrolytes compete for anodic oxidation, and as a consequence, the steady-state concentration of active chlorine radical species are reduced.

The sodium chloride concentration is observed to play a negative role on cathodic hydrogen production, even when present with $\mathrm{Na_2SO_4}$. For example, the current efficiency for the hydrogen production is optimized at 96% under 50 mM $\mathrm{Na_2SO_4}$, decreases to 80% under 50 mM NaCl + 50 mM $\mathrm{Na_2SO_4}$, and is further lowered to 73% under 50 mM NaCl. This observation further confirms that active chlorine radical species act as an electron-shuttle between the anode and the cathode, whereas the primary oxidized sulfate species is not an effective electron shuttle. Therefore, electrolytic production of active chlorine species from chloride has a negative effect on the net cathodic process of H_2 production relative to sulfate, but a positive effect on the anodic substrate oxidation.

In addition to the concentration of the supporting electrolyte, the applied cell current also directly affects the efficiencies of the hybrid reactions. $-k_{\mathrm{obs}}^{\mathrm{S}}$ is linearly correlated to I_{cell} with a slope of 12.6 $\mathrm{min^{-1}A^{-1}cm^{2}}$ ($R^2 > 0.98$). As a consequence, the reaction of 1 mM phenol at I_{cell} values up to 40 mA $\mathrm{cm^{-2}}$ is in the reaction-limited regime. In this regime, the overall reaction rate is limited by the low steady-state concentration of aqueous oxidizing radicals within the dynamic reaction zone. Thus, less-active chlorine species are produced at the anode than are required to oxidize all of the substrate molecules that enter the reaction zone. The pseudo-first-order kinetics is representative of competition between the initial substrate and its intermediates for oxidizing radicals. The number of dichloride radical anions can be estimated in this regime (eq. 11.9).

$$\mathrm{N}_{\mathrm{Cl}_2^{\bullet-}} = \frac{-k_{\mathrm{obs}}^{\mathrm{S}}}{k_{\mathrm{Cl}_2^{\bullet-}+\mathrm{S}}} \tag{11.9}$$

At a $I_{\mathrm{cell}} = 14.7$ mA/$\mathrm{cm^2}$, ($[\mathrm{Cl_2}^{\bullet-}]_{\mathrm{ss}}$ is calculated to be 1.4×10^{-11} mol $\mathrm{L^{-1}}$). This value is three orders of magnitude greater than the number of hydroxyl radicals estimated from eq. 11.5, but still many orders of magnitude lower than typical substrate concentration, [S]. In contrast, the cathodic hydrogen production rate does not correlate linearly with the I_{cell}; rather, its current efficiency increases from 45% at 7 mA $\mathrm{cm^{-2}}$ to 67% at 14.7 mA $\mathrm{cm^{-2}}$, and then levels off at higher I_{cell}.[8] As the I_{cell} value increases, more H_2 is produced. However, the H_2 current efficiency decreases due to increasing number of dichloride radical anions that are produced, which can scavenge electrons.

In a sodium sulfate electrolyte system, analogous to the chloride system, a one-electron oxidation of sulfate to the sulfate radical ($SO_4^{\bullet-}$) is predicted to produce the primary reactive species (eq. 11.10). In spite of the high redox potential of the sulfate radical, the substrate oxidation rates are two orders of magnitude lower than observed with sodium chloride. This is at variance with expectations from previously reported $SO_4^{\bullet-}$ oxidation kinetics (i.e, $k_{SO_4^- + Ar} / k_{Cl_2^- + Ar}$ = 10 - 100).[36] Thus, if free $SO_4^{\bullet-}$ was produced, phenol degradation in Na_2SO_4 would be faster than in NaCl, suggesting that if $SO_4^{\bullet-}$ is produced, it is strongly bound to the metal oxide surface. Surface-bound $SO_4^{\bullet-}$ may react with another surface-bound $SO_4^{\bullet-}$ to produce persulfate, $S_2O_8^{2-}$ (eq. 11.11) or surface-bound $SO_4^{\bullet-}$ may react with surface-bound $^{\bullet}OH$ to produce peroxymonosulfate, SO_5H^-. As non-radical species that would require a two-electron reduction, $S_2O_8^{2-}$ would scavenge cathodic electrons at a much slower rate than $Cl_2^{\bullet-}$. Persulfate can be homolytically cleaved into two sulfate radicals photolytically or thermally[44,45]. but is stable under ambient conditions. Persulfate can be transformed into two sulfate anions and oxygen (eq 11.12) or a peroxymonosulfate and sulfate (eq 11.13). Peroxymonosulfate can be transformed into hydrogen peroxide and sulfate (eq 11.14).

$$> \text{Ti-OH}^{\bullet} + SO_4^{2-} \rightarrow\ > \text{Ti-OH}\ (e^-) + SO_4^{\bullet-} \qquad (11.10)$$

$$SO_4^{\bullet-} + SO_4^{\bullet-} \rightarrow S_2O_8^{\ 2-} \qquad (11.11)$$

$$S_2O_8^{\ 2-} + H_2O \rightarrow 2SO_4^{2-} + 2H^+ + 0.5O_2 \qquad (11.12)$$

$$S_2O_8^{\ 2-} + H_2O \rightarrow SO_5^{2-} + SO_4^{2-} + 2H^+ \qquad (11.13)$$

$$SO_5^{2-} + H_2O \rightarrow H_2O_2 + SO_4^{2-} \qquad (11.14)$$

Figures

Figure 11.1. H_2, O_2, and CO_2 production during phenol electrolysis. $E_{cell} = 3.1$ V. The BiO_x-TiO_2-Ti anode and stainless-steel cathode couple was immersed in 50 mM NaCl (0.2 L) where N_2 was continuously purged through solution. 1.0 mM phenol was spiked at intervals into the solution (as indicated by arrows). The system control was H_2 production via pure water electrolysis without addition of phenol.

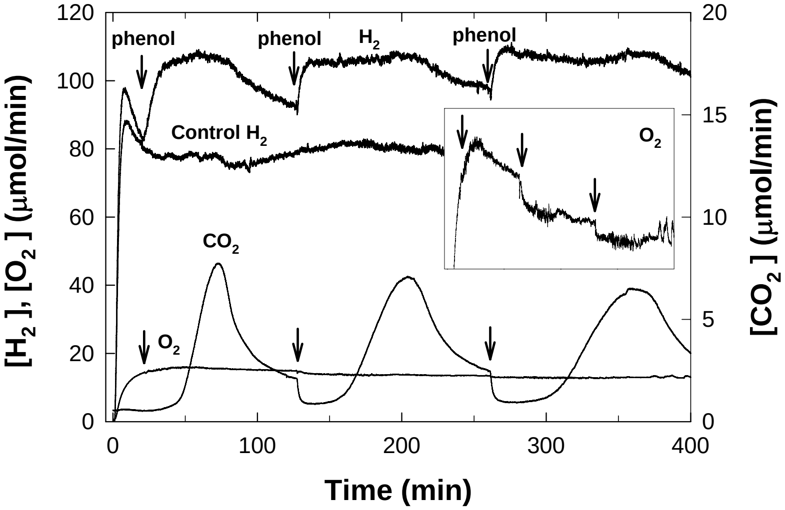

Figure 11.2. A) Effect of various substrate additions on the H_2 production rate. Constant E_{cell}s in 50 mM NaCl solution. See Table 11.1 for E_{cell}s. The sidebars refer to hydrogen production rates of 5 × 10^{-6} mol/min. B) Time profiles of the electrolytic degradation of substrates (1 mM) at I_{cell} = 0.375 A in 50 mM sodium chloride solution. See Table 11.1 for more information.

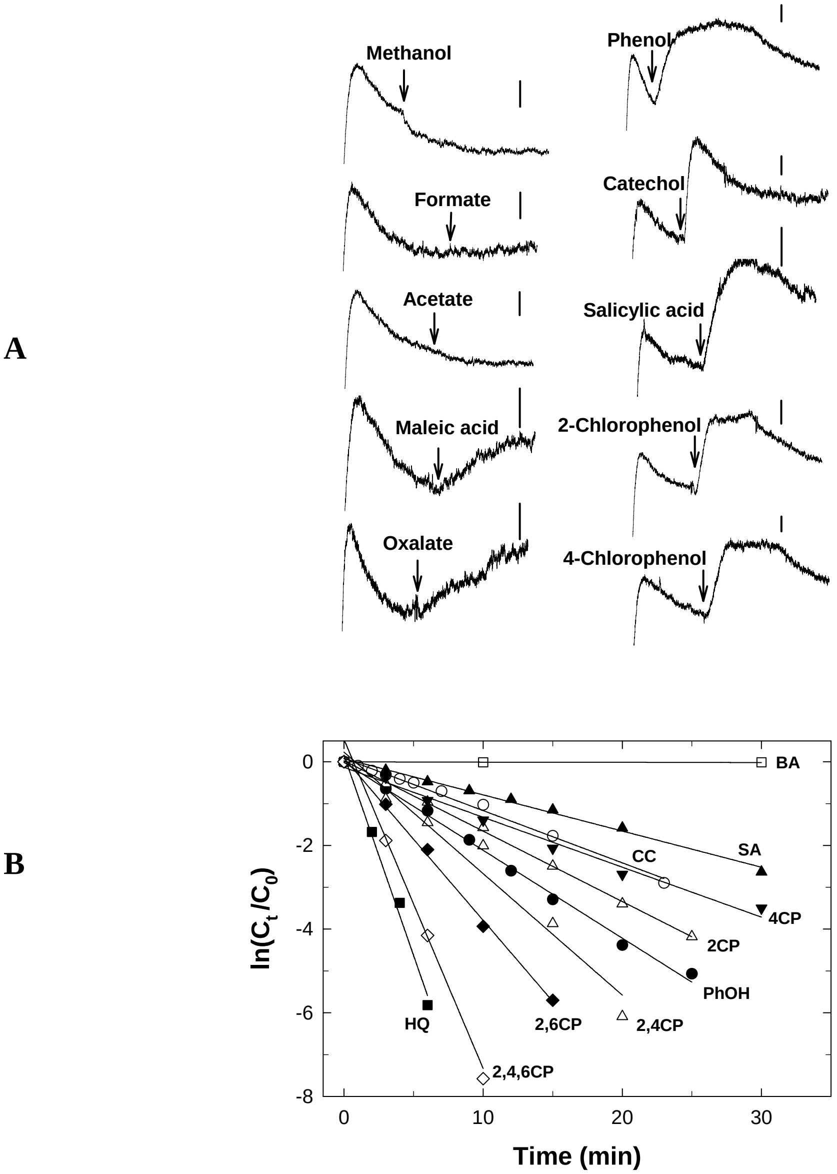

Figure 11.3. Effect of electrolyte, NaCl vs. Na_2SO_4, on electrochemical processes. A) Energy efficiencies for the electrolytic hydrogen production as a function of applied cell power in 50 mM sodium sulfate or 50 mM sodium chloride. B) Effect of 1 mM phenol addition on the electrolytic hydrogen production in 50 mM sodium sulfate. E_{cell} = 3.04 V. C) Time profiles of the electrolytic degradation of substrates (~ 1 mM) in 50 mM sodium sulfate at I_{cell} = 0.375 A. (The NaCl data in (a) is taken from reference 8 for comparison.)

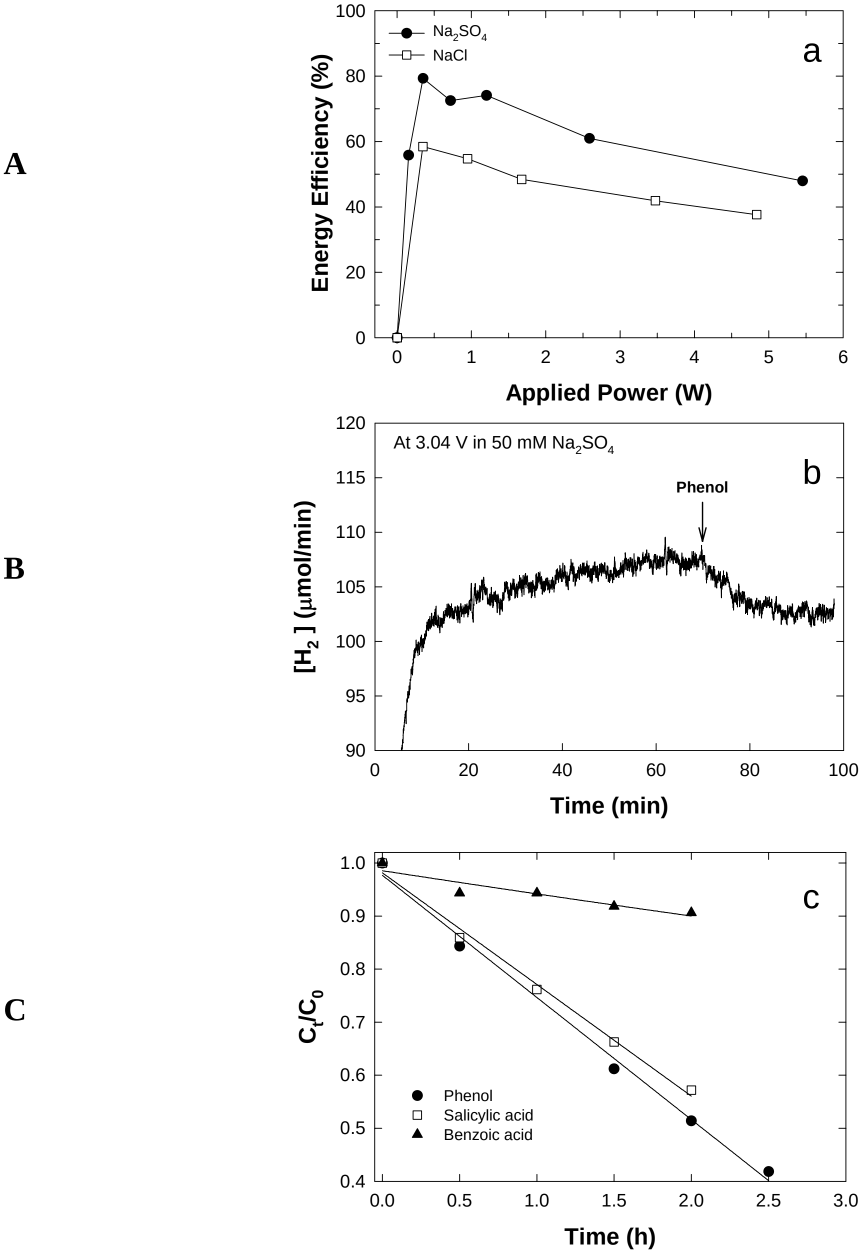

Figure 11.4. Time profiles of pH variation during electrolysis with and without phenol. $[\text{Phenol}]_0$ = 1 mM A) in 50 mM sodium chloride and B) in 50 mM sodium sulfate. I_{cell} = 0.375 A. (Figure (A) is taken from reference 8 for comparison.)

A

B

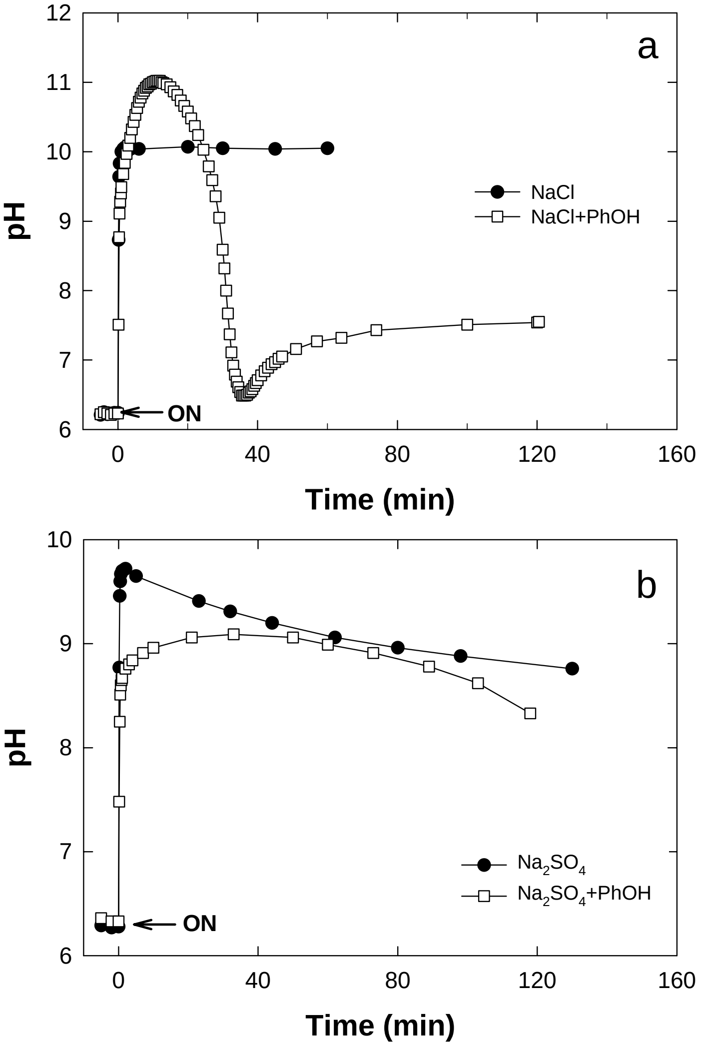

Figure 11.5. Relationships between k^0_{obs}, k^0_{OH}, $k^0_{\mathrm{Cl}_2^{\bullet-}}$, k^0_{HClO}. A) k^0_{obs} vs. k^0_{OH}. B) k^0_{obs} vs. $k^0_{\mathrm{Cl}_2^{\bullet-}}$ C) k^0_{obs} vs. k^0_{HClO}, and D) Hammett constant vs. k^0_{obs}. See Table 11.1 and text for more detailed information

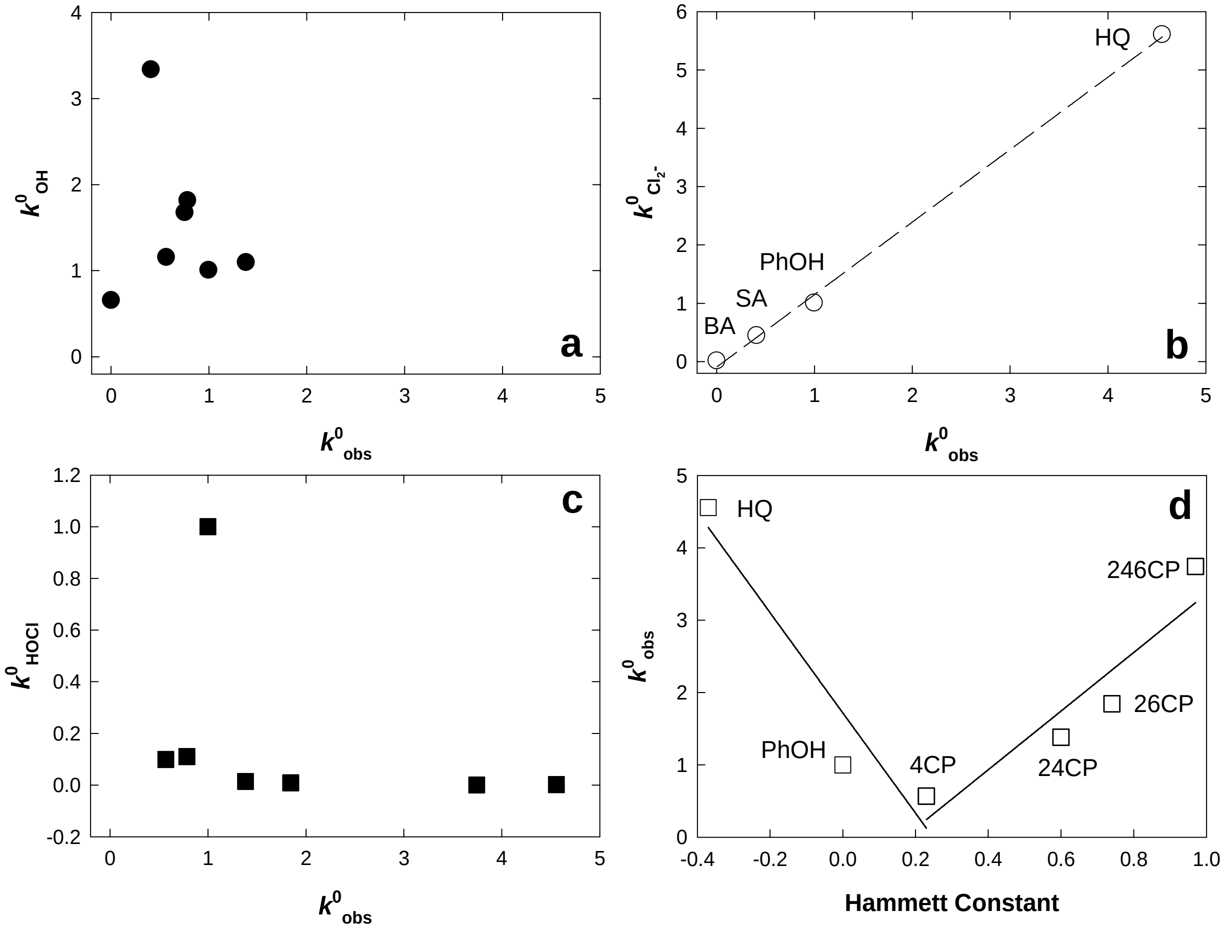

Figure 11.6. Hypochlorite production during electrolysis. A) [NaCl] = 50 mM. The inset shows the UV-vis absorption spectrum of the produced hypochlorite. I_{cell} = 0.375 A. B) Effects of spiking 5 mM sodium hypochlorite on the hydrogen and oxygen production, and on the change of I_{cell}. E_{cell} = 3.17 V. [NaCl] = 50 mM

A

B

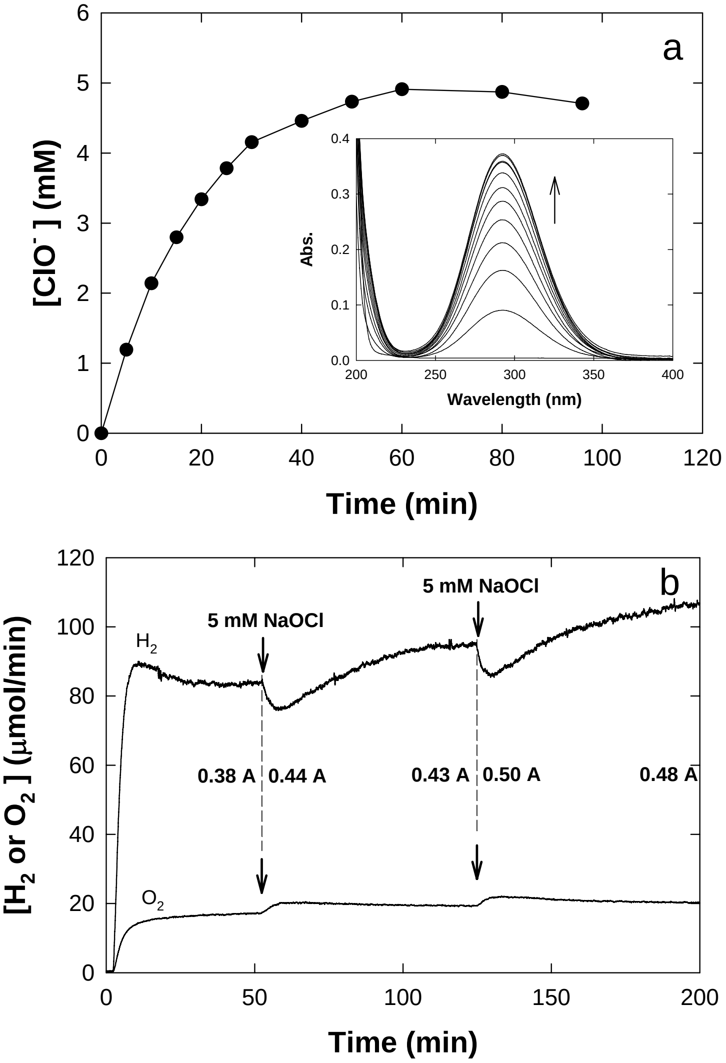

Figure 11.7. Electrochemical relationships of $-k_{\text{obs}}$ vs. ΔI_{cell} and $-k_{\text{obs}}$ vs. ΔEE. (See Table 11.1 and the text for more detailed information.)

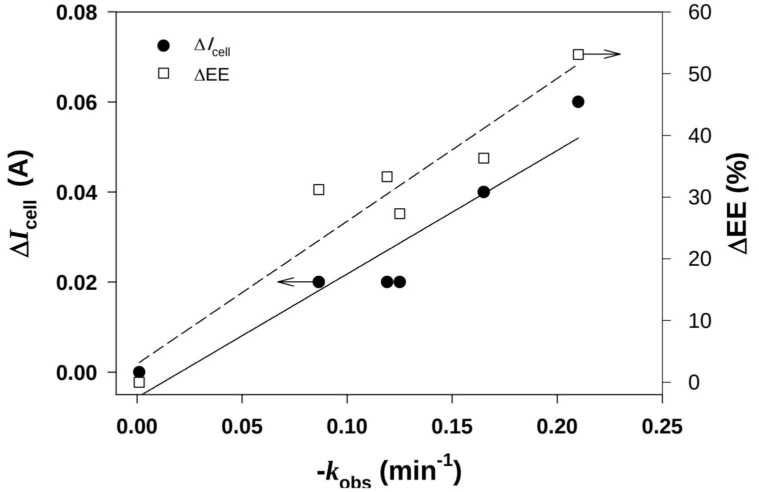

Figure 11.8. $-k_{obs}$ and I_{cell} vs. NaCl concentration in 50 mM Na_2SO_4. A) the electrolytic degradation rates of 1 mM phenol and on B) the current efficiencies for the hydrogen production. I_{cell} = 0.375 A; [Na_2SO_4] = 50 mM. NaCl only refers to 50 mM NaCl without Na_2SO_4. The numbers in insets refer to [NaCl] (mM)

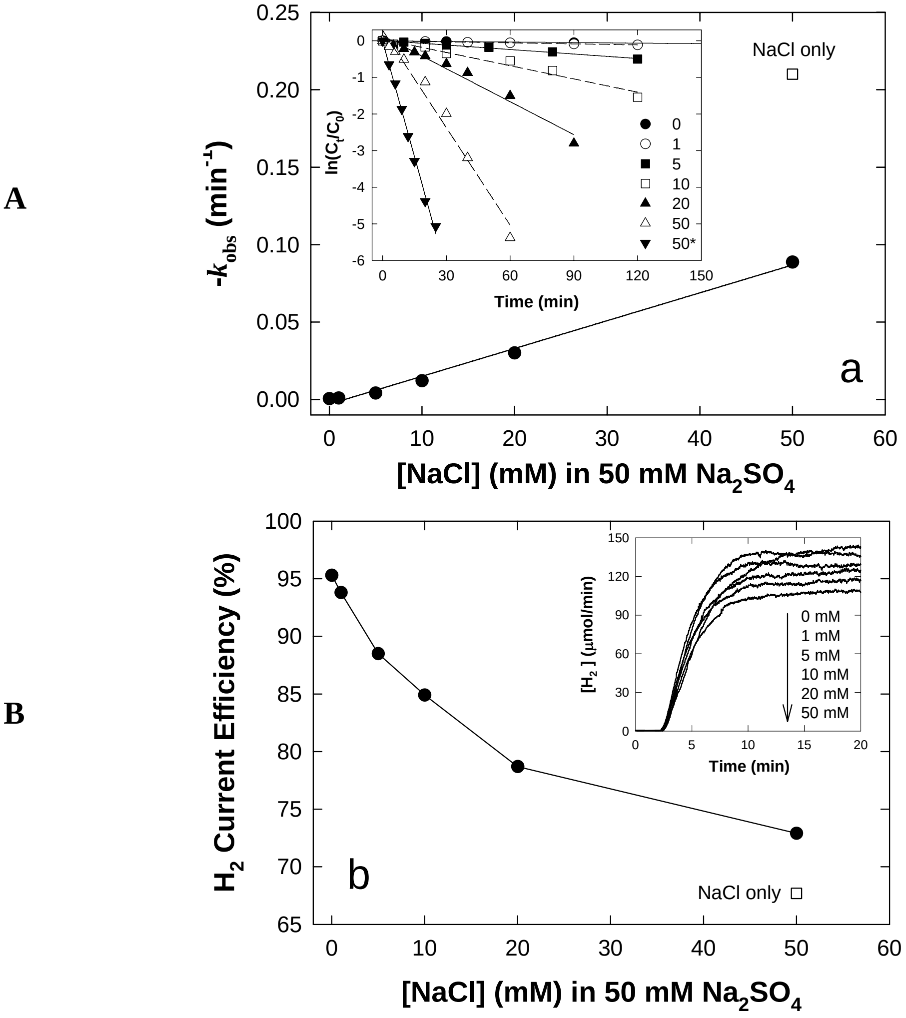

Figure 11.9. Effect of applied cell current (I) on $-k_{obs}$ of phenol. [NaCl] = 50 mM

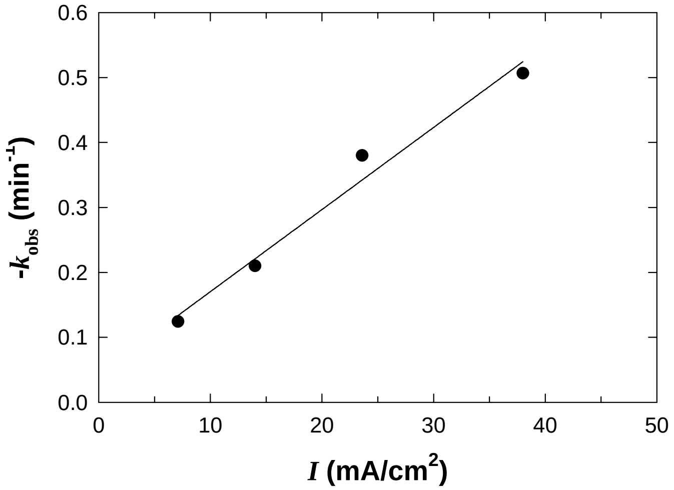

Schemes

Scheme 11.1. Representation of electrochemical reaction network

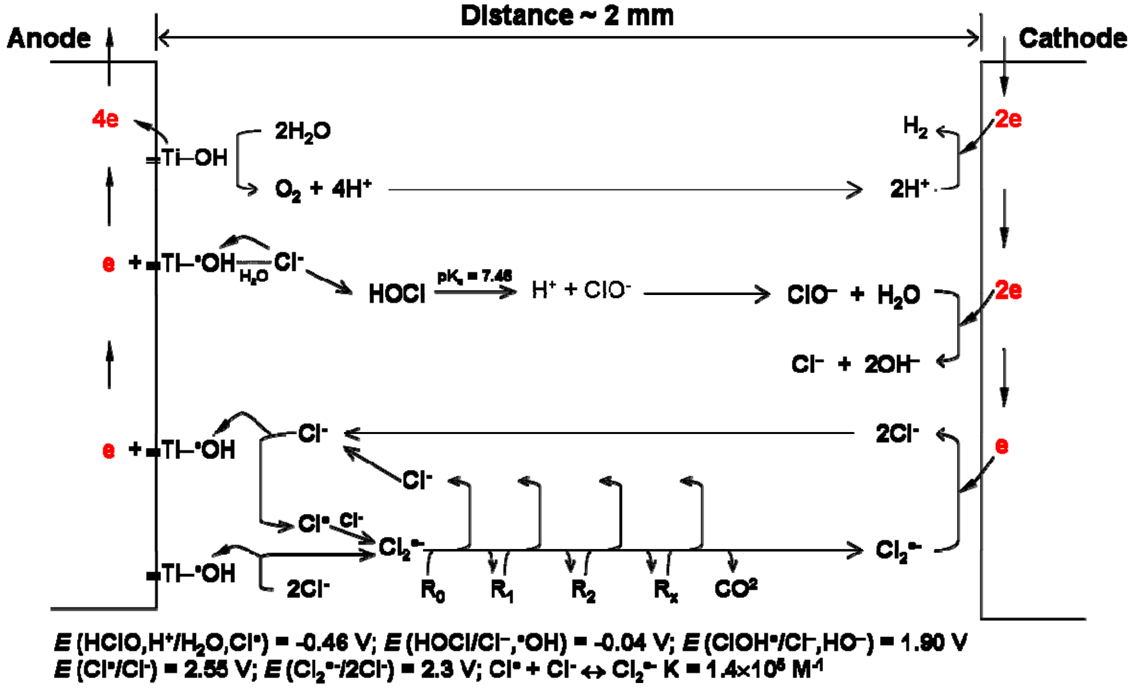

Tables

Table 11.1. Electrochemical reaction rates and properties of the substrates

Substrate	$-k^{S}_{obs}$ (min^{-1})[b] in NaCl	$-k^{S}_{obs}$ (min^{-1})[b] in Na_2SO_4	k_{OH+S} ($M^{-1}s^{-1}$)[e]	$k_{Cl\bullet+S}$ ($M^{-1}s^{-1}$)[f]	$k_{Cl_2^{\bullet-}+S}$ ($M^{-1}s^{-1}$)[f]	k_{HOCl+S} ($M^{-1}s^{-1}$)[g]	$E_{1/2}$ (V_{SCE})[h]	pK_a	E_{cell} (V)[i]	ΔH_2 (µmol /min)[i]	ΔI_{cell} (A)[i]	ΔEE (%)[i]
Methanol			9.7×10^{8}		3.5×10^{3}			15.5	3.10	0	0	0
Formate			3.2×10^{9}	1.3×10^{8}	1.9×10^{6}				3.15	0	0	0
Formic acid			1.3×10^{8}		6.7×10^{3}			3.75				
Acetate			8.5×10^{7}						3.10	0	0	0
Acetic acid			1.6×10^{7}	2.0×10^{8}	$< 1\times10^{4}$			4.76				
Maleic acid			6.0×10^{9}						3.07	+5	0	8.0
Malonic acid			1.6×10^{7}									
Oxalate			7.7×10^{6}						3.05	+7	0	10.2
Oxalic acid			1.4×10^{6}									
PhOH[a]	[c]0.210 (*1*)[d]	[c]5.64×10^{-3} (*1*)	6.6×10^{9} (*1*)	2.5×10^{10}	2.5×10^{8} (*1*)	2.19×10^{4} (*1*)	0.633	9.95	3.10	+20	–0.06	53.1
CC	0.125 (*0.59*)		1.1×10^{10} (*1.67*)				0.507	9.85	3.25	+22	–0.02	27.3
HQ	0.957 (4.55)		5.2×10^{9} (*0.79*)		1.4×10^{9} (*5.6*)	4.5×10^{1} (2.1×10^{-3})	0.507	9.96				
2CP	0.165 (*0.78*)		1.2×10^{10} (*1.81*)			2.42×10^{3} (*0.11*)	0.625	8.29	3.14	+14	–0.04	36.3
4CP	0.119 (*0.57*)		7.6×10^{9} (*1.15*)			2.17×10^{3} (*0.10*)	0.653	9.14	3.18	+20	–0.02	33.3
24CP	0.290 (*1.38*)		7.2×10^{9} (*1.09*)			3.03×10^{2} (*0.014*)	0.645	8.09				
26CP	0.388 (*1.84*)					1.94×10^{2} (8.9×10^{-3})		6.8				
246CP	0.787 (*3.74*)		5.4×10^{9} (*0.82*)			1.28×10^{1} (5.8×10^{-4})	0.637	6.21				
SA	0.0865 (*0.41*)	4.59×10^{-3} (*0.81*)	2.2×10^{10} (*3.33*)		1.1×10^{8} (*0.44*)		0.845 (pH 13)	2.97	3.17	+12	–0.02	31.2
BA	1×10^{-3} (*0.0045*)	7.55×10^{-4} (*0.13*)	4.3×10^{9} (*0.65*)		2×10^{6} (*0.008*)			4.20	3.15	0	0	0

a. PhOH: phenol, CC: catechol, HQ: hydroquinone, 2CP: 2-chlorophenol, 4CP: 4-chlorophenol, 24CP: 2,4-dichlorophenol, 26CP: 2,6-dichlorophenol, 246CP: 2,4,6-trichlorophenol, SA: salicylic acid (2-hydroxy benzoic acid), BA: benzoic acid.

b. The observed pseudo-first order reaction rates of substrates in 50 mM NaCl or 50 mM Na_2SO_4.

c. Concentrations of substrates, 1 ~ 2×10^{-3} M; $I_{cell} = 0.375$ A in 50 mM NaCl or 50 mM Na_2SO_4.

d. The numbers in parenthesis are the reaction rates of the substrate with respect to phenol.

e. See ref. 27

f. See ref. 28 and 29.

g. See ref. 39.

h. Half wave potential measured at pH 5.6 in 50% aqueous isopropyl alcohol unless noted otherwise. For more information see ref 31.
i. At constant cell potential (E_{cell}) a corresponding substrate was added, and then the consequent difference of hydrogen production rate (ΔH_2 = rate after addition – rate before addition), cell current (ΔI_{cell} = current after addition – current before addition), and energy efficiency (ΔEE = (EE after addition – EE before addition) / EE before addition × 100%) were measured and calculated.

Table 11.2. Elementary electrochemical reaction steps

Entry	Reaction	Value
	Reaction Initiation and Generation of Reactive Species	
A1-a	$>\text{Ti-OH} \rightarrow\ >\text{Ti-OH}^{\bullet} + e^-$	I_{an}^{OH}
A1-b	$\equiv\text{Ti-OH}^{\bullet} + H_2O \rightarrow \equiv\text{Ti-OH} + OH^{\bullet} + H^+ + e^-$	I_{an}^{OH}
A2	$\equiv\text{Ti-OH}^{\bullet} + 0.5H_2O \rightarrow \equiv\text{Ti-OH} + 0.25O_2 + H^+ + e^-$	$I_{an}^{O_2}$, k_{O_2}
A3	$\equiv\text{Ti-OH}^{\bullet} + 0.5H_2O + 0.25O_2 \rightarrow \equiv\text{Ti-OH} + 0.5H_2O_2$	$k_{H_2O_2}$
A4-a	$\equiv\text{Ti-OH}^{\bullet} + Cl^- \rightarrow \equiv\text{Ti-OHCl}^{\bullet -}$	k_{OHCl}
A4-b	$\equiv\text{Ti-OHCl}^{\bullet -} + H_2O + H^+ \rightarrow \equiv\text{Ti-OH} + 2H_2O + Cl^{\bullet}$	$k_{OH,Cl}$
A5	$\equiv\text{Ti-OH}^{\bullet} + Cl^- + H_2O \rightarrow \equiv\text{Ti-OH} + HOCl + H^+ + e^-$	
A6	$\equiv\text{Ti-OH}^{\bullet} + R_n \rightarrow \equiv\text{Ti-OH} + R_n^{\bullet}$	$k_{Rn,OH}$
A7-a	$O_2 + e^- \rightarrow O_2^{\bullet -}$	E = – 0.33 V
A7-b	$O_2^{\bullet -} + H^+ \rightarrow HOO^{\bullet}$	$pK_a = 4.88$
A7-c	$2HOO^{\bullet} \rightarrow H_2O_2 + O_2$	
	Reactions of Reactive Species (no distinction between >Ti-OH• and OH•)	
B1	$OH^{\bullet} + Cl^- \rightleftharpoons ClOH^{\bullet -}$	K = 0.70
B2	$ClOH^{\bullet -} + H^+ \rightleftharpoons Cl^{\bullet} + H_2O$	$K = 1.6\times10^{7}$
B3	$Cl^{\bullet} + Cl^{\bullet} \rightarrow Cl_2$	k_{2Cl}
B4a	$Cl^{\bullet} + Cl^- \rightarrow Cl_2^{\bullet -}$	$k = 8.5\times10^{9}\ M^{-1}\ s^{-1}$
B4b	$Cl_2^{\bullet -} \rightarrow Cl^{\bullet} + Cl^-$	$k = 6.0\times10^{4}\ s^{-1}$
B5	$Cl^{\bullet} + Cl_2^{\bullet -} \rightarrow Cl^- + Cl_2$	$k = 1.4\times10^{9}\ M^{-1}\ s^{-1}$
B6	$Cl_2^{\bullet -} + Cl_2^{\bullet -} \rightarrow 2Cl^- + Cl_2$	$k = 3.5\times10^{9}\ M^{-1}\ s^{-1}$
B7	$Cl_2^{\bullet -} + H_2O \rightarrow HOCl + Cl^- + H^+ + e^-$	$k[H_2O] < 1300\ s^{-1}$
B8	$Cl_2^{\bullet -} + OH^{\bullet} \rightarrow HOCl + Cl^-$	
B9	$OH^{\bullet} + OH^{\bullet} \rightarrow H_2O_2$	
B10	$H_2O_2 + OH^{\bullet} \rightarrow HOO^{\bullet} + H_2O$	$k = 3.2\times10^{7}\ M^{-1}\ s^{-1}$
B11	$H_2O_2 + Cl^{\bullet} \rightarrow HOO^{\bullet} + H^+ + Cl^-$	$k = 2.0\times10^{9}\ M^{-1}\ s^{-1}$
B12	$H_2O_2 + Cl_2^{\bullet -} \rightarrow HOO^{\bullet} + H^+ + 2Cl^-$	$k = 1.4\times10^{5}\ M^{-1}\ s^{-1}$
B13	$HOO^{\bullet} + Cl_2^{\bullet -} \rightarrow O_2 + H^+ + 2Cl^-$	$k = 3.1\times10^{9}\ M^{-1}\ s^{-1}$

B14	$H_2O_2 + Cl^- + H^+ \rightarrow HClO + H_2O$	
B15	$H_2O_2 + HClO \rightarrow H_2O + O_2 + H^+ + Cl^-$	
B16	$HClO \rightleftharpoons H^+ + ClO^-$	$pK_a = 7.46$
B17	$HClO + H^+ \rightleftharpoons Cl^+ + H_2O \rightleftharpoons H_2ClO^+$	
B18	$2HClO + H^+ \rightarrow Cl_2O + H^+ + H_2O$	
B19	$HClO + H^+ + Cl^- \rightarrow Cl_2 + H_2O$	
B20	$HClO + 0.5H_2O \rightarrow 1/3ClO_3^- + 2/3Cl^- + 2H^+ + 0.25O_2 + e^-$	

Reactions of Reactive Species with Substrates

C1	$OH^\bullet + H\text{-}Ph\text{-}OH \rightarrow\rightarrow$ Degradation products	
C2	$H_2O_2 + H\text{-}Ph\text{-}OH \rightarrow\rightarrow$ Degradation products	
C3	$HClO + PhOH \rightarrow\rightarrow$ Degradation products	
C4	$Cl^\bullet + H\text{-}Ph\text{-}OH \rightarrow\rightarrow$ Degradation products	
C5-a	$Cl_2^{\bullet -} + H\text{-}Ph\text{-}OH \rightarrow H\text{-}Ph^{\bullet +}\text{-}OH + 2Cl^-$	
C5-b	$H\text{-}Ph^{\bullet +}\text{-}OH + \rightleftharpoons H\text{-}Ph\text{-}O^\bullet + H^+$	$pK_a = -2.0$
C5-c	$H\text{-}Ph\text{-}O^\bullet + Cl_2^{\bullet -} \rightarrow Cl\text{-}Ph\text{-}OH + Cl^-$	
C5-d	$Cl\text{-}Ph\text{-}OH + Cl_2^{\bullet -} \rightarrow\rightarrow$ Degradation products	

Annihilation of Reactive Species

D1	$Cl^\bullet + e^- \rightarrow Cl^-$	E = 2.4 V
D2	$Cl_2^{\bullet -} + e^- \rightarrow 2Cl^-$	E = 2.0 V
D3a	$HClO + H^+ + e^- \rightarrow 0.5Cl_2 + H_2O$	E = 1.63 V
D3b	$HClO + H^+ + 2e^- \rightarrow Cl^- + H_2O$	E = 1.49 V
D3a	$ClO^- + 2e^- + H_2O \rightarrow Cl^- + 2OH^-$	E = 0.90 V

Cathodic Hydrogen and Oxygen Production

E1	$O_2 + 4H^+ + 4e^- \rightarrow 2H_2O$	E = 1.23 V
E2	$H_2O + e^- \rightarrow 0.5H_2 + OH^-$	E = - 0.83 V

References

(1) *International Energy Outlook 2006*; Energy Information Administration.

(2) Penner, S. S. *Energy* **2006**, *31*, 33.

(3) *Solar and Wind Technologies for Hydrogen Production*, available at http://www.hydrogen.energy.gov/congress_reports.html.

(4) Ivy, J. *Summary of Electrolytic Hydrogen Production: Milestone Completion Report*, available at www.nrel.gov/hydrogen/pdfs/36734.pdf.

(5) Kroposki, B.; Levene, J.; Harrison, K.; P.K., S.; Novachek, F. *Electrolysis: Information and opportunities for electric power utilities*, available at http://www.osti.gov/bridge.

(6) *Water and Wastewater Industry Energy Efficiency: A Research Roadmap*, available at http://www.energy.ca.gov/2004publications/CEC.

(7) Park, H.; Vecitis, C. D.; Choi, W.; Weres, O.; Hoffmann, M. R. *J. Phys. Chem. C* **2008**, *112*, 885.

(8) Park, H.; Vecitis, C. D.; Hoffmann, M. R. *J. Phys. Chem. A* **2008**, *112*, 7616.

(9) Weres, O. *National Science Foundation Phase I Final Report (SRC-020)* **1995**.

(10) Comninellis, C.; Nerini, A. *J. Appl. Electrochem.* **1995**, *25*, 23.

(11) Lin, S. H.; Shyu, C. T.; Sun, M. C. *Water Res.* **1998**, *32*, 1059.

(12) Bonfatti, F.; Ferro, S.; Lavezzo, F.; Malacarne, M.; Lodi, G.; De Battisti, A. *J. Electrochem. Soc.* **2000**, *147*, 592.

(13) Korbahti, B. K.; Salih, B.; Tanyolac, A. *J. Chem. Technol. Biotechnol.* **2002**, *77*, 70.

(14) Wang, J. K.; Farrell, J. *Environ. Sci. Technol.* **2004**, *38*, 5232.

(15) Fino, D.; Jara, C.; Saracco, G.; Specchia, V.; Spinelli, P. *J. Appl. Electrochem.* **2005**, *35*, 405.

(16) Rajkumar, D.; Kim, J. G.; Palanivelu, K. *Chem. Eng. Technol.* **2005**, *28*, 98.

(17) Bonfatti, F.; De Battisti, A.; Ferro, S.; Lodi, G.; Osti, S. *Electrochim. Acta* **2000**, *46*, 305.

(18) Martinez-Huitle, C. A.; Ferro, S.; De Battisti, A. *Electrochem. Solid State Lett.* **2005**, *8*, D35.

(19) Nikolaevsky, R.; Monosov, M.; Monosov, E.; Sharony, E.; Gurevich, D. *Method for Purification of Wastewater from Soluble Substances;* U.S. Patent 5,792,336; Aug. 11, **1998**.

(20) Zhan, X. M.; Wang, J. L.; Wen, X. H.; Qian, Y. *Environ. Technol.* **2001**, *22*, 1105.

(21) Naumczyk, J.; Szpyrkowicz, L.; ZilioGrandi, F. *Water Sci. Technol.* **1996**, *34*, 17.

(22) Weres, O. *Electrode with Surface Comprising Oxides of Titanium and Bismuth and Water Purification Process Using This Electrode,* U.S. Patent 0,000,774 A1, Jan. 4, **2007**.

(23) Murugananthan, M.; Yoshihara, S.; Rakuma, T.; Uehara, N.; Shirakashi, T. *Electrochim. Acta* **2007**, *52*, 3242.

(24) Kaba, L.; Hitchens, G. D.; Bockris, J. O. *J. Electrochem. Soc.* **1990**, *137*, 1341.

(25) Zhu, X.; Shi, S.; J, W.; Lu, F.; Zhao, H.; Kong, J.; He, Q.; Ni, J. *Environ. Sci. Technol.* **2007**, *41*, 6541.

(26) Torres, R. A.; Torres, W.; Peringer, P.; Pulgarin, C. *Chemosphere* **2003**, *50*, 97.

(27) Buxton, G. V.; Greenstock, C. L.; Helman, W. P.; Ross, A. B. *J. Phys. Chem. Ref. Data* **1988**, *17*, 513.

(28) Yu, X. Y. *J. Phys. Chem. Ref. Data* **2004**, *33*, 747.

(29) Neta, P.; Huie, R. E.; Ross, A. B. *J. Phys. Chem. Ref. Data* **1988**, *17*, 1027.

(30) Kesselman, J. M.; Weres, O.; Lewis, N. S.; Hoffmann, M. R. *J. Phys. Chem. B* **1997**, *101*, 2637.

(31) Wardman, P. *J. Phys. Chem. Ref. Data* **1989**, *18*, 1637.

(32) Buxton, G. V.; Bydder, M.; Salmon, G. A.; Williams, J. E. *Phys. Chem. Chem. Phys.* **2000**, *2*, 237.

(33) Gilbert, B. C.; Stell, J. K.; Peet, W. J.; Radford, K. J. *J. Chem. Soc.—Faraday Trans. I* **1988**, *84*, 3319.

(34) Buxton, G. V.; Bydder, M.; Salmon, G. A. *J. Chem. Soc.—Faraday Trans.* **1998**, *94*, 653.

(35) Alegre, M. L.; Gerones, M.; Rosso, J. A.; Bertolotti, S. G.; Braun, A. M.; Martire, D. O.; Gonzalez, M. C. *J. Phys. Chem. A* **2000**, *104*, 3117.

(36) Hasegawa, K.; Neta, P. *J. Phys. Chem.* **1978**, *82*, 854.

(37) Padmaja, S.; Neta, P.; Huie, R. E. *J. Phys. Chem.* **1992**, *96*, 3354.

(38) Anslyn, E. V.; Dougherty, D. A. *Modern Physical Organic Chemistry*; University Science Books: Sausalito, CA, **2006**.

(39) Richard, J. P.; Jencks, W. P. *J. Am. Chem. Soc.* **1982**, *104*, 4689.

(40) Gallard, H.; von Gunten, U. *Environ. Sci. Technol.* **2002**, *36*, 884.

(41) Ferro, S.; De Battisti, A.; Duo, I.; Comninellis, C.; Haenni, W.; Perret, A. *J. Electrochem. Soc.* **2000**, *147*, 2614.

(42) Vione, D.; Maurino, V.; Minero, C.; Calza, P.; Pelizzetti, E. *Environ. Sci. Technol.* **2005**, *39*, 5066.

(43) Moye, C. J.; Sternhel, S. *Aust. J. Chem.* **1966**, *19*, 2107.

(44) Hori, H.; Yamamoto, A.; Hayakawa, E.; Taniyasu, S.; Yamashita, N.; Kutsuna, S. *Environ. Sci. Technol.* **2005**, *39*, 2383.

(45) Canizares, P.; Saez, C.; Lobato, J.; Rodrigo, M. A. *Ind. Eng. Chem. Res.* **2004**, *43*, 6629.